UNIVERSIDADE FEDERAL DE MINAS GERAIS
Instituto de Ciências Exatas
Programa De Pós-graduação em Física

Gabriel Bruno Garcia De Souza

THERMOELECTRIC PROPERTIES OF $M_2AgAlBr_6$ DOUBLE PEROVSKITES / MOLECULAR DYNAMICS STUDY OF TRANSITION METAL DICHALCOGENIDES USING MACHINE LEARNING FORCE FIELDS

Belo Horizonte
2025

Gabriel Bruno Garcia de Souza

THERMOELECTRIC PROPERTIES OF $M_2AgAlBr_6$ DOUBLE PEROVSKITES / MOLECULAR DYNAMICS STUDY OF TRANSITION METAL DICHALCOGENIDES USING MACHINE LEARNING FORCE FIELDS

Tese apresentada ao Programa de Pós-Graduação em Física do Instituto de Ciências Exatas da Universidade Federal de Minas Gerais como requisito parcial para obtenção do título de Doutor em Ciências.

Orientador: Von Braun Nascimento

Coorientadora: Rosângela de Paiva

Belo Horizonte

2025

Dados Internacionais de Catalogação na Publicação (CIP)

S729t Souza, Gabriel Bruno Garcia de.
Thermoelectric properties of M2AgAlBr6 double perovskites/Molecular dynamics study of Transition Metal Dichalcogenides using Machine Learning Force Fields / Gabriel Bruno Garcia de Souza. – 2025.
177 f. : il.

Orientador: Von Braun Nascimento.
Coorientadora: Rosangela de Paiva.
Tese (doutorado) – Universidade Federal de Minas Gerais, Departamento de Física.
Bibliografia: f. 128-148.

1. Aprendizado do computador. 2. Redes neurais. 3. Dinâmica molecular. 4. Teoria do funcional da densidade. I. Título. II. Nascimento, Von Braun. III. Paiva, Rosangela de. IV. Universidade Federal de Minas Gerais, Departamento de Física.

CDU – 539.2 (043)

Ficha catalográfica elaborada por Romário Martins Ribeiro – CRB6 3595
Biblioteca Professor Manoel Lopes de Siqueira – Departamento de Física - UFMG

UNIVERSIDADE FEDERAL DE MINAS GERAIS

ATA

ATA DA SESSÃO DE ARGUIÇÃO DA 452ª TESE DO PROGRAMA DE PÓS-GRADUAÇÃO EM FÍSICA, defendida por **GABRIEL BRUNO GARCIA DE SOUZA** orientado pelo professor Von Braun Nascimento e coorientado pela professora Rosângela de Paiva (Departamento de Estatística, Física e Matemática/UFSJ) para obtenção do grau de **DOUTOR EM CIÊNCIAS, área de concentração Física**. Às quinze horas do dia vinte e oito de novembro de dois mil e vinte e cinco reuniu-se, por videoconferência, a Comissão Examinadora composta pelos professores **Von Braun Nascimento** (Orientador - Departamento de Física/UFMG), **Rosângela de Paiva** (Coorientadora - DEFIM/UFSJ), **Mário Sérgio Carvalho Mazzoni** (Departamento de Física/UFMG), **Lucas Alvares da Silva Mól** (Departamento de Física/UFMG), **David Paul Landau** (University of Georgia/UGA), **Silvio Antonio Sachetto Vitiello** (Instituto de Física Gleb Wataghin/UNICAMP) e **Júlio César Siqueira Rocha** (Departamento de Física/UFOP) para dar cumprimento ao Artigo 37 do Regimento Geral da UFMG, submetendo **GABRIEL BRUNO GARCIA DE SOUZA** à arguição de seu trabalho, que recebeu o título de **"Thermoelectric properties of $M_2AgAlBr_6$ double perovskites/Molecular dynamics study of Transition Metal Dichalcogenides using Machine Learning Force Fields"**. O candidato fez uma exposição oral de seu trabalho durante aproximadamente 50 minutos. Após esta, os membros da comissão prosseguiram com a sua arguição, e apresentaram seus pareceres individuais sobre o trabalho, concluindo pela aprovação do candidato.

Belo Horizonte, 28 de novembro de 2025.

Prof. Von Braun Nascimento
Orientador do estudante
Departamento de Física/UFMG

Profa. Rosângela de Paiva
Coorientadora do estudante
Departamento de Estatística, Física e Matemática/UFSJ

Prof. Mário Sérgio Carvalho Mazzoni
Departamento de Física/UFMG

Prof. Lucas Alvares da Silva Mól
Departamento de Física/UFMG

Prof. David Paul Landau
University of Georgia (UGA)

Prof. Silvio Antonio Sachetto Vitiello
Instituto de Física Gleb Wataghin/UNICAMP

Prof. Júlio César Siqueira Rocha
Departamento de Física/UFOP

CANDIDATO: Gabriel Bruno Garcia de Souza

De acordo com o Regulamento do Programa, para dar andamento ao processo de efetivação do grau obtido, o candidato deverá, no prazo máximo de 01 (um) mês após a aprovação da sua dissertação ou tese, encaminhar à Secretaria a versão final da mesma.

Documento assinado eletronicamente por **Von Braun Nascimento**, **Professor do Magistério Superior**, em 02/12/2025, às 16:35, conforme horário oficial de Brasília, com fundamento no art. 5º do Decreto nº 10.543, de 13 de novembro de 2020.

Documento assinado eletronicamente por **Gabriel Bruno Garcia de Souza**, **Usuário Externo**, em 02/12/2025, às 18:22, conforme horário oficial de Brasília, com fundamento no art. 5º do Decreto nº 10.543, de 13 de novembro de 2020.

Documento assinado eletronicamente por **Lucas Alvares da Silva Mol**, **Professor do Magistério Superior**, em 02/12/2025, às 19:06, conforme horário oficial de Brasília, com fundamento no art. 5º do Decreto nº 10.543, de 13 de novembro de 2020.

Documento assinado eletronicamente por **David Paul Landau**, **Usuário Externo**, em 02/12/2025, às 19:53, conforme horário oficial de Brasília, com fundamento no art. 5º do Decreto nº 10.543, de 13 de novembro de 2020.

Documento assinado eletronicamente por **Julio Cesar Siqueira Rocha**, **Usuário Externo**, em 03/12/2025, às 11:41, conforme horário oficial de Brasília, com fundamento no art. 5º do Decreto nº 10.543, de 13 de novembro de 2020.

Documento assinado eletronicamente por **Rosangela de Paiva**, **Usuária Externa**, em 03/12/2025, às 13:36, conforme horário oficial de Brasília, com fundamento no art. 5º do Decreto nº 10.543, de 13 de novembro de 2020.

A autenticidade deste documento pode ser conferida no site https://sei.ufmg.br/sei/controlador_externo.php?acao=documento_conferir&id_orgao_acesso_externo=0, informando o código verificador **4775226** e o código CRC **D96FB2FB**.

Referência: Processo nº 23072.273196/2025-78 SEI nº 4775226

I dedicate this thesis in memoriam of Maria do Carmo Garcia e Silva (1943–2023) and Maria José de Carvalho Souza (1928–2019).

Acknowledgements

First and foremost, I would like to express my sincere gratitude to Dr. Von Braun Nascimento for his exceptional guidance, mentorship, and encouragement throughout these four years of my doctoral studies. His insight and support have been invaluable to both my professional and personal growth.

I am deeply grateful to my family for their constant love and support during my journey as a physicist and researcher, especially my father, Wellington Carvalho de Souza, my mother, Valéria Garcia e Silva, and my grandfather, João de Oliveira e Silva.

I would also like to extend my gratitude to Dr. David Paul Landau, who served as my unofficial co-advisor through the International Cooperative Agreement (ICA) between UFMG and the University of Georgia (UGA). His guidance and support provided me with the invaluable opportunity to study in the United States, thereby fulfilling one of my greatest dreams. I also thank everyone I met during my time at the Center for Simulational Physics (CSP) at UGA, particularly Steven Bennett Hancock for his stimulating discussions and Dr. Shan-Ho Tsai for his technical expertise and assistance at the Georgia Advanced Computing Resource Center (GACRC).

I wish to thank my co-advisor, Dr. Rosângela de Paiva from the Universidade Federal de São João del-Rei (UFSJ), for her continuous support and for all the knowledge and experience shared during these years.

I am grateful to my research group colleagues, João Victor Campos, Luiza Andrade, Ariel Sousa and Pietra Lanciotti, as well as to my friends from the Physics Department, especially Laura Detoni, Catarina Haase, and Lucas Menicucci, for their companionship and encouragement.

I also wish to thank my friends outside the academic environment, especially Paulo Cacau, Bernardo Lemos, and William Velasquez, for their friendship and support throughout this journey.

My appreciation extends to all professors, technical staff, and administrative personnel of UFMG, particularly those from ICEx and the Department of Physics, for providing a stimulating and supportive academic environment.

Finally, I acknowledge the financial support received from CNPq for the doctoral scholarship, CAPES for funding my sandwich doctorate through the CAPES/PrInt program, FAPEMIG for supporting our laboratory, and the University of Georgia and the Simons Foundation for partial financial support.

Resumo

O primeiro capítulo desta tese é destinado ao estudo das propriedades estruturais, eletrônicas e termoelétricas dos compostos $K_2AgAlBr_6$, $Rb_2AgAlBr_6$ e $Cs_2AgAlBr_6$, pertencentes à classe das perovskitas duplas, utilizando técnicas de primeiros princípios. O objetivo principal deste trabalho é o de determinar a estrutura eletrônica dos compostos $K_2AgAlBr_6$, $Rb_2AgAlBr_6$ e $Cs_2AgAlBr_6$ de modo a obtermos as propriedades termoelétricas desses semicondutores (coeficiente de Seebeck, condutividades térmica e elétrica, fator de potência térmico e figura de mérito). O estudo destes compostos baseado na figura de mérito sugerem que esses materiais possuem potencial para aplicações em dispositivos termoelétricos.

O segundo capítulo desta tese é destinado ao estudo de dinâmica molecular feito sobre as monocamadas dos dicalcogenetos de metais de transição (TMD) MoS_2 e $MoSe_2$ empregando potenciais de interação com precisão semelhante a *ab initio*. Aqui explicamos como usamos o método de pseudopotenciais de ondas planas para criar um banco de dados dos mencionados materiais com base na Teoria do Funcional da Densidade. Esse banco de dados foi utilizado para treinar uma rede neural artificial (ANN) e com o objetivo de desenvolver os potenciais interatômicos. Os resultados revelaram que os potenciais conseguem reproduzir com precisão razoável as curvas de dispersão de fônons, tanto em comparação com dados experimentais quanto com resultados teóricos obtidos por métodos de primeiros princípios. Notavelmente, os potenciais demonstraram uma precisão superior quando comparados aos potenciais semi-empíricos disponíveis na literatura. Além disso, utilizando esses potenciais em simulações de dinâmica molecular, calculamos o espectro dielétrico na faixa de 100 cm^{-1} a 500 cm^{-1}. Ao comparar esses resultados com dados experimentais, observamos uma atividade infravermelha (IR) semelhante nos modos E' e A_2'', em concordância com as observações experimentais. A habilidade de realizar simulações com milhares de átomos permitiu que nosso sistema pudesse acomodar flutuações espontâneas na altura e ondas propagando-se no material. Como resultado delas, nossas simulações sugerem a existência de atividade IR nos modos E' e A_2'', com polarizações invertidas, assim como a presença de atividade IR em frequências próximas a E'' e A_1', que são geralmente considerados inativos no infravermelho.

Palavras-chave: Machine Learning, Redes Neurais, Dinâmica Molecular, Teoria do Funcional da Densidade, Propriedades Termoelétricas, Física Simulacional.

Abstract

The first chapter of this thesis is dedicated to the study of the structural, electronic, and thermoelectric properties of the compounds $K_2AgAlBr_6$, $Rb_2AgAlBr_6$, and $Cs_2AgAlBr_6$, belonging to a class known as double perovskites, using first-principles techniques. The main objective of this work is to determine the electronic structure of the compounds $K_2AgAlBr_6$, $Rb_2AgAlBr_6$, and $Cs_2AgAlBr_6$ in order to obtain the thermoelectric properties of these semiconductors (Seebeck coefficient, thermal and electrical conductivities, thermoelectric power factor, and figure of merit). The study of these compounds based on the figure of merit suggest that these kind of materials are potential candidates for thermoelectric device applications.

The second chapter of this thesis is dedicated to the molecular dynamics study of the transition metal dichalcogenides (TMD) monolayers MoS_2 and $MoSe_2$ using interaction potentials with accuracy similar to *ab initio* methods. Here, we explain how we used the plane-wave pseudopotential method to create a database of the mentioned materials based on Density Functional Theory. This database was used to train an artificial neural network (ANN) with the goal of developing interatomic potentials. The results revealed that the potentials can precisely reproduce phonon dispersion curves, both when compared to experimental data and theoretical results obtained from first-principles methods. Notably, the potentials demonstrated superior accuracy when compared to semi-empirical potentials available in the literature. Additionally, using these potentials in molecular dynamics simulations, we calculated the dielectric spectrum in the range of 100 cm^{-1} to 500 cm^{-1}. When comparing these results with experimental data, we observed similar infrared (IR) activity in the E' and A_2'' modes, in agreement with experimental observations. The ability to perform simulations with thousands of atoms allowed our system to accommodate spontaneous fluctuations in height and waves propagating through the material. As a result, our simulations suggest the existence of IR activity in the E' and A_2'' modes, with reversed polarizations, as well as the presence of IR activity at frequencies near E'' and A_1', which are generally considered IR inactive.

Keywords: Machine Learning, Neural Networks, Molecular Dynamics, Density Functional Theory, Thermoelectric Properties, Simulational Physics.

Contents

Overview

This thesis investigates the properties of materials with technological relevance for energy applications, with emphasis on the thermoelectric behavior of halide double perovskites and the vibrational phenomena in two-dimensional transition metal dichalcogenides (TMDs). The work combines first-principles methodologies with data-driven approaches, aiming both to predict fundamental properties and to expand the applicability of computational simulations to systems of increasing complexity. The manuscript is organized into five main chapters, followed by appendices that present technical details and didactic resources.

Chapter 1 establishes the scientific motivation and introduces the materials investigated. It first reviews perovskite compounds, including single and double perovskites, with particular attention to their structural and electronic features relevant for optoelectronic and thermoelectric applications. Subsequently, it examines transition metal dichalcogenides, focusing on monolayer MoS_2 and $MoSe_2$, and discusses their electronic structure, vibrational characteristics, and the physical significance of rippling phenomena. This introductory chapter sets the stage by contextualizing both classes of materials and explaining their technological and scientific importance.

Chapter 2 develops the theoretical and methodological background necessary for the subsequent analyses. The discussion begins with Density Functional Theory (DFT), which provides the foundation for the first-principles calculations performed throughout the thesis. It then addresses semiclassical Boltzmann transport theory as the formalism used to obtain thermoelectric coefficients, followed by the principles of Molecular Dynamics (MD) simulations for describing finite-temperature phenomena. The chapter further examines the construction and training of Machine Learning Force Fields (MLFFs), which bridge accuracy and efficiency, thereby enabling simulations with thousands of atoms. Finally, it presents the theory of phonons and their interaction with light, which forms the basis for the investigation of vibrational and dielectric properties.

Chapter 3 is devoted to the thermoelectric properties of $M_2AgAlBr_6$ (M = K, Rb, Cs) halide double perovskites. Using a combination of DFT and Boltzmann transport theory, the structural stability, electronic band structure, and transport coefficients of these compounds are systematically characterized. The results indicate that these materials possess direct band gaps within the visible range, favorable electronic states at the band edges, and competitive thermoelectric performance with figures of merit approaching unity near room temperature. Their chemical stability, elemental abundance, and lead-free composition reinforce their potential as sustainable candidates for thermoelectric applications, providing a viable alternative to more established but less environmentally

benign materials.

Chapter 4 shifts the focus to two-dimensional materials and explores the dielectric response of MoS_2 and $MoSe_2$ monolayers using molecular dynamics simulations based on machine learning potentials. Artificial neural networks were trained on extensive DFT datasets to construct interatomic potentials capable of reproducing phonon dispersions with high fidelity. Large-scale MD simulations employing these potentials reveal effects that are inaccessible to either small-scale ab initio calculations or traditional empirical models. In particular, the simulations highlight the role of rippling in activating vibrational modes that are nominally infrared-inactive, thereby modifying the far-infrared dielectric spectra. These findings demonstrate how machine learning approaches provide access to emergent phenomena in extended systems, bridging the gap between accuracy and computational scalability.

Chapter 5 synthesizes the conclusions of the thesis. Two principal outcomes are emphasized: first, that aluminum-based double perovskites are viable candidates for thermoelectric applications, combining favorable optoelectronic and transport properties with environmental safety; and second, that machine learning force fields constitute a powerful tool for the study of two-dimensional materials, capable of uncovering ripple-induced effects with significant implications for thermal and vibrational behavior. The chapter also discusses possible directions for future research, including experimental validation of the thermoelectric performance, exploration of strain and confinement effects in perovskites, and further application of MLFFs to nonlinear phonon interactions and defect-related processes in TMDs.

1 Introduction

This chapter provides an overview of the materials investigated in this thesis. The discussion begins with perovskites (Sec. 1.1), emphasizing their structural and electronic properties relevant for thermoelectric applications. It then turns to the two-dimensional transition-metal dichalcogenides MoS_2 and $MoSe_2$ (Sec. 1.2), highlighting their structural, vibrational, and electronic features. The aim is to present the essential background and context for the systems examined in the subsequent chapters.

1.1 Perovskites

1.1.1 Single Perovskites

The perovskite family is a broad class of compounds with stoichiometry ABX_3, where "A" denotes a cation, "B" typically a transition metal, and "X" an anion—most commonly oxygen in oxide perovskites or a halogen in halide perovskites. This family was named after the mineralogist Lev Perovski after the calcium titanite mineral ($CaTiO_3$) was discovered in 1839 [1]. Later, the name was used to designate not only the original discovered mineral but all materials with the structure shown in Figure 1.1a). The figure also shows how diverse the family of perovskites are as they can be formed with a vast majority of the periodic table. Furthermore, the "A" site can be occupied nor only with a atomic cation but can be an organic cation which is the case for Methylammonium lead iodide ($CH_3NH_3PbI_3$ or $MAPbI_3$), with $CH_3NH_3^+$ (MA^+) being "A" [3]. As one can see, there is a wide range of materials that can form the perovskite structure and consequently, these compounds present interesting and diverse physical properties such as ferroelectricity [4],

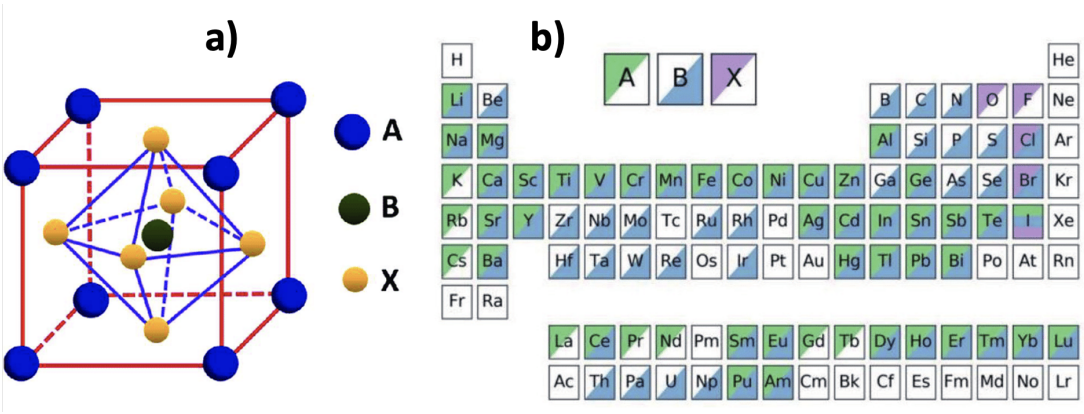

Figure 1.1 – (a) Arrangement of atoms in the ABX_3 cubic perovskite structure and (b) Elements which can be utilized to form perovskite structures. Adapted from Ref. [2].

piezoelectricity [5,6], magnetism [7], superconductivity [8] and catalysis [9] just to mention a few of them. Moreover, research on the formability of potential perovskites has primarily focused on examining the Goldschmidt tolerance factor [10]:

$$t = \frac{1}{\sqrt{2}} \frac{(r_A + r_X)}{(r_B + r_X)} \tag{1.1}$$

where r_i $(i = A, B, X)$ are the ionic radii if the constituent atoms. This happens because in a perfect cubic perovskite structure, twice the B–X bond length equals the unit lattice constant, and twice the A–X bond length equals the face diagonal of the cubic cell. Therefore, if the bond distance is considered as the sum of the two ionic radii, the Goldschmidt factor would be exactly $t = 1$ for a perfect cubic perovskite. Experimentally, most materials with a perfect cubic perovskite structure occur with t between the range 0.8-0.9 [11].

A significant portion of the physical properties of perovskites originates from the arrangement and distortion of the BX_6 octahedra. As illustrated in Figure 1.2, the structural phase of a perovskite is closely linked to the tilting patterns of these octahedra. In the high-symmetry cubic phase (Figure 1.2a), the octahedra are perfectly aligned, exhibiting no tilting, which typically results in optimal overlap between atomic orbitals and is thus highly desirable for optoelectronic applications. In the tetragonal phase (Figure 1.2b), the octahedra rotate around the crystallographic *c*-axis, introducing an in-plane tilt that lowers the symmetry. In the orthorhombic phase (Figure 1.2c), additional out-of-plane tilting occurs, resulting in a more distorted structure. These subtle distortions in the tilt angles, both in-plane and out-of-plane, significantly influence key material properties such as the electronic band gap, carrier mobility, and dielectric response [13]. Consequently,

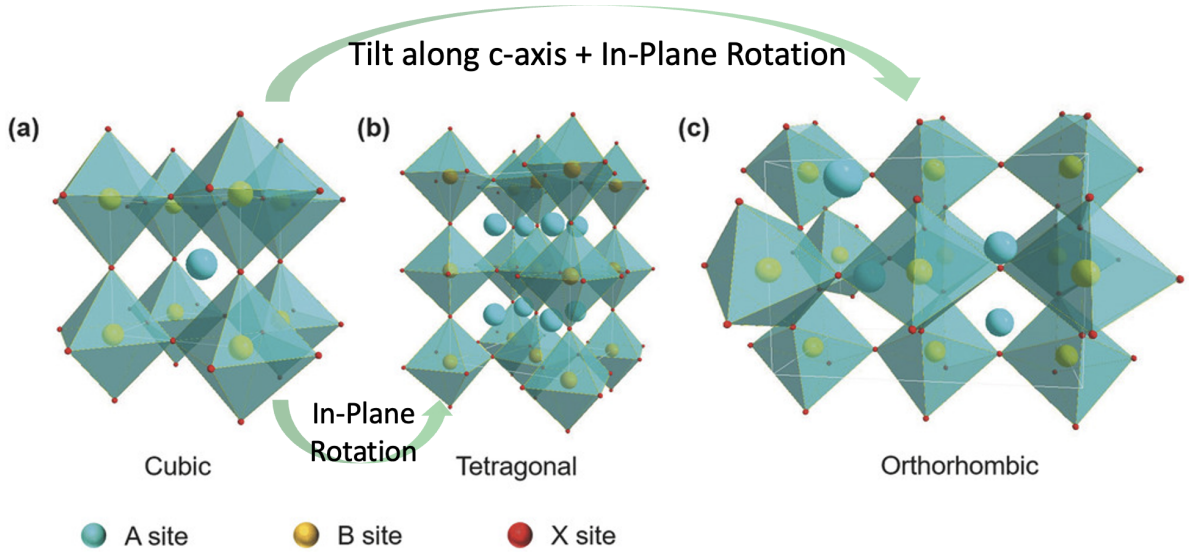

Figure 1.2 – Crystal structures of perovskite materials with different symmetries: a) cubic phase, b) tetragonal phase, and c) orthorhombic phase. Adapted from Ref. [12]

understanding and controlling octahedral tilting is essential for tuning the functionality of perovskite-based materials.

These materials have been also widely investigated in the last decade due to their photovoltaic capability [14], with perovskite solar cells reaching a power conversion efficiency larger than 25% [15] which is suitable for commercial purposes. Also, metal halide perovskites could serve as a renewable energy source not only as photovoltaic cells but also as thermoelectric materials due to very low thermal conductivity [16–18] and this means that they can directly convert heat energy into electric energy through the movement of their charge carriers, consequently producing clean energy. Until nowadays, most of the work regarding metal halide perovskites has focused on lead-based ones, i.e., $MAPbI_3$, $CsPbI_3$ or $FAPbI_3$ [3, 19, 20]. Those presented the best performance in solar cell applications. However, two main issues impede their use in practical devices: *i*) the lead toxicity; *ii*) their chemical instability [21]. Since then, recent literature on the subject has seen a great effort in the search for perovskites that do not contain lead in their composition, which are known as *Lead Free Perovskites* [22].

1.1.2 Double Perovskites

One way to overcome the problems related to the toxicity and instability of the lead element is to replace the divalent Pb^{2+} in perovskite halides with a combination of monovalent and trivalent metals to form a double perovskite structure with the form $A_2B^+B^{3+}X_6$ ($A_2BB'X_6$). Recent review articles on these compounds suggest that double perovskites represent the main alternative to lead-based halide perovskites [23, 24]. An example of the arrangement of a double perovskite is shown at Figure 1.3 in which the BX_6 and $B'X_6$ octahedra are arranged in a checkerboard pattern and , due to their similarities to single perovskites, the Goldschmidt factor can also be used to determine if they can form a cubic structure by exchanging r_B by the mean of the B and B' atomic radii $(r_B + r_{B'})/2$. Maybe one of the most investigated double perovskites is $Cs_2AgBiBr_6$, which has been the focus of several experimental [26] and theoretical studies [27–29]. Absorption efficiency in the visible range of the solar spectrum as well as impressive moisture and optical stabilities [30–32] have been reported for $Cs_2AgBiBr_6$. Another stable perovskite that was recently investigated and showed interesting results concerning indirect-direct gap engineering was $Cs_2AgSbCl_6$ [33–36]. The introduction of the element indium at double perovskites structures have shown promising results on finding alternatives for $MAPbI_3$. Density functional theory (DFT) calculations performed for $Cs_2InBiCl_6$ and $Cs_2InSbCl_6$ showed that both have direct band gaps of 0.91 eV and 1.02 eV respectively [37]. Unfortunately, the instability of the ion In^+ impede their synthesis and practical applications. Furthermore, most experimentally synthesized inorganic double perovskites, such as $Cs_2AgInCl_6$ ($t = 0.94$) [38], $Cs_2AgSbCl_6$ ($t = 0.93$) [39], and $Cs_2AgBiBr_6$ ($t = 0.93$) [40], exhibit tolerance factors close to 1. As

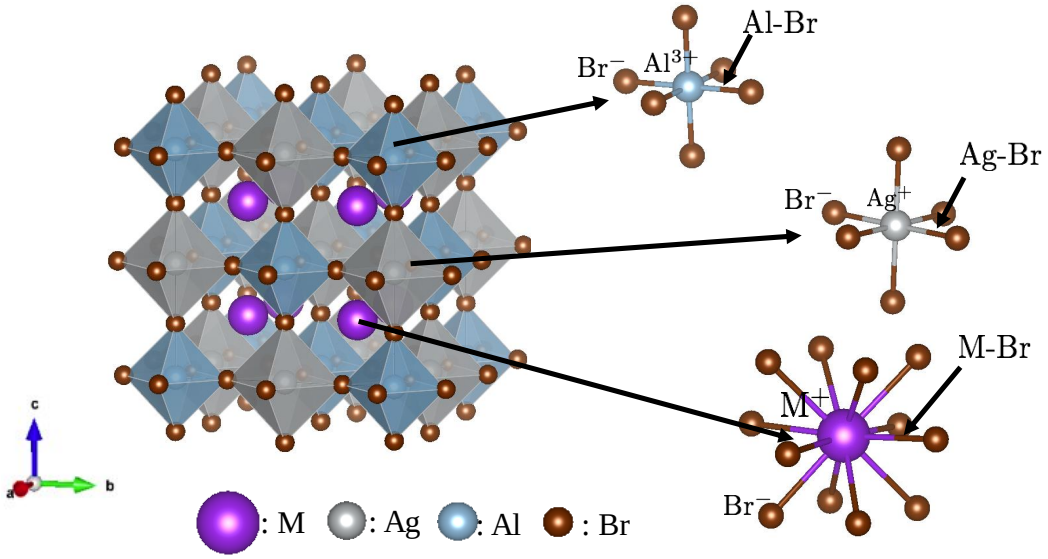

Figure 1.3 – Crystal structure of face-centered-cubic double perovskite $M_2AgAlBr_6$ (M = K, Rb, Cs) and coordination environments around Al^{3+}, Ag^{+}, and M^{+}. Reproduced from Ref. [25]

a result, these compounds crystallize in the cubic phase at room temperature. However, most current studies on double perovskites are theoretical. Only a small fraction of the investigated compounds have been successfully synthesized and properly characterized.

The role of aluminum in known double perovskites has also been the subject of research [41, 42]. For example, L. Li *et al.* [43] synthesized Al^{+3} doped $Cs_2AgBiCl_6$ and reported that the doped compound presented a direct band-gap unlike indirect gap known for the undoped one, which enhanced significantly its photo-luminescence efficiency. Moreover, Ghosh and Sil [44] reported that the formation of perovskite thin films with aluminum chloride ($AlCl_3$) exhibited enhanced photo-luminescence and photo-response. Motivated by the latter study and by the abundance and low toxicity of aluminum, Tian-Yu Tang *et. al.* [45] investigated theoretically the properties of aluminum-based double perovskites with the form M_2AgAlX_6 (M = Cs, Rb, K; X = Cl, Br, I). Since all of their compounds had a expected tolerance factor of at least 0.9, all of those compounds may be able to form double perovskites. Tang *et. al.* also calculated the formation energies for $Cs_2AgAlCl_6$ (-0.82 eV), $Cs_2AgAlBr_6$ (-0.32 eV), Cs_2AgAlI_6 (1.64 eV), $Rb_2AgAlBr_6$ (-0.31 eV) and $K_2AgAlBr_6$ (-0.52 eV), indicating the thermodynamic stability of all compounds but Cs_2AgAlI_6. They have also been noted for their suitability in photovoltaic applications, owing to the direct band gaps ranging from 0.773 eV to 3.430 eV observed among the studied compounds. Another theoretical study reported the structural, electronic, optical, and transport properties for A_2AgAlI_6 (A = Rb, K, Na) [46]. In particular, we believe that $M_2AgAlBr_6$, illustrated in Figure 1.3, deserves more detailed theoretical investigation, especially for the cases where M = K or Rb, due to the abundance of these elements in the Earth's crust and their

potential economic advantage for large-scale applications. A preliminary analysis of carrier mobility had already been conducted by Tang *et al.*, who calculated effective masses for electrons and holes in the material. However, a comprehensive investigation of its transport properties remains absent from the literature. In this context, the work developed in Chapter 3 aims to address this gap by exploring the carrier transport mechanisms in $M_2AgAlBr_6$.

In general, double perovskites often exhibit very stable and robust crystal structures, making them attractive for practical applications in renewable energy and electronics. They provide a pathway to develop non-toxic, lead-free materials with optoelectronic properties comparable to traditional lead-based perovskites, addressing environmental and health issues and the ability to select and combine different B-site cations enables precise control over bandgap, conductivity and other properties, which is crucial for optimizing devices such as solar cells, LEDs, sensors, and photocatalysts [47].

1.2 Transition Metal Dichalcogenides

Transition Metal Dichalcogenides (TMDs) form a well established class of layered materials, with compounds than can potentially be used to produce 2D crystals. Its most common have the stoichiometry MX_2 with M being a transition metal atom from group IV (e.g., Ti, Zr, Hf), group V (e.g., Nb, Ta) or group VI (e.g., Mo,W) and X belonging to the chalcogen family (e.g., X = S, Se, Te). MX_2 monolayers are composed of a single layer of metal atoms sandwiched between two layers of chalcogen atoms and in which the bond between those layer are predominately covalent. In the bulk form, these monolayers are stacked together through weak van der Waals interactions.

Layered TMDs exhibit three main polymorphs, determined by the way successive layers of chalcogen-metal-chalcogen (X–M–X) units are stacked. These are denoted as 1T, 2H, and 3R, corresponding to octahedral, hexagonal, and rhombohedral symmetries, respectively. The terminology "1T", "2H", and "3R" reflects both the coordination of the metal atom and the periodicity of the stacking sequence. In the 1T phase, each metal atom is coordinated octahedrally by six chalcogen atoms, and the layers stack directly on top of each other in an AAA sequence, meaning all layers are aligned. In the 2H phase, which is the most stable for many semiconducting TMDs such as MoS_2 and $MoSe_2$, the metal atoms are coordinated trigonal-prismatically, and the stacking follows an $ABAB$ sequence: alternating layers are shifted relative to each other, producing hexagonal symmetry. Finally, in the 3R phase, the coordination is also trigonal prismatic, but the layers follow an $ABCABC$ sequence, where each successive layer is shifted relative to the one below in a three-layer repeating pattern, giving rise to rhombohedral symmetry. These differences in stacking order, illustrated in Figures 1.4 and 1.5, in which the latter highlights the relative displacements between

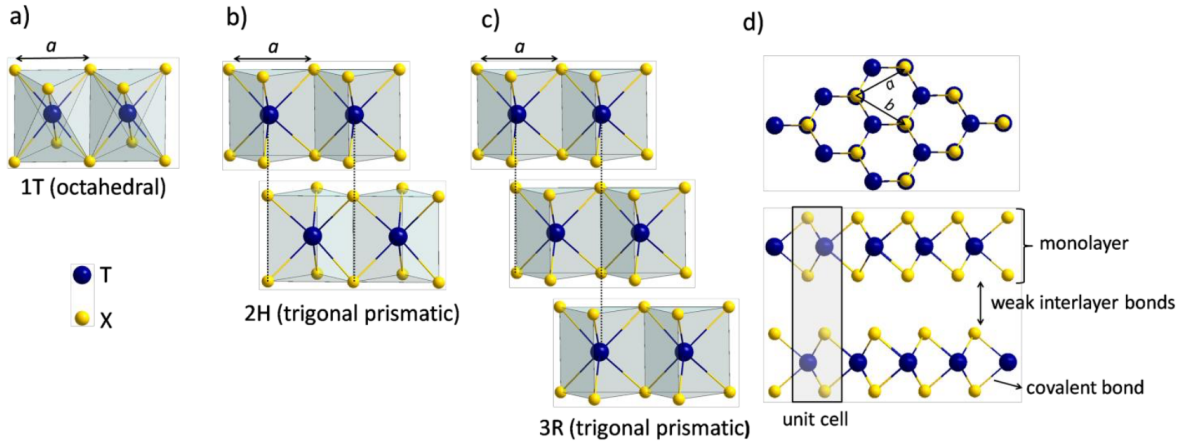

Figure 1.4 – Crystal structures of MX_2 monolayers in their main polymorphs: (a) 1T (octahedral), (b) 2H (trigonal prismatic), and (c) 3R (trigonal prismatic) phases, differing by stacking order. (d) Highlights the in-plane atomic arrangement and unit cell. Reproduced from Ref. [48].

adjacent MoS_2 hexagonal layers. These patterns not only define the symmetry of the crystal but also influence its electronic and vibrational properties. It is known that, for those materials, the 2H polymorph is the most stable phase, being the most common in mechanically exfoliated crystals. Moreover, it has been shown that alternative forms of TMD, such as fullerene-like [49] structures and nanotubes [50], can also be synthesized.

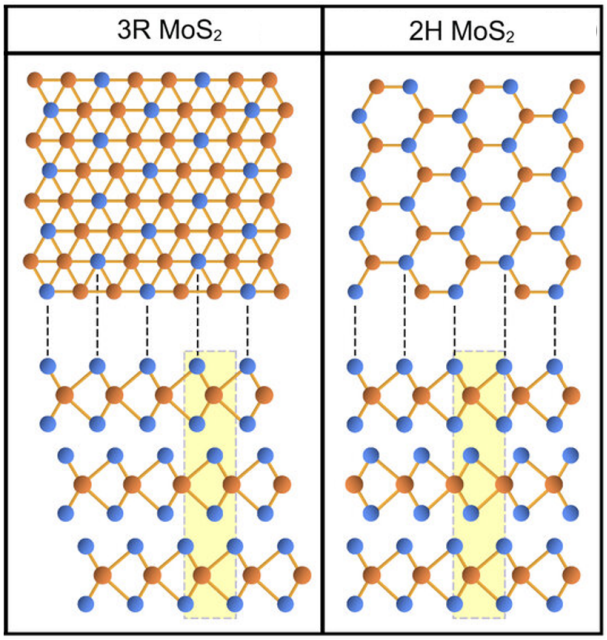

Figure 1.5 – Top view comparison of stacking sequences in MoS_2: (Left) the 3R phase with *ABCABC* stacking, and (Right) the 2H phase with *ABAB* stacking. The yellow regions highlight the relative displacements between adjacent layers. Adapted from Ref. [51]

.

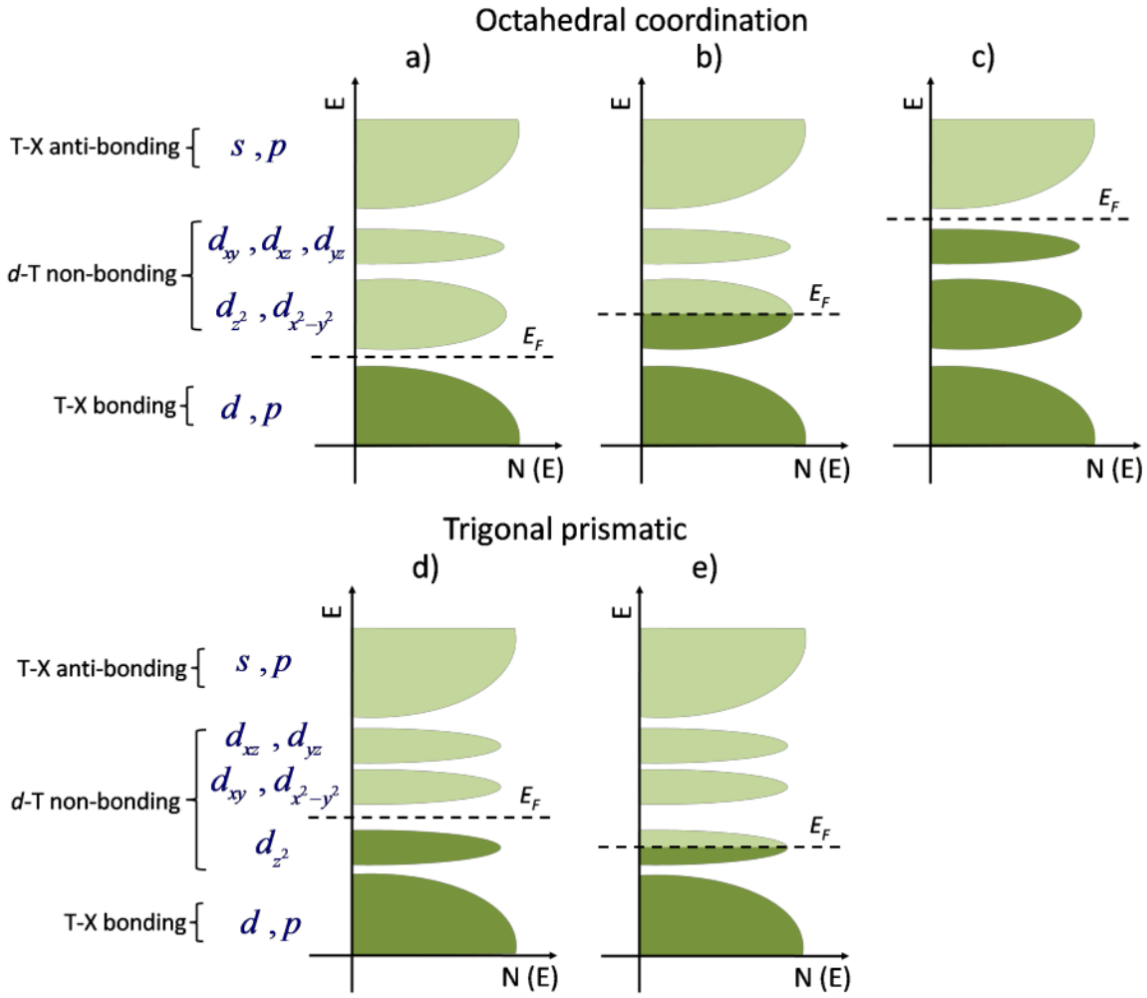

Figure 1.6 – Schematic orbital occupations in TMDs monolayers with transition metals from group IV (a), VII (b), VIII (c), VI (d) and V (e). Dark and light green indicate occupied and unoccupied states, respectively. Dashed line represents the Fermi level. Reproduced from Ref. [48].

The electronic and structural properties of TMDs monolayers are very dependent of their elemental composition and the coordination environment of the transition metal M. When the metal belongs to the to the groups IV, VII and VIII, the most common coordination is the octahedral, while for groups V and VI is trigonal prismatic. It is possible to categorize the electronic structure of each group because of the distance of the energy levels of the atomic orbitals in these compounds, giving birth to bonding and anti-bonding bands. This is shown at Figure 1.6, which shows that the states that determine the electronic structure near the Fermi level are the non-bonding d orbitals. For the octahedral coordination, the d orbitals split into two bands, one that groups the d_{xy}, d_{xz} and d_{yz} orbitals and one that groups the $d_{x^2-y^2}$ and d_{z^2} orbitals. Within this coordination, the only TMDs known to be metals are the ones in which the transition metal belongs to group VII while groups IV and VIII are semiconductors. On the other hand, for the trigonal prismatic coordination, the d orbitals split into three bands, one that groups the d_{xz} and d_{yz} orbitals, one that groups

the d_{xy} and $d_{x^2-y^2}$ orbitals and one solely for the d_{z^2} orbital. Within this coordination, TMDs of the group VI such as MoS_2 and $MoSe_2$ are known to be semiconductors with the Fermi level being between the d_{z^2} and $d_{xy}/d_{x^2-y^2}$ orbitals while TMDs of the group V such as NbS_2 have half-filled d_{z^2} and therefore have metallic character. In fact, monolayer MoS_2 is known for having a direct bandgap suitable for light absorption in the visible range of 1.88 eV while its bulk counterpart has an indirect bandgap of 1.29 eV [52] and, in a similar way, $MoSe_2$ is known to share such optical properties with MoS_2, having a direct bandgap optimal for visible range (1.63 ± 0.01) eV [53]. Additional discussions into the electronic properties of TMDs are available in several review articles [54–56].

Owing to the weak interlayer interactions in layered TMDs, mechanical exfoliation provides a simple and cost-effective method for producing atomically thin nanosheets [57]. This technique relies on micromechanical cleavage, in which individual layers are peeled from bulk TMD crystals to form stable monolayers. The exfoliated layers typically exhibit low defect concentrations, though they may retain natural impurities. Since the 1960s, this method has been employed to prepare and investigate layered TMDs such as MoS_2 and $NbSe_2$ [58]. In addition to mechanical exfoliation, other synthesis techniques include liquid-phase exfoliation [59, 60] and chemical vapor deposition (CVD) [61], which offer different levels of scalability and control. Once the material is synthesized, its thickness, structural, and vibrational properties can be characterized by techniques such as atomic force microscopy (AFM) [62] and Raman spectroscopy [63], the latter being especially valuable due to its nondestructive nature.

Layered TMDs have garnered significant attention due to their rich physical properties and broad applicability across various technological domains [64,65]. Their atomically thin nature, combined with strong in-plane covalent bonding and weak van der Waals interlayer interactions, enables their isolation in monolayer form and integration into nanoscale devices. For example, monolayer MoS_2 exhibit a transition from an indirect to a direct band gap upon exfoliation from the bulk, making them highly suitable for nanoelectronic and optoelectronic applications [66]. Notably, they have been successfully implemented in field-effect transistors, photodetectors, and memory devices such as memtransistors [67,68]. Furthermore, excitonic effects—arising from strong electron-hole interactions in these reduced-dimensional systems—play a dominant role in the optical response of TMDs, particularly in the visible range [69, 70]. These effects result in pronounced excitonic resonances in optical spectra and enable the exploration of many-body phenomena in solid-state physics, including valley-selective optical excitation and exciton–phonon coupling. In addition to their electronic and optical characteristics, TMD monolayers also exhibit favorable thermal transport properties [71], which stem from both lattice dynamics and carrier transport mechanisms. These attributes collectively position TMDs as promising candidates for fundamental research in two-dimensional materials and for the development of future technologies in nanoelectronics, photonics, and energy conversion. In summary,

TMDs combine unique structural, electronic, and vibrational properties, making them a versatile class of materials and a valuable platform for exploring fundamental phenomena in two-dimensional systems.

1.2.1 Ripples in TMDs

In theory, perfect two-dimensional crystals should be unstable at any finite temperature. Mermin's theorem [72] rigorously shows that long-range crystalline order is destroyed by long-wavelength thermal fluctuations in 2D for typical interatomic potentials. This implies that a free-standing 2D lattice cannot remain flat, but will be destabilized by bending fluctuations. In practice, however, truly two-dimensional materials like graphene and transition-metal dichalcogenides (TMDs), such as MoS_2, nevertheless exist as high-quality crystals. The apparent paradox is resolved by noting that anharmonic coupling between in-plane "stretching" modes and out-of-plane "bending" modes stiffens the membrane and suppresses the diverging fluctuations [73,74]. In other words, the membrane remains globally intact by developing corrugations or ripples in the third dimension, and these ripples *stabilize* the 2D lattice against crumpling. Anharmonic stabilization has a clear signature in the fluctuation spectrum. Fasolino *et al.* [74] performed Monte Carlo simulations of graphene and emphasized that although the Mermin theorem precludes a flat 2D crystal, coupling between bending (ZA) and stretching phonon modes can indeed stabilize a flat (but corrugated) phase. In their words, "these fluctuations can, however, be suppressed by anharmonic coupling between bending and stretching modes meaning that a 2D membrane can exist but will exhibit strong height fluctuations." Similar arguments appear in more recent studies of other 2D sheets: the suppression of long-wavelength ripples by mode coupling essentially provides a mechanism for 2D crystals to remain ordered [73]. In short, the key theoretical insight is that a purely flat phase is not observed. Instead, the membrane buckles into the perpendicular dimension, and this rippling relieves the dangerous divergence of fluctuations. The ripples themselves are thus an intrinsic thermodynamic feature of 2D crystals at finite temperature. The morphology of these ripples has been measured in both graphene and some TMD monolayers. In suspended graphene, transmission electron microscopy and simulations consistently find ripple wavelengths on the order of a few tens of nanometers (typically 50–100 Å) and heights on the order of 5–10 Å [75]. Likewise, suspended monolayer MoS_2 shows comparable behavior: Brivio *et al.* [76], through High-Resolution Transmission Electron Miscroscopy (HRTEM) imaging and Selected Area Electron Diffraction (SAED), report that single-layer MoS_2 is highly crystalline yet exhibits surface ripples up to about 1 nm in height. Ripples have important consequences for macroscopic properties, notably thermal expansion. In graphene and other honeycomb layers (e.g., h-BN), the out-of-plane bending modes lead to a *negative* in-plane thermal expansion: as temperature rises, the lattice contracts slightly due to the increased rippling. This has been confirmed by detailed simulations performed by

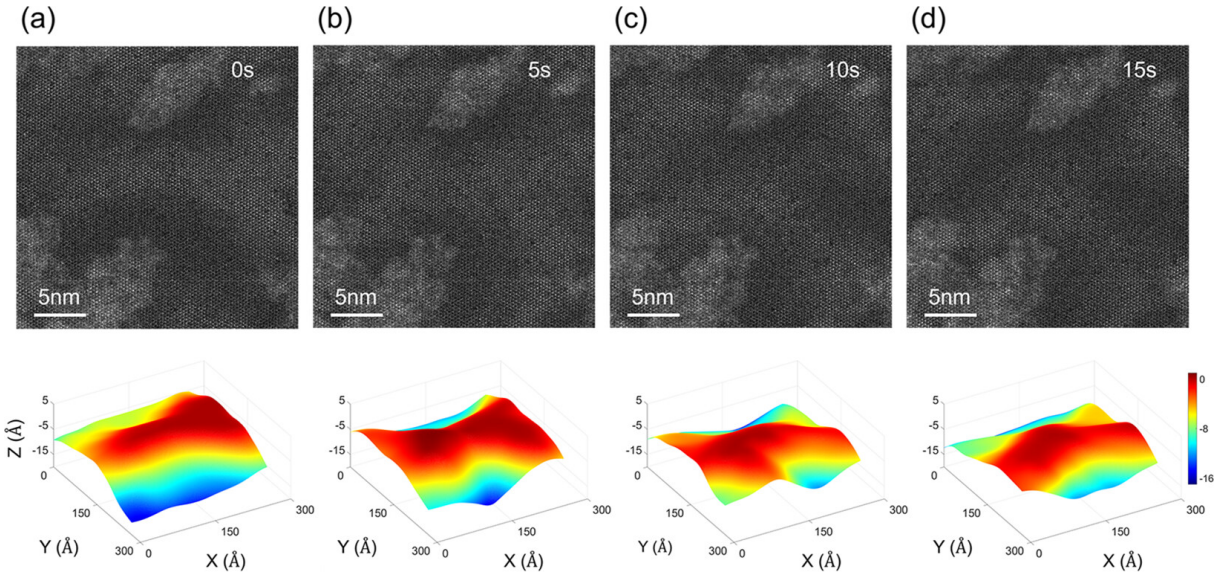

Figure 1.7 – Reconstructed 3D profiles of ripple evolution in monolayer $MoSe_2$. Panels (a)–(d) show STEM snapshots and corresponding 3D surface plots at 0, 5, 10, and 15 s, highlighting the temporal evolution of out-of-plane deformations. Reproduced from Ref. [78]

Anees *et al.* [77]. Also, in their simulations, they have shown that in monolayer MoS_2 rippling still occurs, but all phonon branches (including the flexural modes) contribute normally, so MoS_2 actually shows positive thermal expansion. This is due to the fact that monolayer MoS_2 consists of three atomic planes, with a molybdenum layer sandwiched between two sulfur layers. In practical terms, this means that ripples help stabilize, even though the latter remains more "thermally rigid". In any case, all simulations agree that neglecting ripples (i.e., forcing a strictly flat sheet) would incorrectly predict the thermal expansion for all studied compounds. Finally, the intricate 3D structure of ripples is itself an active area of research. Traditional HRTEM imaging only projects the corrugation into two dimensions, but new techniques are reconstructing the full 3D ripple geometry. For example, Li *et al.* [78] used aberration-corrected scanning transmission electron microscopy (STEM) to reconstruct the atomic-scale 3D ripple structure of freestanding monolayer $MoSe_2$ from single-frame images. By carefully analyzing the intensity of each atomic column, they mapped the vertical displacements of Se atoms and directly visualized the ripple distortions in three dimensions. Their work even allows testing the classical theory of membrane fluctuations against experiment. These image-reconstruction efforts represent the cutting edge of visualizing ripples: they go beyond earlier tomography approaches and open the possibility of watching ripples dynamically. In summary, ripples in TMDs are not just a curious phenomena but rather essential features that emerge from fundamental 2D physics and that significantly influence the material's mechanical and thermal behavior.

2 Theoretical Background

This chapter presents the theoretical background and computational methodologies that support the results of this thesis. The discussion begins with the fundamentals of Density Functional Theory (DFT), which provide the basis for most of the calculations performed. It then moves to the semiclassical Boltzmann transport theory, used to evaluate electronic transport coefficients, followed by an introduction to Molecular Dynamics (MD) simulations and their role in capturing finite-temperature behavior. Next, attention is given to the development of Machine Learning Force Fields (MLFFs), an approach that combines accuracy with computational efficiency. Finally, the theory of phonons is addressed, providing the framework for analyzing vibrational and dynamical properties. Together, these topics establish the theoretical and methodological foundation for the analyses presented in the subsequent chapters.

2.1 Density Functional Theory

The development and application of theoretical models to describe material properties is known as *materials modeling*, which spans a wide range of techniques in materials science and physical chemistry. Modern computational methods for modeling materials heavily rely on techniques known as first-principles approaches (or, in Latin, *ab initio*). A first-principles methodology refers to modeling materials without the use of empirical parameters, relying instead on fundamental physical theories that govern behavior at the atomic scale.

Fortunately, such a theory exists in the form of *Quantum Mechanics*, which provides a framework for understanding the behavior of electrons and nuclei. In many cases, the properties of materials can be effectively described by focusing on the interactions among the outermost, or *valence*, electrons once they are most involved in bonding, charge transport, and optical processes. However, this approximation is not universally valid. For example, phenomena such as superconductivity often require the inclusion of electron-phonon coupling and many-body effects beyond standard valence-electron frameworks. Additionally, contributions from core states can play a critical role in magnetic behavior and other subtle electronic properties. Despite these limitations, valence-electron models still offer a remarkably successful starting point for describing a wide range of material properties.

Among the most powerful and widely adopted techniques for this purpose is *Density Functional Theory* (DFT), which allows for a tractable approximation of the full many-electron *Schrödinger equation*. The development of DFT builds upon early quantum

chemical approaches and has become a cornerstone of modern materials modeling. For a more comprehensive and detailed treatment of DFT, the reader is referred to Ref. [79].

2.1.1 The Full Many-Body Problem

All the information about a many-body system can be condensed in one single equation. For a system of N electrons and P atomic nuclei, the full many-body Hamiltonian takes the form:

$$\hat{H}_{MB} = \overbrace{-\sum_{i=1}^{N}\frac{\hbar^2}{2m_e}\nabla_i^2 + \frac{e^2}{2}\sum_{i=1}^{N}\sum_{j\neq i}^{N}\frac{1}{|\mathbf{r}_j-\mathbf{r}_i|}}^{\text{electrons}} \underbrace{-\sum_{I=1}^{P}\frac{\hbar^2}{2M_I}\nabla_I^2 + \frac{e^2}{2}\sum_{I=1}^{P}\sum_{J\neq I}^{P}\frac{Z_I Z_j}{|\mathbf{R}_J-\mathbf{R}_I|}}_{\text{nuclei}} \underbrace{- e^2\sum_{i=1}^{N}\sum_{I=1}^{P}\frac{Z_I}{|\mathbf{r}_i-\mathbf{R}_I|}}_{\text{electron-nuclei interaction}}. \tag{2.1}$$

We can write the same expression as

$$\hat{H}_{MB} = \hat{T}_e + \hat{V}_{e-N} + \hat{V}_{e-e} + \hat{T}_N + \hat{V}_{N-N} \quad \text{in which:}$$

$$\hat{T}_e = -\sum_{i=1}^{N}\frac{\hbar^2}{2m_e}\nabla_i^2 \quad \text{is the electron kinetic energy}$$

$$\hat{V}_{e-N} = -e^2\sum_{i=1}^{N}\sum_{I=1}^{P}\frac{Z_I}{|\mathbf{r}_i-\mathbf{R}_I|} \quad \text{is the electron-nuclei potential energy}$$

$$\hat{V}_{e-e} = \frac{e^2}{2}\sum_{i=1}^{N}\sum_{j\neq i}^{N}\frac{1}{|\mathbf{r}_j-\mathbf{r}_i|} \quad \text{is the Coulomb repulsion energy}$$

$$\hat{T}_N = -\sum_{I=1}^{P}\frac{\hbar^2}{2M_I}\nabla_I^2 \quad \text{is the ionic kinetic energy and}$$

$$\hat{V}_{N-N} = \frac{e^2}{2}\sum_{I=1}^{P}\sum_{J\neq I}^{P}\frac{Z_I Z_J}{|\mathbf{R}_j-\mathbf{R}_i|} \quad \text{is the potential energy between nuclei.}$$

The sets of coordinates $\{\mathbf{r}_i\}$ and $\{\mathbf{R}_I\}$ denote the electronic and nuclear coordinates respectively, m_e and M_I refers to the electron and ionic masses respectively, e is the electron charge and Z_I refers to the nuclear charge of ion I. In principle, the Hamiltonian of Eq. 2.1 could be used to solve the time-independent Schrödinger equation

$$\hat{H}_{MB}\Psi_n(\{\mathbf{r}_i\},\{\mathbf{R}_I\}) = \xi_n\Psi_n(\{\mathbf{r}_i\},\{\mathbf{R}_I\}) \tag{2.2}$$

in which ξ_n are the eigenenergies and the Ψ_n are the many-body wavefunctions that solve the above eigenvalue problem. In principle, those functions depend both of the coordinates of all electrons $\{\mathbf{r}_i\}$ and the coordinates of all ions $\{\mathbf{R}_I\}$, i.e., a $3(N+P)$ variable problem.

However, there are several approximations we can make to reduce the complexity of the problem. The first of them is the so called *Born-Oppenheimer approximation* [80] which proposes that one can decouple the nuclear and electronic motions. This is motivated by the masses of the nuclei being much larger than those of the electrons (a proton is ∼2000 times the mass of an electron). Under the assumption that they are experiencing the same forces, the kinetic energies of the nuclei become negligible in comparison to those of the electrons and can be ignored in the calculation of the wavefunctions. Therefore, the ions will only contribute to the system as an external potential $\hat{V}_{ext}$. Then, we can write an equation for just the electrons:

$$\begin{aligned}\hat{h}_e &= \hat{T} + \hat{V}_{e-e} + \hat{V}_{ext} \\ &= -\frac{\hbar^2}{2m_e}\sum_{i=1}^{N}\nabla_i^2 + \frac{e^2}{2}\sum_{i=1}^{N}\sum_{j\neq i}^{N}\frac{1}{|\mathbf{r}_j - \mathbf{r}_i|} - \sum_{i=1}^{N}\sum_{I=1}^{P}\frac{Z_I e^2}{|\mathbf{r}_i - \mathbf{R}_I|}\end{aligned} \tag{2.3}$$

which will lead to a $3N$ variable eigenvalue problem for the electrons:

$$\hat{h}_e\Psi_n(\mathbf{r}_1,\ldots,\mathbf{r}_N) = E_n\Psi_n(\mathbf{r}_1,\ldots,\mathbf{r}_N). \tag{2.4}$$

Moreover, we need to account for the indistinguishability of the electrons, i.e., the probability $|\Psi_n|^2$ to find a given electron at a given place should not depend of the label of the electron. For fermions, this means that the wavefunction needs to be antisymmetric with respect to the exchange of two particles:

$$\Psi_n(\mathbf{r}_1,\ldots,\mathbf{r}_i,\ldots,\mathbf{r}_j,\ldots,\mathbf{r}_N) = -\Psi_n(\mathbf{r}_1,\ldots,\mathbf{r}_j,\ldots,\mathbf{r}_i,\ldots,\mathbf{r}_N). \tag{2.5}$$

Those are the main rules for the electronic many-body problem. It is well known that the only problem that had been solved analytically is the hydrogen atom and similar one electron problems (ionized helium He^+, ionized hydrogen molecule H_2^+) and so on. Numerically, there are solutions with remarkable precision for two electron systems like helium [81] and the hydrogen molecule H_2 [82], with a precision of more than 15 digits for the ground state energy of those systems. However, for systems with more than 10 electrons, the determination of a many-body wavefunction becomes intractable even computationally given the computational time and the amount of memory necessary to store those wavefunctions. Therefore, it was necessary to develop approximations for the solutions of Eq. 2.4 in order to obtain its wavefunctions and energies, some of which we will discuss here.

2.1.2 Approximate Methods for the Many-Body Problem

Before introducing DFT, it is useful to recall some of the historical and conceptual approximations that were proposed to deal with the many-body Hamiltonian in Eq. 2.4.

These approaches illustrate the progression from independent-electron models to mean-field descriptions, and ultimately motivate the development of DFT.

In fact, the origin of all problems related to solving the many-body Hamiltonian can be assigned to one single term in Eq. 2.4: the Coulomb repulsion between electrons:

$$\hat{V}_{e-e} = \frac{e^2}{2} \sum_{i=1}^{N} \sum_{j \neq i}^{N} \frac{1}{|\mathbf{r}_j - \mathbf{r}_i|} \tag{2.6}$$

which makes the $\{\mathbf{r}_i\}$ variables in the equation non-separable. As a first approximation, we assume that the electrons do not interact with each other, i.e., $\hat{V}_{e-e} = 0$. This is known as the *independent electron approximation*. While this assumption may appear overly simplistic, it is instructive to explore how far one can progress within this framework. By setting $\hat{V}_{e-e} = 0$, we can write:

$$\left(-\frac{\hbar^2}{2m_e} \sum_{i=1}^{N} \nabla_i^2 - \sum_{i=1}^{N} \sum_{I=1}^{P} \frac{Z_I e^2}{|\mathbf{r}_i - \mathbf{R}_I|} \right) \Psi(\mathbf{r}_1, \ldots, \mathbf{r}_N) = E \Psi(\mathbf{r}_1, \ldots, \mathbf{r}_N). \tag{2.7}$$

In the independent-electron approximation, one can define a single-particle Hamiltonian

$$\hat{h}(\mathbf{r}) = -\frac{\hbar^2}{2m_e} \nabla_{\mathbf{r}}^2 + \sum_{I=1}^{P} \frac{Z_I e^2}{|\mathbf{r} - \mathbf{R}_I|}, \tag{2.8}$$

such that Eq. 2.7 can be rewritten as

$$\hat{h}(\mathbf{r}) \psi_n(\mathbf{r}) = \epsilon_n \psi_i(\mathbf{r}) \ \forall \ i \in \{1, \ldots, N\}. \tag{2.9}$$

Therefore, for a non-interacting system, the Hamiltonian of the system can be written as N independent single-particle Hamiltonians and the energy of the full system is the sum of the energies of the individual systems:

$$\Psi(\mathbf{r}_1, \ldots, \mathbf{r}_N) = \psi_1(\mathbf{r}_1) \ldots \psi_N(\mathbf{r}_N) \ ; \ E = \sum_{i=1}^{N} \epsilon_i. \tag{2.10}$$

Since we are completely ignoring the Coulomb repulsion, this approach will underestimate the energy considerably. However, there are ways to improve this approximation. In fact, since we are dealing with differential equations, we will have a *variational principle* which will be related to the energy as a *functional* of the wavefunction. With E_0 being the ground state energy ($E \geq E_0$), the following expression is valid (minimization condition for the ground state energy):

$$E[\Psi] = \frac{\langle \Psi | \, \hat{h}_e \, | \Psi \rangle}{\langle \Psi | \Psi \rangle} \ ; \ \left. \frac{\delta E}{\delta \Psi} \right|_{E=E_0} = 0. \tag{2.11}$$

We can use the *ansatz* in Eq. 2.10 as a trial solution to Eq. 2.11. The variational principle will force the energy to be a minimum of the functional for each one electron wave function. Therefore, the variational principle will lead to N equations for single particle wavefunctions:

$$\left[-\frac{\hbar^2}{2m_e}\nabla_i^2 - \sum_{I=1}^{P}\frac{Z_I e^2}{|\mathbf{r}_i - \mathbf{R}_I|} + \underbrace{e^2\sum_{j=1}^{N}\int \mathrm{d}^3 r_j \frac{|\psi_j(\mathbf{r}_j)|^2}{|\mathbf{r}_i - \mathbf{r}_j|}}_{V_H}\right]\psi_i(\mathbf{r}_i) = \epsilon_i\psi_i(\mathbf{r}_i) \tag{2.12}$$

which are known as Hartree equations. This was the first time that the *ansatz* solution was used to obtain a approximated solution to Eq. 2.4 that does not ignore the Coulomb interaction. It is said that the solution puts each electron of the system in an orbital, similar to the orbitals characteristic of the Hydrogen atom. We can notice that we have a new term in the equation, the so called *Hartree potential*

$$V_H = e^2\sum_{j=1}^{N}\int \mathrm{d}^3 r_j \frac{|\psi_j(\mathbf{r}_j)|^2}{|\mathbf{r} - \mathbf{r}_j|} \tag{2.13}$$

which means the average potential that the electron in the position $\mathbf{r}$ "feels" due to a electronic "cloud" formed by all the other electrons. Because of that, this approach is also called a *mean-field approximation* [83]. Although this approach took by Douglas Hartree in 1928 was revolutionary at the time, this solution did not account for the indistinguishability of the electrons and consequently did not satisfy the Pauli exclusion principle. In 1930, Slater suggested that, in order to Hartree's method to account for indistinguishability, one should use the following determinant as a trial solution:

$$\Psi(\mathbf{r}_1, \ldots, \mathbf{r}_N) = \frac{1}{\sqrt{N!}}\begin{vmatrix} \psi_1(\mathbf{r}_1) & \psi_1(\mathbf{r}_2) & \cdots & \psi_1(\mathbf{r}_N) \\ \psi_2(\mathbf{r}_1) & \psi_2(\mathbf{r}_2) & \cdots & \psi_2(\mathbf{r}_N) \\ \vdots & \vdots & \ddots & \vdots \\ \psi_N(\mathbf{r}_1) & \psi_N(\mathbf{r}_2) & \cdots & \psi_N(\mathbf{r}_N) \end{vmatrix} \tag{2.14}$$

which is known as the Slater determinant. One can notice that it satisfies the antisymmetry condition in Eq. 2.5. Applying this solution in the variational principle at Eq. 2.11 and deriving the proper differential equations leads to a correction for the energy obtained using the Hartree method in Eq. 2.12: the *exchange potential*

$$V_X(\mathbf{r}, \mathbf{r}') = -\sum_{j=1}^{N}\frac{\psi_j^*(\mathbf{r}')\psi_j(\mathbf{r})}{|\mathbf{r} - \mathbf{r}'|} \tag{2.15}$$

which accounts for the additional energy that ensures that the individual orbitals satisfy the Pauli exclusion principle. In fact, since two electrons cannot be close to each other

by the principle, the Coulomb repulsion cannot be very large. Therefore, the exchange potential is an attractive one that weakens the effect of the Coulomb repulsion given by Hartree potential, i.e., V_X is a correction term to V_H which is overestimated compared with the real case. Moreover, this correction is a non-local potential in the single-particle equations. Non-local means that its evaluation involves an integration over the additional variable $\mathbf{r}'$. The numerical evaluation of those integrals are known to be very expensive computationally, which makes the task of finding wavefunctions while still including Eq. 2.15 exactly impracticable for a lot of systems of interest. One common thing between the terms V_H and V_X is that both of them were obtained through a variational principal in Eq. 2.11, i.e., we wrote the energy of the system as a functional of the wavefunction and minimized it. In the next sections we will discuss that the energy can also be written as a functional of another quantity, which will be crucial in the development of DFT.

Before moving to the next section, it is important to clarify the concept of *correlation energy*. Mean-field approaches, in which the many-electron wavefunction is approximated by a single Slater determinant, neglect the fact that electrons avoid one another more strongly than an averaged potential would suggest, since they repel each other instantaneously. Suppose you know the exact ground-state energy E of a system, either by experiment or by solving the many-body problem numerically to high accuracy. The *correlation energy* is formally defined as the difference between E and the energy obtained including both V_H and V_X in the calculations. In this sense, it measures the part of the electron–electron interaction missing from the approximated solution obtained with the Slater determinant, which already includes the exchange interaction but not the instantaneous dynamical correlations. It is also common to introduce the concept of *exchange–correlation energy*, E_{XC}, defined as the sum of the exchange contribution E_{X} and the correlation energy E_{C}. Treating exchange and correlation together through E_{XC}, rather than handling them separately, proves advantageous and will become particularly relevant in the framework of DFT.

2.1.3 The Electron Density

Given the indistinguishability of electrons, it might be more appropriate to ask the following question "*What is the probability to find any electron at the position* $\mathbf{r}$?" rather than asking "*What is the probability to find electron A or B at the position* $\mathbf{r}$?". This is precisely the quantity described by the electron density function, $n(\mathbf{r})$, which gives the probability density of finding an electron at position $\mathbf{r}$, irrespective of which electron it is. We begin by recalling the expression for the probability density of finding electron 1 at position $\mathbf{r}$, as determined from the many-body wavefunction.

$$P(\mathbf{r}_1 = \mathbf{r}) = \int |\Psi(\mathbf{r}, \mathbf{r}_2, \ldots, \mathbf{r}_N)|^2 \mathrm{d}^3 r_2 \ldots \mathrm{d}^3 r_N. \tag{2.16}$$

More precisely, the above expression tells the probability to find electron 1 at position $\mathbf{r}$ while electrons 2, 3, ..., N can be anywhere. This leads to the integration over all variables except $\mathbf{r}_1$, to account for the fact that the remaining electrons may occupy any position in space. Therefore, if the probability of any electron at position $\mathbf{r}$ is desired, we need to sum among all the electrons:

$$n(\mathbf{r}) = P(\mathbf{r}_1 = \mathbf{r}) + P(\mathbf{r}_2 = \mathbf{r}) + \dots P(\mathbf{r}_N = \mathbf{r}) \tag{2.17}$$

which is enough to define the quantity $n(\mathbf{r})$, known as the electron density. Since all electrons are indistinguishable, any electron i can be relabeled as electron 1. Although this relabeling introduce a sign change in the wavefunction due to its antisymmetric nature, it has no effect on the probability density, which depends on the squared modulus of the wavefunction. Hence, all probabilities will be equal to $P(\mathbf{r} = \mathbf{r}_1)$ which allow us to write

$$n(\mathbf{r}) = N \times P(\mathbf{r} = \mathbf{r}_1) = N \int |\Psi(\mathbf{r}, \mathbf{r}_2, \dots, \mathbf{r}_N)|^2 \mathrm{d}^3 r_2 \dots \mathrm{d}^3 r_N. \tag{2.18}$$

Eq. 2.18 provides the most general definition of the electron density, without imposing any constraints on the form of the wavefunction. In cases where the wavefunction is approximated as a linear combination of products of single-electron orbitals —as in the approximations discussed in 2.1.2— the electron density reduces to the sum of the squared modulus of the individual single-particle orbitals:

$$\Psi(\mathbf{r}_1, \dots, \mathbf{r}_N) = \psi_1(\mathbf{r}_1) \dots \psi_N(\mathbf{r}_N) \implies n(\mathbf{r}) = \sum_{i=1}^{N} |\psi_i(\mathbf{r})|^2. \tag{2.19}$$

The electron density is known to satisfy some properties due to the normalization conditions of the wavefunctions

$$\langle \Psi | \Psi \rangle = \int n(\mathbf{r}) \mathrm{d}^3 r \tag{2.20}$$

and the average of other observables can be calculated using the electron density instead of the wavefunction. For example, the Hartree potential in Eq. 2.13 can be rewritten in terms of $n(\mathbf{r})$:

$$V_H = e^2 \int \mathrm{d}^3 r' \frac{n(\mathbf{r}')}{|\mathbf{r} - \mathbf{r}'|}. \tag{2.21}$$

At this point, the importance of the electron density and the role it plays in the many-body problem become evident. Unlike the many-body wavefunction, which depends on $3N$ spatial coordinates for a system of N electrons, the electron density is a function of only three spatial variables. In fact, the electron density is fundamentally as important as the wavefunction, as it is unequivocally determined by the Hamiltonian of the system. This is the subject of the theorems to be discussed in the following section.

2.1.4 The Hohenberg-Kohn Theorems

Here we introduce the key and breakthrough idea at the core of Density Functional Theory (DFT): that the ground-state properties of a many-electron system are fully determined by its electron density $n(\mathbf{r})$. This concept, established by the Hohenberg–Kohn theorems, allows DFT to reformulate the many-body problem, which was originally defined in terms of the 3N variables $\{\mathbf{r}_i\}$, in terms of a function $n(\mathbf{r})$ of only three spatial variables, which is the main reason for its efficiency and wide applicability.

Firstly, a functional is a mathematical object that assigns a function to a scalar value. In the context of the many-body problem, the total energy of a system can be expressed as a functional of either the many-body wavefunction or the electron density. In Sec. 2.1.2, we have already written the energy as a functional of the wavefunction in Eq. 2.11. According to the variational principle, the ground-state wavefunction is the one that minimizes the energy functional, meaning that the physical (i.e., ground-state) wavefunction yields the lowest possible energy among all admissible trial functions. Hohenberg and Kohn showed in 1964 that the same logic can be applied to the electron density [84].

Theorem 1: *The external potential of a system of interacting particles is uniquely determined by the ground-state electron density, apart from an additive constant.*

The first theorem states that, with the knowledge of $V_{ext}(\mathbf{r})$ given by the position of the ions and hence the full determination of the Hamiltonian, the ground-state density $n(\mathbf{r})$ will correspond to one and only one external potential and therefore to a unique physical system. There is not any degenerate density for the ground state and the density will dictate all electronic properties of the ground-state of the system, including the energy defined by Eq. 2.1. Using the Born-Oppenheimer approximation, one can decompose the energy in a formally exact way in three terms:

$$E[n] \equiv T[n] + E_{e-e}[n] + \int V_{ext}(\mathbf{r}) n(\mathbf{r}) \mathrm{d}^3 r \tag{2.22}$$

with the three above terms establishing a direct correspondence to $\hat{T}_e$, $\hat{V}_{e-e}$ and $\hat{V}_{e-N}$ in Eq. 2.1 respectively. The exact form of the of the functionals $T[n]$ and $E_{e-e}[n]$ are unknown. The second theorem provides a variational principle that allows one to obtain the ground-state energy by minimizing the energy functional with respect to the electron density.

Theorem 2: *For any given external potential, a functional of energy in terms of the particle density can be defined. The functional attains its minimum only at the ground-state density.*

The significance of the second theorem lies in its central implication: since the total energy of a system can be expressed as a functional of the electron density, the ground-state density can, in principle, be obtained by performing a variational minimization of this

functional. Its relevance becomes evident upon recognizing that it ensures the energy of a system can always be written in the following form:

$$\begin{aligned} E &= \langle \Psi[n] | \hat{h}_e | \Psi[n] \rangle \\ &= \langle \Psi[n] | \hat{T} + \hat{V}_{e-e} | \Psi[n] \rangle + \int V_{ext}(\mathbf{r}) n(\mathbf{r}) \mathrm{d}^3 r \\ &= F[n] + \int V_{ext}(\mathbf{r}) n(\mathbf{r}) \mathrm{d}^3 r \\ &\geq E[n_0] = E_0 = \langle \Psi[n_0] | \hat{h}_e | \Psi[n_0] \rangle . \end{aligned} \tag{2.23}$$

The term $F[n] = \langle \Psi[n] | \hat{T} + \hat{V}_{e-e} | \Psi[n] \rangle$ is a universal functional, true for all systems of interacting electrons, independent of the potential in which they are subject to. Together, the two Hohenberg–Kohn theorems establish the foundational framework of Density Functional Theory, demonstrating that the ground-state properties of an interacting electron system are fully determined by its electron density, and that this density can be obtained through a variational principle applied to a universal energy functional.

2.1.5 The Kohn-Sham Scheme

While the Hohenberg-Kohn theorems establish the existence of such a electron density and energy functional, they do not provide means to construct it. A significant step towards the practicability of DFT was taken by Kohn and Sham in 1965 when they provided a method in which they were able to deal with the unknown functional $F[n]$ [85]. We begin this discussion by noting that the difficulty of the determination of $F[n]$ comes from the fact that the T and $\hat{V}_{e-e}$ are the kinetic and electron-electron energies of the system with interacting electrons. However, for a system with non-interacting electrons in which we can write the wavefunction as a product of orbitals as in Eq. 2.10, both T and $\hat{V}_{e-e}$ are known:

$$T_0[n] = -\frac{\hbar^2}{2m_e} \sum_{i=1}^{N} \int \psi_i^*(\mathbf{r}) \nabla^2 \psi_i(\mathbf{r}) \mathrm{d}^3 r \quad \text{(Kinetic Energy)} \tag{2.24}$$

$$V_H[n] = \frac{e^2}{2} \int \int \frac{n(\mathbf{r}) n(\mathbf{r}')}{|\mathbf{r} - \mathbf{r}'|} \mathrm{d}^3 r \mathrm{d}^3 r' \quad \text{(Hartree Energy).} \tag{2.25}$$

The key insight introduced by Kohn and Sham was to express the energy functional separating the kinetic and Coulomb energy of *independent electrons* and adding an additional term which accounts for the difference.

$$E[n] = \int V_{ext}(\mathbf{r}) n(\mathbf{r}) \mathrm{d}^3 r + \overbrace{T_0[n]}^{\text{KE}} + \overbrace{V_H[n]}^{\text{Hartree}} + E_{XC}[n] \tag{2.26}$$

The extra term, E_{XC}, contains everything that is left out and is called the *exchange-correlation energy*. Notice that in Eq. 2.26, the exchange-correlation energy also accounts for the exchange energy in Eq. 2.15, being treated like an unknown just as the correlation energy. If E_{XC} were known, we would be able to calculate the total ground-state energy of the system using the electron density. Yet, we still need to determine the actual ground-state density. Since the ground-state density, n_0, is precisely the function that minimizes the total energy, $E[n]$, the following variational principle is valid:

$$\frac{\delta E[n]}{\delta n}\bigg|_{n=n_0} = 0. \tag{2.27}$$

The variational principle, combined with the expression of the density as a sum of squared norm of the orbitals (Eq. 2.19) and the orthonormality constraint, leads to a differential equation for each orbital.

$$\left[-\frac{\hbar^2}{2m_e}\nabla^2 + V_{ext} + V_H + V_{XC}\right]\psi_i(\mathbf{r}) = \epsilon_i\psi_i(\mathbf{r}) \tag{2.28}$$

in which V_{ext} and V_H are the external and Hartree potentials respectively and V_{XC} is the exchange-correlation potential given by

$$V_{XC} = \frac{\delta E_{XC}[n]}{\delta n}\bigg|_{n(\mathbf{r})}. \tag{2.29}$$

This set of equations (Eq. 2.28) are called Kohn–Sham equations and form the basis of the Kohn–Sham theory. The eigenvalues ϵ_i are called the Kohn-Sham energies, the ψ_i are the Kohn-Sham orbitals and so on. Notice that the potentials V_{ext}, V_H and V_{XC} and the Kohn-Sham orbitals are *interdependently defined*: these potentials depend on the electron density, but the density itself is obtained from the Kohn–Sham orbitals which are themselves solutions to equations that include the potentials. Because of this circular dependence, a *self-consistent procedure* is required: you start with an initial guess for one quantity (e.g., the density), compute the dependent quantities (e.g., the orbitals and potentials), update the original guess, and repeat the cycle until convergence. In practice, the Hartree potential is calculated from the electron density using a relation from *classical electrostatics*:

$$\nabla^2 V_H(\mathbf{r}) = -4\pi n(\mathbf{r}) \tag{2.30}$$

which is totally equivalent to Eq. 2.21. The self-consistent cycle is represented in Figure 2.1. The inclusion of a mixing parameter α in the self-consistent cycle aims to improve the stability and convergence of the iterative procedure toward the self-consistent solution. Once the self-consistent solution is reached, the orbitals can provide not only the electron density, but also several other observables, such as the kinetic energy, the effective interaction

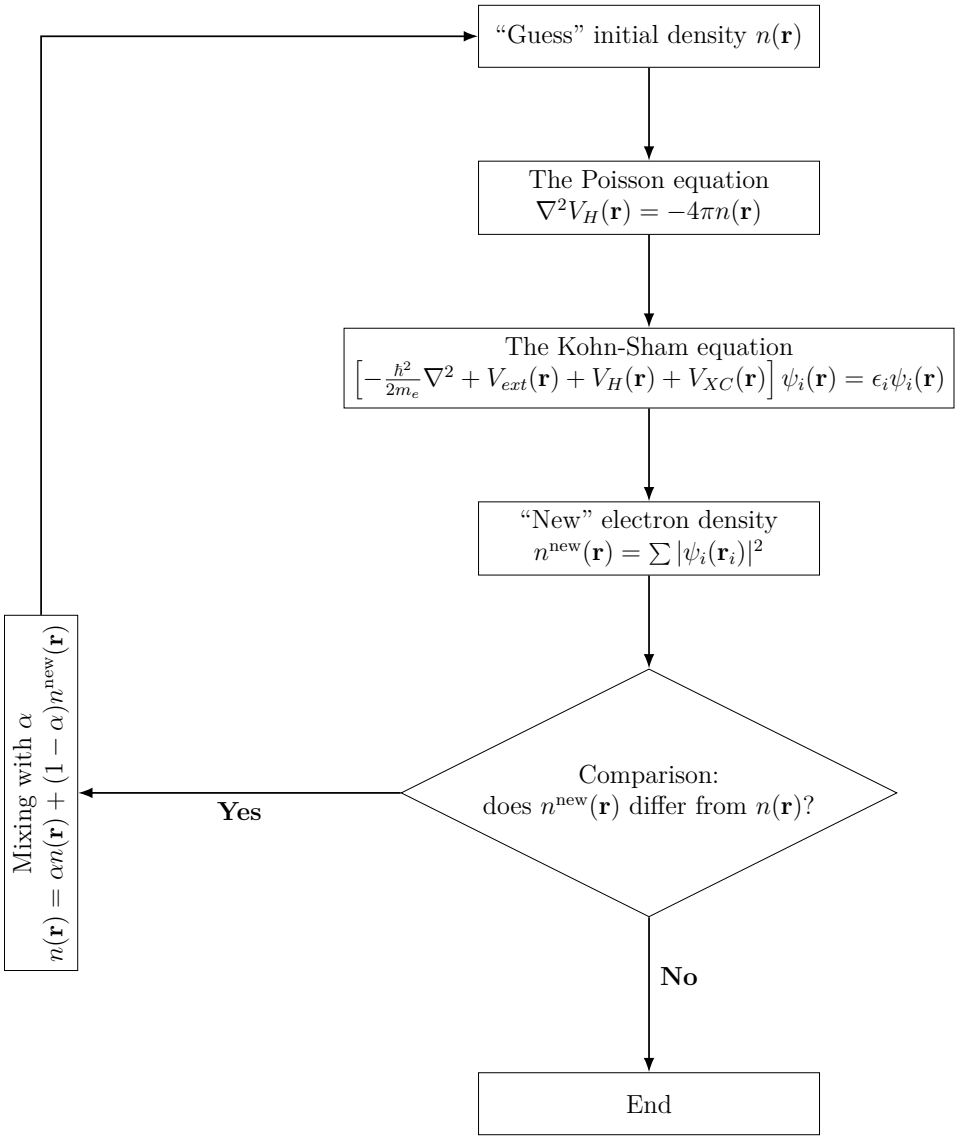

Figure 2.1 – Schematic representation of the self-consistent cycle in Kohn-Sham DFT.

potentials, and even the total energy of the system. At that point, if we knew how to express the contributions from the exchange-correlation functional, DFT would be a complete and exact theory. However, this functional needs to be approximated and the approximations to this functional are well established in the electronic structure literature, which motivates a discussion of some of the most commonly used forms.

2.1.6 The Exchange-Correlation Functional

Since the development of Kohn–Sham theory, substantial effort has been dedicated to the construction of accurate exchange-correlation functionals E_{XC} to enable the practical solution of the Kohn–Sham equations. Some of these, such as the Local Density Approximation [86] and the Generalized Gradient Approximation [87], are particularly notable for their historical significance, as they paved the way for the practical success of DFT by enabling accurate and efficient calculations for a wide range of real materials and molecular

systems.

2.1.6.1 Local Density Approximation

The first approximation for E_{XC} that had a remarkable accuracy and correlation with experimental results was the *Local Density Approximation (LDA)* and it is based on the assumption that, in cases where the electron density varies slowly in space, the exchange-correlation energy can be approximated by that of a homogeneous electron gas [88]. In that case, the contribution from the nuclear ions is treated as an uniform-positive-charged background. The ground-state of this system is also a uniform-negative-charged background which cancels the ionic potential ($V_H + V_{ext} = 0$) and the total energy will only have contributions from the kinetic energy and the exchange energy given by Eq. 2.15, both of them calculated exactly. The total energy per electron is expressed by

$$\frac{E}{N} = C_1 n^{\frac{2}{3}} + C_2 n^{\frac{1}{3}} \; ; \; C_1 = \frac{3}{10}\left(3\pi^2\right)^{\frac{2}{3}} \approx 2.871 \; ; \; C_2 = -\frac{3}{4}\left(\frac{3}{\pi}\right)^{\frac{1}{3}} \approx -0.738 \tag{2.31}$$

with the first term representing the kinetic energy and the second term representing the electron-electron exchange energy. The main idea behind LDA is to write the exchange-correlation functional as:

$$E_{XC}^{LDA}[n(\mathbf{r})] = \int n(\mathbf{r})\epsilon_{XC}[n(\mathbf{r})]\mathrm{d}^3r = \int n(\mathbf{r})[\underbrace{\epsilon_X(\mathbf{r})}_{C_2 n^{\frac{1}{3}}} + \epsilon_C(\mathbf{r})]\mathrm{d}^3r \tag{2.32}$$

where ϵ_X matches that of the homogeneous electron gas and ϵ_C is approximated as an expansion that need to satisfy some limits ($n \to 0$ and $n \to \infty$). A remarkable and accurate numerical determination of ϵ_C was made by Ceperley and Alder using Quantum Monte Carlo methods in 1980 [89]. Figure 2.2 summarizes the ground-state energy per particle obtained for different phases of the electron gas as a function of the Wigner radius r_s which is a density parameter. It illustrates the phase transitions between the unpolarized and polarized Fermi fluids and eventually to the Wigner crystal [90] phase as density decreases (i.e., as r_s increases). These data, while obtained through a complex and computationally demanding method, serve as a cornerstone for the widely-used LDA approach in DFT and, since then, a great part of LDA functionals found nowadays are different parametrizations obtained by fitting the numerical results obtained by Ceperley and Alder.

Although LDA may appear simplistic at first, as it treats exchange and correlation effects as purely local despite their inherently non-local nature, it has proven to be surprisingly effective. For example, LDA typically reproduces lattice constants within 1–2% of experimental values and some of the deviations are generally systematic. The local treatment of exchange-correlation leads to slightly more uniform charge densities, often resulting in the *underestimation* of bond lengths and contributing to the observed

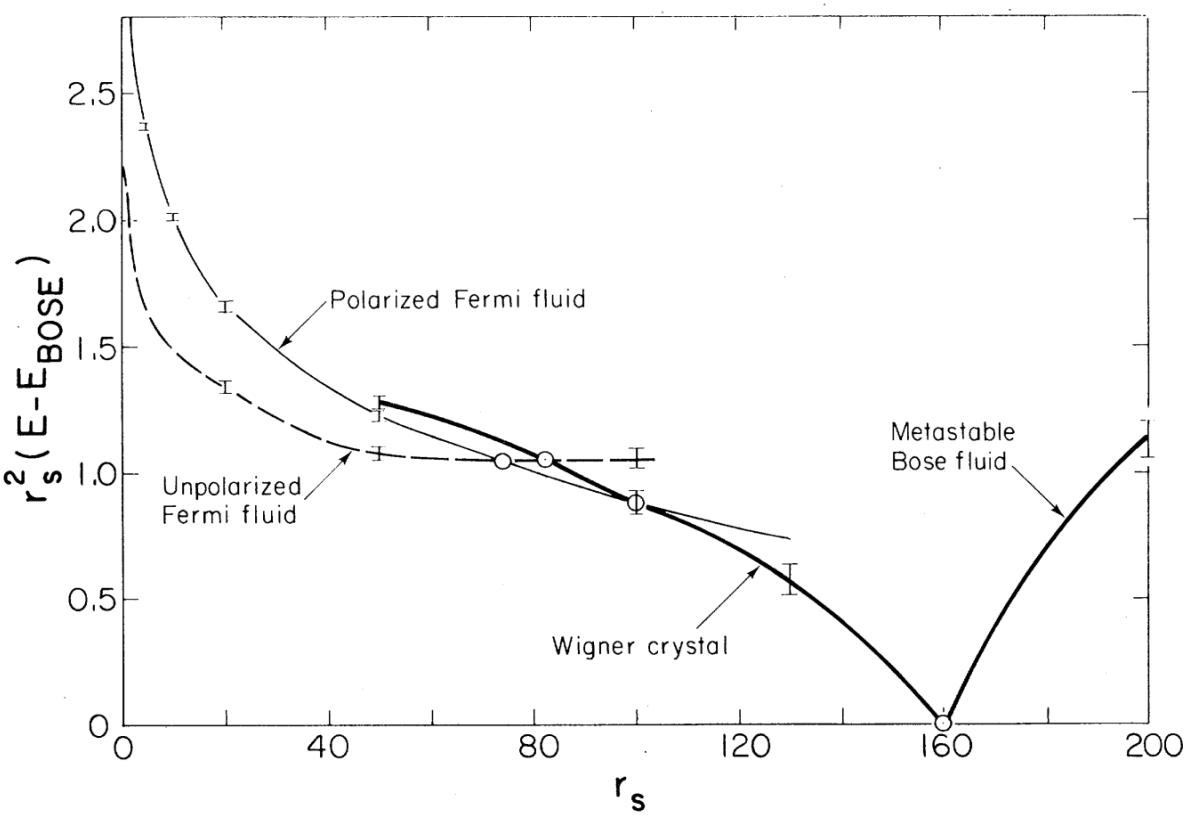

Figure 2.2 – Ground-state energy of the electron gas in various phases (unpolarized/polarized Fermi fluids and Wigner crystal) as a function of Wigner radius r_s. Reproduced from Ref. [89].

differences. While its performance significantly declines in the presence of strong electron correlation, LDA remains remarkably useful across a broad range of systems.

2.1.6.2 Generalized Gradient Approximation

Some of the systematic errors of LDA, such as its tendency to underestimate equilibrium lattice constants and overbind atoms, can be addressed using a more flexible approximation known as the *Generalized Gradient Approximation (GGA)*. While LDA assumes that the exchange-correlation energy density at each point in space depends only on the local value of the electron density $n(\mathbf{r})$, GGA incorporates the spatial variation of the density by including terms that depend on the density gradient $\nabla n(\mathbf{r})$:

$$E_{xc}^{\mathrm{GGA}}[n(\mathbf{r})] = \int n(\mathbf{r})\epsilon_{xc}\left[n(\mathbf{r}), \nabla n(\mathbf{r})\right] \mathrm{d}^3 r. \tag{2.33}$$

This additional dependence allows GGA functionals to account for local inhomogeneities in the electron density, which makes them particularly useful for describing systems with chemical bonding and directional interactions. As a result, GGA often improves upon LDA in predicting structural properties such as bond lengths, vibrational frequencies, and lattice constants. However, GGA does not universally outperform LDA. In some

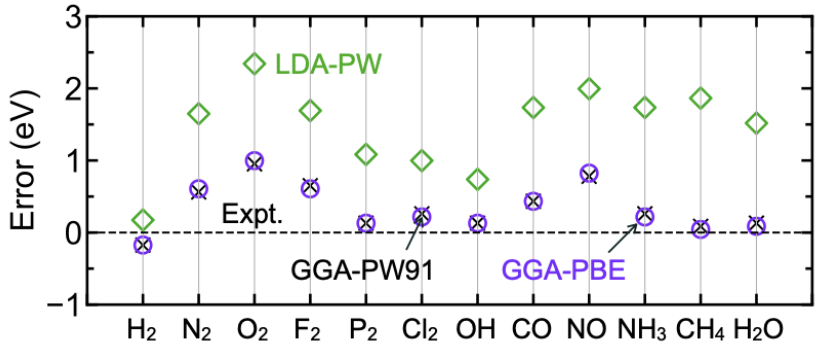

Figure 2.3 – Errors in atomization energies (in eV) for various molecules computed using different exchange-correlation functionals. The dashed line represents the experimental reference. Symbols denote results from LDA (diamonds), GGA-PW91 (crosses), and GGA-PBE (circles). Reproduced from [91].

systems, it can lead to over-delocalization of charge densities and overestimated bond lengths. Nonetheless, both LDA and GGA have been extensively tested and shown to offer reliable results across a wide range of materials.

A widely adopted GGA functional is the Perdew–Burke–Ernzerhof (PBE) form, which balances accuracy and simplicity without relying on empirical fitting to experimental data. PBE remains one of the most popular exchange-correlation functionals in modern electronic structure calculations due to its good performance in both solids and molecules. Figure 2.3 presents a comparison of atomization energy errors for several small molecules calculated using three different exchange-correlation functionals: LDA, GGA-PW91 [92], and PBE. The dashed line at zero indicates the experimental reference values. As shown, the LDA functional systematically overbinds, leading to significant overestimations in atomization energies across all molecules studied. In contrast, both GGA functionals (PW91 and PBE) substantially reduce these errors, with PBE generally yielding the smallest deviations from experiment. This demonstrates the effectiveness of the GGA in correcting the overbinding tendency of the LDA, especially for systems where the electron density varies more rapidly.

2.1.6.3 Hybrid Functionals

In the DFT literature, it is well known an issue called the "band-gap problem": LDA and GGA calculations are known to systematically underestimate the band-gap energy of insulators and semiconductors. This discrepancy originates from the absence of a derivative discontinuity in the exchange-correlation potential $V_{XC}[n]$. In exact Kohn–Sham theory, the fundamental band gap is composed of two contributions: the Kohn–Sham gap ε_g, which is the difference between the highest occupied and lowest unoccupied Kohn–Sham eigenvalues, and an additional term Δ_{xc} arising from a discontinuous shift in V_{XC} when the number of electrons changes by one ($E_g = \varepsilon_g + \Delta_{xc}$). However, both LDA and GGA approximate V_{XC} as a smooth and continuous functional of the electron density, inherently neglecting the

Δ_{xc} contribution. As a result, these approximations systematically yield $E_g = \varepsilon_g$, thereby missing the true energy gap by an often substantial margin. To overcome this limitation, hybrid functionals incorporate a fraction of exact exchange energy defined in Hartree–Fock theory, introducing a non-local component to the exchange-correlation potential that partially recovers the missing discontinuity and improves band gap estimations. The exchange energy can be obtained from Hartree-Fock as

$$E_X^{HF} = \frac{1}{2}\sum_{i=1}^{N}\sum_{j\neq i}\int\int \frac{\psi_i^*(\mathbf{r})\psi_j^*(\mathbf{r}')\psi_j(\mathbf{r})\psi_i(\mathbf{r}')}{|\mathbf{r}-\mathbf{r}'|}\mathrm{d}^3r\mathrm{d}^3r' \tag{2.34}$$

where the 1/2 factor accounts for double counting. A well known hybrid functional used for solids nowadays is the functional proposed by Heyd, Scuseria and Ernzerhof (HSE) [93], with the following form:

$$E_{XC}^{HSE}[n] = aE_X^{HF,SR}(\eta) + (1-a)E_X^{PBE,SR}(\eta) + E_X^{PBE,LR}(\eta) + E_C^{PBE}(\eta) \tag{2.35}$$

with $a = 1/4$ and $\eta = 0.106$. SR and LR are abbreviations for *short range* and *long range* interactions respectively. Since the function $1/r$ diverges for $r \to \infty$ and to ensure convergence of the exchange energy in periodic systems, e.g., solids, the Coulomb interaction is divided into a long and a short range term by using the Ewald summation as

$$\frac{1}{r} = \underbrace{\frac{1-\mathrm{erf}\,(\eta r)}{r}}_{SR} + \underbrace{\frac{\mathrm{erf}\,(\eta r)}{r}}_{LR} \tag{2.36}$$

where erf is the error function [1]. The screening of the Coulomb interaction improves the convergence. It is important to highlight that, in essence, the HSE functional does not constitute a purely DFT approach, as it is not entirely expressed in terms of the electronic density. Instead, it requires a step back in the theoretical framework to represent the exchange energy explicitly in terms of the Kohn–Sham orbitals. This characteristic is what defines hybrid functionals: they incorporate elements from both DFT theory and wavefunction-based methods.

2.1.7 Practical Implementation Details

Since the DFT formalism was well established in the previous sections, we dedicate this following one to the discussion of how the theory is implemented in our calculations.

Basis Sets: The representation of the Kohn-Sham orbitals will require a suitable basis set onto which the components of the orbitals will be projected. For crystals, the periodic nature of the potential $V(\mathbf{r}) = V(\mathbf{r}+\mathbf{R})$ with $\mathbf{R}$ being a real-space lattice vector in the

[1] $\mathrm{erf}(x) = \frac{2}{\sqrt{\pi}}\int_0^x \exp(-t^2)\mathrm{d}t$

Bravais lattice. In periodic potentials, the Bloch theorem is satisfied and the Kohn-Sham orbitals will take the form of *Bloch States*:

$$\psi_{n,\mathbf{k}}(\mathbf{r}) = e^{i\mathbf{k}\cdot\mathbf{r}} u_{n,\mathbf{k}}(\mathbf{r}) \tag{2.37}$$

in which $u_{n,\mathbf{k}}(\mathbf{r})$ is a function that preserves the periodicity of the lattice. It should be noted that the orbitals, and consequently the energies, are indexed not only by their discrete index n but also by a continuous index $\mathbf{k}$ which is the crystal momentum vector in reciprocal space, meaning that the energy of an orbital will also be dependent of which direction the electron is traveling through the crystal. We can also observe that the orbitals for different cells of the crystal will differ only by a phase factor:

$$\psi_{n,\mathbf{k}}(\mathbf{r}+\mathbf{R}) = e^{i\mathbf{k}\cdot\mathbf{R}} \psi_{n,\mathbf{k}}(\mathbf{r}) \tag{2.38}$$

and therefore the probability densities of states in different unit cells will be the same, meaning we can calculate the properties of the entire crystal only with the knowledge of a single unit cell. The fact that the Kohn–Sham orbitals are Bloch states naturally motivates the choice of plane waves as a basis set. The expansion of the periodic parts of the Bloch functions into Fourier series takes the form

$$u_{n,\mathbf{k}}(\mathbf{r}) = \sum_{\mathbf{G}} C_{n,\mathbf{G}}(\mathbf{G}) e^{i\mathbf{G}\cdot\mathbf{R}} \tag{2.39}$$

with $\mathbf{G}$ representing a reciprocal-space lattice vector, defined with respect to the real-space by $\mathbf{G}\cdot\mathbf{R} = 2\pi j$ with j an integer. Substituting the expansion in Eq. 2.39 in Eq. 2.37 we have

$$\psi_{n,\mathbf{k}}(\mathbf{r}) = \sum_{\mathbf{G}} C_{n,\mathbf{k}+\mathbf{G}}(\mathbf{G}) e^{i(\mathbf{k}+\mathbf{G})\cdot\mathbf{R}} \tag{2.40}$$

with the plane waves being a complete and orthonormal basis set of the Hilbert space. In principle, an infinite number of these terms is needed to describe the orbitals perfectly. On the other hand, contributions from plane waves of high kinetic energies decrease exponentially in a way that the series expansion can be truncated with a sufficiently high energy cutoff, and only including plane waves with kinetic energy less than this value:

$$\left| \frac{\hbar^2(\mathbf{k}+\mathbf{G}_{max})^2}{2m_e} \right| \leq E_{cut}. \tag{2.41}$$

The cutoff enables the electron orbitals to be represented with arbitrary precision, allowing for systematic improvement of the representation by increasing the cutoff energy. The validity of a given cutoff energy E_{cut} is assessed by performing total energy calculations and increasing E_{cut} until convergence is achieved within the desired precision. This allows

a controlled trade-off between computational cost and accuracy, tailored to the needs of the study.

***k*-space sampling:** Since Bloch's theorem (Eq. 2.37) introduces the wave vector **k** as a label for the wavefunctions, we are faced with the following challenge: there are infinitely many **k**-points in the Brillouin zone that must be considered to compute the electron density:

$$n(\mathbf{r}) = \frac{\Omega}{(2\pi)^3} \sum_{i=1}^{N} \int_{\mathrm{BZ}} \mathrm{d}^3k \, |\psi_{i,\mathbf{k}}(\mathbf{r})|^2 \tag{2.42}$$

where Ω is the Brillouin zone volume. However, to address this issue and since the wavefunctions of **k**-points sufficiently close to each other in principle should be very similar, we can achieve results over a representative sample of **k**-points that will be able of representing the wavefunctions across most of the Brillouin zone. The most famous way of generating a **k**-point grid that sufficiently samples the Brillouin zone was proposed by Monkhorst and Pack [94] which approximates the Brillouin zone integral as a discrete sum over special **k**-points:

$$\int_{\mathrm{BZ}} \mathrm{d}^3k \, |\psi_{i,\mathbf{k}}(\mathbf{r})|^2 \approx \sum_{j=1}^{N_k} w_j \left|\psi_{i,\mathbf{k}_j}(\mathbf{r})\right|^2 \tag{2.43}$$

where N_k is the total number of k-points and w_j are the corresponding weights, which satisfy $\sum_j w_j = 1$. In practical calculations, the integration over the Brillouin zone is replaced by a discrete summation over a finite k-point mesh. The distribution of these k-points and their associated weights are typically generated using schemes which provides a uniform sampling of the reciprocal space consistent with the crystal's symmetry. The use of symmetry operations allows the integration to be restricted to the irreducible portion of the Brillouin zone, thereby reducing the number of unique k-points that must be explicitly evaluated. As with the energy cutoff, the convergence of the total energy with respect to the density of the k-point mesh should be carefully verified to ensure the accuracy of the calculations.

Pseudopotentials: Although it is possible to model all electrons in a system explicitly, doing so is neither computationally efficient nor strictly necessary. Core electrons, which remain tightly bound near the nucleus, are largely chemically inert with almost no contribution for the bonding. However, the wavefunctions of the Coulomb potential tend to rapidly oscillate as $r \to 0$ and represent this behavior in a plane-wave basis demands a large number of Fourier components, making the explicit treatment of core electrons inefficient. To address these issues in plane-wave DFT, *pseudopotentials* are introduced. The central idea behind the pseudopotential approach is to replace the all-electron potential of an atom with a smoother, effective potential that replicates the influence of the atomic core on the valence electrons. By doing so, the rapidly oscillating behavior of core electron

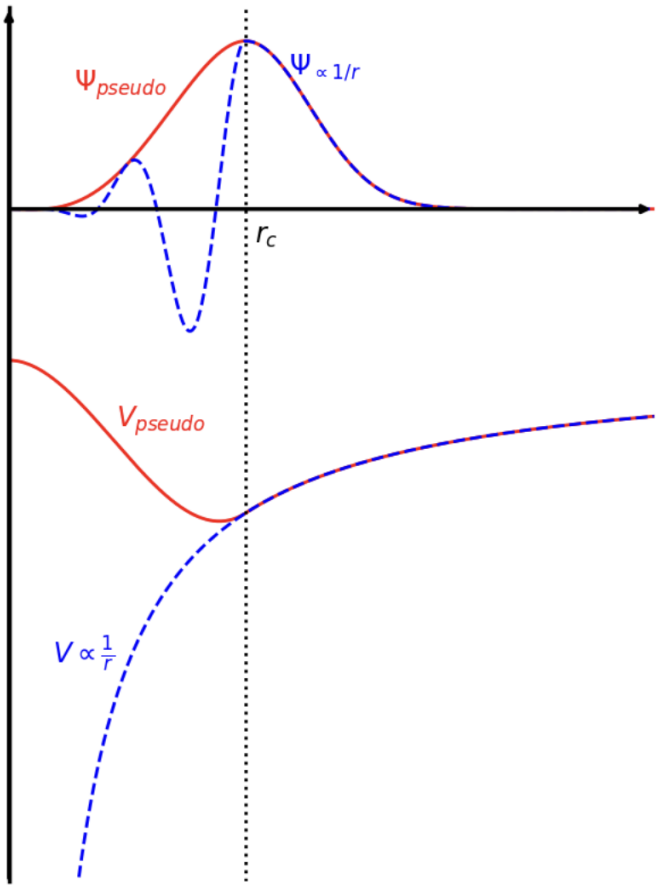

Figure 2.4 – An example illustrating how the use of an ionic core potential can smooth the wavefunction of a valence electron within the cutoff radius.

wavefunctions near the nucleus is removed, allowing the valence states to be described with a significantly smaller plane-wave basis set.

A pseudopotential is constructed in order to satisfy some properties related to a DFT calculation in which the core electrons are also included, also known as *all-electron calculation*. Firstly the pseudopotential must ensure that the pseudo-wavefunction accurately mimics the all-electron wavefunction beyond a specified cutoff radius, reproducing the same eigenenergies and effectively capturing the correct behavior of the valence electrons in that region. Secondly, the pseudopotential should ensure that the pseudo-wavefunction remains nodeless and smooth within the cutoff radius. Thirdly, the pseudopotential depends on the angular momentum, i.e., it is appropriately optimized for different types of orbitals, e.g., s, p, d and f. Figure 2.4 gives a good representation on how a pseudopotential work.

Two widely used classes of pseudopotentials in plane-wave-based DFT calculations are the *norm-conserving* and *ultrasoft* pseudopotentials. Norm-conserving pseudopotentials (NCPPs) are constructed to reproduce the scattering properties of the all-electron calculation while ensuring that the pseudo-wavefunction $R^{\ell}_{\mathrm{PS}}(\epsilon, r)$ matches the true all-electron wavefunction $R^{\ell}_{\mathrm{AE}}(\epsilon, r)$ beyond a chosen cutoff radius r_c, and more importantly, that the norm of the pseudo-wavefunction within the core region equals that of the all-electron

wavefunction:

$$\int_0^{r_c} \left|R^{\ell}_{\mathrm{PS}}(\epsilon, r)\right|^2 r^2\, dr = \int_0^{r_c} \left|R^{\ell}_{\mathrm{AE}}(\epsilon, r)\right|^2 r^2\, dr. \tag{2.44}$$

This *norm-conservation condition* ensures high transferability and allows the pseudopotential to accurately represent various chemical environments. However, it also imposes a constraint on the shape of the pseudo-wavefunction, typically leading to a requirement for a larger number of plane waves and, consequently, a *higher kinetic energy cutoff*. To illustrate commonly employed NCPPs, we highlight the Optimized Norm-Conserving Vanderbilt (ONCV) pseudopotentials [95, 96], as well as the Open-source Pseudopotential Interface / Unification Module (OPIUM) code, which is frequently used to generate NCPPs [97, 98].

In contrast, *ultrasoft pseudopotentials (USPPs)* relax the norm-conservation constraint, allowing the pseudo-wavefunctions to be smoother and thus requiring *fewer plane waves* for convergence. This results in a significantly lower energy cutoff, improving computational efficiency. On the other hand, USPPs introduce *augmentation charges* to compensate for the norm loss inside the core, which makes the formalism more complex and may reduce the transferability in certain conditions. A significant number of widely used USPPs in contemporary DFT calculations are based on the methodology introduced by David Vanderbilt [99]. Notable examples include the Garrity-Bennett-Rabe-Vanderbilt (GBRV) pseudopotential library, which provides coverage for nearly the entire periodic table [100].

A third approach is the *projector augmented-wave (PAW)* method, which provides an all-electron reconstruction of the wavefunctions by combining the efficiency of pseudopotentials with the accuracy of all-electron methods. PAW is often seen as a generalization of both NCPP and USPP schemes and is widely used in modern DFT codes due to its balance between efficiency and accuracy.

In this thesis, Quantum Espresso [101] was the chosen DFT package. It is a robust, open-source software suite widely used in the solid-state physics community, known for its reliability and compatibility with various other computational tools.

2.2 Semiclassical Boltzmann Theory for Transport

Understanding the transport properties of materials is essential for interpreting and predicting their behavior in applications ranging from electronics to thermoelectrics. In this section, we turn to the semiclassical Boltzmann transport theory, a powerful framework that enables the calculation of key transport coefficients, such as electrical conductivity, thermal conductivity, and the Seebeck coefficient, based on the electronic structure obtained from first-principles methods. By connecting microscopic carrier dynamics with macroscopic transport behavior, this theory provides a bridge between quantum mechanical descriptions and experimentally measurable quantities. Particular emphasis will be given

to its application in thermoelectric phenomena, where the interplay between charge and heat transport plays a central role and for a more comprehensive and detailed treatment of Boltzmann transport, the reader is referred to Ref. [102].

2.2.1 The Kinetic Method

The most elementary formulation used to describe the flow of electrical and thermal currents, while still yielding results in reasonable agreement with experiment, is known as the *kinetic method*. This approach constitutes the preliminary level of description from which the Boltzmann transport theory is developed, and it provides a useful framework for building intuition about transport processes in solids.

The idea here is to treat all excitations (electrons, holes and phonons) as particles and follow the motion of one of them at a time. For example, suppose an electron in a metal has velocity $\mathbf{v}$ and is moving through an electric field $\mathbf{E}$. The amount of energy gained by the electron from the field after a time t is:

$$\delta\mathcal{E} = e(\mathbf{v}\cdot\mathbf{E})t \tag{2.45}$$

which will increase its velocity by an amount $\delta\mathbf{v}$ such that[2]

$$\delta\mathbf{v}\cdot\frac{\partial\mathcal{E}}{\partial\mathbf{v}} = \delta\mathcal{E} \tag{2.46}$$

in which $\delta\mathbf{v}$ is called *drift velocity* of the electron. The electron will carry the acceleration provided by the field until it interacts with another impurity or excitation and lose its drift velocity. Since we can not determine the exact moment this collision will happen, we treat those effects probabilistically assuming that those collisions are governed by a characteristic *relaxation time* τ. The only property we impose on this constant is the probability of a particle will suffer a collision in a infinitesimal time $\mathrm{d}t$ is $\mathrm{d}t/\tau$. If $P(t)$ is the probability that the particle has survived without colliding, we see that it must decrease at a rate

$$\frac{\partial P(t)}{\partial t} = -\frac{P(t)}{\tau} \implies P(t) = \exp\left(-\frac{t}{\tau}\right) \tag{2.47}$$

and after each collision, the particle will regain its drift velocity from the beginning. On the average, over a sufficiently long time, it will acquire from the field an extra energy

$$\overline{\delta\mathcal{E}} = \int_0^\infty e(\mathbf{v}\cdot\mathbf{E})t\frac{\partial P(t)}{\partial t}\mathrm{d}t = e(\mathbf{v}\cdot\mathbf{E})\tau \tag{2.48}$$

and if $\partial\mathcal{E}/\partial\mathbf{v}$ happens to be parallel to $\mathbf{v}$, the average drift velocity will be parallel to $\mathbf{E}$, of amount

[2] The partial derivative over a vector is a notation for gradient in $\mathbf{v}$: $\frac{\partial\mathcal{E}}{\partial\mathbf{v}} = \nabla_{\mathbf{v}} = \left(\hat{\mathbf{x}}\frac{\partial}{\partial v_x} + \hat{\mathbf{y}}\frac{\partial}{\partial v_y} + \hat{\mathbf{z}}\frac{\partial}{\partial v_z}\right)$

$$\overline{\delta \mathbf{v}} = \frac{e\upsilon\tau}{\partial\mathcal{E}/\partial\upsilon}\mathbf{E}. \tag{2.49}$$

For n electrons per unit volume, this means a *current density*

$$\mathbf{J} = ne\overline{\delta \mathbf{v}} = \frac{ne^2\upsilon\tau}{\partial\mathcal{E}/\partial\upsilon}\mathbf{E} \tag{2.50}$$

which defines the *electrical conductivity* σ:

$$\mathbf{J} = \sigma\mathbf{E} \ ; \ \sigma = \frac{ne^2\upsilon\tau}{\partial\mathcal{E}/\partial\upsilon} = \frac{ne^2\tau}{m} \tag{2.51}$$

where m is the free electron mass. A more appropriate way to describe σ is in terms of the *mean free path*

$$\Lambda = \upsilon\tau \tag{2.52}$$

which is the average traveled distance between two collisions and is more directly related to the distribution of "colliding" objects in the solid and, therefore, independent of υ. Then, Eq. 2.51 can be written as

$$\sigma = \frac{ne^2\Lambda}{m\bar{\upsilon}}. \tag{2.53}$$

In the kinetic formulation of *thermal conduction*, we consider a temperature gradient ∇T established in an electron gas. Assuming each electron has an atomic heat c, it requires an energy $c\,\delta T$ to change the temperature of its local surroundings by δT. Thus, a particle moving with velocity $\mathbf{v}$ from one region to another will have its energy changed at the rate

$$\frac{\partial\mathcal{E}}{\partial t} = c\mathbf{v}\cdot\nabla T \tag{2.54}$$

so that it is always in equilibrium with its vicinities. If a particle moves freely for a time t, its contribution to the thermal current per unit area, $\mathbf{U}$, depends on the distance υt it travels before colliding. As noted in Eq. 2.48, the average of this distance is $\upsilon\tau$. Summing over all particles, the resulting heat current becomes[3]

$$\mathbf{U} = \frac{nc\tau\upsilon^2}{3}\nabla T = \frac{C\bar{\upsilon}\Lambda}{3}\nabla T \tag{2.55}$$

where C is the total specific heat nc and Λ is given by Eq. 2.52. In other words, the *thermal conductivity* κ is given by

$$\mathbf{U} = \kappa\nabla T \ ; \ \kappa = \frac{C\bar{\upsilon}\Lambda}{3}. \tag{2.56}$$

[3] This in only true for isotropic media. A more general equation is defined in terms of a tensor product: $\mathbf{U} = nc\tau\overline{\mathbf{vv}}\cdot\nabla T$ where $\mathbf{vv}$ is a matrix: $(\mathbf{vv})_{ij} = v_i v_j$ with i and $j = x, y, z$

Both Eqs. 2.53 and 2.56 are of a great practical utility because of their simplicity and straightforward physical interpretation. Moreover, we can deduce an important relation between electrical and thermal conductivities in which Λ can be eliminated between the two equations, giving

$$\frac{\kappa}{\sigma} = \frac{1}{3}\frac{Cm\bar{v}^2}{ne^2}. \tag{2.57}$$

Considering that, in a classical gas the average energy of a particle is $m\bar{v}^2/2 = 3k_BT/2$ (where k_B is the Boltzmann constant) while the specific heat is $3n\kappa/2$, we have

$$\frac{\kappa}{\sigma} = \frac{3}{2}\left(\frac{k_B}{e}\right)^2 T. \tag{2.58}$$

In other words, the ratio $\kappa/\sigma T$ is a constant which is called *Lorenz number*. Eq. 2.58 is called the *Wiedemann-Franz Law*. This relation is also satisfied by a Fermi gas, but with a different coefficient. If we consider that only the electrons at the Fermi surface are able to move, the aforementioned law takes the form

$$\frac{\kappa}{\sigma T} = \frac{\pi^2}{3}\left(\frac{k_B}{e}\right)^2 = \mathfrak{L}_0 \tag{2.59}$$

which is around 2.4453×10^{-8} V^2 K^{-2}. The Wiedemann-Franz Law is often well satisfied experimentally, specially for systems in which Λ is a well-defined quantity. While the kinetic formulation provides valuable intuition and captures essential features of thermal and electrical transport, it relies on simplified assumptions about carrier motion and scattering, i.e., collisions. To achieve a more accurate and general description, especially in systems with complex band structures or non-trivial scattering mechanisms, we now turn to the Boltzmann transport theory.

2.2.2 The Boltzmann Equation

We begin by assuming that the charge carriers in the material are distributed in momentum space $\mathbf{k}$ according to the function $f_{\mathbf{k}}(\mathbf{r}, t)$, which may also depend on the temperature T. In the case of thermal equilibrium, this function corresponds to the Fermi–Dirac distribution in a neighborhood of $\mathbf{r}$:

$$f^0_{\mathbf{k}} = \frac{1}{\exp\left(\frac{\mathcal{E}_{\mathbf{k}} - \mathcal{E}_F}{k_BT}\right) + 1} \tag{2.60}$$

where $\mathcal{E}_{\mathbf{k}}$ is the energy of the carrier and $\mathcal{E}_F$. In the case of non-equilibrium, the distribution function will be affected by the following mechanisms:

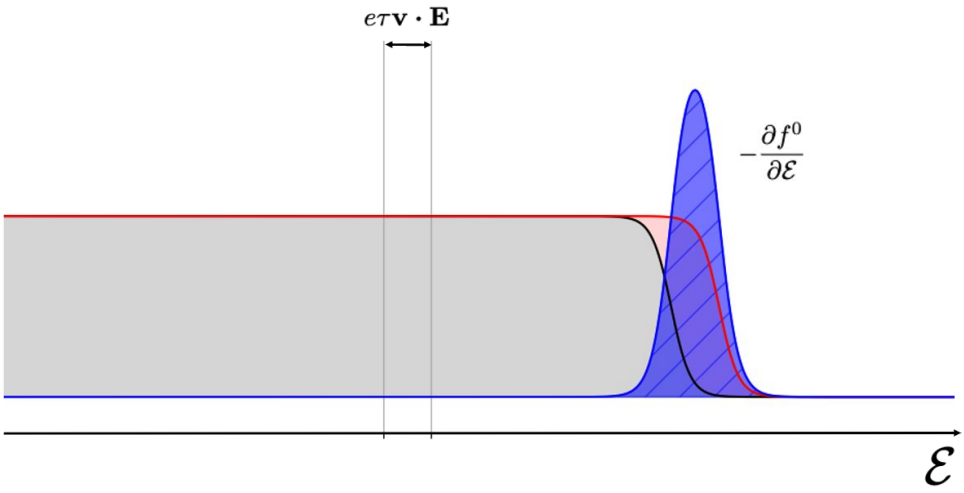

Figure 2.5 – Displaced Fermi–Dirac distribution under the influence of an external electric field. The shaded gray region represents the equilibrium distribution $f^0(\varepsilon)$, while the red curve shows the shifted distribution due to the perturbation $e\tau\mathbf{v}\cdot\mathbf{E}$. The blue curve illustrates the derivative $-\partial f^0/\partial\varepsilon$, which determines the range of states contributing to electronic transport.

- **Diffusion:** Due to the velocities $\mathbf{v_k}$, carriers can move into or out of the neighborhood of $\mathbf{r}$, leading to spatial variations in carrier concentration. If $f_\mathbf{k}$ varies across space, its time evolution at each point tends to follow the rate:

$$\left.\frac{\partial f_\mathbf{k}}{\partial t}\right|_{diff} = -\mathbf{v_k}\cdot\frac{\partial f_\mathbf{k}}{\partial \mathbf{r}}. \tag{2.61}$$

  A correspondence between diffusion processes and the temperature gradient can be made if the distribution $f_\mathbf{k}$ in question is the Fermi-Dirac distribution as shown in Equation 2.60:

$$\mathbf{v_k}\cdot\frac{\partial f_\mathbf{k}}{\partial \mathbf{r}} = \mathbf{v_k}\cdot\frac{\partial f^0_\mathbf{k}}{\partial \mathbf{r}} = \mathbf{v_k}\cdot\frac{\partial}{\partial \mathbf{r}}\left[\frac{1}{\exp\left(\frac{E_\mathbf{k}-E_F}{k_BT}\right)+1}\right] \tag{2.62}$$

  where the temperature $T = T(\mathbf{r})$ is a function of position that represents the average kinetic energy of the carriers in a vicinity around $\mathbf{r}$. Applying the derivative, we obtain the following expression:

$$\frac{\partial f^0_\mathbf{k}}{\partial \mathbf{r}} = -\frac{\partial f^0_\mathbf{k}}{\partial E_\mathbf{k}}\left[(E_\mathbf{k}-E_F)\frac{\nabla T(\mathbf{r})}{T(\mathbf{r})} - \nabla(E_\mathbf{k}-E_F)\right] \tag{2.63}$$

  making it clear that the diffusion processes occurring in the system are related to the temperature gradient.

- **External Fields:** A carrier is subject to the Lorentz force in the presence of the fields $\mathbf{E}$ and $\mathbf{B}$. Since $\mathbf{F} = \dot{\mathbf{p}} = \hbar\dot{\mathbf{k}}$, we can say that the vector $\mathbf{k}$ varies in time according to the following formula:

$$\dot{\mathbf{k}} = \frac{e}{\hbar}\left(\mathbf{E} + \frac{\mathbf{v_k}}{c} \times \mathbf{B}\right) \tag{2.64}$$

where c is the speed of light. Such motion of carriers due to external fields will correspond to variations in $f_{\mathbf{k}}$ as follows:

$$\left.\frac{\partial f_{\mathbf{k}}}{\partial t}\right|_{field} = -\frac{e}{\hbar}\left(\mathbf{E} + \frac{\mathbf{v_k}}{c} \times \mathbf{B}\right) \cdot \frac{\partial f_{\mathbf{k}}}{\partial \mathbf{k}}. \tag{2.65}$$

- **Scattering:** Other interactions of carriers among themselves and with phonons in the lattice have the effect of changing their $\mathbf{k}$ state. Such processes, on average, give rise to a variation rate

$$\left.\frac{\partial f_{\mathbf{k}}}{\partial t}\right|_{scat} \tag{2.66}$$

whose analytical form depends on the specific scattering process considered.

An example of the action of these mechanisms on the Fermi distribution is illustrated in Figure 2.5. Adding the three mechanisms, the total variation in the distribution is

$$\frac{\partial f_{\mathbf{k}}}{\partial t} = \left.\frac{\partial f_{\mathbf{k}}}{\partial t}\right|_{diff} + \left.\frac{\partial f_{\mathbf{k}}}{\partial t}\right|_{field} + \left.\frac{\partial f_{\mathbf{k}}}{\partial t}\right|_{scat}. \tag{2.67}$$

In the steady-state situation, the three variations must cancel out ($\partial_t f_{\mathbf{k}} = 0$), resulting in the equation:

$$\left.\frac{\partial f_{\mathbf{k}}}{\partial t}\right|_{scat} - \mathbf{v_k} \cdot \frac{\partial f_{\mathbf{k}}}{\partial \mathbf{r}} - \frac{e}{\hbar}\left(\mathbf{E} + \frac{\mathbf{v_k}}{c} \times \mathbf{B}\right) \cdot \frac{\partial f_{\mathbf{k}}}{\partial \mathbf{k}} = 0 \tag{2.68}$$

known as the *Boltzmann equation for transport* in its most general form. The difficulty of Eq. 2.68 lies in the complexity of the scattering term. We need to consider the contributions from all transition rates into the $\mathbf{k}$-th state, which themselves depend on the occupations of those states. This leads to a term that, in general, will be an integral over all possible values of $\mathbf{k}$ with $f_{\mathbf{k}}$ itself on the integrand, i.e., an integro-differential equation. However, there are some simplifications we can do to deal with Eq. 2.68. One simplifying assumption that is always made is that, *in equilibrium*, the scattering term must vanish:

$$\left.\frac{\partial f^0_{\mathbf{k}}}{\partial t}\right|_{scat} = 0 \tag{2.69}$$

so that *detailed balance* is satisfied. In general we can define the deviation from the steady state distribution

$$g_{\mathbf{k}} = f_{\mathbf{k}} - f^0_{\mathbf{k}} \tag{2.70}$$

which will not vanish unless all fields and temperature gradients are zero. Thus, for small deviations from equilibrium, we can take the lowest term of the power expansion from the scattering term in which $g_{\mathbf{k}}$ will not vanish. Omitting intermediate algebraic steps, this leads to the *linearized Boltzmann equation*[4]:

$$-\mathbf{v}_{\mathbf{k}} \cdot \frac{\partial f^0_{\mathbf{k}}}{\partial T}\nabla T - \mathbf{v}_{\mathbf{k}} \cdot e\frac{\partial f^0_{\mathbf{k}}}{\partial \mathcal{E}_{\mathbf{k}}}\mathbf{E} = \int (g_{\mathbf{k}} - g_{\mathbf{k}'})\mathcal{Q}^{\mathbf{k}'}_{\mathbf{k}}\mathrm{d}^3k' \tag{2.71}$$

which the integral comes from the scattering term with $\mathcal{Q}^{\mathbf{k}'}_{\mathbf{k}}$ being the transition probability for each process. The solution for Eq. 2.71, whichever it is, must be a linear function of $\mathbf{E}$ and ∇T. We can simplify this problem even further and assume that all collisions between carriers in the material will be elastic. This makes the scattering probability term to be dependent only of the angle θ between $\mathbf{k}$ and $\mathbf{k}'$. Hence we can define a differential transition probability $\mathcal{Q}(k,\theta)\mathrm{d}\Omega$ and change the integral in $\mathbf{k}'$ into an integral in $\mathrm{d}\Omega$:

$$\int (1-\cos\theta)\mathcal{Q}(k,\theta)\mathrm{d}\Omega = \frac{1}{\tau(k)}. \tag{2.72}$$

Dimensional analysis show that the above integral has units of inverse time. A more complete derivation can be found in Sec. 7.3 of *Principles of the Theory of Solids* by J. M. Ziman [103]. This is in fact the *relaxation time* discussed in Sec. 2.2.1 but, this time, it was obtained from Eq. 2.71 and can also be related to a *mean free path* by Eq. 2.52 . In general, it is a function of k but it is often taken as a constant. If the scattering processes are much faster than those of diffusion and field, any deviations in $g_{\mathbf{k}}$ caused by the action of external fields and temperature gradients must decay to zero as:

$$-\frac{\partial g_{\mathbf{k}}}{\partial t} = \frac{g_{\mathbf{k}}}{\tau} \implies g_{\mathbf{k}}(t) = g_{\mathbf{k}}(0)e^{-t/\tau}. \tag{2.73}$$

That is, $g_{\mathbf{k}}$ undergoes the effect of an average scattering process that decays to zero according to the relaxation time. In semiconductors, this relaxation time is in the order of 10^{-13} to 10^{-14} seconds [104]. Also, the existence of a relaxation time means that the Wiedemann-Franz law should hold.

Whether an analytic solution for Eq. 2.71 exists or not, we shall always find that the electrical and thermal currents are linear functions of $\mathbf{E}$ and ∇T, i.e.,

$$\begin{aligned}\mathbf{J} &= \int e\mathbf{v}_{\mathbf{k}} f_{\mathbf{k}} d^3k = L_{EE}\mathbf{E} - L_{ET}\nabla T \\ \mathbf{U} &= \int \mathcal{E}_{\mathbf{k}}\mathbf{v}_{\mathbf{k}} f_{\mathbf{k}} d^3k = L_{TE}\mathbf{E} - L_{TT}\nabla T\end{aligned} \tag{2.74}$$

which follows directly from the linearity of the integral equation. The study of these coefficients, also called *transport coefficients* or *thermoelectric properties*, is what is called the study of *thermoelectricity*.

[4] Here we ignored the magnetic term

2.2.3 Thermoelectricity

The treatment of the Boltzmann transport equation, along with the relaxation time approximation developed in the previous section, provides the necessary formal framework for deriving transport coefficients and, in turn, evaluating the thermoelectric properties of a given material. In reality, the coefficients listed in Eq. 2.74 are not directly observed in experiments but we are able to measure the following quantities:

Electrical Conductivity σ: When we keep the material at a constant temperature and apply an electric field $\mathbf{E}$, a current density $\mathbf{J}$ is observed such that

$$\mathbf{J} = \sigma \mathbf{E} \tag{2.75}$$

Obviously, if we consider $\nabla T = 0$,

$$\sigma = L_{EE} \tag{2.76}$$

and its inverse corresponds to the resistivity ($\rho = \sigma^{-1}$).

Thermal Conductivity κ: Here, the material is electrically insulated to prevent any electric current flowing through it. A thermal gradient is maintained and the heat flux is measured. The required coefficient is κ in the relation

$$\mathbf{U} = -\kappa \nabla T. \tag{2.77}$$

Since, in this situation $\mathbf{J} = 0$, Eq. 2.74 gives us

$$\mathbf{E} = -\frac{L_{ET}}{L_{EE}} \nabla T \tag{2.78}$$

and hence

$$\mathbf{U} = L_{TT} \nabla T - \frac{L_{ET} L_{TE}}{L_{EE}} \nabla T \implies \kappa = -\Big(L_{TT} - \frac{L_{ET} L_{TE}}{L_{EE}} \Big). \tag{2.79}$$

This means that to stop the electric current generated by carrier motion due to the thermal gradient, an electric field builds up along the material to counteract this motion, slightly reducing the thermal current, so that κ is not simply L_{TT}. It is important to mention that the thermal conductivity considered here is only takes into account the contribution of the carriers while there is also a contribution from the vibrations of the lattice which is not considered here.

Seebeck Coefficient S: Let us consider the electric field described in Eq. 2.78 to maintain $J = 0$. Therefore, the entire temperature gradient generated in the material is converted into an electromotive force. This effect is commonly known as Seebeck effect and the

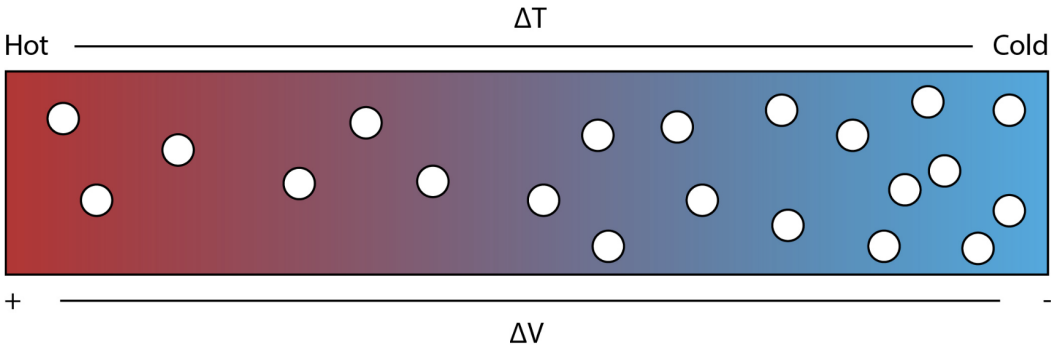

Figure 2.6 – Schematic illustration of the Seebeck effect.

proportionality constant between the temperature gradient and the field is known as *Seebeck coefficient* or *thermopower*:

$$\mathbf{E} = S\nabla T \ ; \ S = -\frac{L_{ET}}{L_{EE}}. \tag{2.80}$$

This effect can be well understood looking at Figure 2.6. Consider that the left side of metallic bar was heated while the right side was maintained cold. Naturally the electrons (represented by white circles) of the left side are more thermally excited and hence more spatially separated than the ones on the right side. This means that the left side is less dense in electrons than in the right side, i.e., there is more electrons in the right than in the left. Since the bar is electrically isolated and therefore there is no electrical current, an electric field will naturally appear to maintain difference in densities between both sides. This is the physical principle underlying thermocouple thermometers that are used on a very broad range of industrial application due to their precision in situations of extreme temperatures. While the Seebeck effect involves the generation of electricity using thermal gradients, there is an analogous effect, known as the Peltier effect, which utilizes electricity to generate thermal gradients and a similar coefficient can be defined such that

$$\mathbf{U} = \Pi\mathbf{J} \ ; \ \Pi = \frac{L_{TE}}{L_{EE}} \tag{2.81}$$

known as the *Peltier Coefficients*. An important aspect of the transport coefficients defined in Eq. 2.74 is their interdependence, governed by the Onsager reciprocal relations, which play a fundamental role in the framework of the *thermodynamics of irreversible processes*. For example, those relations require the Peltier coefficient to be equal to the Seebeck coefficient times the temperature. There are also two coefficients defined to measure how good is the performance of a thermoelectric material. Those coefficients are combinations of the ones we discussed before:

Power Factor $S^2\sigma$: It is a fundamental quantity in the evaluation of thermoelectric performance. It reflects the efficiency with which a material converts a thermal gradient

Table 2.1 – Figures of merit in various materials. The materials in the right-hand column are known for their use in thermoelectric devices.

Material	Figure of Merit	Material	Figure of Merit
InSe (Monolayer)[a]	≈ 0.36	Bi_2Te_3 (Bulk)[d]	≈ 1.0
Silicene (Si Monolayer)[b]	≈ 0.36	Bi_2Te_3 (Thin Film)[e]	≈ 2.4
MoS_2 (Monolayer)[c]	≈ 0.58	SnSe (Thin Film)[f]	≈ 2.6
		$FeV_{0.8}W_{0.2}Al$ (Thin Film)[g]	≈ 5.0

[a] Ref. [105] [b] Ref. [106] [c] Ref. [107] [d] Ref. [108] [e] Ref. [109] [f] Ref. [110] [g] Ref. [111]

into electrical power. A higher power factor indicates that, for a given temperature difference, the material can generate more electrical power through carrier transport. As such, optimizing the power factor is a central goal in the design of high-performance thermoelectric materials, requiring a careful balance between high electrical conductivity and a large Seebeck coefficient.

Figure of Merit ZT $S^2\sigma T/\kappa$: It is a dimensionless parameter that characterizes the thermoelectric efficiency η of a material. A higher figure of merit ZT reflects reduced irreversible heat loss and enhanced energy conversion efficiency in thermoelectric devices [112]. The concept of ZT emerges when the thermoelectric device is modeled as a heat engine, enabling the quantification of the portion of thermal energy converted into useful electrical work versus the fraction dissipated as waste heat [113]. In principle, ZT can assume arbitrarily high values, and as it increases, the efficiency of the device approaches the Carnot limit. Consequently, the design and synthesis of thermoelectric materials aim to maximize ZT. Table 2.1 presents a comparison of ZT values for a variety of materials, encompassing both bulk and thin-film compounds that exemplify the current state of the art in thermoelectric performance. Notably, bulk Bi_2Te_3 is widely employed in thermoelectric heat pumps, which form the core of practical devices such as cooling systems for small refrigerators. As an example, a notable demonstration of the practical potential of thermoelectric materials is a prototype vehicle which employed a thermoelectric generator (TEG) to convert exhaust heat into electricity using Bi_2Te_3-based modules for higher-temperature operation [114].

For the results discussed in Chapter 3, all the thermoeletric properties were calculated as functions of the temperature and chemical potential using the BoltzTraP code [115]. Since the carriers velocities can be obtained using the band structure of the material ($\mathbf{v_k} = \hbar^{-1}\partial_{\mathbf{k}}\epsilon_{i\mathbf{k}}$), BoltzTraP calculates all transport coefficients within the *relaxation time*

approximation based on the electronic structure of the valence and conduction bands and the equations described above.

2.3 Molecular Dynamics

There are several computational/simulational methods in condensed matter physics, e.g., the *ab initio* calculations already discussed in Sec. 2.1. To mention some other methods commonly used, we have *finite element methods* which rely on the discretization of time and space to solve partial differential equations that are usual in material modeling [116] and we have *Monte Carlo methods* which relies on the sampling of random numbers to make stochastic simulations of materials [117]. Each method has its advantages and disadvantages, e.g., finite element methods are appropriate to test elasticity in meso-to-macroscopic scales but fails to reproduce properties on a finer scales and Monte Carlo methods are appropriate to determine ground state statistical properties but cannot give properties that are truly time dependent except for pure diffusion. Another class of simulational methods in condensed matter physics are the so called *Molecular Dynamics methods* (MD), which investigates the motion of atoms and molecules, assuming that an empirical interatomic potential governing their interactions is known. Given the potential energy function for a system of N particles, the time evolution of their positions and velocities is obtained by numerically integrating Newton's equations of motion. For a more comprehensive and detailed treatment of those methods, the reader is referred to Refs. [118] and [119].

2.3.1 Observables in MD

The theoretical basis for MD simulations embodies many of the important results that compose the foundations of classical mechanics, with an special attention to the theorems of uniqueness of solutions of trajectories in the Hamiltonian formulation [120]. Thus, before delving into the algorithms commonly used in MD, it is worthwhile to discuss how physical properties can be extracted from the atomic trajectories as a function of time. After all, these trajectories represent the primary source of information provided by a MD simulation. In a system of N particles, the phase space Γ is a vector of $6N$ coordinates:

$$\Gamma = (\mathbf{r}_1, \ldots, \mathbf{r}_N, \mathbf{p}_1, \ldots, \mathbf{p}_N) \tag{2.82}$$

where each vector $\mathbf{r}$ indicating position and each vector $\mathbf{p}$ indicating momentum. Integrating the equations of motion from an initial point Γ_0 in phase space yields the trajectory of the particles, the information of which is contained in $\Gamma(t)$. In this way, we can define macroscopic observables $B(t) = B(\Gamma(t))$, which are calculated in terms of the positions and velocities of the system's particles. Some examples of such observables include:

- Total kinetic energy:

$$T(t) = \sum_{i=1}^{N} \frac{|\mathbf{p}_i(t)|^2}{2M_i} \tag{2.83}$$

- Total potential energy:

$$V(t) = \sum_{i=1}^{N} \sum_{j>i} V(|\mathbf{r}_i(t) - \mathbf{r}_j(t)|) \tag{2.84}$$

- Dipole moment (for charged particles with charge q_i):

$$\mathbf{M}(t) = \sum_{i=1}^{N} q_i \mathbf{r}_i(t) \tag{2.85}$$

among many other examples of observables that can be considered. In experiments, what is actually measured are the averages of such observables and, in the context of molecular dynamics, these averages correspond to time averages of the form:

$$\langle B \rangle = \lim_{\tau \longrightarrow \infty} \frac{1}{\tau} \int_{t_0}^{\tau} B(t) \mathrm{d}t. \tag{2.86}$$

The interpretation of this expression lies in the experimental procedure where, at an initial time t_0, a measurement device is activated and, at successive time intervals $\mathrm{d}t$, measurements of the observable B are recorded over a duration τ, resulting in the computation of the average of the values obtained throughout the process. This is the most common procedure for calculating quantities such as the average temperature or pressure in a simulation.

As important as the averages of dynamical variables are the correlation functions between two dynamical variables, defined as follows for variables A and B:

$$\langle A(0)B(t) \rangle = \lim_{\tau \longrightarrow \infty} \frac{1}{\tau} \int_{0}^{\tau} A(t')B(t+t') \mathrm{d}t'. \tag{2.87}$$

From these functions, we gain information about the coefficients of dissipative processes, which are typically related to fluctuations in dynamical variables. Examples of such coefficients include the diffusion coefficient D and thermal conductivity κ of the material media, as described by Green–Kubo theory [121]:

- Diffusion Coefficient:

$$D = \frac{1}{3N} \int_{0}^{\infty} \left\langle \sum_{j=1}^{N} \mathbf{v}_j(t) \cdot \mathbf{v}_j(0) \right\rangle \mathrm{d}t \tag{2.88}$$

- Thermal Conductivity:

$$\kappa = \frac{1}{k_B T^2 V} \int_0^\infty \langle \mathbf{J}_E(0) \cdot \mathbf{J}_E(t) \rangle \, \mathrm{d}t, \quad \mathbf{J}_E(t) = \frac{\mathrm{d}}{\mathrm{d}t} \left[\sum_{i=1}^{N} E_i(t) \mathbf{r}_i(t) \right] \tag{2.89}$$

  where $\mathbf{J}_E$ is is the energy current (heat flux) defined in terms of a time derivative of the energy moment, i.e., the first moment of the energy distribution with respect to position.

Furthermore, the Fourier transform of such correlation functions is related to the characteristic frequency spectrum of the system, e.g., the *vibrational power spectra* is a quantity directly proportional to the vibrational density of states and it is defined in terms of a Fourier transform of the velocity autocorrelation function:

$$I(\omega) = \frac{1}{N} \int_{-\infty}^{\infty} \left\langle \sum_{j=1}^{N} \mathbf{v}_j(t) \cdot \mathbf{v}_j(0) \right\rangle e^{i\omega t} \mathrm{d}t \tag{2.90}$$

which contains information of all vibrational modes capable to propagate through the material. Moreover, a procedure for obtaining dielectric functions using molecular dynamics simulations can be found in Ref. [122] and is based on the expression of the dielectric function as the Fourier transform of the average total dipole moment:

$$\varepsilon(\omega) = 1 + \frac{1}{3\varepsilon_0 V k_B T} \left[\left\langle \mathbf{M}^2 \right\rangle + i\omega \int_0^\infty \langle \mathbf{M}(t) \cdot \mathbf{M}(0) \rangle \, e^{i\omega t} \mathrm{d}t \right] \tag{2.91}$$

where $\mathbf{M}$ is the total dipole moment of the system as defined in Eq. 2.85, ε_0 is the vacuum permittivity, V is the system volume, k_B is the Boltzmann constant, and ω is the angular frequency. The resulting $\varepsilon(\omega)$ from simulations carries information about the lattice vibrations capable of absorbing light. There are other quantities of great importance in the context of MD, such as the pair distribution function $g(\mathbf{r})$ and its Fourier transform, known as the structure factor $S(\mathbf{k})$, but these lie beyond the scope of this thesis.

2.3.2 Potentials and Models

The potential energy $V(r)$ contains the relevant information regarding the interatomic interactions, i.e., the functional form that models the interactions between different atoms. In theory, the form of these potentials is governed by the behavior of valence electrons, as previously discussed in the context of Density Functional Theory (DFT) in Sec. 2.1. However, employing such first-principles methods within molecular dynamics simulations entails prohibitively high computational costs, even for relatively small systems, making them impractical for simulations at the scales of interest. To overcome this limitation, empirical potentials (also known as empirical force fields), i.e., interatomic potentials parameterized based on data obtained from either quantum mechanical calculations or

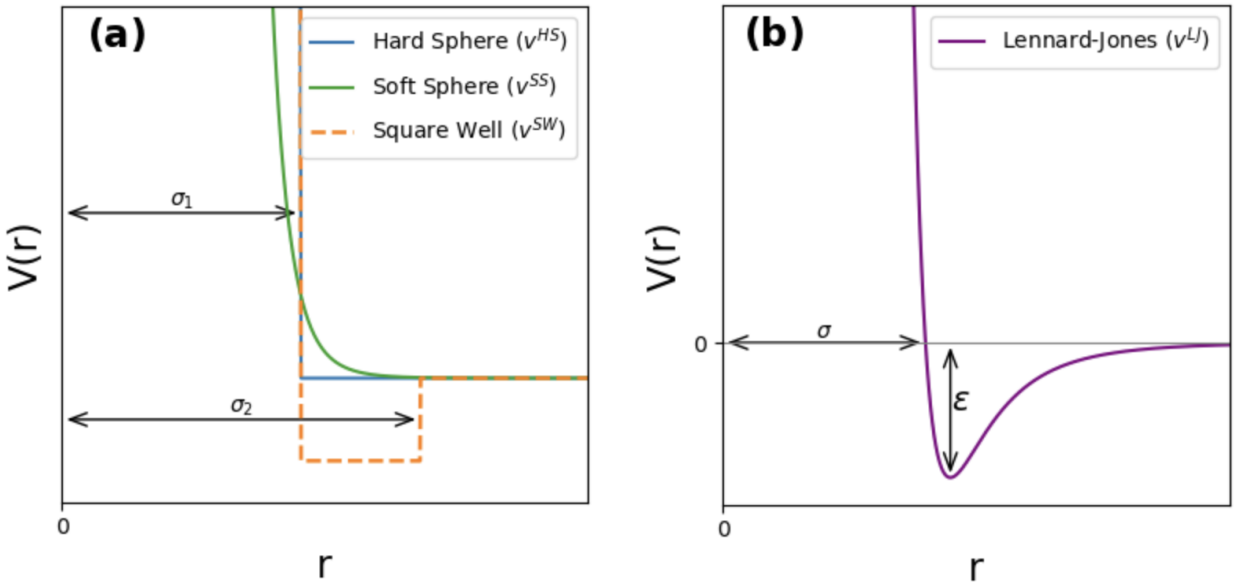

Figure 2.7 – Examples of empirical pair potentials. (a) Idealized spherical models: hard sphere, square well, and soft sphere. (b) Lennard-Jones 12-6 pair potential.

experimental measurements, are often used to model the interaction between atoms. The total potential energy given by those empirical force fields may be divided into terms depending on the coordinates of individual atoms, pairs, triplets and so on:

$$V = \sum_{i=1}^{N} v_1(\mathbf{r}_i) + \sum_{i=1}^{N}\sum_{j>i} v_2(\mathbf{r}_i, \mathbf{r}_j) + \sum_{i=1}^{N}\sum_{j>i}\sum_{k>j>i} v_3(\mathbf{r}_i, \mathbf{r}_j, \mathbf{r}_k) + \dots \tag{2.92}$$

where v_1 could model the effects of an external field such as an electric field or even walls on a simulation box, v_2 models a pair potentials that relies only on the distance between atoms $r_{ij} = |\mathbf{r}_2 - \mathbf{r}_1|$ and v_3 is a three body potential that is usually dependent on the angle between these three atoms $\theta_{ijk} = \angle(\mathbf{r}_1, \mathbf{r}_2, \mathbf{r}_3)$. Here we will discuss some of the most memorable of those potentials.

2.3.2.1 Spherical Potentials

Perhaps the simplest of the two body potentials is the hard sphere potential, which models atoms as non-overlapping spheres with infinite repulsion at contact and no interaction otherwise:

$$v^{HS}(r) = \begin{cases} \infty, & r < \sigma_1 \\ 0, & r \geq \sigma_1 \end{cases} \tag{2.93}$$

where σ is the characteristic diameter of the atom. Although this potential seems unrealistic, it allows the modeling of very simple liquids and has a great importance in liquid-state

theory. Other two simple potentials with similar importance in simulations of very simple systems are the square well potential

$$v^{SW}(r) = \begin{cases} \infty, & r < \sigma_1 \\ -\varepsilon, & \sigma_1 \leq r < \sigma_2 \\ 0, & r \geq \sigma_2 \end{cases} \tag{2.94}$$

built upon the hard sphere model by introducing an attractive region of finite depth ε just beyond the hard core, representing weak bonding interactions, and the soft-sphere potential

$$v^{SS}(r) = \varepsilon\left(\frac{\sigma_1}{r}\right)^{\nu} = ar^{-\nu} \tag{2.95}$$

where ν is a parameter, often chosen to be an integer, that determines the steepness of the repulsion, avoiding discontinuities on the derivative. The three spherical potentials are shown in Figure 2.7a and serve as foundational models in molecular simulations, offering analytical and computational tractability while capturing key physical behaviors of more complex interatomic interactions.

2.3.2.2 Lennard-Jones Potential

The Lennard-Jones potential is perhaps the most widely used empirical potential for describing interatomic interactions, specially in noble gases and non-bonded interactions in molecular systems. It captures the essential features of short-range repulsion and long-range van der Waals attraction using a simple analytical form.

The energy between two atoms separated by a distance r, shown in Figure 2.7b, is given by

$$V^{LJ}(r) = 4\epsilon\left[\left(\frac{\sigma}{r}\right)^{12} - \left(\frac{\sigma}{r}\right)^{6}\right] \tag{2.96}$$

where ϵ is the depth of the potential well, representing the strength of the interaction, and σ is the finite distance at which the interparticle potential is zero. The r^{-12} term accounts for the strong repulsive force due to Pauli exclusion principle, while the r^{-6} term is derivable from first principles and models the attractive dipole-dipole interaction [123]. To highlight the historical significance of the Lennard-Jones potential, it is worth mentioning the first MD simulation ever performed for liquid argon, carried out by A. Rahman in 1964 [124]. The parameters used for liquid argon were $\sigma = 3.405$ Å and $\epsilon/k_B = 119.8$ K. To reduce computational cost in MD simulations, the Lennard-Jones potential is often truncated beyond a cutoff radius r_c, where interactions are assumed negligible. However, directly setting the potential to zero at $r > r_c$ introduces a discontinuity at the cutoff, which can

result in spurious forces when particles cross this boundary. To address this, a common approach is to use the *shifted Lennard-Jones potential*, defined such that the potential smoothly goes to zero at $r = r_c$. This is accomplished by subtracting the value of the potential at the cutoff, ensuring continuity in $V(r)$:

$$V^{LJ,\text{shift}}(r) = \begin{cases} 4\epsilon\left[\left(\frac{\sigma}{r}\right)^{12} - \left(\frac{\sigma}{r}\right)^{6}\right] - V^{LJ}(r_c), & r < r_c \\ 0, & r \geq r_c. \end{cases} \tag{2.97}$$

This modification eliminates the abrupt jump in potential energy at the cutoff, improving numerical stability and avoiding non-physical behavior in the simulation. This is one of the several common approaches in MD simulations to ensure smoothness at $r = r_c$. As a final remark, we point out that while the Lennard-Jones potential is widely used for modeling simple fluids and noble gases, its applicability to solid-state systems is limited. As a purely isotropic two-body potential, it can only accurately describe close-packed structures such as face-centered cubic (FCC) and hexagonal close-packed (HCP) lattices, where the stability arises primarily from uniform pairwise interactions. However, many materials of interest, including covalently bonded crystals like diamond and silicon, require a more detailed representation of interatomic forces that accounts for bond angles and many-body effects. The Lennard-Jones potential lacks bonding information and cannot enforce angular constraints, making it unsuitable for simulating crystals that do not belong to the FCC and HCP classes. As such, more sophisticated potentials that incorporate multi-body interactions or angular dependence are necessary for modeling a wide range of condensed matter systems [125].

2.3.2.3 Stillinger-Weber Potential

Among the various potentials designed to overcome the limitations of the Lennard-Jones potential noted earlier, the Stillinger–Weber potential is a prominent example [126]. It is composed of two terms:

$$V^{SW} = \sum_{i<j} V_2(r_{ij}) + \sum_{i<j<k} V_3(r_{ij}, r_{ij}, \theta_{jik}) \tag{2.98}$$

in which the index of each term denotes the two and three-body potential. The two-body term can be seen as a generalization of the Lennard-Jones potential:

$$V_2(r) = \begin{cases} A\left[B\left(\frac{\sigma}{r}\right)^{p} - \left(\frac{\sigma}{r}\right)^{q}\right] f_c(r, r_c; \sigma), & r < r_c \\ 0, & r \geq r_c. \end{cases} \tag{2.99}$$

where A is the overall energy scaling factor, B controls the relative strength between the repulsive and attractive components of the potential, σ represents the van der Waals radius,

and r_c is the cutoff radius. A function f_c, known as the cutoff function, is introduced with a purpose similar to that of the shifted potential in Eq.2.97, namely, to ensure that the potential is smooth at $r = r_c$:

$$f_c(r;\alpha) = \exp\left(\frac{\alpha}{r - r_c}\right). \tag{2.100}$$

One can verify that $f_c \to 0$ as $r \to r_c$. The three-body term is introduced to energetically favor a specific bond angle θ_0, corresponding to the ideal local geometry of the crystal. This term penalizes deviations from θ_0, allowing internal bond angles to fluctuate thermally around this preferred value while maintaining structural stability:

$$V^{(3)}(r_{ij}, r_{ik}, \theta_{jik}) = \begin{cases} \lambda A \left[\cos\theta_{jik} - \cos\theta_0\right]^2 f_c(r_{ij};\gamma) f_c(r_{ik};\gamma), & r_{ij}, r_{ik} < r_c \\ 0, & r_{ij}, r_{ik} \geq r_c \end{cases} \tag{2.101}$$

where λA is also interpreted as the overall interaction strength and γ is a decay parameter that governs the rate at which the bond-angle interaction diminishes as the inter-particle distance r_{ij} increases. Figure 2.8 shows both terms of the Stillinger Weber potential considering $p = 4$ and $q = 0$, a typical choice for those exponents. It is worth emphasizing that, although the Stillinger–Weber potential enables the modeling of crystal structures beyond simple FCC and HCP lattices, the symmetry of the target structure must be provided in advance. In other words, before constructing the potential, i.e., fitting its parameters, the underlying lattice symmetry must be known a priori to ensure that the potential accurately captures the structural properties of a given material. There are many other potentials and methods beyond the Stillinger–Weber model that are commonly

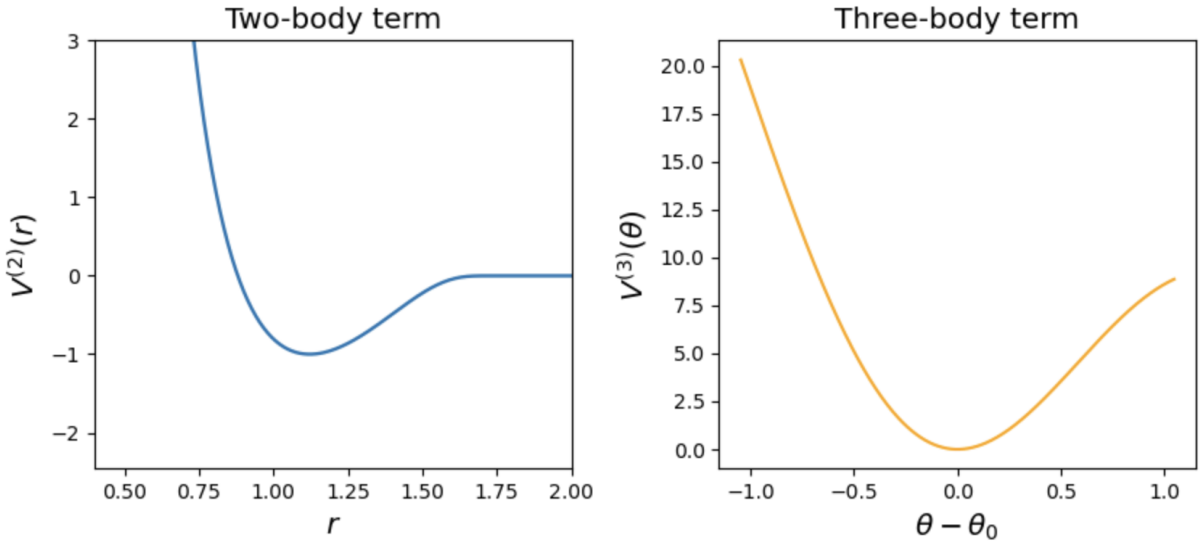

Figure 2.8 – Stillinger-Weber potential. (Left) Two-body term illustrating pairwise interactions. (Right) Three-body term depicting the angular dependence of interactions among triplets. Parameters taken from Ref. [126]

employed in the simulation of crystalline materials. To cite a few examples: the Tersoff potential is widely used for carbon-based systems [127] while TIP3P is frequently applied in simulations of water [128–130], the Embedded Atom Method (EAM) is prevalent in the study of metallic alloys [131] and the Vashishta potential is commonly utilized for both amorphous and crystalline SiO_2 [132]. Numerous examples exist, but all empirical potentials share a common limitation: their accuracy in reproducing experimental results typically does not match that of *ab initio* methods. While some of these potentials are parameterized based on data obtained from *ab initio* calculations, their predictive accuracy tends to degrade when extrapolated beyond the conditions under which they were fitted. Thus, computational methods in condensed matter physics often involve a trade-off between the desired level of accuracy and the associated computational cost. Later in Sec. 2.4, we will discuss what are known as *Machine Learning Force Fields (MLFFs)* developed to overcome this limitation by offering results with accuracy comparable to *ab initio* methods, but at a significantly reduced computational cost.

2.3.3 Integration Methods

Since MD is inherently based on the time evolution governed by Newton's equations of motion, it is essential to select an integration method that is both efficient and accurate. The choice of integration scheme plays a critical role in ensuring the numerical stability of simulations, controlling systematic finite element errors, minimizing computational cost, and preserving the physical fidelity of dynamical trajectories over extended time scales. Here, we will discuss some of the most commonly used integration methods, addressing their implementation strategies and analyzing how the numerical error scales with the size of the timestep. This will allow for a systematic comparison of their accuracy, stability, and computational efficiency. Moreover, each integration method is characterized by a specific *local truncation error* and *cumulative truncation error*. The *local truncation error* is defined as the error introduced in a *single integration step*, assuming that the exact solution is known at the beginning of that step. In other words, it measures the discrepancy between the exact solution and the numerical approximation after advancing by one timestep. The *cumulative truncation error*, on the other hand, represents the *total error* accumulated over many timesteps across the entire integration interval. The magnitudes of those errors scale with a power n of the timestep δt and this scaling behavior is commonly expressed using the big-$\mathcal{O}$ notation, written as $\mathcal{O}(\delta t^n)$, which indicates that the error grows proportionally to $(\delta t)^n$ as the timestep becomes small.

2.3.3.1 Euler Method

This is perhaps the simplest of them. The *Euler method* is a first-order numerical integration scheme that approximates the time evolution of a system by using the derivative information

at the current timestep to estimate the state at the next timestep. Given a system described by Newton's second law:

$$\frac{d\mathbf{r}}{dt} = \mathbf{v}(t), \qquad \frac{d\mathbf{v}}{dt} = \frac{\mathbf{F}(\mathbf{r}(t))}{m}, \tag{2.102}$$

where $\mathbf{r}(t)$ and $\mathbf{v}(t)$ are the position and velocity vectors, $\mathbf{F}$ is the force, and m is the mass, the Euler method advances the position and velocity as:

$$\mathbf{r}(t+\delta t) = \mathbf{r}(t) + \mathbf{v}(t)\delta t, \quad \mathbf{v}(t+\delta t) = \mathbf{v}(t) + \frac{\mathbf{F}(\mathbf{r}(t))}{m}\delta t. \tag{2.103}$$

The *local truncation error* of the Euler method is proportional to $\mathcal{O}(\delta t^2)$, making the *cumulative truncation error* scale as $\mathcal{O}(\delta t)$. Due to this relatively low accuracy, the Euler method is rarely used in molecular dynamics simulations where long-term stability and energy conservation are critical. However, it remains a useful pedagogical example to illustrate the basic principles of numerical integration.

2.3.3.2 Runge-Kutta Method

The *Runge-Kutta methods* represent a family of higher-order integration schemes designed to improve the accuracy of numerical solutions to differential equations while maintaining computational efficiency. Among these, the most commonly used is the *fourth-order Runge-Kutta method* (RK4), which achieves a local truncation error of order $\mathcal{O}(\delta t^5)$ and a cumulative error of order $\mathcal{O}(\delta t^4)$. Considering a system governed by Newton's second law just as in Eq. 2.102 the RK4 method advances the solution from time t to $t+\delta t$ using a *weighted average* of several intermediate evaluations of the derivative. For the velocity update, these are defined as:

$$\begin{aligned}
\mathbf{k}_1 &= \delta t\, \mathbf{a}(t, \mathbf{r}(t)), \\
\mathbf{k}_2 &= \delta t\, \mathbf{a}\left(t + \frac{\delta t}{2}, \mathbf{r}(t) + \frac{\mathbf{k}_1 \delta t}{2}\right), \\
\mathbf{k}_3 &= \delta t\, \mathbf{a}\left(t + \frac{\delta t}{2}, \mathbf{r}(t) + \frac{\mathbf{k}_2 \delta t}{2}\right), \\
\mathbf{k}_4 &= \delta t\, \mathbf{a}\left(t + \delta t, \mathbf{r}(t) + \mathbf{k}_3 \delta t\right),
\end{aligned} \tag{2.104}$$

where $\mathbf{a}(t, \mathbf{r}(t)) = \mathbf{F}(\mathbf{r}(t))/m$ is the acceleration. The new velocity and position are then updated as:

$$\mathbf{v}(t+\delta t) = \mathbf{v}(t) + \frac{1}{6}\overbrace{(\mathbf{k}_1 + 2\mathbf{k}_2 + 2\mathbf{k}_3 + \mathbf{k}_4)}^{\text{weighted average}}, \quad \mathbf{r}(t+\delta t) = \mathbf{r}(t) + \mathbf{v}(t)\delta t. \tag{2.105}$$

This formulation offers a significant improvement in accuracy over simpler methods such as the Euler one. However, this comes at the cost of a greater number of floating-point operations per timestep, since multiple force evaluations are required for each update.

2.3.3.3 Predictor-Corrector Methods

Predictor-Corrector schemes are a class of algorithms that improve the accuracy of numerical integration by combining an initial prediction of the system state with a subsequent correction based on updated information. In MD, such methods are commonly used to enhance the precision of position and velocity updates while maintaining computational efficiency. A well-known example of such an approach is *Beeman algorithm*, which can be considered a *Predictor-Corrector scheme*. The central idea is to first predict the positions and velocities using past and present accelerations, then correct these predictions using more accurate force evaluations at the new predicted positions. The prediction step is typically expressed as:

$$x(t+\delta t) = x(t) + v(t)\delta t + \frac{1}{6}\left[4a(t) - a(t-\delta t)\right]\delta t^2 + \mathcal{O}(\delta t^4), \tag{2.106}$$

where $a(t)$ and $a(t-\delta t)$ are the accelerations at the current and previous timesteps, respectively. After predicting the position, the velocity is also predicted by:

$$v(t+\delta t) = v(t) + \frac{1}{6}\left[2a(t+\delta t) + 5a(t) - a(t-\delta t)\right]\delta t + \mathcal{O}(\delta t^4), \tag{2.107}$$

where $a(t+\delta t)$ is calculated from the predicted position. Once the predicted positions $x(t+\delta t)$ are obtained, the forces (and hence the accelerations $a(t+\delta t)$) are recalculated. These updated accelerations are then used in the *corrector step* to refine the velocity. The Predictor-Corrector method also allows for a *local truncation error* of order $\mathcal{O}(\delta t^4)$ and a *cumulative truncation error* of $\mathcal{O}(\delta t^3)$, providing higher accuracy compared to simpler schemes. However, this comes at the cost of additional memory and computational requirements, since accelerations at multiple previous timesteps must be stored and used.

2.3.3.4 Leapfrog Method

The *Leapfrog method* is widely used in MD due to its simplicity, time-reversibility, and favorable energy conservation properties over long simulations. It is classified as a second-order accurate method, with a local truncation error of order $\mathcal{O}(\delta t^3)$ and a cumulative error of order $\mathcal{O}(\delta t^2)$. Its central idea is to update positions and velocities in a "staggered" fashion, i.e., the velocity is computed at half-integer time steps $(t+\delta t/2)$ while the position is computed at integer time steps $(t, t+\delta t)$. This staggered update allows the method to "leapfrog" over the position and velocity updates. The velocity update is given by:

$$\mathbf{v}\left(t+\frac{\delta t}{2}\right)=\mathbf{v}\left(t-\frac{\delta t}{2}\right)+\delta t\,\mathbf{a}(t) \tag{2.108}$$

and the position is then updated using:

$$\mathbf{r}(t+\delta t)=\mathbf{r}(t)+\delta t\,\mathbf{v}\left(t+\frac{\delta t}{2}\right). \tag{2.109}$$

This procedure is repeated iteratively for each timestep. The main advantages of the Leapfrog method include its simplicity, ease of implementation, and good long-term energy conservation, which is essential for stable simulations. It is the default numerical integrator in GROMACS, a open source MD code well established for the simulation of biochemical molecules such as proteins, lipids, and nucleic acids, where it models complex bonded and non-bonded interactions to study their structure and dynamics over time [133].

2.3.3.5 Verlet Method

We now discuss the method most commonly employed in MD, which was the selected method to the simulations in this thesis: *the Verlet method*. It relies on a Taylor series expansion of $\mathbf{r}(t\pm\delta t)$ around time t:

$$\mathbf{r}(t+\delta t)=\mathbf{r}(t)+\mathbf{v}(t)\,\delta t+\frac{1}{2}\mathbf{a}(t)\,\delta t^2+\ldots \tag{2.110}$$

$$\mathbf{r}(t-\delta t)=\mathbf{r}(t)-\mathbf{v}(t)\,\delta t+\frac{1}{2}\mathbf{a}(t)\,\delta t^2+\ldots \tag{2.111}$$

By summing the two expansions, the velocity dependence is eliminated from the trajectory update, resulting in the following expression:

$$\mathbf{r}(t+\delta t)=2\mathbf{r}(t)-\mathbf{r}(t-\delta t)+\mathbf{a}(t)\,\delta t^2. \tag{2.112}$$

Once the new positions at $t+\delta t$ are obtained, the velocity (necessary, for instance, to compute the kinetic energy) can be recovered by subtracting the two Taylor expansions:

$$\mathbf{v}(t)=\frac{\mathbf{r}(t+\delta t)-\mathbf{r}(t-\delta t)}{2\delta t}. \tag{2.113}$$

The Verlet method incurs a local truncation error of order $\mathcal{O}(\delta t^4)$ at each timestep δt and a global cumulative truncation error of $\mathcal{O}(\delta t^2)$. In fact, the Verlet method is widely regarded as one of the most effective integration schemes for molecular dynamics simulations due to its simplicity, numerical stability, and favorable long-term energy conservation properties. Its second-order accuracy offers a good balance between computational efficiency and precision, with only a modest computational cost per timestep. Hence, it is a standard choice in MD simulations, being the main numerical integrator implemented in the open

Table 2.2 – Comparison of integration methods commonly used in MD simulations.

Method	**Floating Point Operations**	**Local Error**	**Global Error**
Euler	Low	$\mathcal{O}(\delta t^2)$	$\mathcal{O}(\delta t)$
Runge-Kutta (RK4)	High	$\mathcal{O}(\delta t^5)$	$\mathcal{O}(\delta t^4)$
Predictor-Corrector	Moderate to High	$\mathcal{O}(\delta t^4)$	$\mathcal{O}(\delta t^3)$
Leapfrog	Low	$\mathcal{O}(\delta t^3)$	$\mathcal{O}(\delta t^2)$
Verlet	Low	$\mathcal{O}(\delta t^4)$	$\mathcal{O}(\delta t^2)$

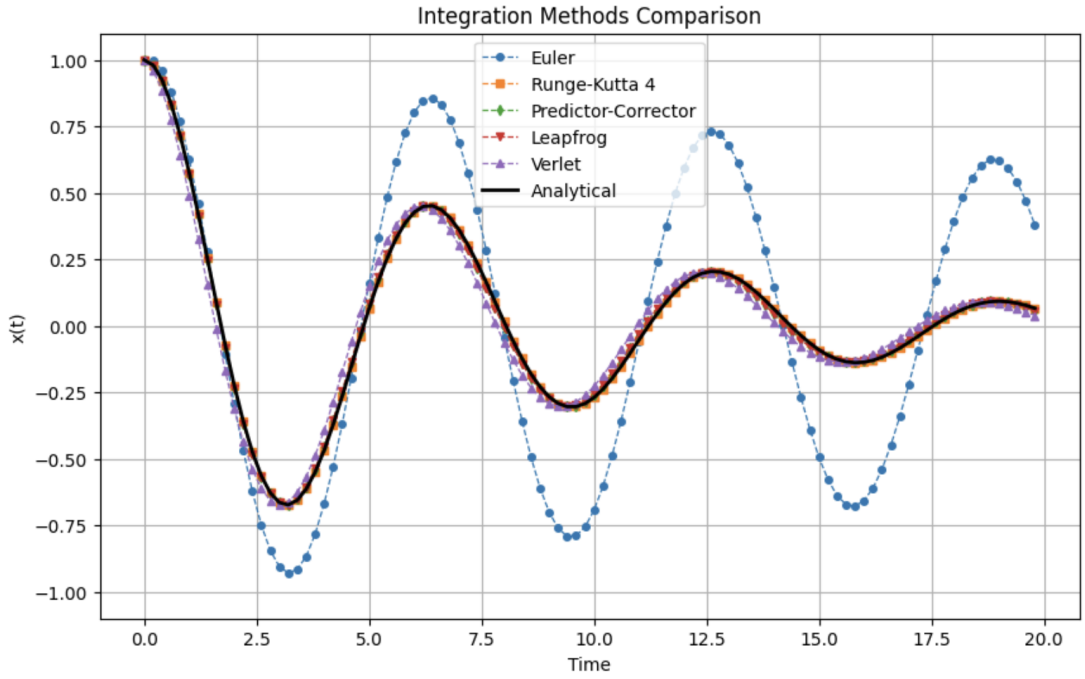

Figure 2.9 – Comparison of numerical integration methods with the analytical solution for an damped harmonic oscillator.

source code LAMMPS, which was used in all simulations in this thesis [134]. LAMMPS also include implementations of the RESPA integrator [135] which is used in more specific kinds of simulations and whose discussion is beyond the scope of this thesis. Table 2.2 provides a comparative overview of several integration methods commonly employed in simulations. The comparison includes an assessment of the computational cost, expressed qualitatively in terms of the amount of floating-point operations required per timestep, as well as the orders of the *local truncation error* and the *global accumulated error* associated with each method, summarizing the trade-offs between computational efficiency and numerical accuracy, which are central considerations when selecting an appropriate integration scheme for a given simulation. Moreover, Figure 2.9 shows how each integration method captures the characteristic features of the damped harmonic oscillator, including the gradual amplitude decay and oscillatory behavior, allowing for a direct comparison of their numerical accuracy and stability. In order to obtain Figure 2.9, a Python code that solves the equations of motion of the damped harmonic oscillator numerically using all the discussed methods was written and is included in Annex A. To provide an estimate

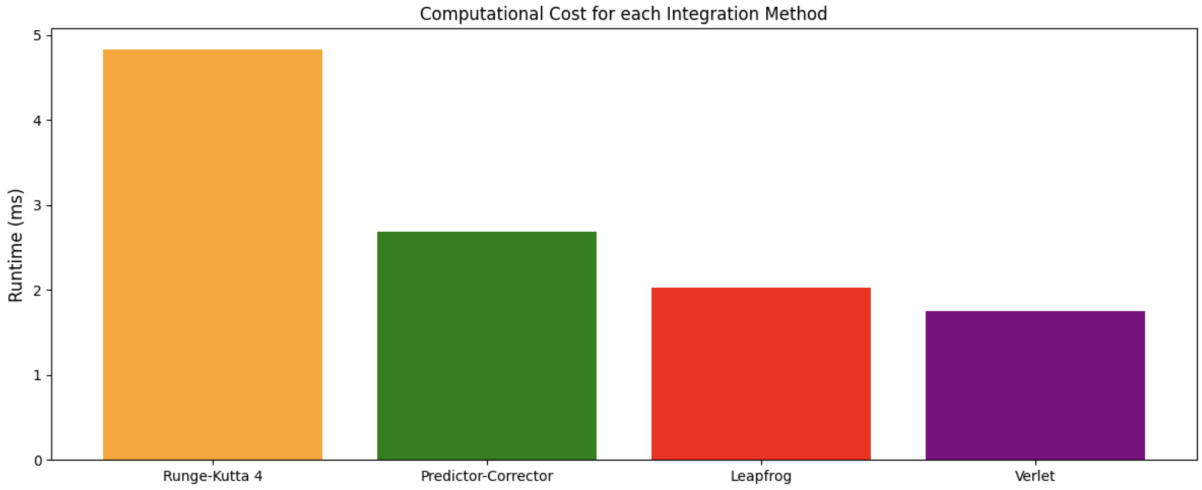

Figure 2.10 – Computational cost of different numerical integration methods for the damped harmonic oscillator. The runtime corresponds to a benchmark run of 500 time steps using the Python code provided in Annex A.

of the number of floating-point operations associated with each method (which serves as an indicator of computational cost), Figure 2.10 has been included. From the results, it is evident that the Verlet algorithm exhibits the lowest computational cost, whereas the fourth-order Runge–Kutta method is the most computationally demanding. This observation explains why LAMMPS predominantly employs the Verlet algorithm: in large-scale molecular dynamics simulations, the reduced number of floating-point operations outweighs the marginal gains in accuracy provided by higher-order methods, making Verlet particularly well-suited for such applications.

2.3.4 Thermostats

Since MD is a method that solves the equations of motion to obtain the observables discussed in Sec.2.3.1, conventional MD inherently conserves the total energy of the system and, therefore, is naturally suited to generate thermodynamic configurations within the microcanonical ensemble (NVE). To perform simulations in other ensembles, such as the canonical ensemble (NVT), it is necessary to modify the equations of motion to account for the effects of maintaining a fixed temperature, typically achieved by introducing a *thermostat* into the system. In this section, we discuss the fundamental principles underlying thermostatting, which can also be extended to enable simulations in other ensembles, such as the isothermal-isobaric ensemble (NPT).

2.3.4.1 Nosé-Hoover Thermostat

The Nosé-Hoover thermostat, which constitutes the default implementation in LAMMPS, operates by coupling the physical system to an external heat bath through the introduction of a virtual degree of freedom [136]. Consider a system of N point particles. Within

the Lagrangian formalism, the system possesses $3N$ degrees of freedom—three spatial coordinates per particle—and its Lagrangian is expressed as $\mathcal{L} = \mathcal{T} - \mathcal{V}$, where $\mathcal{T}$ and $\mathcal{V}$ denote the total kinetic and potential energies, respectively. The Nosé-Hoover thermostat couples the heat bath to the physical system by introducing an additional fictitious degree of freedom, $s = s(t)$, which rescales the velocities according to $\mathbf{v}_i = s\dot{\mathbf{r}}_i$. Consequently, the system is extended to $3N + 1$ degrees of freedom, and its dynamics are governed by an augmented Lagrangian of the form:

$$\mathcal{L} = \frac{1}{2}\sum_{i=1}^{N} m_i s^2 \dot{\mathbf{r}}_i^2 - \sum_{i<j} U(r_{ij}) + \frac{1}{2} M_s \dot{s}^2 - n_f k_B T_{eq} \ln(s) \tag{2.114}$$

where m_i is the mass of particle i, $U(r)$ is the interaction potential between the particles, $n_f = 3N + 1$ is the number of degrees of freedom of the extended system, T_{eq} is the desired temperature, and M_s can be interpreted as an inertial parameter that controls the amount of energy exchanged between the physical system and the thermal reservoir. The equations of motion are given by the Euler-Lagrange equations:

$$\frac{\mathrm{d}}{\mathrm{d}t}\frac{\partial \mathcal{L}}{\partial \dot{q}} - \frac{\partial \mathcal{L}}{\partial q} = 0 \tag{2.115}$$

where q represents the generalized coordinate associated with each degree of freedom in the extended system. A common choice for M_s in MD simulations is $M_s = 100\delta t$, which provides a suitable balance between maintaining a stable coupling to the heat bath and allowing the physical system to effectively sample the canonical ensemble without introducing significant perturbations to the dynamics. Figure 2.11 shows the velocity histogram obtained from MD a simulation of a Lennard-Jones fluid using the Nosé-Hoover thermostat with different coupling parameters ($M_s = 0.1$ and $M_s = 1.0$), showing that the distributions converge to the theoretical Maxwell-Boltzmann distribution at long times no matter the chosen coupling parameter, demonstrating the correct sampling of the NVT ensemble.

2.3.4.2 Langevin Thermostat

The Langevin thermostat models the interaction of a system with a thermal bath by introducing both a frictional force and a stochastic random force into the equations of motion. The resulting Langevin equation for a particle of mass m can be written as:

$$m\frac{d^2\mathbf{r}}{dt^2} = -\nabla U(\mathbf{r}) - \gamma\frac{d\mathbf{r}}{dt} + \sqrt{2\gamma k_B T}\mathbf{R}(t), \tag{2.116}$$

where $\nabla U(\mathbf{r})$ represents the deterministic force due to interatomic potentials, γ is the friction coefficient that models energy dissipation to the environment, $k_B T$ sets the strength of thermal fluctuations, and $\mathbf{R}(t)$ is a Gaussian white noise term with zero mean and unit

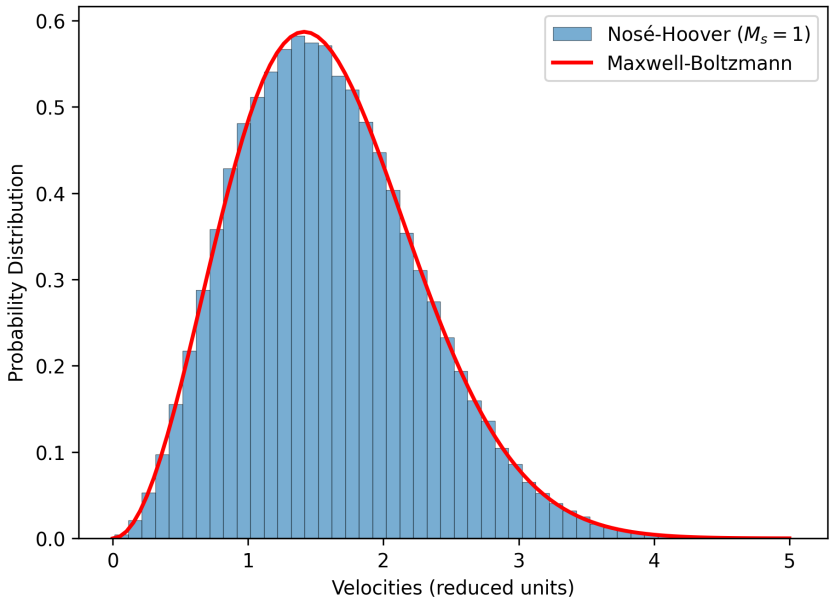

Figure 2.11 – Velocity histograms from Nosé-Hoover simulations with $M_s = 1.0$ for a simple Lennard-Jones fluid, converging to the Maxwell-Boltzmann distribution, confirming proper NVT sampling.

variance. This formulation ensures that the system samples from the canonical ensemble (NVT) by maintaining the correct balance between dissipation and stochastic energy input. Compared to deterministic thermostats like the Nosé-Hoover thermostat, the Langevin approach introduces randomness, making it particularly robust for small systems and short simulations, where ergodicity might be a concern. The stochastic nature of the Langevin thermostat can help the system to overcome energy barriers and more effectively explore the configurational space. However, the Nosé-Hoover thermostat is typically preferred in large-scale simulations where deterministic dynamics and conservation of time-reversal symmetry are important. Nosé-Hoover enables smooth sampling of the canonical ensemble without introducing stochastic forces, making it better suited for systems where accurate dynamical properties are required, such as vibrational spectra or transport coefficients. In contrast, the Langevin thermostat may distort dynamical correlations due to its stochastic nature, but excels in ensuring rapid equilibration and robust temperature control, particularly in systems with poor ergodic properties.

2.3.5 Implementation and Optimizations

LAMMPS (an acronym for Large-scale Atomic/Molecular Massively Parallel Simulator) has been developed with a strong focus on computational efficiency, incorporating numerous optimizations that leverage distributed-memory parallelization to accelerate simulations [134]. These features have established LAMMPS as one of the most widely used open-source packages for MD simulations in materials science. In this section, we discuss some of the key algorithmic and implementation strategies that contribute to LAMMPS's efficiency

and scalability.

2.3.5.1 Verlet lists

We shall start the discussion mentioning *the N^2 problem*. In systems with N particles interacting via pairwise potentials, computing all interactions requires $N(N-1)$ force evaluations per time step, a challenge commonly known as the N^2 problem due to its quadratic scaling with system size. For large systems, this approach becomes computationally prohibitive, especially when interactions are limited by a cutoff radius r_c, as with Lennard-Jones or Stillinger-Weber potentials. In such cases, many force calculations involve particle pairs separated by distances greater than r_c, contributing negligibly to the dynamics. To mitigate this inefficiency, LAMMPS uses *Verlet neighbor lists* (also known simply as Verlet lists) as a key optimization strategy.

There are generally two approaches to implement a cutoff radius r_c in a MD code. The most straightforward method involves calculating the interatomic distance r between two particles and using a conditional ("IF") statement to evaluate the potential energy only when $r < r_c$. However, despite its simplicity, this approach requires a loop over all N particles in the system. Additionally, the overhead introduced by the conditional statement executed at each iteration further contributes to computational inefficiency. Consequently, this method is not well-suited for large-scale simulations where performance optimization is critical. An alternative and more efficient approach to implementing a cutoff radius r_c involves indexing all N atoms in the simulation and storing the indices of the neighboring atoms for a given atom i, i.e., those located within a sphere where $r < r_c$ in a list. This structure, commonly referred to as the *neighbor list*, allows the inner loop for calculating the interactions of atom i to iterate only over a subset of the total system, thereby significantly reducing computational cost. The neighbor list is periodically updated at specified intervals, which can be adjusted to balance the trade-off between computational efficiency and the precision of the interaction calculations.

Verlet took this concept of a neighbor list even further. In his original method, the potential cutoff sphere of a given atom is surrounded by a "skin" s such that if two particles are within a distance $r_l = r_c + s$ they are added to list, as shown in Figure 2.12. This algorithm is successful because the *skin* around r_c is chosen to be thick enough so that between list reconstructions an atom, such as 7 in 2.12 which is not on the list of atom 1, cannot penetrate through the skin into the r_c sphere. The implementation of this method reduces the time complexity from $\mathcal{O}(N^2)$ to $\mathcal{O}(N^{5/3})$. In addition, *cell lists* are a complementary approach to Verlet lists, aimed at improving computational efficiency even further. By partitioning the simulation box into discrete cells with side length $l_{\text{cell}} > r_c$ (the cutoff distance), interactions are limited to particles within neighboring cells, avoiding unnecessary calculations for distant particles. This method is particularly advantageous

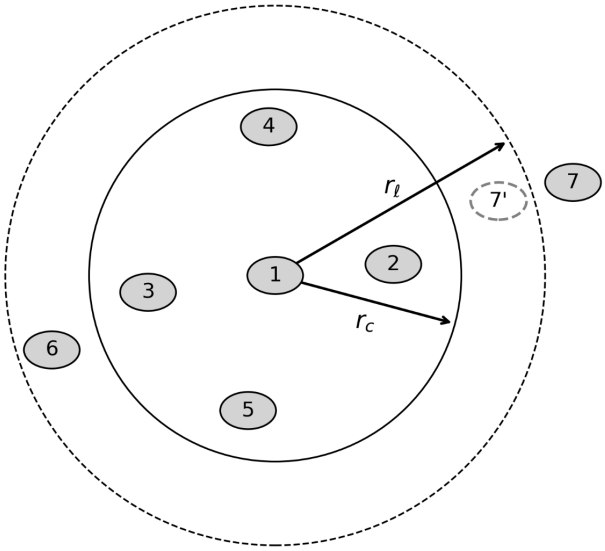

Figure 2.12 – Illustration of the cutoff sphere (radius r_c) and the neighbor list skin (radius r_l) for atom 1. Atoms 2–6 are included in the list, though only atoms 2–4 are within the interaction range.

in condensed matter systems, where particle displacements between cells are infrequent, allowing for infrequent list updates while maintaining accuracy. The use of cell lists reduces the computational complexity from $\mathcal{O}(N^2)$ to $\mathcal{O}(N)$, providing significant performance improvements for large-scale simulations.

Appendix 5 contains a discussion about *parallelization* of MD simulations, its importance for simulating large systems and how it is implemented in LAMMPS. Furthermore, Annex B contains a brief LAMMPS tutorial intended for readers interested in learning how to practically implement it in their simulations. This tutorial was originally prepared as part of a graduate-level course on molecular dynamics.

2.4 Machine Learning Force Fields

Recalling what we said in the end of Sec. 2.3.2, there is a known gap in the study of materials through atomistic simulations: its reliability relies heavily on the quality of the given potential energy surface (PES)[5] and while electronic structure methods provide *ab initio* description of the PES at a high computational expense, empirical interatomic potentials parametrizes the PES in terms of the atomic degrees of freedom, allowing significant speed-ups in simulations, it sacrifices accuracy in return. In recent years, *Machine Learning Force Fields (MLFFs)* have emerged as a groundbreaking alternative that shortens the gap between these two extremes. In general, MLFFs are trained on datasets of *ab initio* calculated energies and forces (e.g, obtained from DFT) for various

[5] Potential energy surface represents the multidimensional potential energy of a system as a function of a set of atomic positions, describing how the energy changes with different atomic configurations.

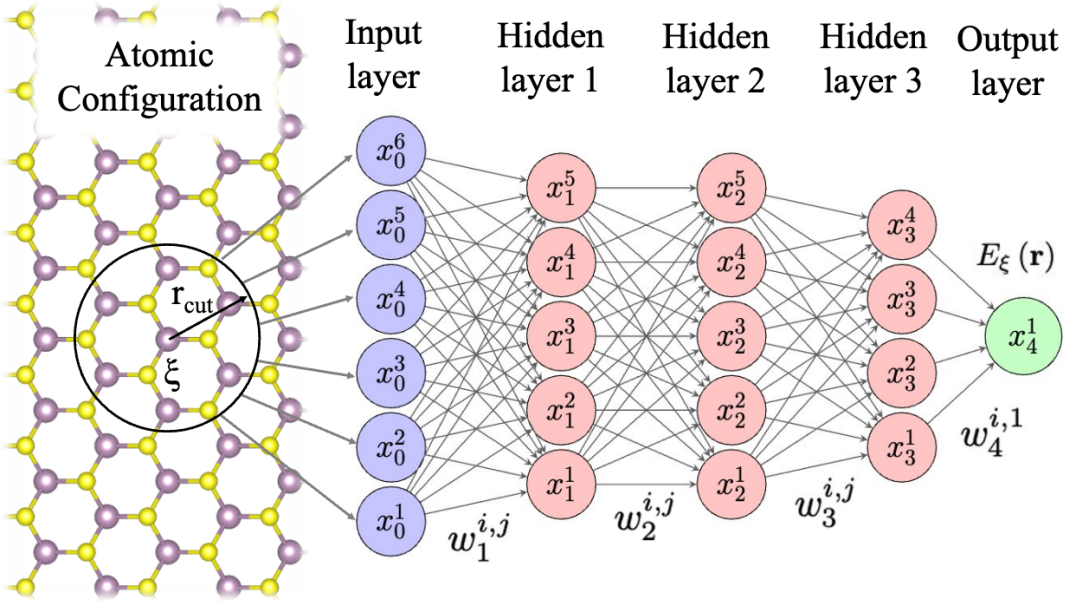

Figure 2.13 – Schematic of an ANN with one input layer, three hidden layers, and one output layer. Neighbor configurations within r_{cut} are mapped to descriptors x_0^i $(i = 1, \ldots, 6)$. Weights are shown as arrows; biases and activations are omitted for clarity.

reference structures. Through regression, models like neural networks are optimized to reproduce DFT results without relying on fixed functional forms. The accuracy of MLFFs depends on the training data and enables simulations with near ab initio precision at significantly lower computational cost. Here, we will be focused on discussing the basic features of an MLFF. For readers interested in a more in-depth exploration of this topic, a comprehensive review is available in Ref. [137].

2.4.1 Artificial Neural Networks

Here, we opted to use an Artificial Neural Network (ANN) as our MLFF as implemented in the Atomistic Energy Network (ænet) code [138, 139], which has tools for generating, training and testing ANNs and is also compatible with LAMMPS [140]. Here we describe its general architecture. The ANN is responsible for mapping input representations of atomic environments to the potential energy and force predictions. The ANN model we adopted used consists of an input layer, multiple hidden (intermediate) layers, and an output layer that predicts the atomic energy $E_\xi(\mathbf{r})$ for each atom ξ in the system based on its local environment. The overall structure is illustrated schematically in Figure 2.13. The input layer receives a vector $\mathbf{x}_0$ representing the so called descriptors of the atomic environment. The forward propagation of information through the ANN proceeds via successive matrix-vector operations and non-linear transformations. For example, considering Figure 2.13, the operation that "connects" the second and third layer is given by:

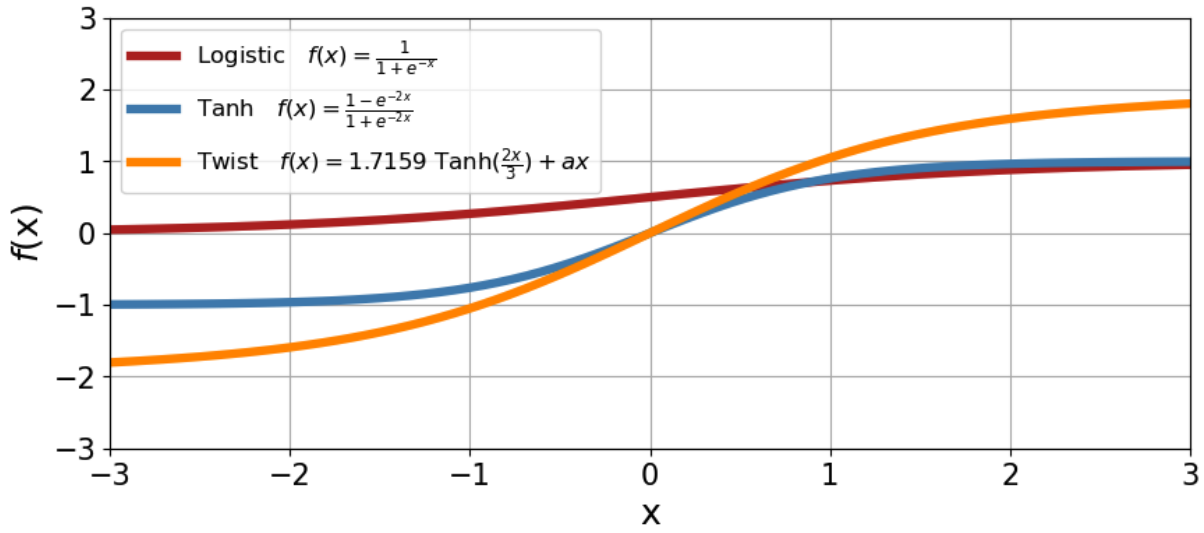

Figure 2.14 – Activation functions implemented in ænet.

$$\begin{pmatrix} w_2^{11} & w_2^{12} & w_2^{13} & w_2^{14} & w_2^{15} \\ w_2^{21} & w_2^{22} & w_2^{23} & w_2^{24} & w_2^{25} \\ w_2^{31} & w_2^{32} & w_2^{33} & w_2^{34} & w_2^{35} \\ w_2^{41} & w_2^{42} & w_2^{43} & w_2^{44} & w_2^{45} \\ w_2^{51} & w_2^{52} & w_2^{53} & w_2^{54} & w_2^{55} \end{pmatrix} \begin{pmatrix} x_1^1 \\ x_1^2 \\ x_1^3 \\ x_1^4 \\ x_1^5 \end{pmatrix} = \begin{pmatrix} y_2^1 \\ y_2^2 \\ y_2^3 \\ y_2^4 \\ y_2^5 \end{pmatrix} \xrightarrow[\text{Activation } f(\mathbf{y}_2)]{} \begin{pmatrix} x_2^1 \\ x_2^2 \\ x_2^3 \\ x_2^4 \\ x_2^5 \end{pmatrix} \tag{2.117}$$

such that a neural network can be understood as a sequence of matrix operations followed by an *activation function*. Those functions introduce non-linearity into the network, enabling it to model complex, non-linear relationships between atomic configurations and their corresponding energies. Figure 2.14 illustrates the three activation functions implemented in the ænet code, and in Eq. 2.117, the function is applied to the vector corresponding to the second layer, with its output used as input for the operation related to the third layer. The operation between two adjacent layers is given by the expression

$$x_{I,j}(\{x_{I-1,k}\}) = f\left(\sum_k w_{k,j}^I x_{I-1,k}\right) \tag{2.118}$$

where $\{x_{I-1,k}\}$ are the input elements coming from the previous layer, and $w_{k,j}^I$ are the elements of the weight matrix $\mathbf{W}_I$ that transfer the signal from layer $(I-1)$ to layer I. The activation function acts on each component of the input vector and, without the function $f(x)$, the neural network would be mapped into a linear algebra problem in which the multiplication of several matrices is reduced to the multiplication of a single matrix with the input vector, thereby reducing the complexity of the model. The only exception where $f(x) = x$ occurs is in the operation performed by $\mathbf{W}_4$ for the output layer of the ANN, ensuring that the potential energy function has an unrestricted domain and can assume any value. According to the universal approximation theorem, any bounded

function in $\mathbb{R}^n$ can be approximated by a neural network with arbitrary precision [141]. This approximation is achieved by minimizing a "cost function" $C(\mathbf{x}_0)$ through a procedure known as "backpropagation", a method that efficiently computes the derivative of $C(\mathbf{x}_0)$ with respect to the weight matrix. This is accomplished by recognizing that each layer only affects the overall performance of the network insofar as it affects the input to the next layer. By recursively calculating the effect of a given weight matrix solely on the next layer, the total derivative of the cost function can be efficiently computed using the chain rule:

$$\frac{\mathrm{d}C}{\mathrm{d}\mathbf{x}_0} = \frac{\mathrm{d}C}{\mathrm{d}\mathbf{x}_L} \cdot \frac{\mathrm{d}f}{\mathrm{d}\mathbf{y}_L} \cdot \frac{\mathrm{d}\mathbf{y}_L}{\mathrm{d}\mathbf{x}_{L-1}} \cdot \frac{\mathrm{d}f}{\mathrm{d}\mathbf{y}_{L-1}} \cdots \frac{\mathrm{d}f}{\mathrm{d}\mathbf{y}_1} \cdot \frac{\mathrm{d}\mathbf{y}_1}{\mathrm{d}\mathbf{x}_0} \tag{2.119}$$

where $\mathbf{x}_L = f(\mathbf{y}_L)$, $\frac{\mathrm{d}C}{\mathrm{d}\mathbf{x}_L}$ is the gradient of the entire neural network, $\frac{\mathrm{d}f}{\mathrm{d}\mathbf{y}_L}$ are the derivatives of the activation function with respect to its input, and $\frac{\mathrm{d}\mathbf{y}_L}{\mathrm{d}\mathbf{x}_{L-1}}$ corresponds to the weight matrix $w_L^{i,j}$. Therefore, generating an ANN for atomistic simulations can be seen as a regression problem, i.e., by treating the neural network as a function, we aim to find the parameters $w_I^{i,j}$ that best fit the values present in the dataset. This is done by selecting the root mean square error (RMSE) as the cost function. Thus, the iterative backpropagation process is responsible for minimizing the RMSE, ensuring that the model accurately reproduces the dataset with arbitrary precision. In addition to neural networks, several other algorithms and architectures are commonly employed in the development of MLFFs. We mention kernel-based methods that utilize mathematical functions to quantify the similarity between atomic environments, enabling the prediction of energies and forces by weighting reference configurations according to their similarity to new inputs. Prominent examples include the Gaussian Approximation Potentials (GAP), which have been successfully applied to model carbon systems [142]. However, these methods can become computationally demanding when applied to large datasets.

2.4.2 Descriptors

The first layer of an ANN is designated to describe the local environment around atom i, and its elements are referred to as *descriptors* which are a set of functions that form a basis in which the PES is represented, and they are essential for characterizing the interaction neighborhood of an atom within a cutoff radius r_{cut}. Since the ANN is intended to model the physics regarding a given material, those descriptors needs to be chosen such that they satisfy specific invariance conditions such as:

- **Translational Invariance:** the descriptor must be unaffected by a uniform translation of the entire system. Shifting all atomic positions should not change the representation.

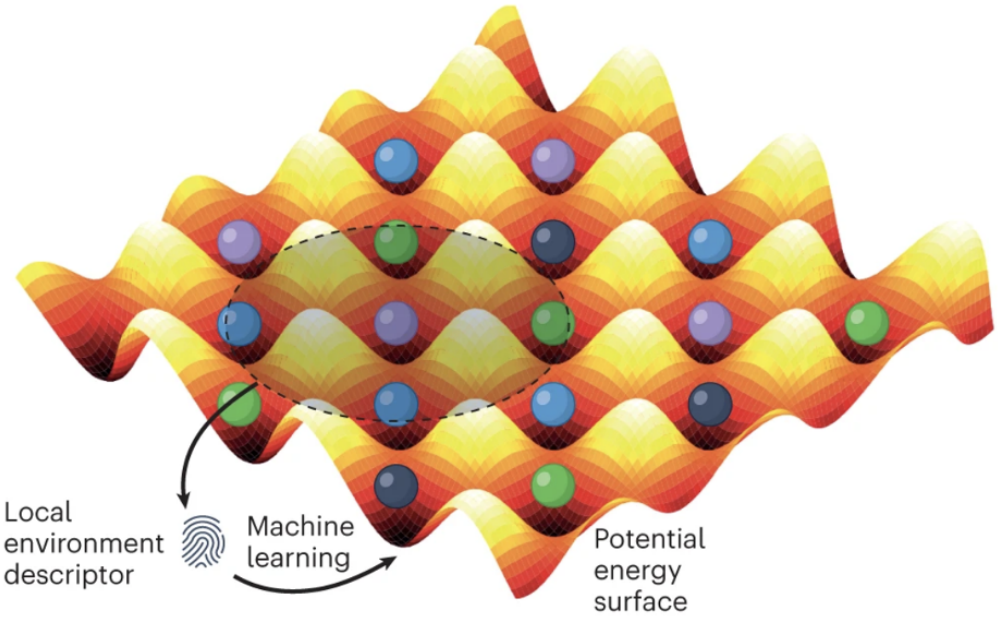

Figure 2.15 – Schematic of how MLFFs describe atomic environments via local descriptors, which are mapped onto the potential energy surface (PES). Adapted from Ref. [143]

- **Rotational Invariance:** the descriptor must yield the same output regardless of the orientation of the system in space. Rotating the atomic configuration should not alter the descriptor values.
- **Permutational Invariance:** the descriptor must be invariant with respect to permutations of identical atoms. Exchanging two atoms of the same specie should not affect the descriptor.

Those conditions grant that the ANN will be able to be a physically plausible model and that quantities such as linear and angular momentum will be conserved during an MD simulation[6]. At present, two primary categories of descriptors are employed in MLFF architectures: local environment descriptors and graph-based descriptors. Local descriptors, such as shown in Figure 2.15, characterize the atomic environment of a given atom through functions that capture features such as atomic densities, bond distances, and angular distributions. A significant milestone in the development of descriptor-based MLFFs was the introduction of *atom-centered symmetry functions* by Behler and Parrinello, which effectively represent two-body and three-body interactions and mark a pivotal advancement in the application of machine learning techniques to materials modeling [144]. On the other hand, graph-based descriptors represent atomic systems as mathematical graphs, where atoms are nodes and interatomic bonds or interactions are edges. These methods

[6] The relation of translational and rotational symmetries and conservation laws can be derived from Noether's theorem. [120]

leverage graph neural networks (GNNs) to learn complex patterns in atomic structures and some state-of-art graph-MLFFs such as MACE [145] had been used to develop what are called as "foundation models" or "universal potentials" for materials simulations since they were trained in datasets that cover the entire periodic table [146], although their validation as truly universal models still requires case-by-case testing and has not yet been fully established. Also, graph-based MLFFs relies on message-passing operations that are more difficult to parallelize than in local MLFFs and therefore are about an order of magnitude more computationally expensive. An efficient implementation for graph MLFFs is still an open challenge until today.

The ænet code relies on a set of local descriptors that represent the *radial distribution function* and the *angular distribution function* (RDF and ADF respectively) in terms of an orthonormal complete basis [147]. The radial and angular distribution functions around atom i can be expressed as:

$$RDF_i(r) = \sum_{R_{ij}<r_{cut}} \delta(r - R_{ij}) f_{cut}(R_{ij}) w_{t_j} \tag{2.120}$$

$$ADF_i(\theta) = \sum_{R_{ij},R_{ik}<r_{cut}} \delta(\theta - \theta_{ijk}) f_{cut}(R_{ij}) f_{cut}(R_{ik}) w_{t_j} w_{t_k} \tag{2.121}$$

where the distances $R_{ij} = \|\mathbf{R}_j - \mathbf{R}_i\|$, the angles $\theta_{ijk} = \angle(\mathbf{R}_j - \mathbf{R}_i, \mathbf{R}_k - \mathbf{R}_i)$, and the weights w_{t_k} serve to differentiate between atomic types. To ensure that both the RDF and ADF vary smoothly as atoms enter or leave the sphere defined by the cutoff radius, a cutoff function f_{cut} is introduced, serving a similar role to the modifications applied in the shifted Lennard-Jones potential (Eq.2.97) and the cutoff function employed in the Stillinger-Weber potential (Eq.2.100):

$$f_{cut}(r) = \begin{cases} \frac{1}{2}\Big[\cos\Big(\frac{\pi r}{r_{cut}}\Big) + 1\Big], & r \leq r_{cut} \\ 0, & r > r_{cut} \end{cases}. \tag{2.122}$$

Both RDF and ADF obey the necessary invariance rules discussed earlier. Given the set of functions $\{\varphi_\alpha\}$ as an orthonormal and complete basis, i.e., $\int \varphi_\alpha^* \varphi_\beta = \delta_{\alpha\beta}$, both distribution functions can be expanded in this basis:

$$RDF_i(r) = \sum_\alpha c_\alpha^{(2)} \varphi_\alpha(r) \quad \text{for} \quad 0 < r < r_{cut} \tag{2.123}$$

$$ADF_i(\theta) = \sum_\alpha c_\alpha^{(3)} \varphi_\alpha(\theta) \quad \text{for} \quad 0 < \theta < \pi \tag{2.124}$$

so that, with this choice, the coefficients are given by:

$$c_\alpha^{(2)} = \sum_{R_{ij}<r_{cut}} \varphi_\alpha(R_{ij}) f_{cut}(R_{ij}) w_{t_j} \tag{2.125}$$

$$c_\alpha^{(3)} = \sum_{R_{ij},R_{ik}<r_{cut}} \varphi_\alpha(\theta_{ijk}) f_{cut}(R_{ij}) f_{cut}(R_{ik}) w_{t_j} w_{t_k}. \tag{2.126}$$

Truncating these expansions at order N_2 and N_3 respectively, the set of coefficients

$$\left\{c_1^{(2)}, \ldots, c_{N_2}^{(2)}, c_1^{(3)}, \ldots, c_{N_3}^{(3)}\right\} \tag{2.127}$$

forms the first layer of the neural network, i.e., the x_0^i layer represented in Figure 2.13. The chosen basis $\{\varphi_\alpha\}$ consists of Chebyshev polynomials of the first kind, whose definition via recurrence relations allows for efficient numerical evaluation of the functions and their derivatives. This method for defining system descriptors offers better scalability with the number of atomic types compared to its predecessors, such as the Behler-Parrinello descriptors.

2.4.3 Training the Potential

What is commonly referred to as "training" of a neural network is, in fact, a regression problem in which the parameters $w_I^{i,j}$ of an ANN (represented by successive operations as in Eq. 2.118) are optimized to minimize the difference between the energy predicted by DFT and the energy estimated by the ANN. Since the reference energies (DFT) are known, this ANN regression is classified as a problem of *supervised learning*. In general, an ANN with ℓ layers can be written as $\mathcal{N}(\mathbf{x}_{0,n}; \{\mathbf{W}_\ell\})$, being a function of an input vector $\mathbf{x}_{0,n}$ (in our case, the descriptors of a structure n from the database) and the set of weights $\{\mathbf{W}_\ell\}$. Suppose the reference set contains N_{samp} structures, so that the vector $\mathbf{y}_n$ is the reference result associated with $\mathbf{x}_{0,n}$ (in our case, the total energy). An error e_n can be defined for each sample n in the reference set as:

$$e_n(\mathbf{x}_{0,n}, \mathbf{y}_n; \{\mathbf{W}_\ell\}) = \mathcal{N}(\mathbf{x}_{0,n}; \{\mathbf{W}_\ell\}) - \mathbf{y}_n. \tag{2.128}$$

Thus, the training of a neural network can be expressed as the following multi-dimensional optimization problem:

$$\left\{\mathbf{W}_\ell^{opt}\right\} = \underset{\{\mathbf{W}_\ell\}}{\operatorname{argmin}}\ \mathcal{E}(\{\mathbf{W}_\ell\}) \quad \text{with} \quad \mathcal{E}(\{\mathbf{W}_\ell\}) = \frac{1}{2}\sum_{n=1}^{N_{samp}} e_n^2 \tag{2.129}$$

where $\mathcal{E}$ is the sum of squared errors and $\left\{\mathbf{W}_\ell^{opt}\right\}$ is the set of optimal weights. The ANN training is performed iteratively using methods based on the gradient of the function $\mathcal{E}$ with respect to the weights:

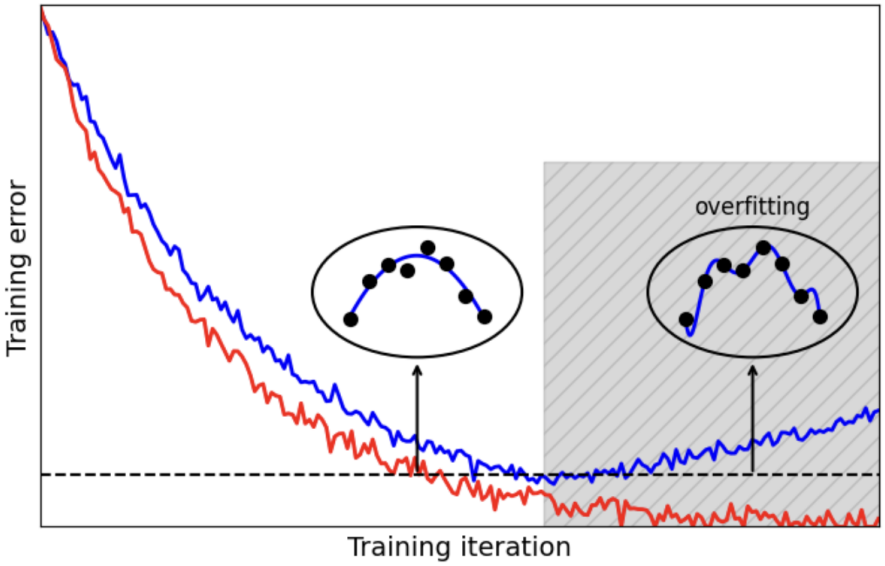

Figure 2.16 – Schematic of ANN training with overfitting: blue curve shows training RMSE, red curve shows test RMSE. Insets depict the fitted potential at each stage.

$$\nabla \mathcal{E} = \mathbf{J}^T \mathbf{e} \quad \text{with} \quad (\mathbf{J})_{\alpha n} = \frac{\partial \mathcal{N}(\mathbf{x}_{0,n})}{\partial w_\alpha} \quad \text{and} \quad (\mathbf{e})_n = e_n \tag{2.130}$$

where $\mathbf{J}$ is the Jacobian matrix of $\mathcal{N}$. Therefore, the weights are updated iteratively. The derivatives of $\mathcal{N}$ are obtained using the chain rule presented in Eq. 2.119, where, by differentiating Eq. 2.118, the contribution of each layer to the derivative of $\mathcal{E}$ is obtained as:

$$\frac{\partial x_{I,j}}{\partial w^I_{m,j}} = f'\left(\sum_k w^I_{k,j} x_{I-1,k}\right) \cdot x_{I-1,m}, \tag{2.131}$$

a process known as "backpropagation" as the derivative is computed from the output layer back towards the input layer. Among the training methods implemented in the ænet code, the one that we adopted was the Broyden-Fletcher-Goldfarb-Shanno (BFGS) method [148]. In this method, at each iteration I, the weights are updated as:

$$\mathbf{w}^{I+1} = \mathbf{w}^I + \Delta \mathbf{w}^{I+1} \quad \text{where} \quad \Delta \mathbf{w}^{I+1} = -\left(\mathbf{H}^I\right)^{-1} \nabla \mathcal{E}^I \tag{2.132}$$

where $\mathbf{H}$ is an estimate of the Hessian matrix based on the second derivative of $\mathcal{E}$ with respect to the weights. Since we used neural networks with a large number of weights in our work, this method proved suitable as it does not require excessive memory, given that storing $\mathbf{H}$ is unnecessary. The training of a neural network can be monitored through the evolution of the RMSE with respect to the reference structures:

$$\text{RMSE} = \sqrt{\frac{1}{N_{samp}} \sum_{\sigma}^{N_{samp}} \left[E^{ANN}(\sigma) - E^{DFT}(\sigma)\right]^2}, \tag{2.133}$$

where a common practice is to divide the reference dataset into a *training set*, used for fitting the ANN, and a *test set*, used to verify the true accuracy of the fit. As it is an optimization process, the training tends to make the model increasingly specialized for the training set, which may result in the neural network being trained to reproduce only the specific data from that set (especially when the number of adjustable weights is very high), which is counterproductive for its application in simulations. One way to assess whether this is occurring is to set aside a portion of the dataset as a *test set*, which is not used to adjust the ANN. The RMSE calculated for the test set is thus a reliable metric for assessing the ANN accuracy. The point at which divergence between the training RMSE and the test RMSE occurs is known as *overfitting* and is shown in Figure 2.16. There are other common ways to split the reference dataset, such as the *train-validation-test* split. In this approach, the training set itself is further divided into a *training subset* and a *validation subset*. By employing a validation set, one can systematically evaluate the effect of different hyperparameter[7] choices, such as the number of layers and nodes, and identify the configuration that yields the best model performance. Unlike the test set, which remains completely unseen until the final evaluation, the validation set is used to guide decisions about model architecture and training parameters. This strategy enhances the robustness of the trained model by ensuring that it generalizes well not only to the training data but also to unseen configurations regardless of the chosen architecture.

2.4.4 Strategies for Data Generation

Here we addresses a fundamental aspect in the development of MLFFs: the generation of a reliable and representative DFT dataset capable of capturing the essential physics of the material under investigation. As will be discussed, multiple strategies can be employed to systematically generate DFT reference data, some of which were adopted by our group for the construction of MLFFs. The main objective is to generate datasets that include atomic configurations that allow the trained model to accurately reproduce the behavior of the target material with a fidelity comparable to first-principles methods. Given the critical role that data quality plays in the performance and transferability of MLFFs, special attention is required to the approaches presented here.

2.4.4.1 AIMD Sampling

Perhaps the most straightforward way to explore configurational space is to assemble the reference dataset by sampling the PES using *ab initio* molecular dynamics (AIMD). In summary, AIMD refers to MD methods where the potential energy $V(\mathbf{r})$ and atomic forces are computed on-the-fly from electronic structure calculations, such as DFT, rather than

[7] Hyperparameters are predefined parameters that govern the structure and training process of a machine learning model. Unlike model weights, they are not learned from the data but are set prior to training.

using empirical potentials, similar to a "mini-DFT" calculation at each timestep [149]. Similarly to DFT calculations, there are several open source codes that are specifically designed to AIMD simulations such as MOTECC-90 [150]. The general approach involves performing an AIMD simulation at a chosen temperature and periodically collecting "snapshots" of the system at specified time intervals. These snapshots, which include atomic positions, forces, and total energies, serve as the reference dataset for training the MLFF. To enhance the exploration of the PES, AIMD simulations are often conducted at temperatures higher than those intended for the subsequent applications of the MLFF. For example, when developing an MLFF for simulations at 300 K, the reference data may be generated from an AIMD simulation performed at 500 K to ensure broader sampling of the configurational space. Sampling at elevated temperatures reduces the risk of the model encountering configurations during production simulations that are not represented in the training dataset. Although conceptually straightforward, this approach typically yields a relatively limited number of reference structures due to the high computational cost associated with AIMD simulations.

2.4.4.2 Normal Mode Sampling

There are several ways to generate DFT data without relying on AIMD simulations. In *normal mode sampling*, the idea is to start from a minimum on the PES and generate distorted structures by randomly displacing atoms along the normal modes of the material. These normal modes will be discussed in greater detail in Sec. 2.5, where we introduce the concept of phonons; for the present discussion, it enough to understand that they represent the characteristic vibrational patterns of the system around its equilibrium configuration. Since they are orthogonal to each other, it is straightforward to combine multiple random displacements along different normal modes such that the resulting structures are sampled from a Boltzmann distribution at a certain temperature. In other words, the normal modes form an orthogonal basis for the vibrational degrees of freedom in the space of atomic displacements. In practice, the method for generating MLFFs using normal mode sampling follows the workflow presented in Figure 2.17. Starting from the relaxed unit cell for, an initial database is generated with random displacements around the equilibrium positions (up to a maximum of 0.2 Å) and for various compressive and tensile strain values applied to the cell lattice parameter. This initial database is then used to generate a preliminary MLFF, which in turn is employed to calculate the phonon dispersion and to perform a preliminary MD simulation to verify the stability of the system. As we proceed to satisfy both criteria, additional structures are incorporated into the initial database to achieve a phonon dispersion as similar as possible to that calculated using DFT. The phonon dispersion of a given MLFF is capable of indicating which points are not well fitted and require additional sampling. Figure 2.18 illustrates the process of improving an MLFF with respect to its phonon dispersion. From left to right, the dispersions were obtained by

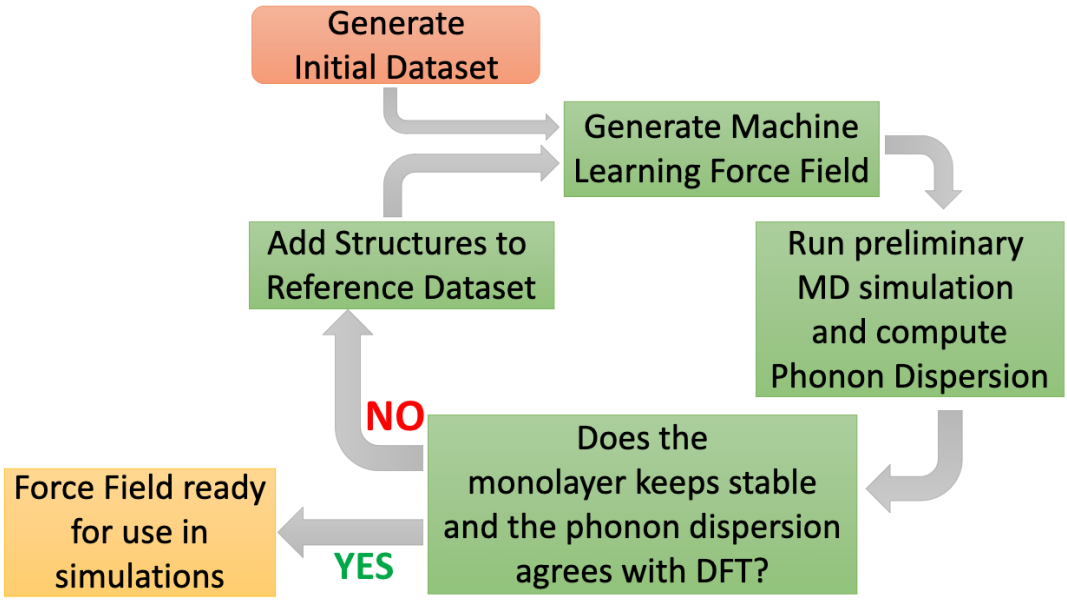

Figure 2.17 – Flowchart for the construction, refinement, and application of MLFFs generated via normal mode sampling.

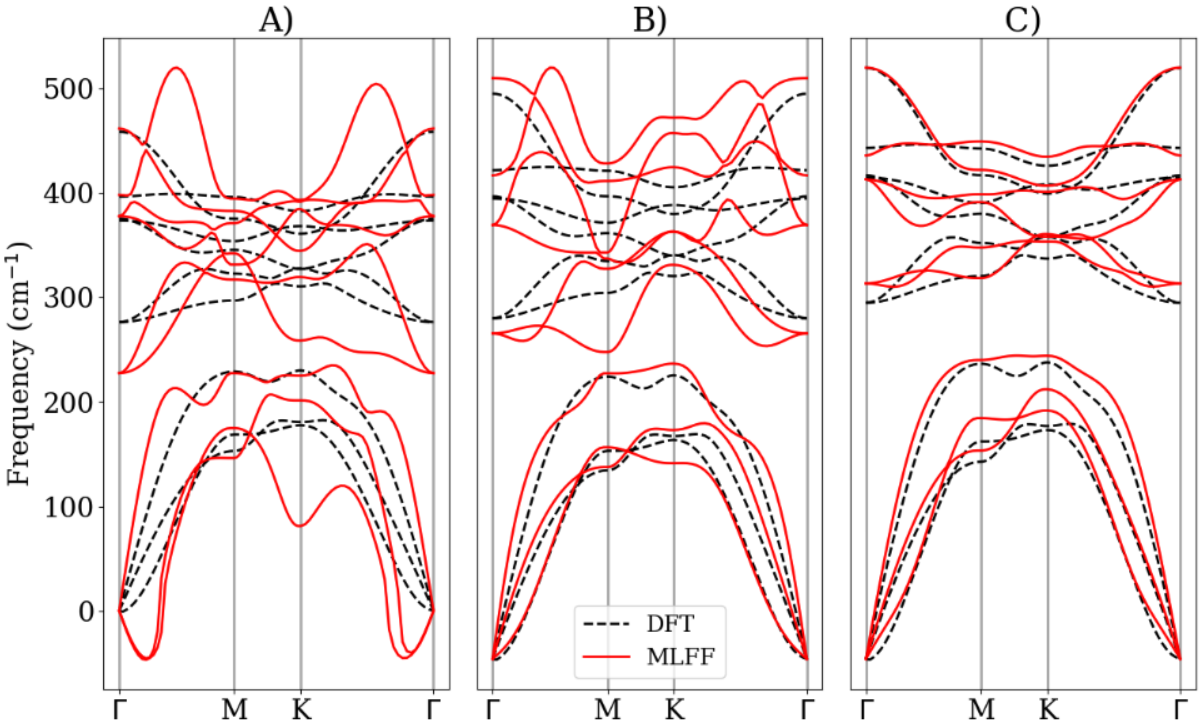

Figure 2.18 – Improvement procedure of MLFF through normal mode sampling in order to develop a reliable potential for MoS_2. The potential with dispersion shown in C was selected for our simulations.

training an MLFF to a dataset containing only random displacements (A), by adding the acoustic modes (B), and by adding both the acoustic and optical modes (C). By "adding a mode", we mean performing a DFT calculation in which the atoms are displaced along the direction of some mode, such that the resulting forces correspond to that mode. It can

be clearly seen in Figure 2.18A that the dispersion predicted by the MLFF significantly deviates from the DFT dispersion, even showing negative phonon frequencies near the Γ point, indicating that a database consisting only of random displacements is not sufficient to reproduce the phonon dispersion of the material and that the model may exhibit dynamical instabilities. Upon adding the acoustic modes, we obtain the MLFF shown in Figure 2.18B, where the issue of negative phonons is resolved, but the optical dispersion still significantly deviates from the DFT prediction. By adding both acoustic and optical modes, we achieve the MLFF shown in Figure 2.18C, where a strong agreement is observed between the phonon dispersions obtained using the MLFF and those from DFT, indicating that the potential is suitable for use in MD simulations. Thus, any MLFF fitted based on this data is expected to reproduce the main motion patterns of the compounds under study with the required accuracy.

2.4.4.3 Adaptive Sampling

Another way to minimize the amount of necessary *ab initio* calculations to generate the databasis is called *adaptive sampling* or *on-the-fly* machine learning. Here, a preliminary MLFF is trained on a small initial dataset, which could also be generated with random displacements and applied strain, and then this initial model is used to run a MD simulation. Probably this initial MLFF cannot reproduce the physics of the material very well because the PES is poorly sampled, i.e., unreliable with comparison with PES obtained through DFT. Therefore, the MD simulation will explore regions of this erratic PES and will give predictions that will be unreliable according to an uncertainty criteria. We can select periodic "snapshots" of this simulation and run DFT calculations on those new structures. Then, those structures are then added to the dataset and a new MLFF is trained using this extended databasis. This process is repeated until no further unreliable regions in the dataset can be discovered during MD simulations. A workflow of the adaptive sampling method is presented in Figure 2.19. When employing this strategy, careful consideration must be given to the frequency at which MD snapshots are incorporated into the dataset. For instance, collecting a snapshot every five timesteps may result in an excessive number of DFT calculations, introducing redundant data points without significantly enhancing the quality of the dataset. On the other hand, MLFFs trained on datasets generated with this strategy can reproduce DFT data as accurately as those trained using normal mode sampling. This is shown in Figure 2.20, the comparison illustrates that high-quality MLFFs can be achieved irrespective of the data generation strategy, as both adaptive sampling and normal mode sampling yielded models capable of accurately reproducing DFT phonon dispersions. This result highlights the robustness of the training procedures and indicates that different sampling approaches can effectively capture the essential features of the PES when sufficiently representative datasets are employed. Ultimately, each sampling strategy discussed here offer viable pathways to constructing reliable MLFFs, exemplifying the

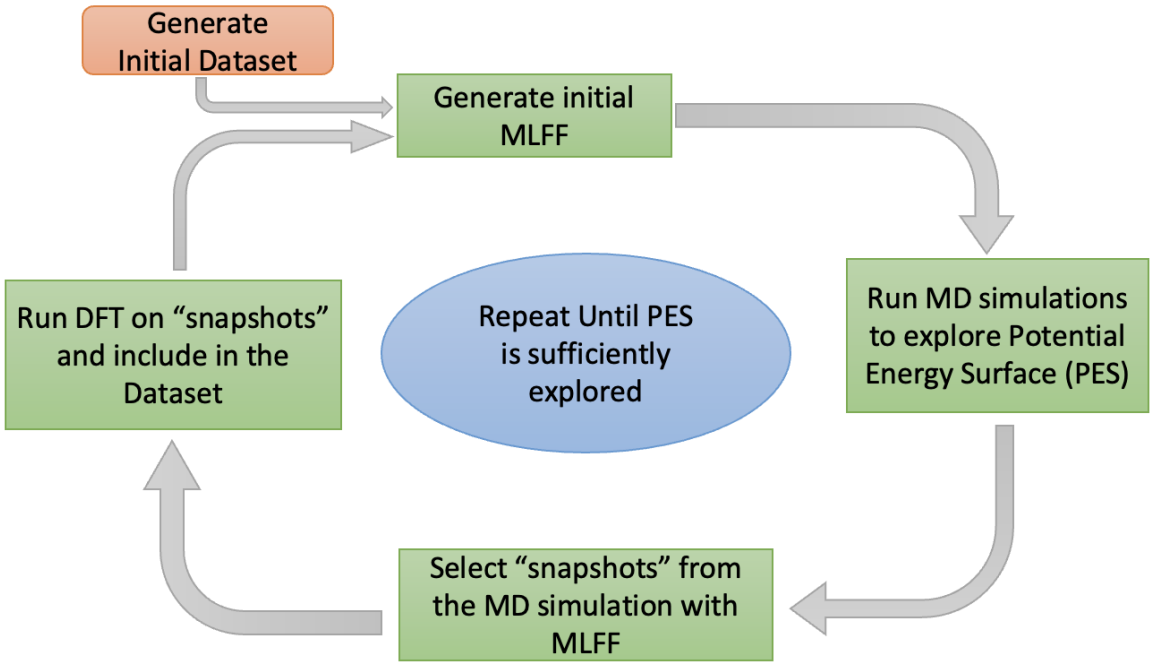

Figure 2.19 – Flowchart for the construction, refinement, and application of MLFFs generated via adaptive sampling.

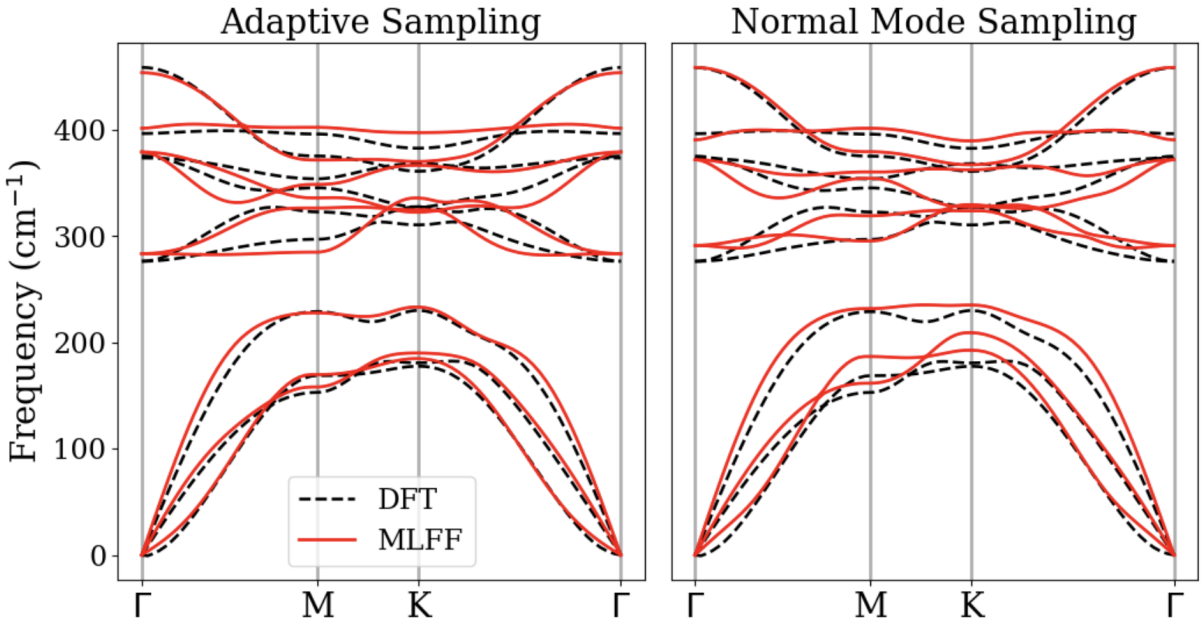

Figure 2.20 – Phonon dispersion comparison for MoS_2: MLFFs trained with adaptive (left) and normal mode sampling (right) vs. DFT (dashed black); MLFF predictions in red.

methodological flexibility available to researchers. Although several other data generation strategies exist, the approaches discussed here were those most relevant to the present work.

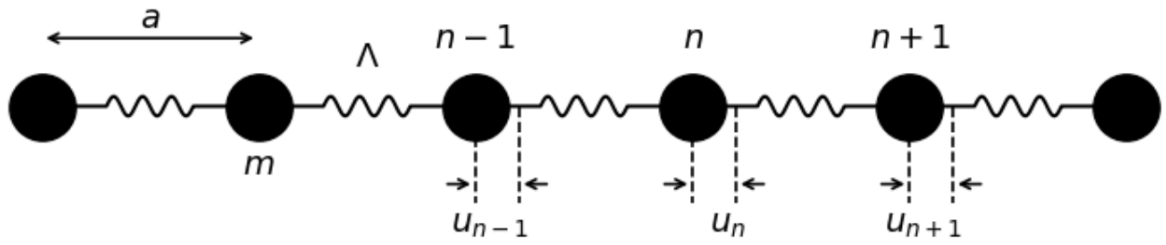

Figure 2.21 – Schematic representation of a monoatomic linear chain with lattice spacing a, spring constant Λ, and mass m. The displacement of the n-th atom from its equilibrium position is denoted by u_n.

2.5 Phonons

The vibrational properties of materials are effectively described in terms of lattice vibrations, or *phonons*, which play a crucial role in determining various physical properties, including thermal conductivity, specific heat, and optical responses. Here, particular emphasis is placed on accurately modeling phonon dispersion relations, as they constitute a critical benchmark for evaluating the reliability of the MLFFs developed herein and is our main research goal. This section therefore offers a brief but comprehensive discussion of phonon theory, ranging from simple examples to practical computational methods for extracting phonon dispersion from simulations. The aim is to establish a solid foundation for the phonon related results presented later in Ch. 4. For readers interested in a more detailed treatment of phonon theory, we recommend Ref. [151].

2.5.1 Phonons in Simple Systems

To build an intuitive understanding of phonons, it is instructive to first consider their behavior in simple systems, such as one-dimensional lattices, where analytical solutions can be derived and fundamental concepts clearly illustrated.

2.5.1.1 Monoatomic Linear Chain

Consider a monatomic linear chain of an infinitely large number N of atoms separated a distance a apart as depicted in Figure 2.21. For all atoms to have an identical environment, it is assumed periodic boundary conditions, i.e., it is a closed chain such that the $(N+1)$th atom is the first one. It is also assumed that only nearest-neighbors forces are significant. Suppose that at a particular time the n-th atom in the chain has a displacement u_n from its equilibrium. Then Newton's second law and Hooke's law gives the following equation of motion:

$$m\ddot{u}_n = \Lambda[(u_{n+1} - u_n) + (u_{n-1} - u_n)]. \tag{2.134}$$

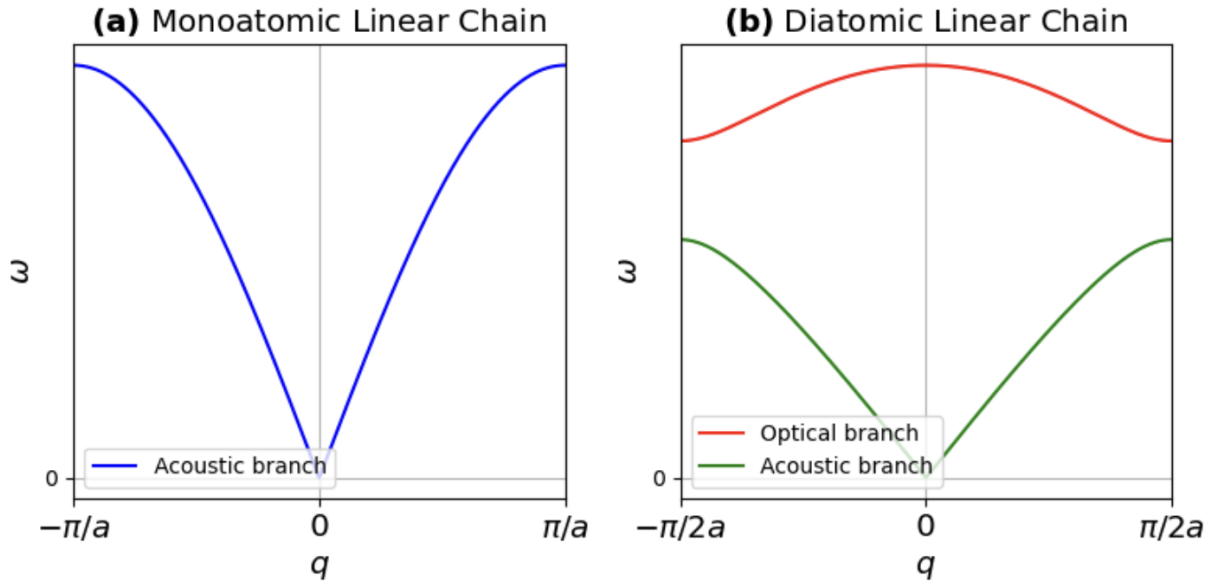

Figure 2.22 – Phonon dispersion for monoatomic (a) and diatomic (b) chains showing single and split branches, respectively, within the first Brillouin zone.

One can try a solution:

$$u_n = A\exp[i(qx - \omega t)] = \exp[i(qna - \omega t)] \tag{2.135}$$

for $x = na$. Here, A is the amplitude of the n-th atom. First, note that the solution is expressed in terms of the wavenumber q, indicating that each q corresponds to a specific vibrational frequency. Second, observe that there is only one vibrational mode per q, regardless of whether the mode is longitudinal, where atoms oscillate along the chain,or transverse, where atoms oscillate perpendicular to the chain. By substituting Eq. 2.135 in Eq. 2.134, we arrive at

$$\omega^2 A = \frac{2\Lambda}{m}(1 - \cos qa)A. \tag{2.136}$$

For a non-trivial solution ($A \neq 0$), Eq 2.136 gives

$$\omega = 2\sqrt{\frac{\Lambda}{m}}\left|\sin\left(\frac{qa}{2}\right)\right| \tag{2.137}$$

The dispersion relation corresponding to Eq.2.137 is shown in Fig.2.22(a). The curve exhibits a linear behavior near $q = 0$, reaching a maximum value ω_{Max}. The plot spans from $-\pi/a$ to π/a, defining the first Brillouin zone. Beyond this range, the dispersion repeats periodically with a period of $2\pi/a$. It is also useful to define two types of phonon velocities. The *phase velocity*, c_p, is the ratio between the frequency ω and the wave vector q, and for this system it is given by:

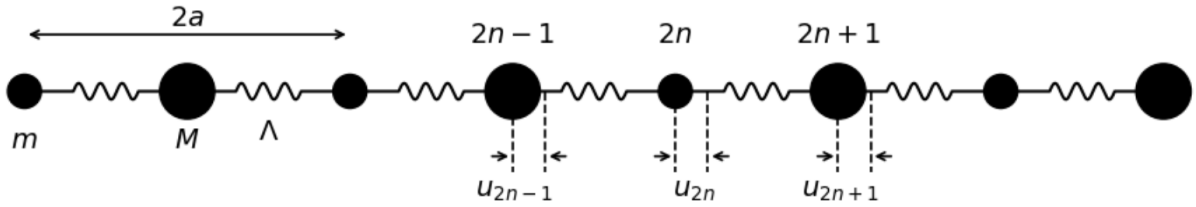

Figure 2.23 – Schematic representation of a diatomic linear chain consisting of masses m and M connected by springs with force constant Λ. The equilibrium spacing between neighboring atoms is a, leading to a basis repeat distance of $2a$. The displacements of the atoms are indexed as $2n-1$, $2n$, and $2n+1$.

$$c_p = v\frac{\sin\left(\frac{qa}{2}\right)}{\frac{qa}{2}}, \tag{2.138}$$

where $v = a\sqrt{\Lambda/m}$ is a characteristic velocity of the system. The *group velocity*, c_g, which represents the velocity at which energy or information propagates through the lattice, is defined by the derivative $c_g = \partial\omega/\partial q$, leading to:

$$c_g = v\cos\left(\frac{qa}{2}\right). \tag{2.139}$$

Two important limiting behaviors arise from these expressions. First, at the Brillouin zone boundary ($q = \pm\pi/a$), the group velocity vanishes ($c_g \to 0$), indicating the formation of standing waves due to Bragg reflection when the wavelength $\lambda = 2a$. This results in a phase difference of π between neighboring atoms, turning the lattice wave into a stationary oscillation.

Second, in the long-wavelength limit ($qa \ll 1$), the phase velocity and group velocity both approach v_s, so $c_p = c_g = v_s$. In this regime, the discrete lattice behaves effectively as a continuum, and the wave corresponds to a sound (or acoustic) wave governed by the classical wave equation:

$$\frac{1}{v_s^2}\frac{\partial^2 u}{\partial t^2} = \frac{\partial^2 u}{\partial x^2}, \quad v_s = \frac{\omega}{q}. \tag{2.140}$$

In this context, the sound velocity of a given vibrational mode can be determined by performing a linear fit to the dispersion relation near the Γ point, i.e., for values of qa very close to zero in Figure 2.22.

2.5.1.2 Diatomic Linear Chain

The monatomic linear chain represents the simplest system that can be studied, yet its dispersion relation provides fundamental insights into the normal modes of a simple (monatomic) crystal. The essential features of lattice dynamics in crystals with a basis of more than one atom can be most effectively understood by examining the dynamics

of a diatomic linear chain, which can be considered as a linear chain with a two-atom basis. Consider an infinitely long chain consisting of $2N$ atoms forming N unit cells, each of length $2a$, as illustrated in Figure 2.23. Assume the system forms a closed chain such that the periodic boundary conditions apply. Let m and M ($m < M$) be the two distinct atomic masses constituting the basis, and consider only nearest-neighbor interactions to be significant. Furthermore, for simplicity, assume that the force constant is identical for interactions involving both types of atoms. In this case, since the basis of length $2a$ consists of two distinct atoms, the system is described by two coupled differential equations, rather than a single equation as in the monatomic chain. These coupled equations account for the dynamics of both atomic species and govern the vibrational behavior of the diatomic chain:

$$m\ddot{u}_{2n} = \Lambda\Big[u'_{2n+1} + u'_{2n-1} + 2u_{2n}\Big] \tag{2.141}$$

$$M\ddot{u}'_{2n+1} = \Lambda\Big[u_{2n+2} + u_{2n} + 2u'_{2n+1}\Big] \tag{2.142}$$

which can assume solutions

$$u_{2n} = A_1 \exp[i(2nqa - \omega t)] \tag{2.143}$$

$$u'_{2n+1} = A_2 \exp\{i[(2n+1)qa - \omega t]\}, \tag{2.144}$$

following a procedure analogous to that used in Eq.2.135. By substituting 2.143 and 2.144 in 2.141 and 2.142 we arrive at the following coupled eigenvalue equations:

$$-\omega^2 m A_1 = \Lambda\Big[A_2 e^{iqa} + A_2 e^{-iqa} - 2A_1\Big] \tag{2.145}$$

$$-\omega^2 M A_2 = \Lambda\Big[A_1 e^{-iqa} + A_1 e^{iqa} - 2A_2\Big]. \tag{2.146}$$

Eqs. 2.145 and 2.146 can be combined into the form:

$$\omega^2 A_i = \sum_{j=1}^{2} D_{ij} A_i, \quad (i = 1, 2) \tag{2.147}$$

in which D is the so called *dynamical matrix* for the diatomic linear chain, given by:

$$D = \begin{bmatrix} \frac{2\Lambda}{m} & -\left(\frac{2\Lambda}{m}\right)\cos qa \\ -\left(\frac{2\Lambda}{m}\right)\cos qa & \frac{2\Lambda}{m} \end{bmatrix}. \tag{2.148}$$

Non-trivial solutions of Eq. 2.147 are given by solving the secular equation:

$$\Big|D_{ij} - \omega^2 \delta_{ij}\Big| = 0 \tag{2.149}$$

where δ_{ij} is the Kronecker delta. The solutions are:

$$\omega^2 = \Lambda\Big(\frac{1}{m} + \frac{1}{M}\Big) \pm \Lambda\sqrt{\Big(\frac{1}{m} + \frac{1}{M}\Big)^2 - \frac{4}{mM}\sin^2 qa}. \tag{2.150}$$

Also, from Eq. 2.145:

$$\frac{A_1}{A_2} = \frac{2\Lambda\cos qa}{2\Lambda - \omega^2 m} = \frac{2\Lambda - M\omega^2}{2\Lambda\cos qa}. \tag{2.151}$$

This results show that, for each wavenumber q that can propagate through the diatomic linear chain, there are two possible oscillation modes which frequencies are given by the two solutions in Eq. 2.150. The two branches of the dispersion corresponding to this system is seen at Figure 2.22(b). Let us consider the two solutions in the small-q region ($qa \ll 1$). For the upper branch in the figure, A_1 and A_2 have opposite signs, indicating that the two atoms within the unit cell move in opposite directions. If these atoms possessed opposite charges, such a vibrational mode could be excited by an electric field of the appropriate frequency. In ionic crystals, this corresponds to the electric field associated with the infrared region of the electromagnetic spectrum. For this reason, the upper branch is referred to as the *optical branch*. On the other hand, for the lower branch, $A_1/A_2 = 1$, signifying that both atoms within the unit cell move in phase with each other. This behavior is characteristic of a sound wave, and hence, the lower branch is called the *acoustic branch*, behaving similar to the monoatomic linear chain and with its sound speed also given by the inclination of the dispersion next to 0 (Eq. 2.140).

The distinction between acoustic and optical phonon modes extends beyond the diatomic linear chain to more complex three-dimensional crystals. In general, acoustic modes are characterized by frequencies that vanish as the wavevector $\mathbf{q} \to 0$, corresponding to collective, in-phase motions of atoms within the unit cell. Conversely, optical modes maintain a finite frequency at $q = 0$ due to out-of-phase relative motions between atoms in the basis. While some optical modes can interact with light through infrared absorption (if they induce a time-varying dipole moment) or scattering, others may be optically inactive. Regardless of their specific light-matter coupling mechanism, such modes are all categorized as "optical" due to their characteristic finite-frequency behavior at the Brillouin zone center.

2.5.1.3 Two-dimensional Monoatomic Lattice

Thus far, we have considered only one-dimensional examples, which effectively illustrate many of the fundamental concepts underlying phonons. However, it is instructive to extend this discussion to a two-dimensional monatomic lattice, as it provides further critical insights into the nature of normal modes and lattice dynamics in higher dimensions. Consider a two-dimensional crystal with a monatomic basis and lattice vectors given by

$\mathbf{R}_{nm} = na\hat{\mathbf{x}} + ma\hat{\mathbf{y}}$. Assuming harmonic interactions with coupling constants γ_1 and γ_2 for first and second neighbors respectively (see Fig.2.24), the equations of motion for the atoms in the lattice will be:

$$M\ddot{\mathbf{u}}(\mathbf{R}_{nm}) = \gamma_1 \sum_{NN} [\mathbf{u}(\mathbf{R}_{ij}) - \mathbf{u}(\mathbf{R}_{nm})] + \gamma_2 \sum_{NNN} [\mathbf{u}(\mathbf{R}_{ij}) - \mathbf{u}(\mathbf{R}_{nm})] \tag{2.152}$$

where in the first sum (NN) the i and j indices are spanning to the first neighbors and in the second sum (NNN) they are spanning to the second neighbors. The solutions to Eq.2.152 of motion can be proposed in the form:

$$\mathbf{u}(\mathbf{R}_{nm}) = \begin{bmatrix} u_x(\mathbf{q}) \\ u_y(\mathbf{q}) \end{bmatrix} \exp[i(\mathbf{q} \cdot \mathbf{R}_{nm} - \omega t)]. \tag{2.153}$$

By substituting 2.153 in 2.152, we arrive at a eigenvalue equation for each wavevector $\mathbf{q}$. The matrix representing this equation of motion is given by:

$$\begin{bmatrix} 4\gamma_1 \sin^2 \frac{q_x a}{2} + 2\gamma_2(1 - w_1) & 2\gamma_2 w_2 \\ 2\gamma_2 w_2 & 4\gamma_1 \sin^2 \frac{q_y a}{2} + 2\gamma_2(1 - w_1) \end{bmatrix} \begin{bmatrix} u_x(\mathbf{q}) \\ u_y(\mathbf{q}) \end{bmatrix} = \omega^2 M \begin{bmatrix} u_x(\mathbf{q}) \\ u_y(\mathbf{q}) \end{bmatrix}, \tag{2.154}$$

where $\mathbf{q}$ can be written as $q_x\hat{\mathbf{x}} + q_y\hat{\mathbf{y}}$ and thus we defined $w_1 = \cos(q_x a)\cos(q_y a)$ and $w_2 = \sin(q_x a)\sin(q_y a)$. Let us consider the long-wavelength limit one more time ($|\mathbf{q}|a << 1$), in which the sine and cosine functions in Eq. 2.154 can be approximated by the first terms of its Taylor series. Thus, near the center of the Brillouin zone (Γ point), this equation simplifies to:

$$\begin{bmatrix} 4\gamma_1 \left(\frac{q_x a}{2}\right)^2 + \gamma_2 a^2(q_x^2 + q_y^2) & 2\gamma_2 a^2 q_x q_y \\ 2\gamma_2 a^2 q_x q_y & 4\gamma_1 \left(\frac{q_y a}{2}\right)^2 + \gamma_2 a^2(q_x^2 + q_y^2) \end{bmatrix} \begin{bmatrix} u_x(\mathbf{q}) \\ u_y(\mathbf{q}) \end{bmatrix} = \omega^2 M \begin{bmatrix} u_x(\mathbf{q}) \\ u_y(\mathbf{q}) \end{bmatrix}. \tag{2.155}$$

In two-dimensional systems, the wavevector $\mathbf{q}$ can approach the Γ point from infinitely many directions, and the direction of approach influences the slope of the phonon branches and, consequently, the sound velocity. We focus on two specific directions: along $(1, 0)$ (toward the X point) and along $(1, 1)$ (toward the M point), as illustrated in Figure 2.25. For the $\Gamma \to X$ path, by setting $q_y = 0$ in Eq.2.155, the eigenvalue problem yields two acoustic branches: the longitudinal acoustic (LA) and transverse acoustic (TA) modes.

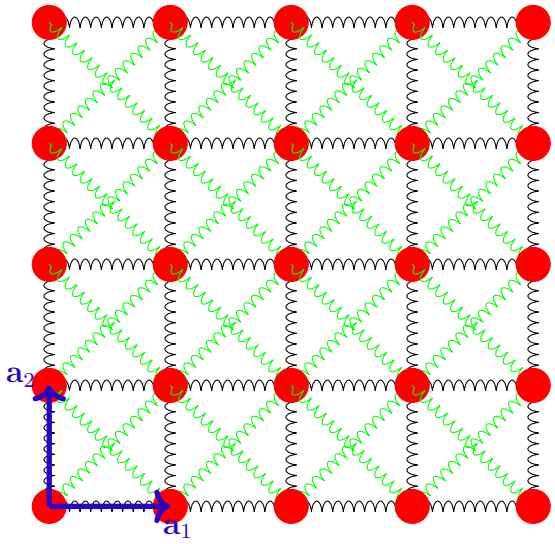

Figure 2.24 – Two-dimensional monatomic square lattice with nearest-neighbor (black) and next-nearest-neighbor (green) spring interactions, γ_1 and γ_2 respectively. Lattice vectors $\mathbf{a}_1 = a\hat{\mathbf{x}}$ and $\mathbf{a}_2 = a\hat{\mathbf{y}}$ are indicated.

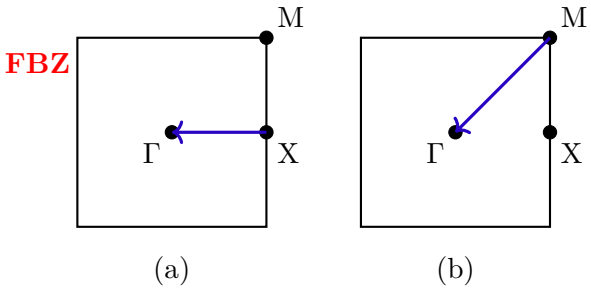

Figure 2.25 – First Brillouin zone (FBZ) of a square lattice highlighting the $\Gamma \to$ X path (a) and the $\Gamma \to$ M path (b).

$$\omega_{LA} = \sqrt{\frac{\gamma_1 + \gamma_2}{M}} q_x a, \qquad \begin{bmatrix} u_x(q_x) \\ u_y(q_x) \end{bmatrix} = A \begin{bmatrix} 1 \\ 0 \end{bmatrix}, \tag{2.156}$$

$$\omega_{TA} = \sqrt{\frac{\gamma_2}{M}} q_x a, \qquad \begin{bmatrix} u_x(q_x) \\ u_y(q_x) \end{bmatrix} = A \begin{bmatrix} 0 \\ 1 \end{bmatrix}. \tag{2.157}$$

Similarly, along the $\Gamma \to M$ direction, setting $q_x = q_y = q$ in Eq. 2.155, the acoustic modes are:

$$\omega_{LA}(q) = \sqrt{\frac{\gamma_1 + 4\gamma_2}{M}} qa, \qquad \begin{bmatrix} u_x(q) \\ u_y(q) \end{bmatrix} = A \begin{bmatrix} 1 \\ 1 \end{bmatrix}, \tag{2.158}$$

$$\omega_{TA}(q) = \sqrt{\frac{\gamma_1}{M}} qa, \qquad \begin{bmatrix} u_x(q) \\ u_y(q) \end{bmatrix} = A \begin{bmatrix} 1 \\ -1 \end{bmatrix}. \tag{2.159}$$

Thus, the eigenvectors resultant for those solutions tells that the longitudinal acoustic (LA) mode corresponds to displacements along the direction of the wavevector, while the

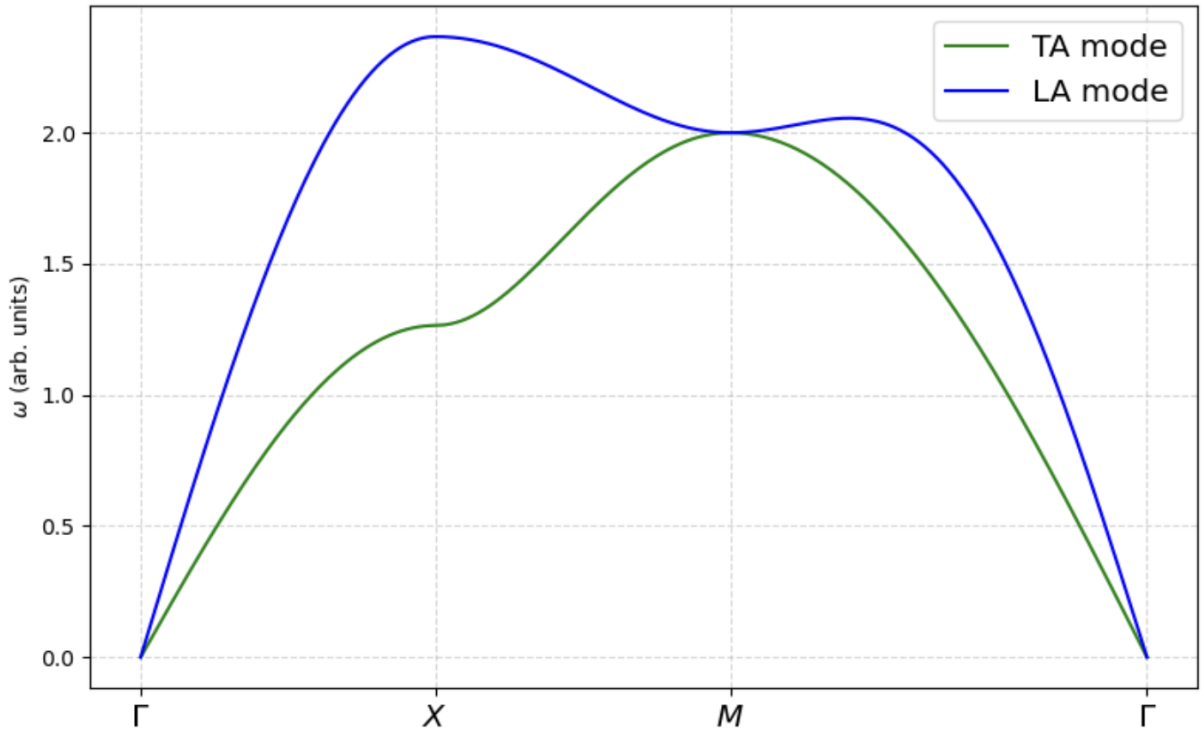

Figure 2.26 – Phonon dispersion of a 2D monatomic square lattice along $\Gamma \to X \to M \to \Gamma$, showing longitudinal (LA) and transverse (TA) acoustic modes.

transverse acoustic (TA) mode corresponds to displacements perpendicular to it. The complete solution of the eigenvalue problem in Eq. 2.154 is presented in Figure 2.26, along a high-symmetry path in the Brillouin zone connecting the Γ, X, and M points. Both the longitudinal acoustic (LA) and transverse acoustic (TA) branches exhibit linear behavior near the Γ point, consistent with the expected acoustic mode dispersion. Notably, the LA and TA modes are degenerate only at the high-symmetry points Γ, as expected, and M, with the LA mode generally exhibiting higher frequencies than the TA mode throughout the path. This example represents one of the simplest cases in which multiple acoustic branches, specifically the TA and LA modes, emerge. While other simple models exist that also illustrate the formation of longitudinal optical (LO) and transverse optical (TO) modes, their inclusion here would unnecessarily extend the discussion without significantly enriching the underlying physical insights.

2.5.2 Methods for Phonon Calculations

So far, we have explored phonon behavior using simplified lattice models that offer valuable physical insight. However, to study real materials with greater accuracy, we need to adopt more general and systematic approaches. Here, we introduce the essential tools and computational techniques that allow us to calculate phonon properties from interatomic interactions, setting the stage for practical phonon analysis in both classical and *ab initio* frameworks.

2.5.2.1 Dynamical Matrix

We now aim to address the general three-dimensional lattice problem for an arbitrary interatomic potential. Consider a crystal with p atoms per unit cell, and let $u_\alpha(lb)$ represent the displacement of the bth atom in the lth unit cell. Assume that the total potential energy $\mathcal{V}$ of the crystal is a function of the instantaneous positions of all atoms. We can expand the potential energy $\mathcal{V}$ in a Taylor series expansion in powers of the atomic displacements $u(lb)$:

$$\begin{aligned}\mathcal{V} &= \mathcal{V}_0 + \sum_{lb\alpha} \left.\frac{\partial \mathcal{V}}{\partial u_\alpha(lb)}\right|_0 u_\alpha(lb) + \frac{1}{2}\sum_{lb,l'b'}\sum_{\alpha\beta}\Phi_{\alpha\beta}(lb;l'b')u_\alpha(lb)u_\beta(l'b') + \dots \\ &= \mathcal{V}_0 + \mathcal{V}_1 + \mathcal{V}_2 + \dots\end{aligned} \tag{2.160}$$

where $\mathcal{V}_0$ is the equilibrium value, and

$$\Phi_{\alpha\beta}(lb;l'b') = \left.\frac{\partial^2 \mathcal{V}}{\partial u_\alpha(lb)\partial u_\beta(l'b')}\right|_0. \tag{2.161}$$

The first term in equation (2.160) is an additive constant and the second term vanishes in equilibrium. Thus, in the harmonic approximation, we have:

$$\mathcal{V}_{\text{harm}} \equiv \mathcal{V}_2 = \frac{1}{2}\sum_{lb,l'b'}\sum_{\alpha\beta}\Phi_{\alpha\beta}(lb;l'b')u_\alpha(lb)u_\beta(l'b'). \tag{2.162}$$

As was done for the simpler systems discussed in Sec. 2.5.1, the equations of motion can be expressed in this generalized form:

$$m_b\ddot{u}_\alpha(lb) = -\sum_{l'b'\beta}\Phi_{\alpha\beta}(lb;l'b')u_\beta(l'b') \tag{2.163}$$

where m_b is the mass of the bth atom, $\alpha,\beta = x,y,z$, and Φ is known as interatomic force constant (IFC) matrix. In fact, $\Phi_{\alpha\beta}(lb;l'b')$ represents the negative of the linear force on atom with indices l and b along the α direction due to a unit displacement of atom $(l'b')$ along the β direction. The IFC matrix Φ obeys two important symmetry relations. From the lattice translational symmetry, we have:

$$\Phi_{\alpha\beta}(lb;l'b') = \Phi_{\alpha\beta}[0b;(l'-l)b'] \tag{2.164}$$

and the infinitesimal translational invariance of the crystal (i.e., when all atoms are equally displaced, there is no net force) leads to:

$$\Phi_{\alpha\beta}(lb;lb) = -\sum_{l'\neq lb'}\Phi_{\alpha\beta}(lb;l'b'). \tag{2.165}$$

Using the lattice translational symmetry, Eq. 2.163 can be expressed as:

$$m_b \ddot{u}_\alpha(lb) = -\sum_{l'b'\beta} \Phi_{\alpha\beta}(0b; l'b') u_\beta(l'b') \tag{2.166}$$

and to solve Eq. 2.166, we try a solution of the form:

$$u_\alpha(lb) = \frac{1}{\sqrt{m_b}} \sum_{\mathbf{q}} U_\alpha(\mathbf{q}; b) \exp[i(\mathbf{q} \cdot \mathbf{x}(l) - \omega t)] \tag{2.167}$$

where $\mathbf{x}(l)$ is the equilibrium position vector of the lth unit cell and $U_\alpha(\mathbf{q}; b)$ is independent of l. By substituting Eq. 2.167 into Eq. 2.166, we obtain:

$$\omega^2 U_\alpha(\mathbf{q}; b) = \sum_{b'\beta} D_{\alpha\beta}(bb'|\mathbf{q}) U_\beta(\mathbf{q}; b') \tag{2.168}$$

such that a non-trivial solution is obtained by solving:

$$\left| D_{\alpha\beta}(bb'|\mathbf{q}) - \omega^2 \delta_{\alpha\beta}\delta_{bb'} \right| = 0 \tag{2.169}$$

The expression for the so called *dynamical matrix* is:

$$D_{\alpha\beta}(bb'|\mathbf{q}) = \frac{1}{\sqrt{m_b m_{b'}}} \sum_{l'} \Phi_{\alpha\beta}(0b; l'b') \exp[i\mathbf{q} \cdot \mathbf{x}(l')]. \tag{2.170}$$

The matrix $D_{\alpha\beta}(bb'|\mathbf{q})$ represents the interatomic force constants (IFCs) in reciprocal space, where the lattice vector $\mathbf{R}_{ll'}$ is transformed into a wavevector $\mathbf{q}$ that defines the direction of wave propagation through the crystal. It is important to note that the dynamical matrix depends explicitly on $\mathbf{q}$. In this generalized eigenvalue problem, determining the vibrational frequencies $\omega(\mathbf{q})$ and corresponding eigenmodes $\mathbf{U}(\mathbf{q}; b)$ requires computing the dynamical matrix, which lies at the core of the lattice vibrational analysis. Therefore, several methods have been developed to compute the dynamical matrix, some of which will be discussed here.

2.5.2.2 Finite Displacement Methods

The finite displacement method, also known as the *frozen phonon* approach, is one of the most commonly used techniques for calculating the dynamical matrix, and hence the vibrational properties of crystals. In this method, the interatomic force constants are computed by systematically displacing atoms from their equilibrium positions and evaluating the resulting forces. Those forces can be obtained through an DFT calculation or simply using an empirical model for your material. To compute the dynamical matrix at arbitrary wavevectors $\mathbf{q}$, it is necessary to construct a supercell that extends beyond a single unit cell. This is because a primitive cell alone only captures vibrational modes where all

atoms oscillate in phase, corresponding to the Γ. By using a supercell and displacing atoms in only one of its constituent unit cells, while keeping equivalent atoms in other cells fixed, one can simulate out-of-phase displacements across the lattice, thereby accessing phonon modes with finite wavelengths. Larger supercells enable the sampling of wavevectors $\mathbf{q}$ closer to Γ, improving accuracy for long-wavelength phonons. The forces resulting from small atomic displacements can be obtained via the Hellmann-Feynman theorem [152] in DFT calculations or directly computed from $F = -\nabla U$, where U represents an empirical potential or MLFF. Within the harmonic approximation, these forces are linearly related to the atomic displacements, and the proportionality coefficients define the IFCs. Once assembled, these IFCs form the dynamical matrix, whose diagonalization yields the phonon frequencies and eigenmodes. For the results presented in Ch. 4, the finite displacement calculations were carried out using the open-source code Alamode [153], which automatically determines the symmetries of the crystal structure and reduces the number of required displacements by considering symmetry-equivalent atomic configurations. This significantly reduces computational cost while maintaining accuracy. Once the forces corresponding to all symmetrically distinct displacements are computed, Alamode reconstructs the real-space force constants, builds the dynamical matrix at any desired wavevector $\mathbf{q}$, and provides access to the full phonon dispersion and vibrational density of states.

2.5.2.3 Density Functional Perturbation Theory

In addition to the finite displacement approach, the dynamical matrix can also be computed using Density Functional Perturbation Theory (DFPT), a technique based on linear response theory [154]. Rather than explicitly displacing atoms and evaluating the forces that arise from such displacements, DFPT evaluates the response of the electronic density $n(\mathbf{r})$ to small perturbations in atomic positions. Within this formalism, the perturbing potential is treated as a first-order correction to the Kohn-Sham Hamiltonian, and the induced change in the electronic density is obtained self-consistently by solving the Sternheimer equation. This procedure allows one to calculate interatomic force constants (IFCs) directly in reciprocal space without resorting to large supercell constructions. An important advantage of DFPT is that phonon frequencies and eigenmodes can be computed at arbitrary wavevectors $\mathbf{q}$ in the Brillouin zone with essentially the same computational cost as at the zone center. This makes the method particularly well suited for the calculation of complete phonon dispersions and vibrational densities of states. In contrast, the finite displacement method requires supercell calculations whose cost increases rapidly with the size of the system and the number of displacements considered. Furthermore, DFPT avoids numerical issues associated with finite difference approximations of forces. Owing to these advantages, DFPT has become a well established approach for lattice-dynamical calculations in plane-wave DFT codes, and it is the method implemented in the Quantum Espresso package, which is widely used in the community.

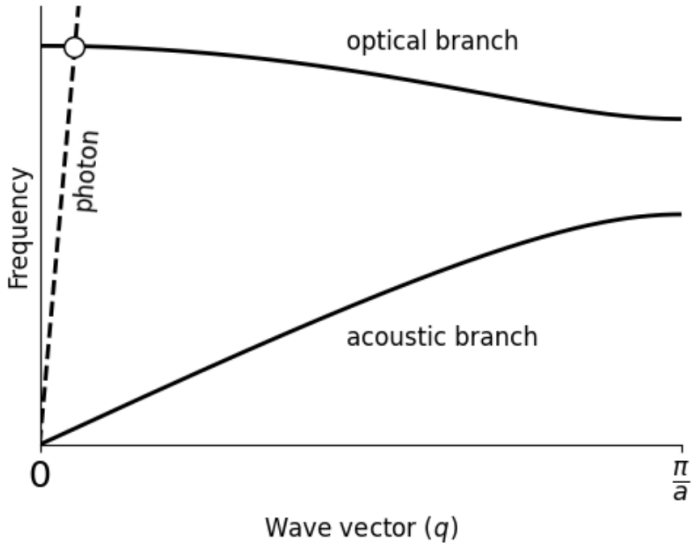

Figure 2.27 – Dispersion relations for the acoustic and optical phonon branches in a typical crystal with lattice constant a. The dotted line represents the dispersion of the photon modes within the crystal.

2.5.3 Phonon Interaction with Light

An important aspect of phonons is their ability to interact with electromagnetic radiation by exchanging energy with photons. In particular, certain lattice vibrations exhibit resonant frequencies within the infrared region of the dielectric spectra. In this section, we focus only on the concepts that are directly relevant for interpreting the results presented in Ch 4. For a more comprehensive reading, the reader is referred to Chapter 10 of Ref. [155].

In general, phonon resonances occur in the infrared region of the electromagnetic spectrum. The modes that couple directly with light are referred to as *infrared active (IR active)* phonons. These modes can absorb photons of specific frequencies, and their interaction with light is governed by selection rules, which depend on the symmetry and polarization of the phonon modes. As anticipated at the end of Sec.2.5.1.2 in which we have discussed the diatomic linear chain, it is to be expected that only the optical modes, rather than the acoustic ones, can exhibit IR activity. Some initial considerations can be made about this activity: suppose that a photon of frequency ω is adsorbed by a phonon of wavevector $\mathbf{q}$. In order for a phonon to interact with a photon, *the conservation of energy and momentum must be satisfied simultaneously*, i.e., the phonon and photon must share the same frequency and wavevector. In a crystal, the dispersion relation for light is approximately linear with a steep slope as shown with the dashed line in Figure 2.27 and its frequency is given by $\omega = c|\mathbf{q}|/n$, where c is the speed of light and n the refractive index. In contrast, the acoustic phonon branches also exhibit linear dispersion at small $\mathbf{q}$, but with a much lower slope corresponding to the sound velocity v_s, such that $c/n \gg v_s$. Therefore, the acoustic phonon and photon dispersion curves can only intersect when $\omega = 0$ at $\mathbf{q} = 0$, i.e., which corresponds to a static non-oscillating field and, therefore, no real photon

absorption can happen through a acoustic mode. Optical phonon modes, however, are typically dispersionless (i.e., with almost zero slope) near the Brillouin zone center as depicted in Figure 2.27. This allows for an intersection with the photon dispersion at a finite frequency $\omega \neq 0$ but still at $\mathbf{q} = 0$. As a result, only optical phonon modes at the Γ point can satisfy the selection rules for IR absorption. One of the key signatures of IR active modes is their influence on the frequency-dependent dielectric response of a material. This interaction can be modeled using the classical oscillator approach, where the motion of charged ions under an external oscillating electric field $\mathbf{E}$ is treated analogously to that of a driven harmonic oscillator:

$$\ddot{x} + \gamma\dot{x} + \Omega^2 x = \frac{q}{\mu}\mathcal{E}(t) \tag{2.171}$$

in which, x is the separation between the two ions, μ is the reduced mass of the two ions in the unit cell, q is the atomic charge, Ω is the phonon frequency, γ is a phenomenological damping constant and $\mathcal{E}(t) = E\exp(i\omega t)$ is the driving field. When the frequency of the incident light matches that of a lattice vibration capable of generating a time-varying dipole moment, the vibration becomes resonant with the electric field and strong coupling occurs, leading to absorption. This coupling modifies the complex dielectric function $\varepsilon_r(\omega) = \varepsilon_1(\omega) + i\varepsilon_2(\omega)$, introducing a characteristic resonance feature at the phonon frequency. The result is that IR-active modes contribute directly to the infrared absorption spectrum and are manifested as peaks in the imaginary part of $\varepsilon_r(\omega)$. Moreover, it is possible to determine whether a given vibrational mode contributes to the dielectric spectra by analyzing the symmetry properties of its eigenvector, obtained from the solution of the problem in Eq.2.168 at the $\mathbf{q} = 0$ point. Chapter 2 of Ref. [156] (particularly Eqs. 112 and 114) introduces the concept of *infrared (IR) intensity* associated with a vibrational mode j, defined as:

$$f(\omega_j) = \sum_{\beta=x,y,z} \left| \sum_{\kappa=1}^{N_{at}} \frac{e_\kappa}{\sqrt{M_\kappa}} U_j(\kappa,\beta) \right|^2, \tag{2.172}$$

where e_κ and M_κ are the charge and mass of atom κ, respectively, and $U_j(\kappa,\beta)$ is the component of the eigenvector corresponding to atom κ and Cartesian direction β. A vibrational mode contributes to the imaginary part of the dielectric function, $\varepsilon_2(\omega)$, only if its IR intensity $f(\omega_j)$ is nonzero, thereby establishing a selection rule for IR activity [157, 158]. In summary, the interaction between phonons and light can be understood through the symmetry properties of vibrational modes, with only certain modes, typically those with nonzero IR intensity at $\mathbf{q} = 0$, contributing to the dielectric response of the material.

3 Thermoelectric Properties of $M_2AgAlBr_6$ Double Perovskites

3.1 Introduction

The role of aluminum in double perovskites has attracted increasing attention in recent years due to its abundance, low toxicity, and potential to tune optoelectronic properties. For instance, Al^{3+} doping in $Cs_2AgBiCl_6$ has been shown to transform the material from an indirect to a direct band-gap semiconductor, thereby enhancing its photoluminescence efficiency. Similarly, the incorporation of $AlCl_3$ in thin-film synthesis improves luminescence and photoresponse . Beyond doping, theoretical efforts have focused on aluminum-based double perovskites of the form M_2AgAlX_6 (M = Cs, Rb, K; X = Cl, Br, I), which have been reported to exhibit thermodynamic stability for most halides and direct band gaps suitable for optoelectronic applications.

Within this family, compounds such as $K_2AgAlBr_6$ and $Rb_2AgAlBr_6$ are particularly appealing due to the abundance of K and Rb in the Earth's crust, which offers a potential cost advantage for large-scale applications. While preliminary studies have reported their structural and electronic properties, including effective carrier masses, a comprehensive investigation of their transport and thermoelectric behavior remains lacking.

In this chapter, we present a detailed study of the structural, electronic, and transport properties of aluminum-based double halide perovskites $M_2AgAlBr_6$ (M = K, Rb, Cs) , employing density functional theory and semiclassical Boltzmann transport theory within the constant relaxation time approximation. Our results reveal that the electronic contribution to the thermoelectric figure of merit approaches unity at room temperature, highlighting these compounds as promising candidates for future thermoelectric applications.

3.2 Results and Discussions

3.2.1 Computational Parameters

All first-principles calculations in this work were carried out using the Quantum Espresso package, a widely adopted open-source suite for electronic structure calculations based on plane-wave density functional theory (DFT). The exchange-correlation energy was treated using the generalized gradient approximation (GGA) in the Perdew-Burke-Ernzerhof (PBE) formulation for all calculations, unless otherwise specified. Norm-conserving (NC) pseudopotentials generated via the `FHI98PP` method [159] were used to model the in-

Table 3.1 – Comparison between obtained lattice constants and bulk moduli for double perovskite $M_2AgAlBr_6$ (M = K, Rb, Cs) and previous theoretical results.

	Lattice constants (Å)		Bulk moduli (GPa)	
	This Work[a]	Tang *et al.*[b]	This Work[a]	Tang *et al.*[b]
$K_2AgAlBr_6$	10.719	10.52	29.0	29.52
$Rb_2AgAlBr_6$	10.714	10.57	29.1	29.53
$Cs_2AgAlBr_6$	10.800	10.65	29.4	28.77

[a] PW-PP (NC) within PBE-GGA (QE code). [b] PW-PP (US) within PBE-GGA (CASTEP code). [45]

teraction between valence electrons and ionic cores. The valence electron configurations adopted were: K $4s^1$, Rb $5s^1$, Cs $6s^1$, Al $3s^2 3p^1$, Ag $5s^2 4d^9$, and Br $4s^2 4p^5$. A kinetic energy cutoff of 50 Ry was used for the plane-wave basis set, and 200 Ry for the charge density. Self-consistent calculations were converged to a threshold of 1.0×10^{-12} Ry for the total energy. Structural relaxations were performed using a $6 \times 6 \times 6$ Monkhorst-Pack k-point grid, and convergence was assumed when all atomic forces were below 1.0×10^{-4} Ry/Bohr. The same PBE-GGA functional was employed for these relaxation steps. Subsequent electronic structure calculations were conducted using the HSE06 hybrid functional, which incorporates a screened Hartree-Fock exchange to correct for the self-interaction errors inherent in conventional DFT and thereby provides more accurate predictions for electronic band gaps. Finally, the thermoelectric and transport properties were computed using the BoltzTraP code, based on electronic structure data obtained from PBE-GGA calculations with a denser $18 \times 18 \times 18$ k-point mesh.

3.2.2 Structural Properties

The $M_2AgAlBr_6$ (M = K, Rb, Cs) double perovskite crystal structure presents a $Fm\bar{3}m$ symmetry [160]. The conventional unit cell can be seen in Figure 1.3, where $AlBr_6$ and $AgBr_6$ octahedras are presented. M^+ is sited in the center of the octahedra. Equilibrium lattice constants and bulk moduli were determined by adjusting our theoretical results with the Murnaghan equation of state [161]. Our obtained lattice constants are presented in Table 3.1. As it can be seen, our lattice values are slightly larger than the ones reported in the work by Tang *et. al.* However, bulk modulus values obtained in ours and Tang *et. al.*´s works are quite similar for each one of the three compounds. The optimized bond lengths, that were indicated at Figure 1.3, are presented in Table 3.2.

3.2.3 Electronic Properties

Calculated band structures of $M_2AgAlBr_6$ (M = K, Rb, Cs) compounds are shown in Figure 3.1. Table 3.3 presents the energy band gap values here obtained as well as the values

Table 3.2 – Obtained bond lengths (Å) for double perovskite $M_2AgAlBr_6$ (M = K, Rb, Cs) as shown in Figure 1.3.

	Al-Br	Ag-Br	M-Br
$K_2AgAlBr_6$	2.524	2.835	3.793
$Rb_2AgAlBr_6$	2.524	2.833	3.791
$Cs_2AgAlBr_6$	2.536	2.864	3.822

obtained by Tang *et. al.* The PBE-GGA was employed in both structure optimization. Band structure calculations were preformed using both PBE-GGA and HSE06 approaches.

A comparison between band structures calculated with both approaches is presented in Figure 3.1. As it can be expected, PBE-GGA energy gaps present an underestimation of the real band gap of the material while HSE06 should give a more accurate value. This usually happens due to the self-interaction effects characteristic of DFT calculations. It can be seen that both valence band maximum (VBM) and conduction band minimum (CBM) are located at the Γ point in the Brillouin zone for all three compounds. As expected, the $M_2AgAlBr_6$ (M = K, Rb, Cs) compounds are semiconductors with a direct band gap. Our calculations with HSE06 are in good agreement with the results present in the work by Tang *et. al.* Figure 3.2 shows the projected density of states of $M_2AgAlBr_6$ (M = K,

Table 3.3 – Bandgap energy (eV) for $M_2AgAlBr_6$ (M = K, Rb, Cs).

	This Work		Tang *et al.*
	PBE-GGA	HSE06	HSE06
$K_2AgAlBr_6$	1.221	2.264	2.245
$Rb_2AgAlBr_6$	1.233	2.259	2.261
$Cs_2AgAlBr_6$	1.231	2.264	2.289

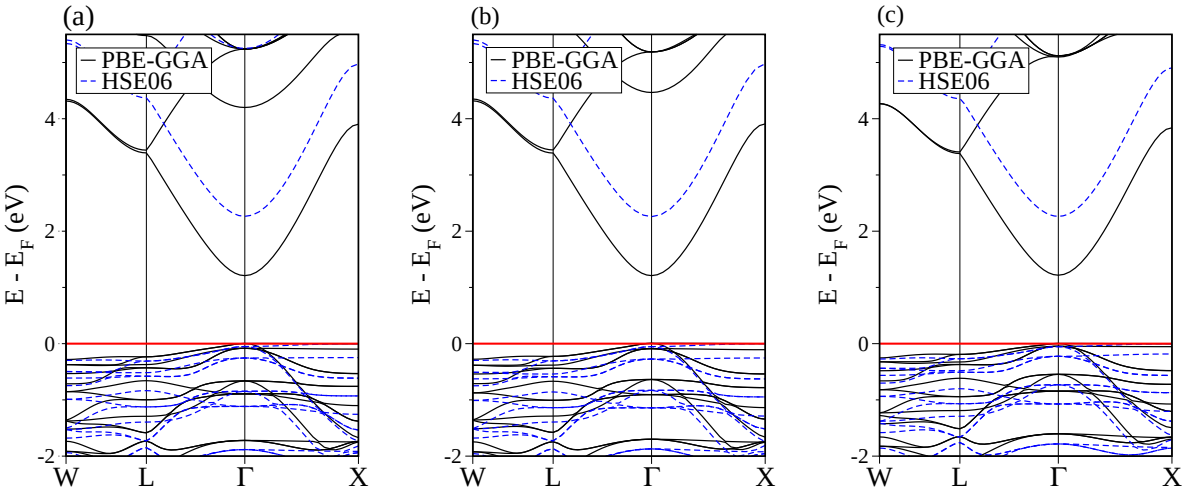

Figure 3.1 – Band structure for $K_2AgAlBr_6$ (a), $Rb_2AgAlBr_6$ (b) e $Cs_2AgAlBr_6$ (c) according to PBE-GGA and HSE06 functionals. Red line indicates Fermi energy.

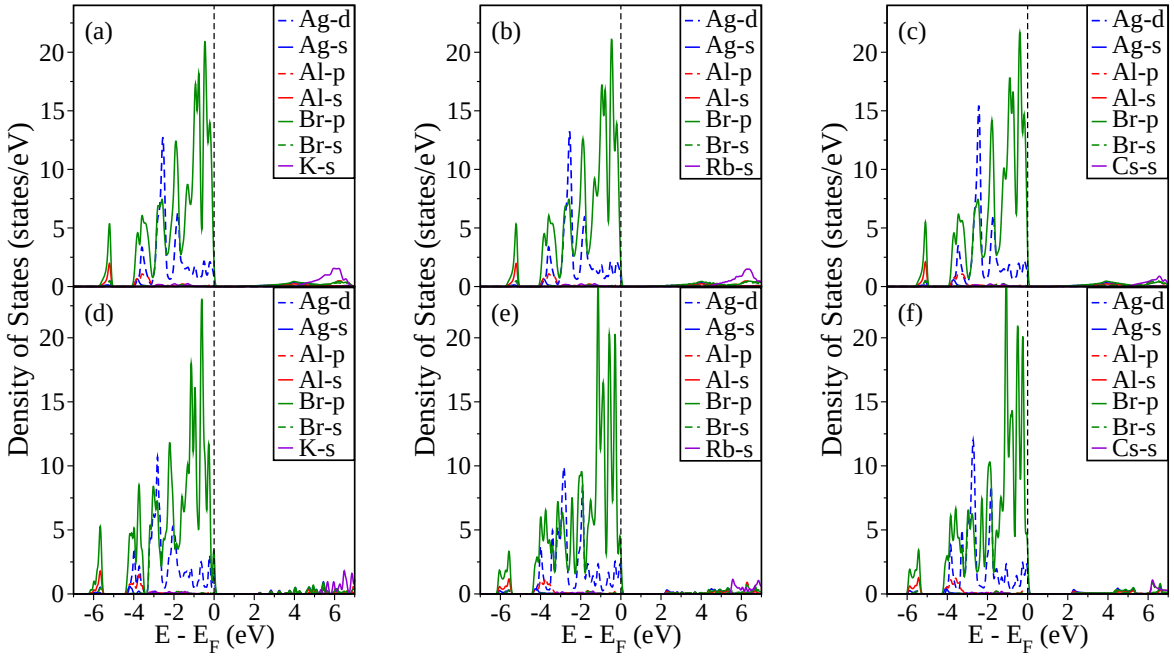

Figure 3.2 – Partial density of states for $K_2AgAlBr_6$ (a, d), $Rb_2AgAlBr_6$ (b, e) e $Cs_2AgAlBr_6$ (c, f) with PBE-GGA (a-c) e HSE06 (d-f). Vertical line indicates Fermi energy.

Rb, Cs) for both PBE-GGA and HSE06 calculations and from it can see that the main driver of the band gap and therefore of the semiconductor properties of the material is the halogen anion Br^-, i.e., the highest occupied state corresponds to the orbital p of Br while the lowest unoccupied state corresponds to an anti-bonding manner predominated by the s and p orbitals of Al with the p orbital from Br [162]. Changes in the alkali metal are not expected to change the band gap of the material.

3.2.4 Thermoelectric Properties

The thermoelectric properties calculated in this study were the Seebeck coefficient, the thermal and electrical conductivities, the thermal power factor and the figure of merit. For the compounds studied here, those properties were calculated and plotted as functions of the chemical potential ($\mu - E_F$) in a -2 to 2 eV energy range and at distinct temperatures, namely 300K, 600K, 900K, and 1200K. Figures 3.3 and 3.4 present our theoretical results. Figure 3.3d-f) presents the theoretical Seebeck coefficient S as a function of chemical potential μ. The observed positive and larger values for S reveal that all $M_2AgAlBr_6$ are p-type materials. High values for S can be seen in the center of the gap, away from the edges. It can be seen that Seebeck coefficient peaks are located in a range of -0.8 eV and 0.8 eV of chemical potential values in all cases. The Seebeck coefficient vanishes outside this range, consequently indicating good thermoelectric properties for $M_2AgAlBr_6$. The investigated double perovskites have a larger Seebeck coefficient at room temperature compared to the values for 600, 900, and 1200K. For p-type doping $K_2AgAlBr_6$ shows a

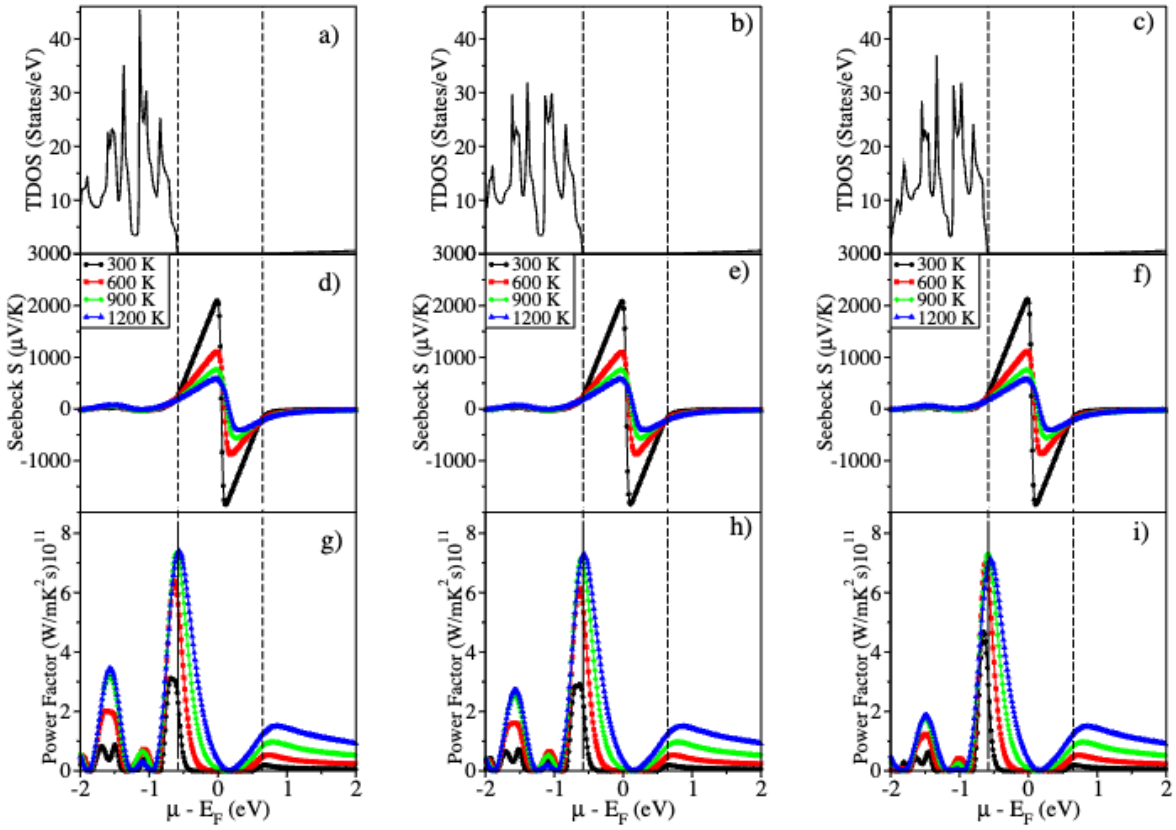

Figure 3.3 – Total density of states (a-c); Seebeck coefficients (d-f) and power factors (g-i) for $K_2AgAlBr_6$ (a, d, g), $Rb_2AgAlBr_6$ (b, e, h) e $Cs_2AgAlBr_6$ (c, f, i), respectively. Fermi level of 0.0 eV means half the gap.

peak value of 2095 μV K^{-1} while $Rb_2AgAlBr_6$ shows 2085 μV K^{-1} for the peak value and $Cs_2AgAlBr_6$ shows 2125 μV K^{-1}. For n-type doping the lowest values of S is obtained at -1843 μV K^{-1} for $K_2AgAlBr_6$, -1838 μV K^{-1} for $Rb_2AgAlBr_6$ and -1844 μV K^{-1} for $Cs_2AgAlBr_6$ which means that all of $M_2AgAlBr_6$ studied here are p-type materials. It is worth noticing that the inflection point of the Seebeck coefficient located at the level 0.0 eV at room temperature walks towards more positive values with the rise of the temperature in all the compounds studied.

In Figure 3.3g-i) we present the power factor for M = K, Rb, and Cs respectively at several temperatures as a function of the chemical potential with respect with the relaxation time (τ). The power factors of $K_2AgAlBr_6$ and $Rb_2AgAlBr_6$ increase with increasing temperature while, for $Cs_2AgAlBr_6$ the peak of the power factor at 1200K is smaller than the one at 900K. Figure 3.4a-c) display the variation of the electrical conductivity divided by the relaxation time (σ/τ). At room temperature, electrical conductivity is zero between -0.51 eV and 0.60 eV for $K_2AgAlBr_6$, -0.45 eV and 0.57 eV for $Rb_2AgAlBr_6$, and -0.47 eV and 0.58 eV for $Cs_2AgAlBr_6$. Beyond this region, the material exhibit good transport properties. We note that, for $\mu - E_F < 0$ eV, the behavior of the electrical conductivity

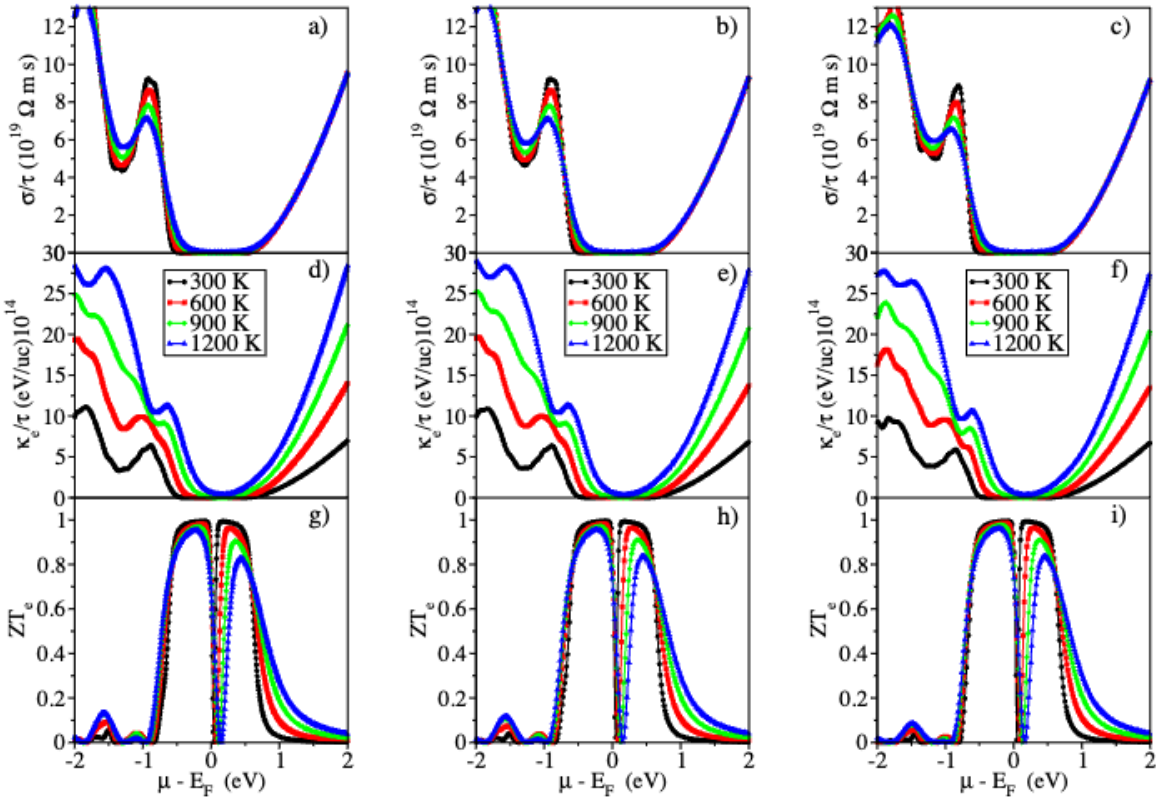

Figure 3.4 – Electrical conductivity (a-c), thermal conductivity (d-f) and figure of merit ZT_e (g-i) for $K_2AgAlBr_6$ (a, d, g), $Rb_2AgAlBr_6$ (b, e, h) and $Cs_2AgAlBr_6$ (c, f, i), respectively. Fermi level of 0.0 eV means half the gap.

changes considerably with the temperature while for $\mu - E_F > 0$ those changes are not significant. In solid material, the thermal conductivity is mainly caused by electrons and lattice vibrations. A small value of thermal conductivity means better performance of the thermoelectronic device.

Before showing our results for the results for the figure of merit ZT, it is worth reminding that, as it was discussed in Sec. 2.2.3, the thermal conductivity ($\kappa = \kappa_e + \kappa_L$) contains two contributions: one from electronic carriers κ_e and the other from phonon vibrations κ_L [163]. However, it is a well-known fact that halide perovskites present ultralow lattice thermal conductivity due to their soft lattice dynamics and strong anharmonic effects [164–166]. Consequently, the lattice contribution to the thermal conductivity will be very small when compared to its electronic counterpart. In this work, only the electronic part of thermal contribution (κ_e) was considered in the calculation of the figure of merit of $K_2AgAlBr_6$, $Rb_2AgAlBr_6$, and $Cs_2AgAlBr_6$. The electronic thermal conductivity (κ_e/τ) for $K_2AgAlBr_6$, $Rb_2AgAlBr_6$ and $Cs_2AgAlBr_6$ as functions of the chemical potential are shown at Figures 3.4d), 3.4e) and 3.4f), respectively. At room temperature, we observe the lowest thermal conductivity for $M_2AgAlBr_6$ (M = K, Rb, Cs) leading automatically to the maximum figure of merit for all three compounds. A figure of merit greater than or equal to 1.0

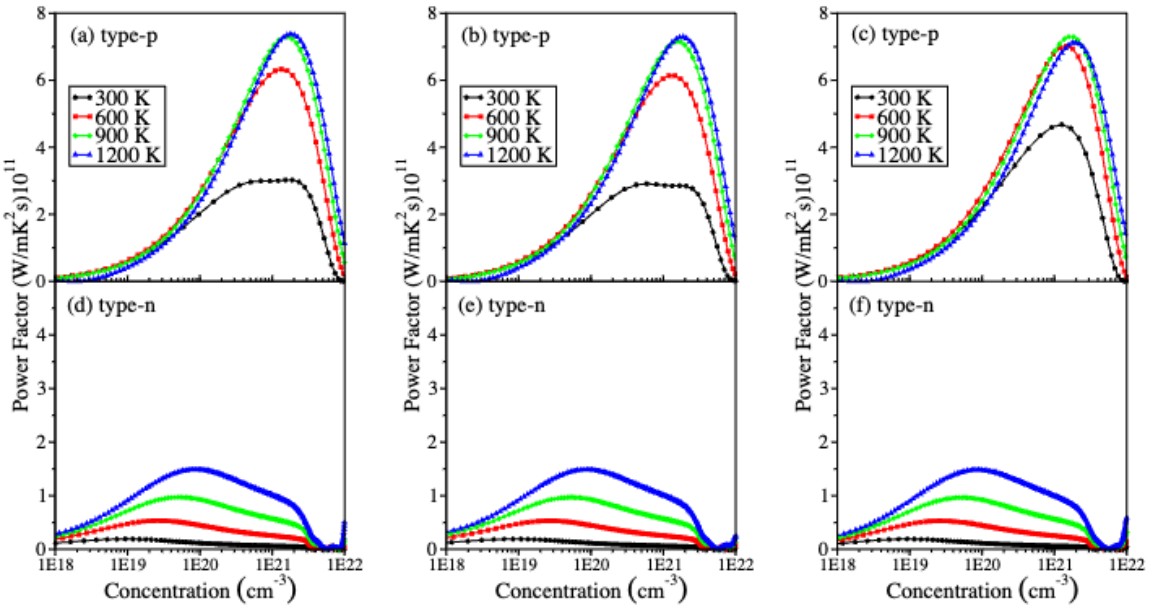

Figure 3.5 – Power factors in terms of carrier concentration for $K_2AgAlBr_6$ (a, d), $Rb_2AgAlBr_6$ (b, e) e $Cs_2AgAlBr_6$ (c, f): p-type (a-c) and n-type (d-f) doping respectively.

gives a good thermoelectric device [167, 168]. Figures 3.4g-i) show ZT_e as functions of the chemical potential at several temperatures. At room temperature, the three compounds have a predicted upper bound of 0.99 for the figure of merit, indicating good thermoelectric properties for $K_2AgAlBr_6$, $Rb_2AgAlBr_6$, and $Cs_2AgAlBr_6$. For higher temperatures, the peaks of the figures of merit at $\mu - E_F > 0$ are considerably lower than the ones at $\mu - E_F < 0$. This means that the three compounds under investigation do not maintain their n-type doping properties as well as they maintain their p-type doping properties, i.e., their thermoelectric performance is poorer for $\mu - E_F > 0$ than for $\mu - E_F < 0$, especially at high temperatures. This happened for all three double perovskites under investigation. In terms of comparison, Rb_2AlInX_6 (X = Cl, Br, I) were reported to have a figure of merit within 0.73 and 0.78 in a temperature range of 200K to 600K [169] and Sr_2CrTaO_6 presents a ZT equal to 0.15 at room temperature and 0.6 at 800K [170], meaning that the compounds studied in this work have better chances of presenting good thermoelectric behavior at room temperature compared with other known double perovskites. Moreover, comparing the figure of merit of the compounds studied here with those in Table 2.1, we notice that it has a figure of merit close to Bi_2Te_3, a material already used in thermoelectric devices.

The optimal doping level at which the power factor reaches its highest values is one of the main aspects in the domain of thermoelectric compounds. Figure 3.5 presents the power factors as functions of carrier concentration for $M_2AgAlBr_6$ (M = K, Rb, Cs) at constant temperatures 300K, 600K, 900K, and 1200K for both type-p and type-n doping. Figures

Table 3.4 – Power factors ($10^{10} \times Wm^{-1}K^{-2}s^{-1}$) and optimal doping levels (carrier per unit cell) for p-type and n-type doping.

Compund	Temperature (K)	p-type	Power Factor	n-type	Power Factor
$K_2AgAlBr_6$	300	0.5843	30.23	0.0029	1.90
	600	0.4115	63.30	0.0080	5.35
	900	0.5059	72.95	0.0165	9.72
	1200	0.5548	73.78	0.0259	14.89
$Rb_2AgAlBr_6$	300	0.1818	29.11	0.0026	1.92
	600	0.4456	61.34	0.0086	5.33
	900	0.4667	71.54	0.0159	9.69
	1200	0.5778	72.87	0.0269	14.85
$Cs_2AgAlBr_6$	300	0.3983	46.76	0.0029	1.91
	600	0.4634	70.26	0.0080	5.31
	900	0.4993	72.30	0.0167	9.65
	1200	0.6288	71.21	0.0280	14.79

3.5 a-c) were plotted with the allowed doping concentrations below the Fermi energy while figures 3.5 d-f) were plotted with the allowed ones above the Fermi energy.

For type-p doping, the three compounds have a small power factor for carrier concentration of about 10^{18} and start rising in the range of 10^{19}. For $K_2AgAlBr_6$ and $Rb_2AgAlBr_6$, figure 3.5a,b) shows that the power factor has a flattened peak at room temperature and this plateau is in the range of 3×10^{20} to 2.5×10^{21} while figure 3.5c) shows that, at room temperature, $Cs_2AgAlBr_6$ has a well-defined maximum at around 10^{21} that is approximately 1.5 times higher than the ones at $K_2AgAlBr_6$ and $Rb_2AgAlBr_6$. From 900 K the power factor seems to stabilize in its highest value and the rise of the temperature does not increase the power factor anymore but, in the case of $Cs_2AgAlBr_6$, it starts to slightly decrease from 900K to 1200K as shown in 3.5c).

For type-n doping, figure 3.5d-f) shows that all the peaks of the power factors are much smaller than the type-p doping ones. In comparison, the peak of type-n doping at 1200K is about two times smaller than the peak of type-p doping at 300K for $K_2AgAlBr_6$ and $Rb_2AgAlBr_6$ and is about three times smaller for $Cs_2AgAlBr_6$. Also, all the type-n doping peaks are in the range of 3×10^{18} to 10^{20}, and, for high temperatures, the power factor does not seem to stabilize in a maximum value but keeps increasing significantly. The maximum value of the power factor and the corresponding optimal doping levels for the three compounds are presented in Table 3.4 and it is clear that, comparing the power factors for both types of doping, the three compounds perform much better as hole-doping materials than electron-doping ones for all the temperatures studied.

3.3 Conclusions

In this chapter, we investigated the structural, electronic, and thermoelectric properties of the aluminum-based halide double perovskites $M_2AgAlBr_6$ (M = K, Rb, Cs) using density functional theory and the Boltzmann transport formalism within the relaxation time approximation. Our structural calculations yielded lattice constants and bulk moduli in good agreement with previous theoretical studies, validating the computational approach employed. The electronic structure analysis revealed that all three compounds exhibit a direct band gap located at the Γ point, with HSE06 values ranging from 2.259 to 2.264 eV. These values are consistent with prior theoretical results and suggest optical activity suitable for photovoltaic or optoelectronic applications. The projected density of states indicates that the valence band is dominated by Br-p states, while the conduction band minimum is primarily composed of Al and Ag orbitals, a band alignment beneficial for thermoelectric performance. Regarding thermoelectric properties, our calculations of the Seebeck coefficient, electrical and thermal conductivities, and power factor demonstrate promising performance. All three materials exhibit a strong p-type character, with large positive Seebeck coefficients exceeding 2000 μV/K at room temperature and moderate doping levels. The power factor increases with temperature up to 900 K for most compounds, after which it stabilizes or slightly decreases. Notably, $Cs_2AgAlBr_6$ reaches a power factor peak at 1200 K that is approximately 1.5 times higher than that of $K_2AgAlBr_6$ and $Rb_2AgAlBr_6$. A key result of this study is the calculated figure of merit (ZT), which approaches 0.99 at room temperature for all compounds, placing them in the same order of magnitude as the state-of-the-art thermoelectric material Bi_2Te_3 in bulk form. It is important to note that our calculations consider only the electronic contribution to the thermal conductivity, excluding the lattice component. In most materials, this omission would lead to an overestimation of ZT. However, halide perovskites are known to possess intrinsically low lattice thermal conductivity. Thus, although the absolute ZT values might be somewhat reduced with the inclusion of κ_L, the overall thermoelectric performance remains promising, and the qualitative trends observed here are expected to hold. Compared to other double perovskites reported in the literature, such as Rb_2AlInX_6 ($ZT \approx 0.73 - 0.78$ between 200–600 K) or Sr_2CrTaO_6 ($ZT = 0.15$ at 300 K and 0.6 at 800 K), the compounds studied here exhibit superior thermoelectric performance. Moreover, their structural simplicity, environmental friendliness due to the absence of lead, and the abundance of constituent elements such as K and Rb further enhance their appeal for scalable applications. These results strongly support the viability of $M_2AgAlBr_6$ as efficient p-type thermoelectric materials. Future studies could investigate their performance under strain or dimensional confinement (e.g., thin films). Additionally, experimental synthesis and characterization are encouraged to validate the theoretical predictions and explore practical device integration.

4 Far-Infrared Dielectric Properties of Transition Metal Dichalcogenides

4.1 Introduction

Classical molecular dynamics (MD) has become an essential tool for investigating the structural and dynamical properties of materials. However, its predictive power depends critically on the accuracy and transferability of the employed interatomic potentials. Traditional force fields, such as Tersoff for carbon,TIP3P for water, Vashishta for silica, and the Embedded Atom Method for metals, are typically parameterized for specific systems and properties, which limits their general applicability. In the case of transition metal dichalcogenides (TMDs), the Stillinger–Weber potential proposed by Jiang [171, 172] reproduces phonon dispersion reasonably well, while the ReaxFF potential [173] captures bond-breaking processes more accurately. Yet, neither provides a fully transferable description across the diverse range of properties of interest, highlighting a central limitation of conventional potentials.

First-principles molecular dynamics (aiMD) offers a more rigorous approach but is restricted to small system sizes due to its computational cost. A promising alternative is the development of Machine Learning Force Fields (MLFFs), which leverage reference datasets generated from density functional theory (DFT) to achieve near first-principles accuracy at a fraction of the cost.

In this chapter, we present the construction of MLFFs for single-layer MoS_2 and $MoSe_2$ using artificial neural networks trained on extensive DFT datasets. The resulting force fields reproduce phonon dispersions with high accuracy and capture the correct Raman and infrared (IR) active modes between 100–600 cm^{-1}. Large-scale MD simulations enabled by these MLFFs reveal spontaneous rippling in the monolayers, which in turn induces non-trivial IR activity. Specifically, our results suggest that ripples break the threefold rotational symmetry of the lattice, activating otherwise forbidden modes and modifying the polarization of the $E^{'}$ and $A_2^{''}$ vibrations. These findings demonstrate both the accuracy of the developed MLFFs and their potential to uncover subtle lattice-dynamical effects inaccessible with conventional force fields.

4.2 Results and Discussions

The results presented in this chapter are organized into three main parts. We first address, in Sec. 4.2.1, the evaluation metrics commonly employed in the MLFF literature to

quantify the accuracy of a model in reproducing DFT reference data. We then examine, in Sec. 4.2.2, the ability of our MLFF to reproduce vibrational properties, with a particular focus on phonon-related quantities obtained through the finite displacement method introduced in Sec. 2.5.2.2. Lastly, in Secs. 4.2.3 and 4.2.4, we present the results of molecular dynamics simulations, highlighting in turn the calculation of dielectric spectra and the characterization of ripple-induced effects.

4.2.1 Accuracy and Validation of MLFFs

Here, Secs. 4.2.1.1 and 4.2.1.2 are devoted to the description of the computational parameters employed in the DFT calculations and the details of the MLFF architecture, respectively. Subsequently, in Sec. 4.2.1.3, we present and analyze the results obtained for the evaluation metrics.

4.2.1.1 DFT Computational Parameters

We briefly describe the DFT parameters underlying the database generation. Calculations were performed using plane-wave pseudopotentials as implemented in the Quantum ESPRESSO package. The exchange-correlation functional was treated within the PBE generalized gradient approximation (GGA), and the interaction between valence electrons and ionic cores was described using Optimized Norm-Conserving Vanderbilt (ONCV) pseudopotentials. A Monkhorst-Pack grid of 6×6×1 was employed for Brillouin-zone integration, with kinetic energy cutoffs of 70 Ry for wavefunctions and 280 Ry for charge density. For SL-MoS_2 , the hexagonal primitive cell (red diamond in Figure 4.1a) was relaxed until the residual forces were below 5.0×10^{-3} eV/Å, with a vacuum spacing of 20 Å to eliminate spurious interactions between periodic images. The optimized lattice constant a_0 (Figure 4.1a) was 3.186 Å, within 0.79% of the experimental value of 3.16 Å [174]. The relaxed Mo–S bond length $d_{\text{Mo-X}}$ was 2.414 Å, and the S–Mo–S angle θ (Figure 4.1b) was 80.76°. For SL-$MoSe_2$, the same k-point grid was used, but with reduced cutoffs of 40 Ry for wavefunctions and 160 Ry for charge density. The optimized lattice constant was 3.32 Å (0.91% deviation from the experimental 3.29 Å [175]), with a Mo–Se bond length of 2.541 Å and a Se–Mo–Se angle of 82.12°. These structural parameters serve as the equilibrium reference for generating the displaced configurations used in the force-field training. Among all pseudopotentials and exchange–correlation functionals tested prior to generating the database, these were the ones that provided the most accurate results for the lattice constant, with deviations from the experimental value of less than 1%.

4.2.1.2 ANN Computational Parameters

To generate the database for the project in this chapter, we followed the *normal mode sampling* strategy as discussed in the Sec. 2.4.4.2 and the workflow illustrated at Fig.

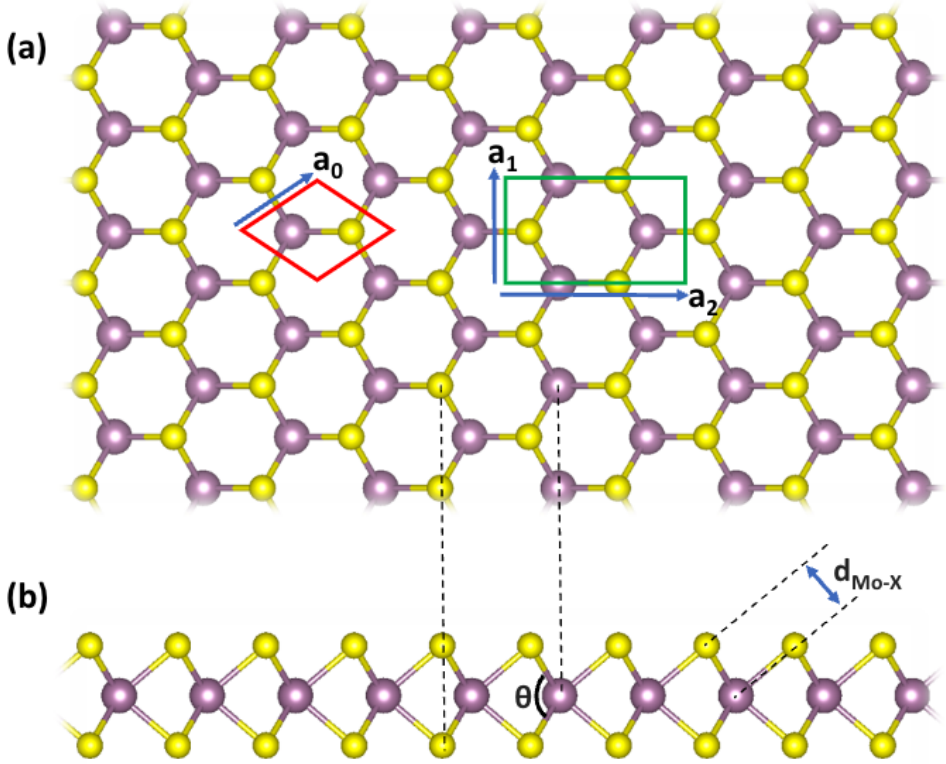

Figure 4.1 – Top (a) and side (b) views of monolayer MoX_2 (X = S, Se). Mo and X atoms are shown in purple and yellow, respectively. The red diamond marks the hexagonal primitive cell with lattice constant a_0, and the green rectangle the rectangular cell with $|\mathbf{a}_1| = a_0$ and $|\mathbf{a}_2| = a_0\sqrt{3}$. The Mo–X bond length is $d_{\text{Mo-X}}$ and the X–Mo–X angle is θ.

2.17. In total, the reference data set comprises a total of 5259 structures for MoS_2 and 6187 for $MoSe_2$, each of which with has the number of atoms in the unit cell ranging from 3 to 48. Moreover, for MoS_2 we built an ANN composed by 2 layers with 24 nodes followed by 2 layers with 20 nodes totaling 4 hidden layers, using *hyperbolic tangent* as the activation function (See Fig. 2.13 for definition of *hidden layers*). For $MoSe_2$ we built an ANN composed by 2 layers with 20 nodes followed by 2 layers with 16 nodes and the same activation function. Furthermore, recalling Eqs. 2.122 to 2.127, we have used the same set of local descriptors for all atom types: a radial r_{cut} of 9.0 Å, a radial order expansion of 16, an angular r_{cut} of 8.0 Å and an angular order expansion of 8. We also tested neural networks with 2 and 3 hidden layers. However, none of them were able to reproduce the desired dynamical properties of the studied systems. Of the diverse number of nodes and layers that were tried, those architectures showed the best results.

4.2.1.3 Results

To check the accuracy of the MLFFs generated in this work on the task of predicting the energies and atomic forces on unseen data (i.e., the *test set* discussed in the end of

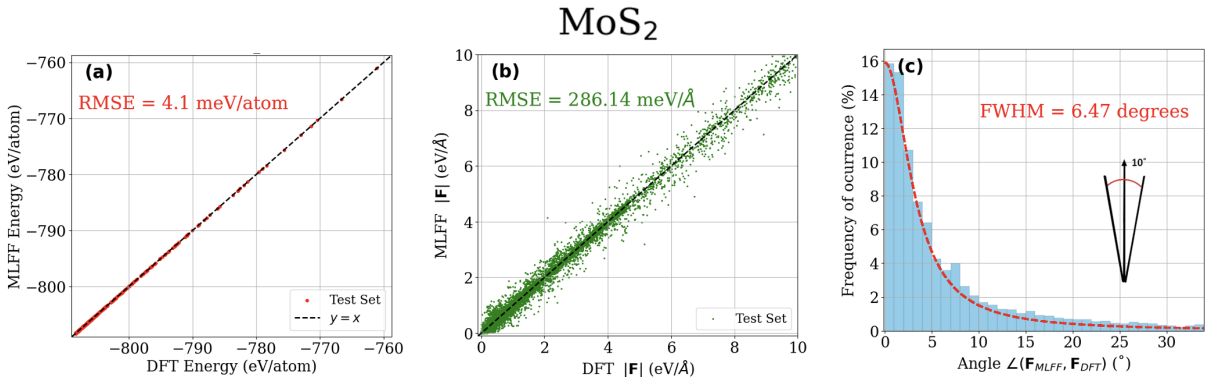

Figure 4.2 – (a,b) Energy and force magnitude comparison between MLFF and DFT for MoS_2. (c) Histogram of force directional errors with a Lorentzian fit (red dashed line)

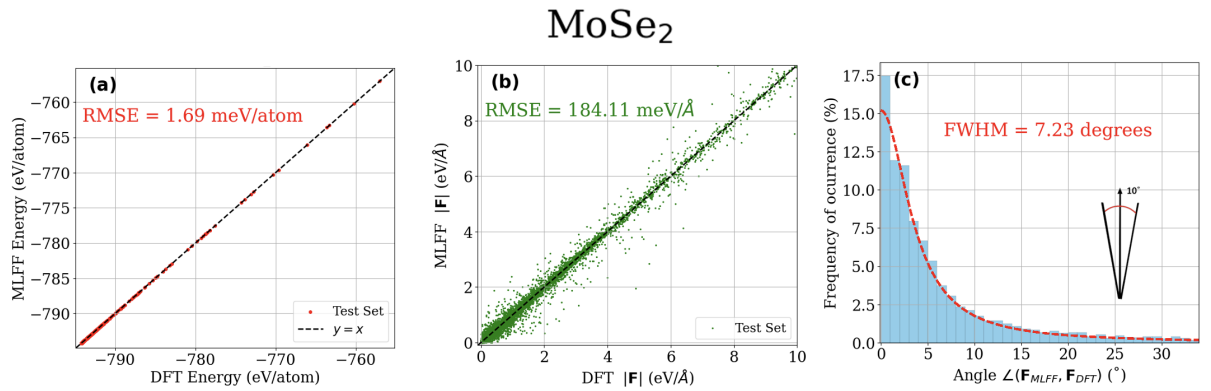

Figure 4.3 – (a,b) Energy and force magnitude comparison between MLFF and DFT for $MoSe_2$. (c) Histogram of force directional errors with a Lorentzian fit (red dashed line)

Sec. 2.4.3) we have included Figures 4.2 and 4.3. Each one of the subfigures was made with 750 structures of the testing set generated at the time of splitting the reference set between training and testing data. Figure 4.2a) and b) shows a comparison between the energies per atom and the absolute value for the atomic forces predicted by the MLFF and the reference DFT values on the data set respectively for MoS_2, with the dashed black line indicating perfect accuracy for the MLFF, i.e., when the MLFF matches DFT without any error. For the structures included in the figure, we obtained a RMSE of 4.1 meV/atom and 286.16 meV/Å for the energies and forces respectively. Figure 4.2 c) shows a histogram of angles between the direction of the MLFF and DFT forces which is a measure of directional error in the sense that the more accurate an MLFF is, the more concentrated at 0° the distribution becomes. Due to the tail of the distribution on angles $\geq$10%, we fitted a Lorentz distribution to the histogram. The red dashed line indicates the fitted curve which has a full width half maximum (FWHM) equal to 6.47° and, of all the forces evaluated with the MLFF and included in the histogram, 60.2% of them have their angle with the DFT force within the range of the FWHM and 72.4% of them have this angle within the range of 10° (see inset at Figure 4.2). The accuracy check of

the MLFF for $MoSe_2$ in Figure 4.3 with each one of the subfigures being made with the same amount structures of the testing set as in Figure 4.2. Figure 4.3a) and b) shows a comparison between the energies per atom and the absolute value for the atomic forces predicted by the MLFF and the reference DFT values on the data set respectively. For the structures included in the figure, we obtained a RMSE of 1.69 meV/atom and 184.11 meV/Å for the energies and forces respectively, both being slightly more accurate than the RMSE obtained for MoS_2. Figure 4.3 c) shows a histogram of angles between the direction of the MLFF and DFT forces. The red dashed line indicates the Lorentzian fitted to the histogram with a FWHM = 7.23° and, of all the forces evaluated with the MLFF and included in the histogram, 64.7% of them have their angle with the DFT force within the FWHM and 72.1% of them have this angle within the range of 10°. Both figures indicates good agreement between the MLFF and DFT estimates for the force, especially on predicting the direction and a comparison with recent literature indicates that our MLFF model demonstrate accuracy comparable to that of "up to date" utilized MLFF for different kinds of systems [176–178].

4.2.2 Phonon Properties

Figure 4.4 shows the results for the phonon dispersion calculated with the developed MLFF for MoS_2 in this study. The comparison with DFT in Figure 4.4a has the purpose of verify how accurately the MLFF reproduces the data on the reference set. One can see that all the main features of the DFT dispersion are reproduced by our MLFF for both the optical and acoustic branches, indicating that our model "learned" the main motion patterns predicted by DFT. Figure 4.4b shows the same MLFF phonon dispersion as Figure 4.4a but compares it with the Stillinger-Weber potential (referred in this section as SW-MoS_2 the parametrization on Ref. [172]) and with Inelastic X-Ray Scattering measurements [179] shown as the black dots. Both MLFF and SW dispersion curves were obtained with the assistance of the Alamode package while the DFT one was obtained using DFPT. The first thing to be noticed here is that, although MLFF had a similar accuracy to SW-MoS_2 for the acoustic branches when compared with experimental data, MLFF follows the experimental results for optical branches closer than SW-MoS_2

When studying the lattice dynamics of a given system, special attention must be paid to the Γ modes, as they can be determined experimentally by IR and Raman measurements. Table 4.1 shows the predicted values for the four modes at Γ, comparing it with SW-MoS_2 and experimental results, each mode sketched in Figure 4.5. It is worth mentioning that of all the modes, only E' and A_2'' are IR active, since their oscillation, as discussed in Sec. 2.5.3, generates an instantaneous dipole moment and produces instantaneous polarization. All the modes are known to be Raman active except A_2'', and both E' and A_1' being used widely in literature to characterize MoS_2 samples.

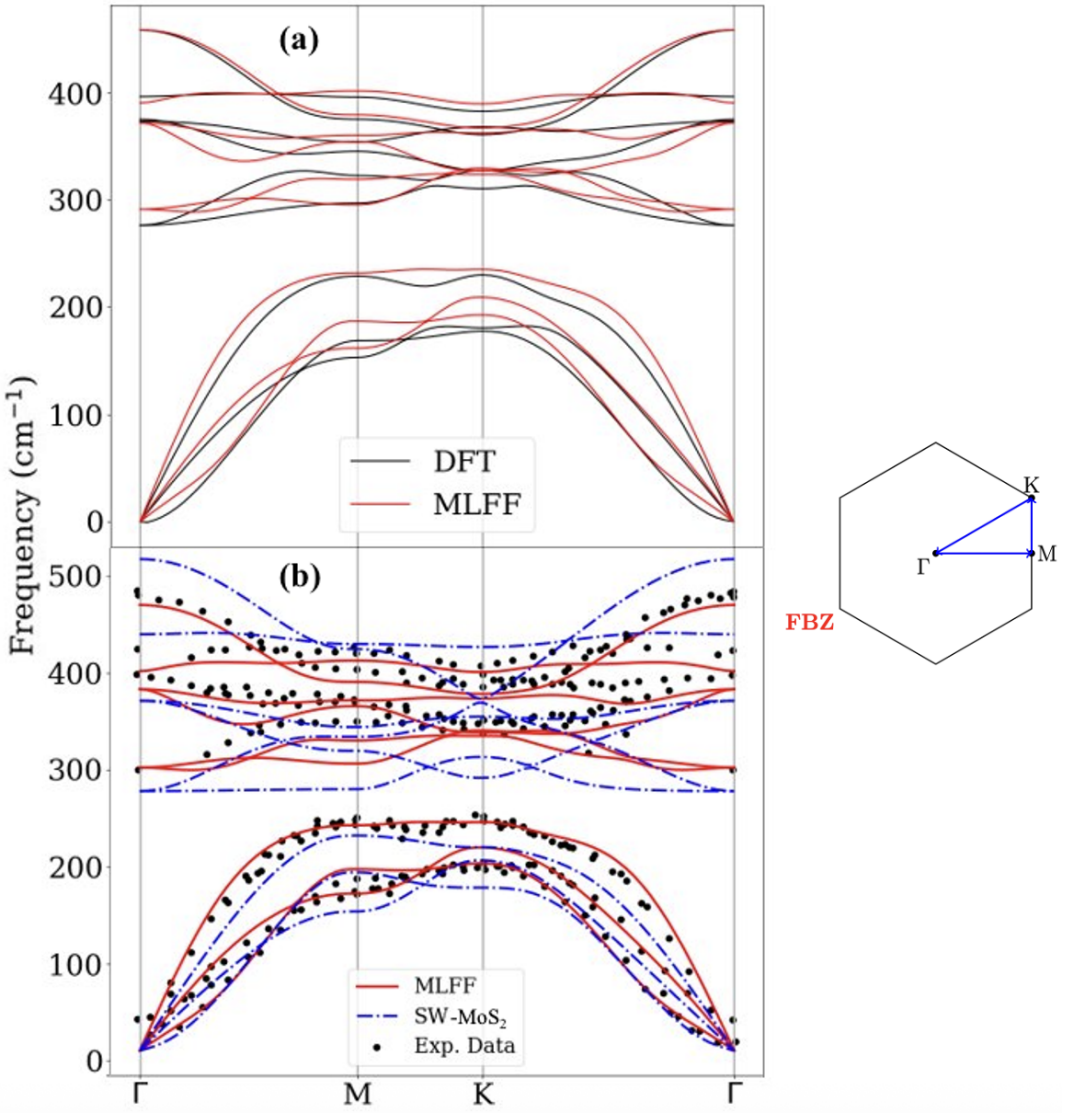

Figure 4.4 – Phonon dispersion of MoS_2 along Γ-M-K-Γ from MLFF, DFT, SW, and Inelastic X-Ray Scattering. First Brillouin zone is shown in the right side of the dispersion

Figure 4.6 presents the phonon dispersion of $MoSe_2$ as calculated using the MLFF developed in this work. The comparison with DFT calculations serves the same purpose as discussed in Figure 4.4, namely to assess the accuracy of the MLFF in reproducing the reference DFT data. However, to the best of our knowledge, there are no experimental reports of

Table 4.1 – Phonon frequencies at Γ of SL-MoS_2 in cm^{-1}.

Mode	MLFF	SW-MoS_2	Exp. Results
E''	291.5	267.3	286[3]
E'	372.3	360.5	384.3[1]; 384.0[2]; 383[3]; 383.7[5]
A_1'	390.8	429.2	403.1[1]; 408[3]
A_2''	459.0	506.8	470.0[2]; 466[4]; 468.2[5]

[1] Ref. [180]. [2] Ref. [181]. [3] Ref. [179]. [4] Ref. [182]. [5] Ref. [183].

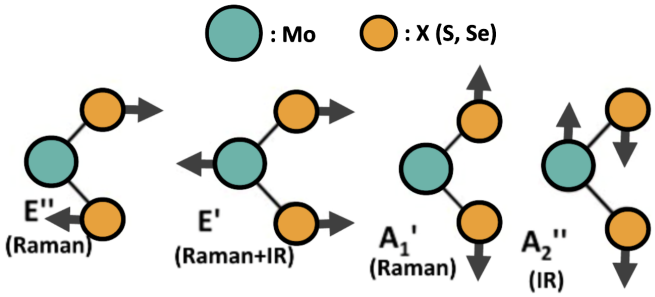

Figure 4.5 – Sketch of the optical phonon modes at Γ for MoX_2 (X = S, Se). Mo in turquoise and X in orange.

the phonon dispersion of $MoSe_2$ beyond the Γ point (such as those available for MoS_2 in Ref. [179]), which explains their absence in Figure 4.6. Our results are compared with those obtained using the Stillinger-Weber potential (referred to in this section as SW-$MoSe_2$) based on the parametrization proposed by Kandemir *et al.* [184]. As expected, the MLFF reproduces the DFT phonon dispersion with significantly higher accuracy, particularly for the optical branches, when compared to SW-$MoSe_2$. Table 4.2 presents the phonon frequencies at the Γ point predicted by the MLFF, alongside the results from SW-$MoSe_2$ and the available experimental data. From Table 4.2, it is evident that SW-$MoSe_2$ consistently underestimates the phonon frequencies relative to experiment, resulting in a pronounced redshift, whereas the MLFF yields values in much better agreement with experimental observations. It is also worth noting that the relative ordering of the E′

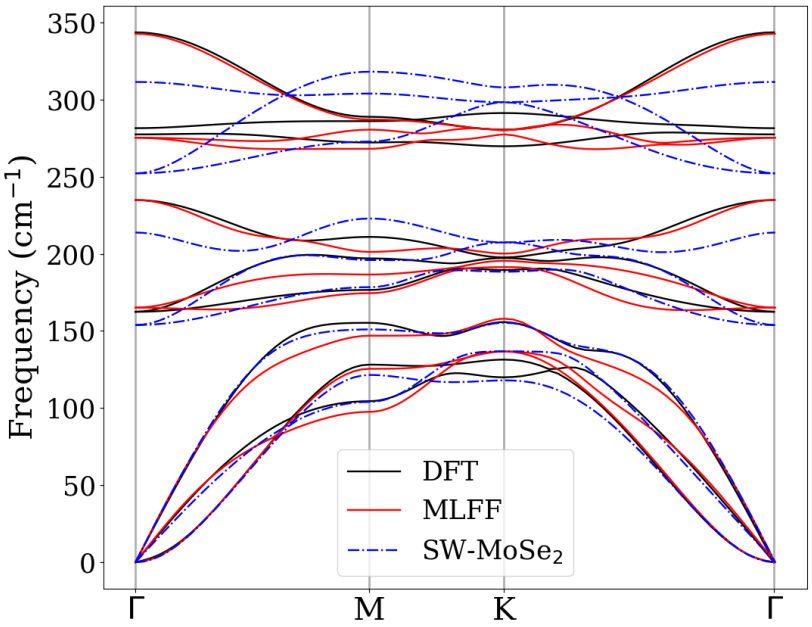

Figure 4.6 – Phonon dispersion of $MoSe_2$ along Γ-M-K-Γ from MLFF, DFT, and SW.

Table 4.2 – Phonon frequencies at Γ of SL-$MoSe_2$ in cm^{-1}.

Mode	MLFF	SW-$MoSe_2$	Exp. Results
E''	165.1	153.8	168[1], 170[2], 175.8[6]
A_1'	234.9	213.8	242[1], 243[2], 241.2[3]
E'	275.3	252.2	286.9[4], 289[1], 287.3[3], 288[5], 286[6], 283[7]
A_2''	342.7	311.5	352[1], 350[5], 352[6]

[1] Ref. [185]. [2] Ref. [186]. [3] Ref. [187]. [4] Ref. [188]. [5] Ref. [189].
[6] Ref. [190]. [7] Ref. [191].

and A_1' modes differs between MoS_2 and $MoSe_2$: while in MoS_2 the E' mode has a lower frequency than the A_1' mode, the inverse relationship is observed in $MoSe_2$.

4.2.3 Far-Infrared Dielectric Spectra

Here, Sec.4.2.3.1 is devoted to a detailed discussion of the setup adopted for the molecular dynamics simulations employed to extract the dielectric spectra. The corresponding results are presented and analyzed in Sec. 4.2.3.2.

4.2.3.1 MD Computational Parameters

Recalling the discussion at the end of Sec. 2.3.1, the procedure for calculating the complex dielectric spectra in the far-infrared region is based on expressing the dielectric response as the Fourier transform of the time autocorrelation function of the total dipole moment, as described in Eq. 2.91. Atomic charges are assigned according to the nominal oxidation states: $+4e$ for Mo and $-2e$ for both S and Se. This choice is justified by the fact that alternative charge definitions would only introduce a uniform scaling factor [192]. In our MD simulations, we used a timestep of dt = 1 fs within the following scheme: the first 250,000 steps were performed with the Nosé-Hoover thermostat (NVT ensemble) turned on at a chosen temperature to equilibrate the system and, after that, the thermostat is turned off and the simulations were carried out in the NVE ensemble, which is required to obtain dynamical properties. Since the Nosé-Hoover thermostat is based on a extended Lagrangian responsible for coupling the system to an external heat-bath as discussed in Sec 2.3.4.1, oscillations of the coupled heat-bath could affect the functions needed in Eq. 2.91. By switching from the NVT to the NVE ensemble, with the appropriate amount of equilibration steps, we were able to prevent these "virtual" oscillations from influencing the final result. After 8,000 steps to equilibrate the system in the NVE ensemble, the subsequent 3,992,000 additional NVE steps were conducted to obtain individual $\mathbf{M}(t)\cdot\mathbf{M}(0)$ functions where t ranges from 0 to 22 ps. Then the overlap approach was used to increase correlation between successive samples, reducing the noise in the Fourier transform [193]. These individual functions were averaged to obtain the main correlation function of dipole moment which was used to obtain the dielectric spectra of the material. To obtain the

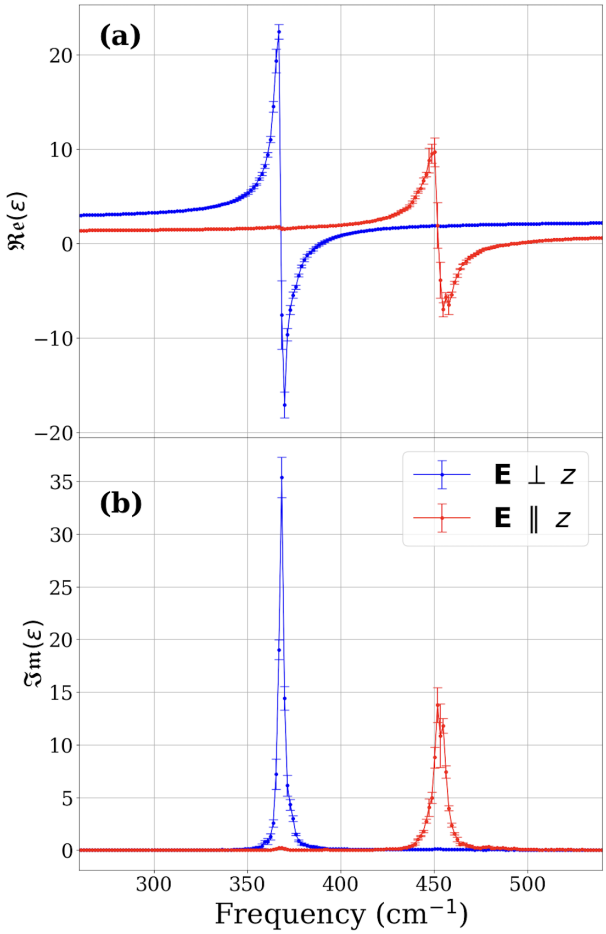

Figure 4.7 – Real (a) and imaginary (b) part of the dielectric spectra for MoS_2 as a result of our MD simulations at 300K.

error bars in our calculations, all $\mathbf{M}(t) \cdot \mathbf{M}(0)$ functions were partitioned in 10 different groups, each one of them giving one estimate to the spectra. Then, those estimates were averaged for the final results. The simulation cell was a rectangular supercell (see green rectangle at Figure 4.1) with a total of 16320 atoms and dimensions 68 $\mathbf{a_1}\times$ 40 $\mathbf{a_2}$ ($\mathbf{a_1} = \mathbf{a_0}$ and $\mathbf{a_2} = \mathbf{a_0}\sqrt{3}$). This size was adopted to minimize finite size effects and simulations with larger lattices did not improve the results.

4.2.3.2 Results

Figure 4.7 presents the dielectric spectra of SL-MoS_2 obtained from molecular dynamics (MD) simulations at 300 K in the far infrared frequency range (100 – 600 cm^{-1}). The spectra are decomposed into two components: the in-plane response, considering only the dipole moment components parallel to the layer (blue curves), and the out-of-plane response, considering the component perpendicular to the layer (red curves). The imaginary part of the out-of-plane dielectric function (Figure 4.7b) exhibits two well-defined narrow absorption peaks. Fitting these peaks with Lorentzian functions yields resonance frequencies of 368.3 ± 0.1 cm^{-1} and 452.8 ± 0.3 cm^{-1}, respectively. This behavior is consistent with the

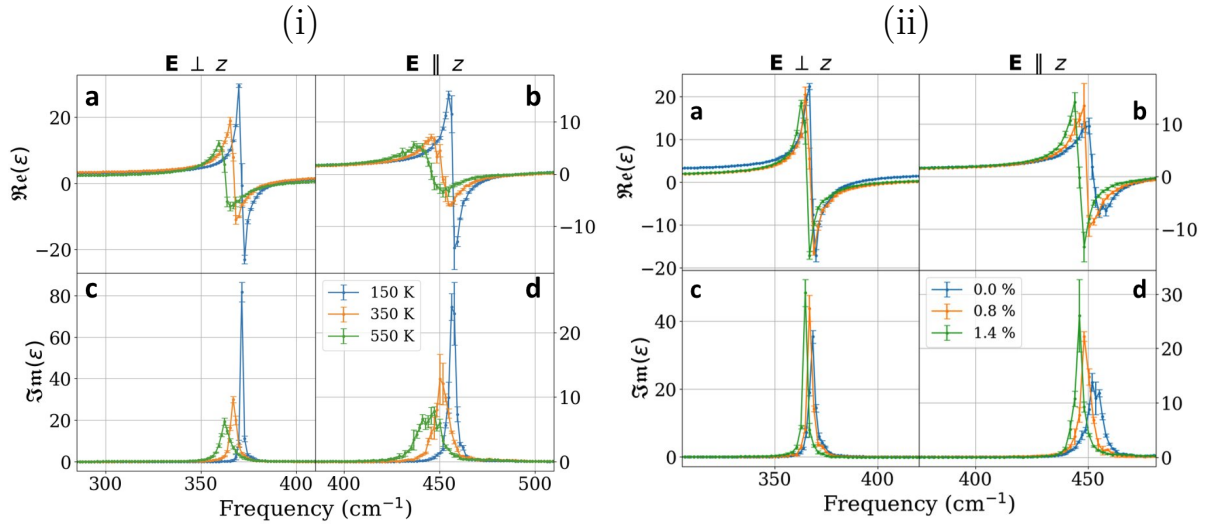

Figure 4.8 – (i) MoS_2 spectra at 150, 350, and 550 K. Peaks in (c) and (d) correspond to $E^{'}$ and $A_2^{''}$ modes from Fig. 4.9A). (ii) MoS_2 spectra at 300 K under strain. Peaks in (c) and (d) correspond to the same modes from Fig. 4.9B). Fewer temperatures/strain levels are shown for clarity.

phonon mode symmetries illustrated in Figure 4.5. Specifically, the eigenvectors of the $E^{'}$ mode induce dipole oscillations exclusively within the plane, while the $A_2^{''}$ mode generates dipole oscillations along the out-of-plane direction. Consequently, the peak associated with the in-plane response (blue curve) corresponds to the $E^{'}$ mode, whereas the out-of-plane peak (red curve) corresponds to the $A_2^{''}$ mode. The resonance frequencies extracted from the dielectric spectra (Figure 4.7b) are in close agreement with those obtained from the phonon dispersion calculations at Γ (Table 4.1), with the minor redshift attributed to finite-temperature effects inherent to the MD simulations. Furthermore, a comparison with experimental infrared reflectivity data reported by Wieting *et al.* [194] (specifically their Figure 6) reveals excellent agreement. The experimental peaks are observed at 384 cm^{-1} for the in-plane mode and 472 cm^{-1} for the out-of-plane mode, closely matching the values obtained in this work using the developed MLFF.

Figure 4.8(i) shows our MD results for the THz dielectric spectra of MoS_2 obtained with the MLFF at 150 K, 350 K and 550 K. From it, we can discern several trends: with increasing temperature, both peaks in Figure 4.8(i) c,d broaden and redshift, a behavior in accordance with experiments [195]. Figure 4.9A) shows the temperature dependence of the $E^{'}$ and $A_2^{''}$ modes based on the peak positions of the imaginary part of the spectra. The numerical values were obtained by fitting Lorentzian oscillators to the peaks presented in the data. To obtain the SW-MoS_2 data points, the same simulation procedure described in Sec. 4.2.3.1 was applied. Both simulations with MLFF and SW-MoS_2 produced a redshift with increasing of temperature. For each mode and for each potential, we performed linear fits (represented by dashed lines) and extracted the slope, which contains information about the average redshift of the system due to temperature. Table 4.3 shows results

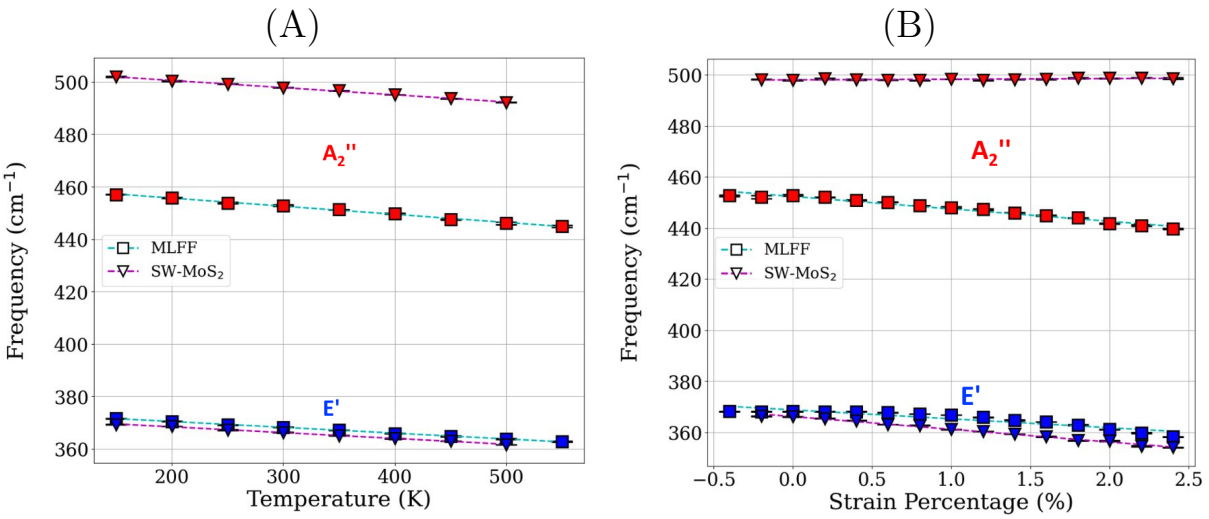

Figure 4.9 – (A) Temperature dependence of IR-active modes in MoS_2 for MLFF and SW-MoS_2. Dashed lines are linear fits used in Table 4.3. (B) Strain dependence of IR-active modes in MoS_2 for MLFF and SW-MoS_2. Dashed lines are linear fits used in Table 4.4.

for the slopes and compares it to experimental results, indicating that our calculations are consistent with literature. Figure 4.8(ii) shows our MD results for the THz dielectric spectra for MoS_2 obtained with the MLFF at 300 K using a unstrained lattice (0.0%), a lattice with 0.8% strain of the original and a lattice with 1.8% strain of the original. Qualitatively, the frequency peaks in Figure 4.8(ii) (c,d) become redshifted with the application of strain, similarly to the reported temperature effects. However, for more strained lattices the peaks are narrower than for unstrained ones. The redshift can be attributed to the weakening of the bonds caused by the tensile strain while the narrowing of the peaks can be attributed to the fact that in a strained lattice, acoustic modes do not propagate as freely as in an unstrained lattice and, therefore, cannot interfere with the propagation of optical modes. Figure 4.9B) shows the strain dependence of the of the $E^{'}$ and $A_2^{''}$ modes. Similar to Figure 4.9A), we performed linear fits and extracted the slope for each mode and for each potential. Table 4.4 shows the results for the temperature coefficients and compares it to experimental and other theoretical results. We notice a qualitative difference between the behavior of the $A_2^{''}$ mode for simulations with MLFF and SW-MoS_2, the latter presenting a slight blueshift with tensile strain, a result significantly different from the DFT prediction. For both modes, The MLFF reproduces DFT results more closely than SW-MoS_2. when comparing with experimental results, both potentials had similar performance for the E' mode. However, the diverse range of results for the E' mode prevents us from making any claims about the accuracy of our calculations regarding the temperature coefficient. Moreover, since the $A_2^{''}$ mode is not Raman active, to our knowledge, there are not any experimental results for its variation with strain. In that sense, our results are a prediction of the $A_2^{''}$ mode redshift including temperature effects.

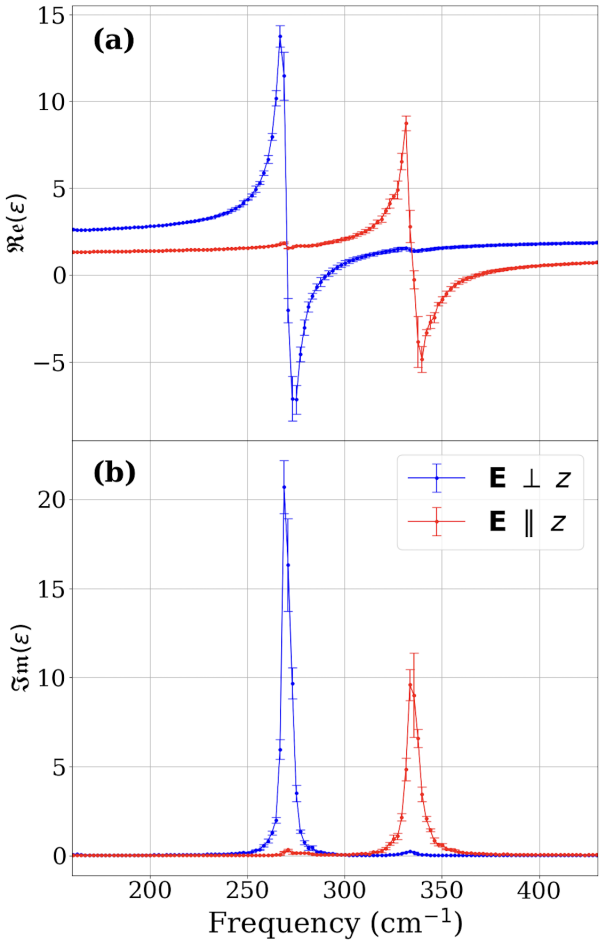

Figure 4.10 – Real (a) and imaginary (b) part of the dielectric spectra for $MoSe_2$ as a result of our MD simulations at 300K.

Figure 4.10 shows the MD results for the $MoSe_2$ far infrared dielectric spectra at long wavelengths similar to Figure 4.7. In Figure 4.10b, the peak for the blue and red curves respectively are localized at 269.8 ± 0.1 cm^{-1} and 334.9 ± 0.1 cm^{-1} respectively, which

Table 4.3 – Temperature coefficient for E′ and A_2'' modes of MoS_2 (10^{-2} cm^{-1}/K).

Mode	MLFF	SW-MoS_2	Exp. Results
E′	-2.2	-2.2	-1.32[1], -1.47[2], -1.41[3], -1.79[4], -1.61[5], -1.36[6], -1.6[7], -1.3[8]
A_2''	-3.1	-2.7	-1.99[5]

[1] Ref. [195]. [2] Ref. [196]. [3] Ref. [197]. [4] Ref. [198]. [5] Ref. [199].
[6] Ref. [200]. [7] Ref. [201]. [8] Ref. [202].

Table 4.4 – Strain coefficient for E′ and A_2'' modes of MoS_2 (cm^{-1}/%).

Mode	MLFF	SW-MoS_2	Exp. Results	DFT
E′	-3.49	-4.98	-7.4[1a]; -3.2[1b]; -4.5[2]; -2.1[3], -4.67[4]	-4.28[5]
A_2''	-4.87	0.26		-4.19[5]

[1a,b] Ref. [203]. [2] Ref. [204]. [3] Ref. [205]. [4] Ref. [206]. [5] Ref. [207].
[1a] Spin coated encapsulation
[1b] Conventional exfoliation

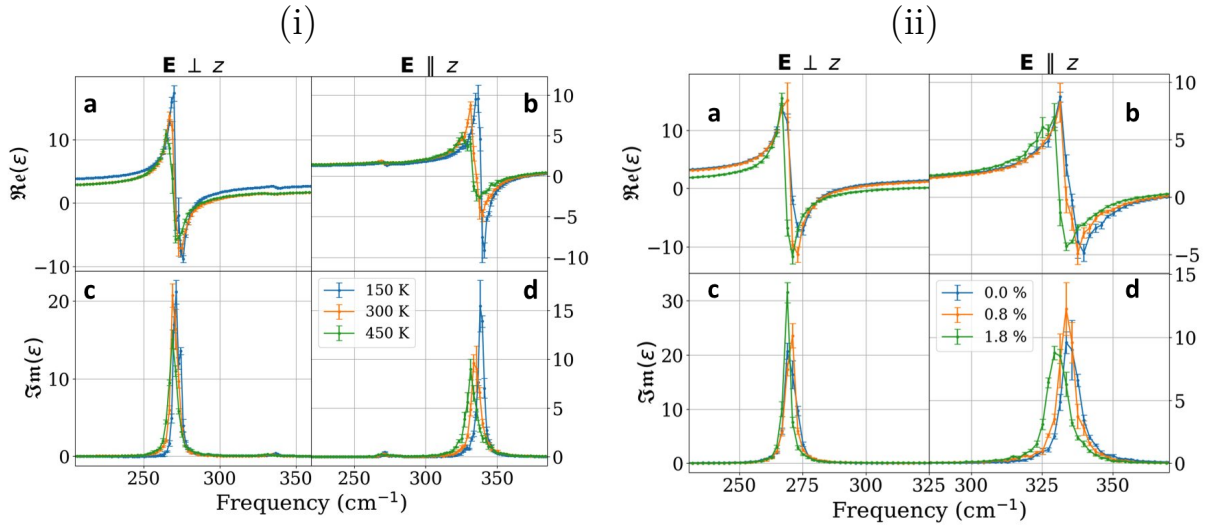

Figure 4.11 – (i) $MoSe_2$ spectra at 150, 350, and 550 K. Peaks in (c) and (d) correspond to the $E^{'}$ and $A_2^{''}$ modes in Fig. 4.12(A). (ii) $MoSe_2$ spectra at 300 K under strain. Peaks in (c) and (d) correspond to the same modes in Fig. 4.12(B). Fewer temperatures/strain levels are shown for clarity.

can be compared directly with the values from Table 4.2 for the E′ and A_2'' for the same reasons given before. Similar to what was observed on MoS_2, we can assign those modes to the peaks, and the difference of the peak positions and the tabled values also can be attributed to a redshift effect due to temperature in our simulations. We can compare our results to infrared reflectance results from Sekine *et. al.* [185] (specifically their Figure 6), as they assigned the values 289 cm^{-1} and 352 cm^{-1} to the modes $E^{'}$ and $A_2^{''}$ respectively.

Figure 4.11(i) shows our MD results for the THz dielectric spectra of $MoSe_2$ obtained with the MLFF at 150 K, 300 K and 450 K. The same qualitative trends observed on our MLFF simulations for MoS_2 can be observed on $MoSe_2$, i.e., the redshift and broadening of the peaks in Figure 4.11(i) c,d. However, the broadening is less pronounced than those in Figure 4.8(i) c,d. Figure 4.12(A) and Table 4.5 shows our results for the temperature dependence of the infrared active phonon modes, comparing it with simulations with SW-$MoSe_2$ and experimental results. We notice that, when comparing with experiments, the simulations with our MLFF predicts more accurate coefficients than SW-$MoSe_2$ and, although the MLFF prediction for the temperature coefficient of the A_2'' mode is considerably different than the experimental values, it is still a better prediction than those given by SW-$MoSe_2$. Also, SW-$MoSe_2$ predicts similar temperature coefficients for the two distinct modes while in the MLFF simulations the temperature coefficient seems to be sensitive to the oscillation mode. Figure 4.11(ii) shows results for the THz dielectric spectra of $MoSe_2$ at 300 K for the unstrained lattice (0.0%), and lattices with 0.8% and 1.8% strain respectively. Although a redshift of the peak is noticed, we did not observe any noticeable changes on the breadth of the peaks. Figure 4.12(B) and Table 4.6 shows our results for the strain dependence of the infrared active phonon modes. The lack of

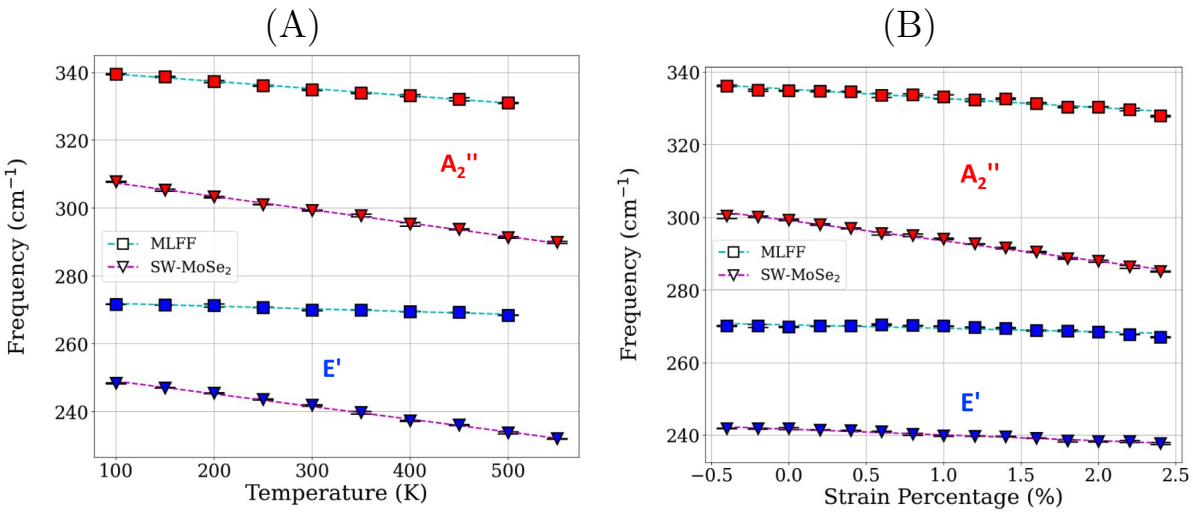

Figure 4.12 – (A) Temperature dependence of IR-active modes in $MoSe_2$ for MLFF and SW-$MoSe_2$. Dashed lines show linear fits used for Table 4.5. (B) Strain dependence of IR-active modes in $MoSe_2$ for MLFF and SW-$MoSe_2$. Dashed lines show linear fits used for Table 4.6.

other reported experimental or theoretical results made it difficult to rate the performance our MLFF. To our knowledge, the references cited at Table 4.6 were the only studies that reported the strain coefficients for the E′ mode and there are no reports for the A_2'' mode. When comparing to these reported data, neither our MLFF nor SW-$MoSe_2$ presented accurate results.

4.2.4 Rippling Effects

Figure 4.13 illustrates the imaginary part of the dielectric spectra for both systems (akin to Figures 4.7(b) and 4.10(b)), but specifically focusing on regions with low absorption intensities. Within the figure, it is evident that each system exhibits four distinct new peaks. Noticeably, two of these peaks align precisely with the frequencies of the E′ and A_2'' modes, however with reversed polarization directions. Additionally, MoS_2 displays peaks

Table 4.5 – Temperature coefficient for E′ and A_2'' modes of $MoSe_2$ (10^{-2} cm^{-1}/K).

Mode	MLFF	SW-$MoSe_2$	Exp. Results
E′	-0.79	-3.9	-1.18[1], -1.21[2], -0.69[3]
A_2''	-2.1	-3.7	-0.64[3], -0.86[4]

[1] Ref. [208]. [2] Ref. [197]. [3] Ref. [209]. [4] Ref. [210].

Table 4.6 – Strain coefficient for E′ and A_2'' modes of $MoSe_2$ (cm^{-1}/%).

Mode	MLFF	SW-$MoSe_2$	Exp. Results	DFT
E′	-0.95	-1.59	-4.93[1]	-4.28[2]
A_2''	-2.54	-5.6		

[1] Ref. [211]. [2] Ref. [212].

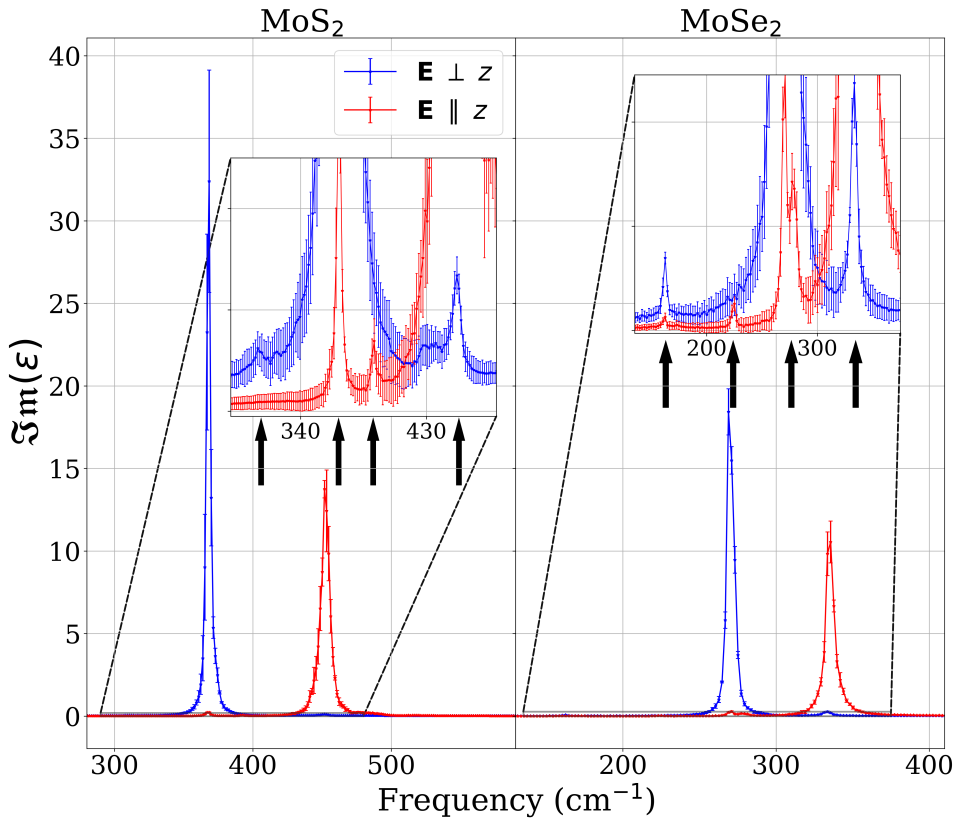

Figure 4.13 – Imaginary part of dielectric spectra for MoS_2 and $MoSe_2$ at 300K with insets in the small intensities region. Arrows indicate peaks centered at 310(163), 368(225), 393(271) and 452(334) for MoS_2 ($MoSe_2$) in cm^{-1}.

at approximately 310 cm^{-1} and 393 cm^{-1}, whereas $MoSe_2$ features peaks around 163 cm^{-1} and 225 cm^{-1}, values closely matching the frequencies of the E″ and A_1' modes as listed in Tables 4.1 and 4.2, respectively. Observing these new peaks allows us to identify two key characteristics in our simulations. Firstly, the E′ and A_2'' modes exhibit infrared (IR) activity in a direction perpendicular to their usual oscillation. Secondly, there is a manifestation of some IR activity, although minimal, by the E″ and A_1' modes, traditionally considered IR inactive.

Furthermore, Figure 4.14 displays the newly observed peaks in the dielectric spectra for both the unstrained lattice and the lattice subjected to 1.4% tensile strain (relative to the relaxed lattice constant). The simulations associated with this figure were conducted under constant volume conditions, employing the NVT ensemble, which enables the introduction of strain by systematically rescaling the in-plane lattice constants while maintaining the atomic volume fixed. A clear trend is observed: the application of tensile strain suppresses these additional peaks, leading to their complete disappearance at 1.4% strain. This behavior indicates that the phenomenon responsible for the emergence of these peaks in the unstrained lattice is, in principle, highly sensitive to lattice deformations and is effectively quenched under moderate tensile strain.

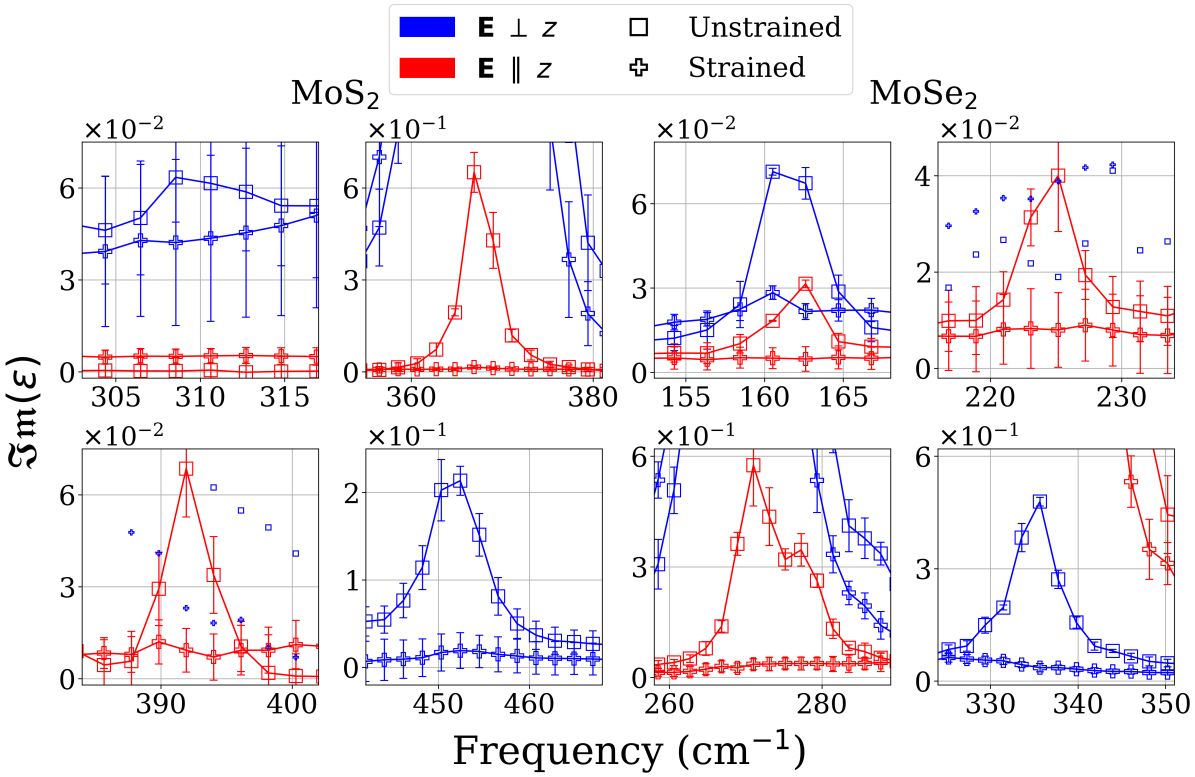

Figure 4.14 – All found low intensity peaks under the effect of strain for MoS_2 and $MoSe_2$. In some graphics, blue markers were reduced with the purpose of avoiding visual overload.

Applying strain to the lattice reduces fluctuations in its height, thereby diminishing the amplitude of ripples, as depicted in Figure 4.15. This figure demonstrates that in both systems, the average height (defined as the difference in the z coordinate between the highest and lowest Mo atom, as illustrated in the figure) decreases with increasing strain. For MoS_2 the average height decreases from 9Å to 2Å while for $MoSe_2$ it decreases from

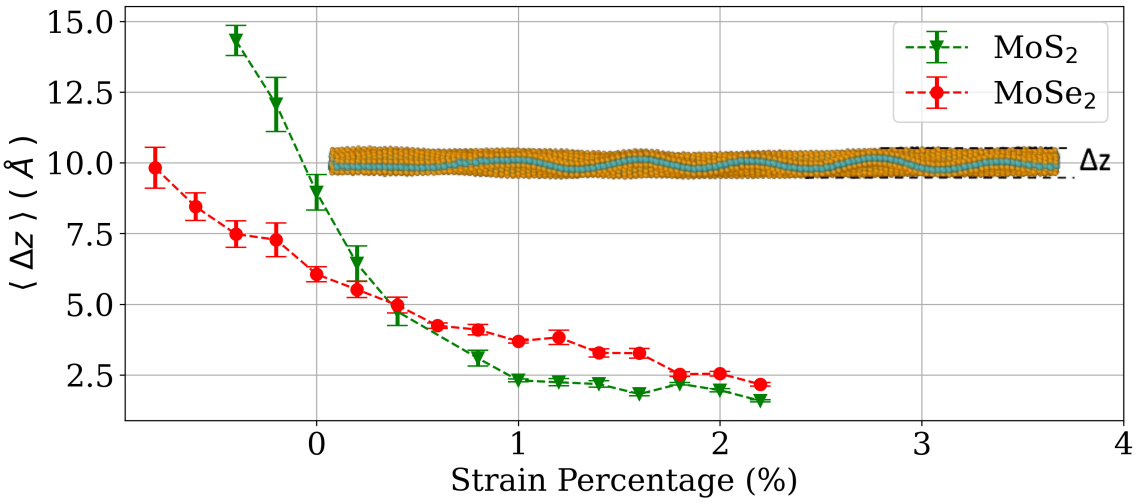

Figure 4.15 – Mean lattice height Δz as a function of strain for MoS_2 and $MoSe_2$. The inset illustrates the definition of Δz in the rippled monolayer.

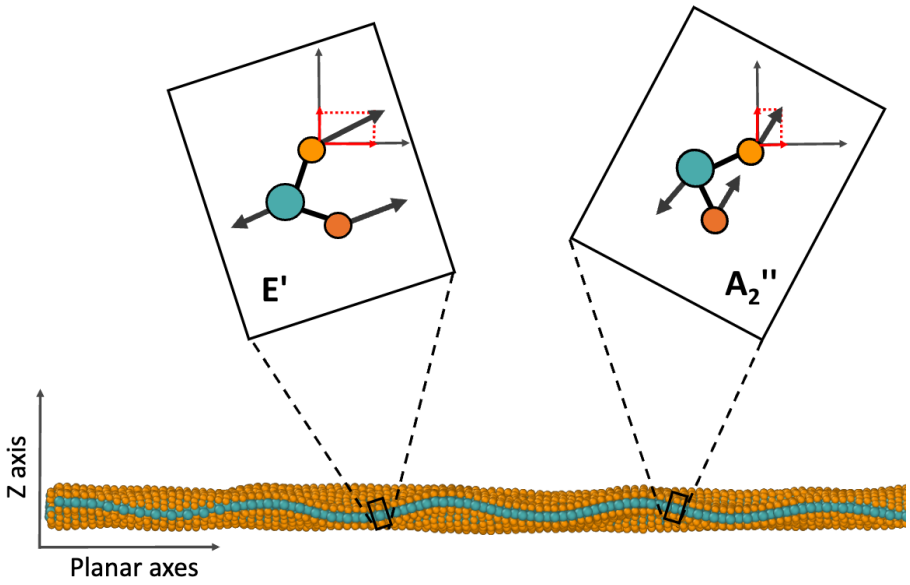

Figure 4.16 – Sketch of the decomposition of the components of the oscillation modes E′ and A_2'' in a rippled lattice.

6Å to 2Å when a strain 2% above the equilibrium lattice constant is applied. Therefore, considering the data presented in Figures 4.13 and 4.15, it can be inferred that the observed low-intensity peaks observed correlate with the ripples present in SL-MoS_2 and $MoSe_2$. It is also worth noting that under the unstrained condition (0% strain), the ripple lengths and heights obtained in our simulations for MoS_2 are in excellent agreement with the experimental measurements reported by Brivio *et al.* in Ref. [76]. In the vicinity of the peaks corresponding to the frequencies adjacent to the E′ and A_2'' modes, the mechanism by which ripples induce IR activity with altered polarizations becomes clearer. By allowing the lattice to ripple, the E′ mode is no longer confined strictly to the plane, and similarly, the A_2'' mode is not restricted solely to the axis perpendicular to the plane. This results in the E′ mode acquiring an out-of-plane component and the A_2'' mode acquiring a planar component, as depicted in Figure 4.16. However, this explanation alone does not suffice to elucidate the observed IR activity near the frequencies associated with the E″ and A_1' modes in our simulations.

To gain further insight into the influence of ripples on the dielectric spectra and to explore potential explanations for the peaks observed at E″ and A_1', we constructed a supercell composed of 1020 atoms. Within this supercell, we introduced a sinusoidal wave characterized by a wave vector $\mathbf{k}$ parallel to the $\hat{\mathbf{x}}$-axis, with a wavelength determined by the total length of the cell in the x-direction. This model for a ripple is well described in Appendix C and depicted in Figure C.1. The model maintains translational symmetry along the y direction and was simple enough that allowed us to qualitatively investigate the origins of the new peaks observed in the spectra in Figure 4.13. Using the MLFFs to model atomic interactions, we employed the Alamode package to compute the phonons of the primitive cell (see Figure C.2 at Appendix C) corresponding to the rippled supercell

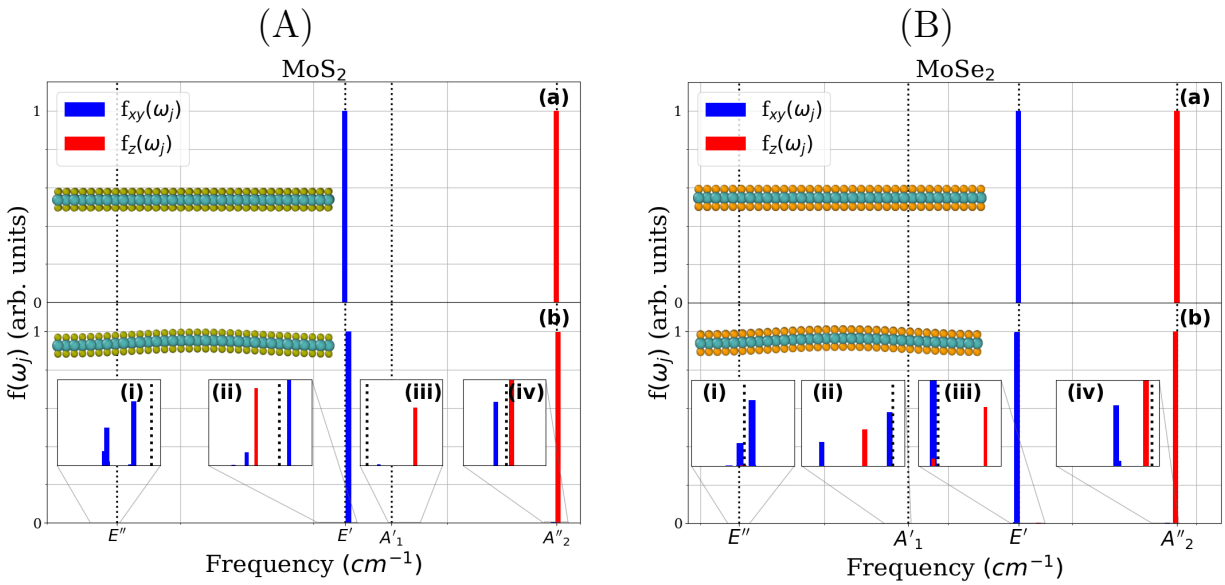

Figure 4.17 – (A) IR intensities for MoS_2. (a) Without ripples. (b) With ripples. Dotted lines indicate frequencies in Table 4.1. (B) IR intensities for MoSe2. (a) Without ripples. (b) With ripples. Dotted lines indicate frequencies in Table 4.2.

at the Γ point. The calculations also provided the eigenvectors $\mathbf{U}_j(\kappa)$ associated with each frequency eigenmode ω_j, just as the ones discussed in Eq.2.168 in Sec. 2.5.2.1.

The determination of the eigenvectors $\mathbf{U}_j(\kappa)$ allow us to calculate the IR intensity discussed in Sec. 2.5.3 through Eq. 2.172 for each eigenmode of the rippled model described above. The IR intensities results for MoS_2 and $MoSe_2$ are shown in Figure 4.17(A) and 4.17(B), respectively. In each, the calculation for the unrippled (flat) cell was included at Figures 4.17(A)a) and 4.17(B)a) for comparison purposes and the insets were included to facilitate visualization of all modes with low intensity $f(\omega_j)$. As expected for the flat cell in both compounds, only the E′ and A_2'' modes showed a non-zero IR response. The E′ mode presents an in-plane response only while the A_2'' mode presents an out-of-plane response only. For the rippled cell, a degeneracy breaking in frequencies is observed due to the breaking of some symmetries of the system caused by the introduction of the ripple. This symmetry breaking causes the only two modes present in the flat cell to split into several bars located at frequencies close to the E′ and A_2'' modes in the flat cell.

However, it is still expected that the new modes introduced by the ripple must have some similarity to those of the original cell due to the fact that they share similar frequencies, which can be seen in Figures 4.17(A)b) and 4.17(B)b) for MoS_2 and $MoSe_2$ respectively. In both compounds the two largest bars, one blue and one red, correspond to the vibrations that best represent the E′ and A_2'' modes of the flat cell in the rippled cell, the characteristic vibration of the E′ in the planar directions and the characteristic vibration of the A_2'' in the out-of-plane direction. This blue bar would correspond to the main blue peak depicted

in Figures 4.7b) for MoS_2 and 4.10b) for $MoSe_2$ while the red bar would correspond to the main red peaks in the aforementioned figures. Looking at the low IR intensity modes, it is noticeable that in both Figures 4.17(A)b) and 4.17(B)b) the presence of a mode with a frequency close to E' that presents out-of-plane IR activity (indicated by the red bar) as well as a mode with a frequency close to A_2'' that presents in-plane IR activity (indicated by the blue bar) in both figures. Furthermore, both figures indicate the presence of modes with IR activity at frequencies close to those of the E'' and A_1' modes which, in the flat cell, are known to be IR inactive. Thus, the degeneracy breaking caused by the introduction of the ripple is also responsible for the splitting of the E'' and A_1' modes into several modes, some of which have some IR activity. The results shown in Figures 4.17(A) and 4.17(B) strengths the hypothesis that lattice ripples would be responsible for the appearance of new peaks present in the simulations and shown in Figures 4.13.

The main advantage of calculating the eigenvectors of the ripples lattice lies in the ability to observe the motion patterns of vibrational modes that are distinct from the flat cell and understand how these modes affect the total electric dipole moment of the cell, which, besides the development of the MLFFs, we consider to be our main contribution to the literature regarding vibrational modes in single layers MoS_2 and $MoSe_2$. This will be shown on the following figures. In this work the following notation is adopted: we denote the modes of the rippled cell with the same notation of Tables 4.1 and 4.2 to indicate the mode of the flat cell that generated the new mode, but we will use a "*" to indicate that this mode belongs to the rippled cell and we will indicate the direction of polarization of the mode in parenthesis.

Figure 4.18 shows the modes $^*E'(z)$ and $^*A_2''(x)$, found to have IR activity next to E' and A_2'' with inverted polarizations at Figures 4.17(A)(b-ii, iv) and 4.17(B)(b-iii, iv). Upon comparing the modes depicted in Figures 4.5 and 4.18, a discernible similarity emerges between modes $^*E'(z)$ and $^*A_2''(x)$ in relation to modes E' and A_2'' respectively. This similarity arises due to certain $MoS(Se)_2$ units within the rippled supercell exhibiting identical vibrational pattern as those observed in the primitive flat cell, leading to similar oscillation frequencies in these modes. However, Figure 4.18 reveals how the oscillation of the whole rippled cell lead to alterations in its total dipole and in which direction. In mode $^*E'(z)$, the cell exhibits a oscillation pattern resembling E', with atoms on either side of the ripple crest moving in opposite directions, which results in the cancellation of the horizontal component of total dipole moment of the mode, leaving only a resultant vertical component. Thus, mode $^*E'(z)$ manifests an out-of-plane infrared (IR) response with a frequency close to E', consistent with the results shown in Figure 4.13. Similarly, in mode $^*A_2''(x)$, the cell displays an oscillation pattern akin to A_2'', also with atoms on either side of the ripple crest moving oppositely similar to $^*E'(z)$. This leads to the cancellation of the vertical component, leaving predominantly only a resultant horizontal component. Consequently, mode $^*A_2''(x)$ exhibits an in-plane IR response with a frequency close to

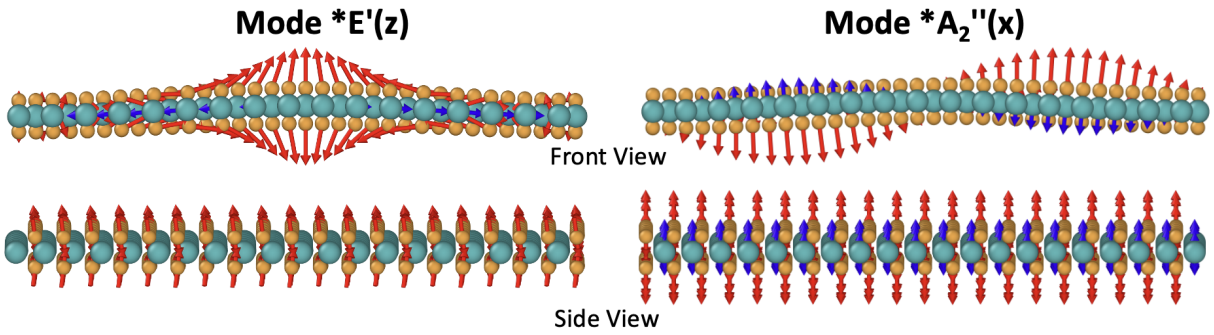

Figure 4.18 – Sketch of the oscillation patterns of the modes *E′(z) and *A$_2''$(x) in the rippled cell. The directions of displacements of the Mo and S(Se) atoms are indicated by blue and red vectors respectively.

A$_2''$, which is also consistent with the results in Figure 4.13. The analysis of modes *E′(z) and *A$_2''$(x) on Figure 4.18 strengths the hypothesis depicted in Figure 4.16, wherein the rippled lattice causes modes E′ and A$_2''$ to acquire out-of-plane and in-plane components, respectively.

Figure 4.19 shows the modes *E″(x) and *E″(y) related to the two highest blue bars at Figure 4.17(A)(b-i) for MoS_2 and Figure 4.17(B)(b-i) for $MoSe_2$, both of them presenting IR activity next to E″. These modes exhibit an oscillation pattern similar to E″, where atoms on opposite sides of the crest move in opposite directions. However, both modes appear to curve next to the ripple, with the *E″(x) curving horizontally and the *E″(y) curving vertically. Thus, the oscillation pattern depicted in Figure 4.19, as predicted by the MLFFs, suggests that the ripple induces curvature in the displacement vector fields of S(Se) atoms, particularly near its inflection point. This curvature, visible on the top view of the sketch of both modes, is responsible for the emergence of a dipole moment perpendicular to the axis along which the atoms predominantly move. In the *E″(x) mode, for instance, S(Se) atoms primarily move in the y direction and the curvature introduces a component of the displacement patterns in the x direction while in the *E″(y) mode, the atoms primarily move in the x direction and the curvature is responsible for the component in the y direction. Therefore, the dipole moment component on the primary axis of movement of the atoms is canceled, and the resultant component on its perpendicular axis is due to curvature induced by the ripple. The emergence of a resultant dipole moment of the cell is apparent on the front view of the *E″(x) mode, with all arrows slightly pointing to the right, and on the side view of the *E″(y), with all arrows slightly pointing to the right and other modes with similar displacement patterns but with atoms on opposite sides of the crest move in the direction were found to have no IR activity. Our results for the eigenmodes suggest that this mechanism described for the *E″(x) and *E″(y) modes is consistent with the appearance of the peaks close to the E″ frequency at Figure 4.13 and provides a feasible explanation for them.

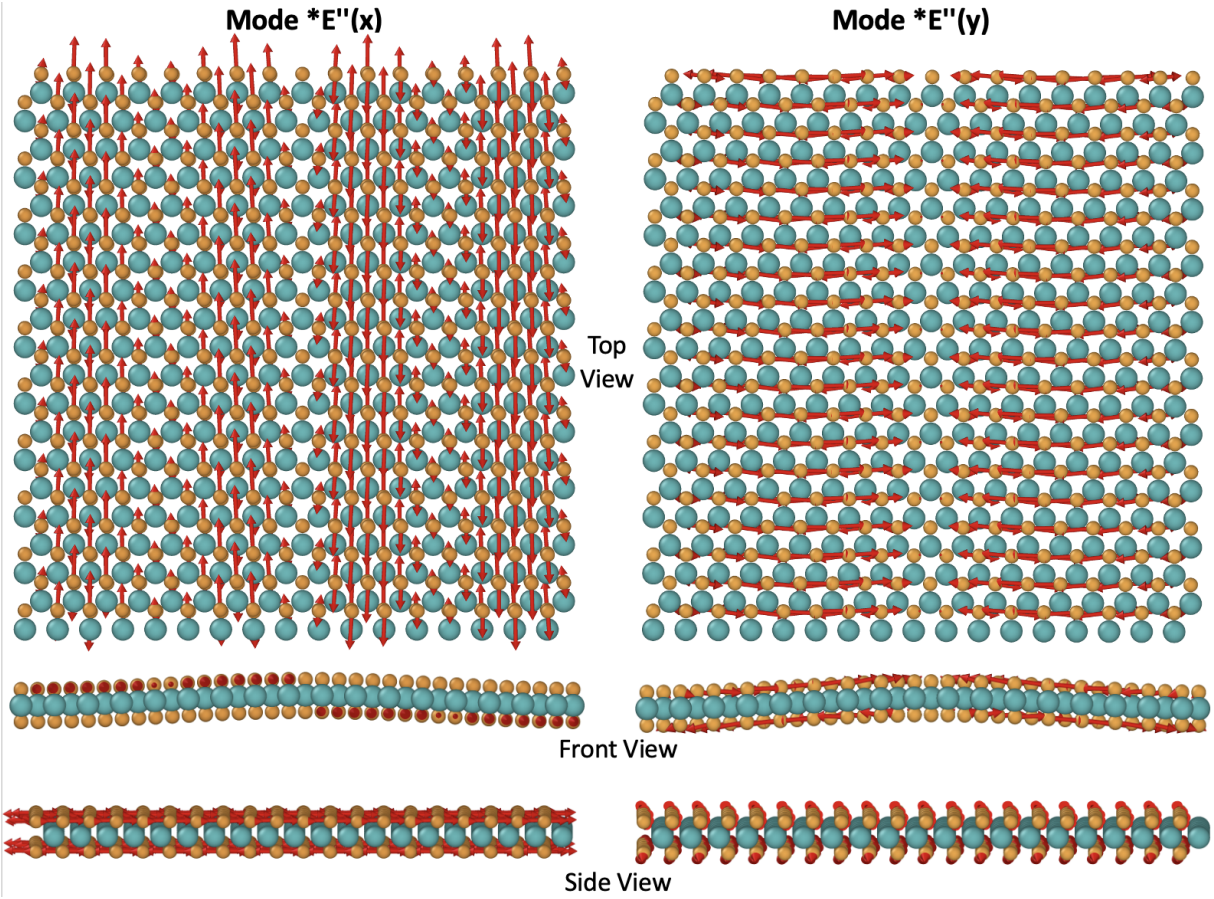

Figure 4.19 – Sketch of the oscillation patterns of the modes *E″(x) and *E″(y) in the rippled cell. The directions of displacements of the S(Se) atoms are indicated by red vectors.

Figure 4.20 illustrates mode *$A_1'(z)$ associated with the red bars in Figure 4.17(A)(b-iii) for MoS_2 and Figure 4.17(B)(b-ii) for $MoSe_2$, indicating their IR activity near A_1'. Displacement vectors are color-coded according to maximum displacement along the z-axis over half oscillation period, with red indicating greater displacement. This mode exhibit an oscillation pattern similar to A_1', with the Mo-layer remaining stationary while the top and bottom S(Se)-layers moving symmetrically. However, upon examining the color of the displacement vectors, it is evident that the bottom layer exhibits larger displacements on average compared to the top layer, resulting in a greater distance from the Mo-layer. This disparity in displacement between the layers can induce a slight modification in the total dipole moment of the cell, thereby generating the observed out-of-plane IR activity depicted in Figure 4.17(A)(b-iii) for MoS_2 and Figure 4.17(B)(b-ii) for $MoSe_2$. Our results for the eigenmodes suggest that this mechanism described for the *$A_1'(z)$ mode is consistent with the appearance of the peaks close to the A_1' frequency at Figure 4.13 and provides a feasible explanation for it. It is noteworthy that several modes exhibiting planar IR activity were identified near the E′ mode in Figure 4.17(A)(b-ii) and near the A_1' mode in Figure 4.17(B)(b-ii). However, since the A_1' frequency is close to the E′ in both compounds, we believe that these peaks were suppressed by the broadening of the E′ mode main blue

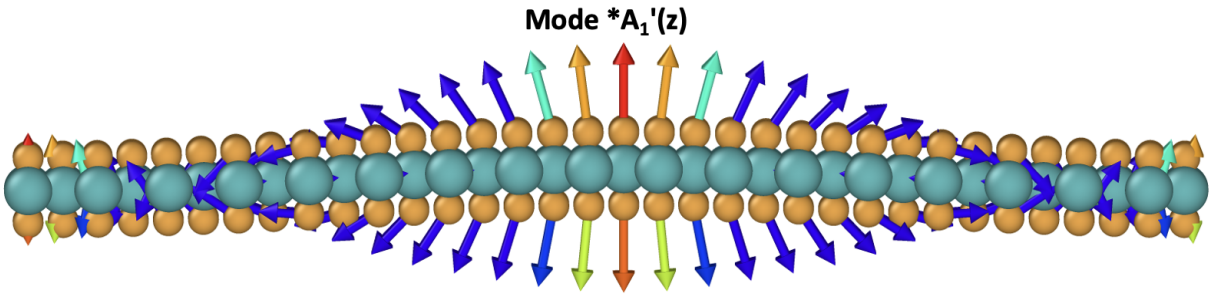

Figure 4.20 – Sketch of the oscillation patterns of the mode $^*A_1'(z)$ in the rippled cell. The directions of displacements along the z-axis of the S(Se) atoms are indicated by vectors and its colors shows the maximum displacement of each during the first half period of oscillation, with the scale increasing from blue to red.

peak in our simulations as shown in Figure 4.13.

Regarding the observation of the peaks shown in Figure 4.13, to the best of our knowledge, there is no experimental evidence explicitly linking rippling to the activation of originally IR-inactive modes in the absorption spectra. However, an important experimental study reported in Ref. [213] used High Resolution Electron Energy Loss Spectroscopy (HREELS) to investigate MoS_2. In HREELS, under dipole scattering conditions, the detected peaks follow the same selection rules as in IR absorption [214]. In that work, a peak was observed near 47.6 meV (384.7 cm^{-1}), which was assigned to the A_1' mode. The presence of this peak has remained unexplained, since the characteristic vibration of the A_1' mode should, in principle, be inactive in such spectra. Our results provide a natural and physically consistent explanation for this experimental observation: the activation of the A_1' mode can be understood as a direct consequence of rippling. This comparison not only reinforces the robustness of our theoretical predictions but also offers new insight into a puzzling experimental feature that had remained unaddressed in the literature. While further experimental confirmation would be valuable, our findings already suggest a reinterpretation of existing HREELS data and highlight the relevance of rippling effects in the vibrational properties of TMDs. To the best of our knowledge, no similar HREELS studies have yet been reported for $MoSe_2$.

4.3 Conclusions

In this work, using machine learning methods, we developed two MLFFs for MoS_2 and $MoSe_2$ that captures their main dynamical properties. We tested its validity by calculating its phonon dispersion and making an accurate correspondence between the structures included in the reference data set and the modes desired to model on MD simulations. With that procedure, we were able to reproduce known experimental dielectric spectra at THz frequencies. To test the performance of the force fields generated in this work, we focused on reproducing results for the peak-frequencies and their redshift due to temperature and

strain, comparing it with well known Stillinger-Weber parametrizations of the respective materials. In general, the phonon dispersion obtained using our MLFF were more accurate than Stillinger-Weber as well the MD results for the IR-active phonon frequencies. For the temperature coefficient, MLFF and SW presented similar capability of recreating experimental results for MoS_2 while for $MoSe_2$ the MLFF has a better performance. For the MoS_2 strain coefficient, SW predicted that the A_2'' mode shows a blueshift, which contradicts other *ab initio* results previously reported. Simulations with MLFF predicted a redshift for the strain coefficient of both infrared active modes, which is in accordance to previous experimental and *ab initio* results.

Furthermore, our simulations reveal the appearance of new low-intensity peaks in the THz dielectric spectra, especially those in proximity to the IR-inactive frequencies E'' and A_1'. MD simulations investigating the height Δz of strained lattices establish a correlation between these emerging peaks and the propagation of thermal ripples, as evidenced by their significant reduction on lattices with smaller Δz. To explore potential explanations for the new observed peaks, we have calculated the eigenfrequencies and eigenmodes of a sine-rippled supercell with wave vector parallel to the zigzag direction using our MLFFs for each compound. The eigenmodes results for the frequencies next to E' and A_2'' with IR activities with inverted polarizations strengths our initial hypothesis suggesting that permitting the layer to undulate frees the modes from oscillating exclusively along their original axis, enabling a component along the perpendicular axis. Moreover, the eigenmodes results for frequencies next to E'' suggests that, according the MLFFs modeled in this work, the ripples induces a curvature on the displacement vector field of the oscillation pattern and this curvature is responsible for the appearance of the peaks related to E'' on the spectra. The reasons for the appearance of such curvature on a rippled layer have not yet been discovered. Finally, the eigenmodes results for frequencies next to A_1' suggests that the resultant dipole moment at z is originated by the disparity of the distance of the top and the bottom layer with respect to the Mo-layer. Our results for the A_1' mode in MoS_2 can be compared with the peak observed near 47.6 meV in HREELS spectra in Ref. [213] and our findings offer a natural and physically consistent interpretation of this experimental feature, attributing the activation of the A_1' mode directly to rippling effects. These results may have far-reaching implications on the understanding of thermal ripples on 2D materials and, after testing the reliability and functionality of the MLFFs, they can be applied to study similar problems related to the phonon properties of MoS_2 and $MoSe_2$.

5 Final Conclusions

The main objective of this thesis was to employ first-principles and data-driven approaches to investigate and predict the properties of materials relevant for energy applications, with a particular focus on thermoelectric and lattice-dynamical phenomena. Two complementary case studies were carried out: the first centered on halide double perovskites, and the second on transition metal dichalcogenides. Together, these studies highlight both the opportunities and challenges of computational materials design, as well as the growing role of machine learning in extending the predictive reach of atomistic simulations.

In Chapter 3, we explored the structural, electronic, and thermoelectric properties of the aluminum-based double perovskites $M_2AgAlBr_6$ (M = K, Rb, Cs) within density functional theory and the Boltzmann transport formalism. The compounds were found to possess direct band gaps in the 2.2–2.3 eV range, a favorable orbital composition at the band edges, and competitive thermoelectric performance, with predicted electronic figures of merit approaching 1.0 near room temperature. These results suggest that such materials combine desirable optoelectronic properties with promising thermoelectric behavior, while also benefiting from low toxicity and elemental abundance.

In Chapter 4, we turned to two-dimensional materials, developing machine learning force fields (MLFFs) for monolayer MoS_2 and $MoSe_2$ trained on DFT reference data. The constructed potentials reproduced phonon dispersions, dielectric spectra, and temperature- and strain-dependent phonon shifts with higher accuracy than conventional Stillinger–Weber parametrizations. Beyond benchmarking, large-scale simulations revealed the emergence of infrared activity in nominally forbidden modes, a phenomenon traced to symmetry breaking induced by thermally activated ripples. These findings underscore the utility of MLFFs for uncovering subtle lattice-dynamical effects that are inaccessible to either conventional force fields or small-scale first-principles simulations.

Taken together, the results presented in this thesis emphasize two central themes. First, chemically simple but environmentally benign materials such as aluminum-based perovskites can achieve performance metrics comparable to established thermoelectrics, thereby broadening the scope of candidate compounds for sustainable technologies. Second, machine learning provides a powerful route to extend the applicability of atomistic simulations, enabling accurate and efficient modeling of complex phenomena in large systems.

Future work may naturally proceed along two directions. On the perovskite side, experimental validation of the predicted transport properties, as well as studies under strain or dimensional confinement, would help assess their practical potential. On the TMD side,

the MLFFs developed here could be applied to investigate nonlinear phonon interactions, thermal transport, or defect-mediated processes in rippled monolayers. More broadly, the approaches demonstrated in this thesis illustrate how combining first-principles accuracy with machine learning efficiency can accelerate the discovery and understanding of functional materials.

Bibliography

[1] Viswanathan, Balasubramanian, V Suryakumar, B Venugopal e Hariprasad Narayanan: *PEROVSKITE MATERIALS-AN INTRODUCTION*. National Centre for Catalysis Research, abril 2023. Citado na página 15.

[2] Suter, Eric: *Ab initio studies of dopant-defect complexes in $KNbO_3$*. Tese de Doutoramento, University of Georgia, 2022. Citado na página 15.

[3] Stranks, S., G. Eperon, G. Grancini, C. Menelaou, M. Alcocer, T. Leijtens, L. Herz, A. Petrozza e J. Henry: *Snaith Electron-Hole Diffusion Lengths Exceeding 1 Micrometer in an Organometal Trihalide Perovskite Absorber*. Science, 342:341–344, 2013. Citado 2 vezes nas páginas 15 e 17.

[4] Gao, W., Y. Zhu, Y. Wang, G. Yuan e J. A Liu: *review of flexible perovskite oxide ferroelectric films and their application*. Journal Of Materiomics, 6:1–16, 2020. Citado na página 15.

[5] Jaffe, B., R. Roth e S. Marzullo: *Piezoelectric properties of lead zirconate-lead titanate solid-solution ceramics*. J. Appl. Phys, 25:809–810, 1954. Citado na página 16.

[6] Saito, Y., H. Takao, T. Tani, T. Nonoyama, K. Takatori, T. Homma, T. Nagaya e M. Nakamura: *Lead-free piezoceramics*. Nature, 432:84–87, 2004. Citado na página 16.

[7] Liu, H. e X. A Yang: *brief review on perovskite multiferroics*. Ferroelectrics, 507:69–85, 2017. Citado na página 16.

[8] Stahn, J., J. Chakhalian, Ch. Niedermayer, J. Hoppler, T. Gutberlet, J. Voigt, F. Treubel, H U. Habermeier, G. Cristiani, B. Keimer e C. Bernhard: *Magnetic proximity effect in perovskite superconductor/ferromagnet multilayers*. Phys. Rev. B, 71:140509, Apr 2005. `https://link.aps.org/doi/10.1103/PhysRevB.71.140509`. Citado na página 16.

[9] De Paoli, Alessandra e Antonello A. Barresi: *Deep Oxidation Kinetics of Trieline over LaFeO3 Perovskite Catalyst*. Industrial & Engineering Chemistry Research, 40(6):1460–1464, 2001. Citado na página 16.

[10] Goldschmidt, Victor Moritz: *Die gesetze der krystallochemie*. Naturwissenschaften, 14(21):477–485, 1926. Citado na página 16.

[11] Zhang, Huan, Na Li, Keyan Li e Dongfeng Xue: *Structural stability and formability of ABO_3-type perovskite compounds*. Acta Crystallographica Section B, 63(6):812–818, Dec 2007. Citado na página 16.

[12] Liu, Yucheng, Zhou Yang e Shengzhong (Frank) Liu: *Recent Progress in Single-Crystalline Perovskite Research Including Crystal Preparation, Property Evaluation, and Applications*. Advanced Science, 5(1):1700471, 2018. `https://advanced.onlinelibrary.wiley.com/doi/abs/10.1002/advs.201700471`. Citado na página 16.

[13] Shao, Yan, Wei Gao, Hejin Yan, Runlai Li, Ibrahim Abdelwahab, Xiao Chi, Lukas Rogée, Lyuchao Zhuang, Wei Fu, Shu Ping Lau *et al.*: *Unlocking surface octahedral tilt in two-dimensional Ruddlesden-Popper perovskites*. Nature communications, 13(1):138, 2022. Citado na página 16.

[14] Kojima, A., K. Teshima, Y. Shirai e T. Miyasaka: *Organometal Halide Perovskites as Visible-Light Sensitizers for Photovoltaic Cells*. J. Am. Chem. Soc, 131:6050–6051, 2009. Citado na página 17.

[15] Yoo, J., G. Seo, M. Chua, T. Park, Y. Lu, F. Rotermund, Y. Kim, C. Moon, N. Jeon, J. Correa-Baena e Others Efficient: *perovskite solar cells via improved carrier management*. Nature, 590:587–593, 2021. Citado na página 17.

[16] Wu, T. e P. Gao: *Development of perovskite-type materials for thermoelectric application*. Materials, 11:999, 2018. Citado na página 17.

[17] Hu, S., Z. Ren, A. Djurišić e A. Rogach: *Metal Halide Perovskites as Emerging Thermoelectric Materials*. ACS Energy Lett, 6:3882–3905, 2021. Citado na página 17.

[18] Hsu, S., W. Zhao, Y. Gao, Segovia Akriti, Xu M. e Boudouris X.: *B. & Dou, L.* Thermoelectric Performance of Lead-Free Two-Dimensional Halide Perovskites Featuring Conjugated Ligands., 21:7839–7844, 2021. Citado na página 17.

[19] Yokoyama, T., D. Cao, C. Stoumpos, T. Song, Y. Sato, S. Aramaki e M. Kanatzidis: *Overcoming Short-Circuit in Lead-Free $CH_3NH_3SnI_3$ Perovskite Solar Cells via Kinetically Controlled Gas–Solid Reaction Film Fabrication Process*. J. Phys. Chem. Lett, 7:776–782, 2016. Citado na página 17.

[20] Cui, Xiaxia, Junjun Jin, Qidong Tai e Feng Yan: *Recent Progress on the Phase Stabilization of FAPbI3 for High-Performance Perovskite Solar Cells*. Solar RRL, 6(10):2200497, 2022. `https://onlinelibrary.wiley.com/doi/abs/10.1002/solr.202200497`. Citado na página 17.

[21] Volonakis, G., M. Filip, A. Haghighirad, N. Sakai, B. Wenger, H. Snaith e F. Giustino: *Lead-Free Halide Double Perovskites via Heterovalent Substitution of Noble Metals*. J. Phys. Chem. Lett, 7:1254–1259, 2016. Citado na página 17.

[22] Gao, Yuting, Yufeng Pan, Feng Zhou, Guangda Niu e Chunjie Yan: *Lead-free halide perovskites: a review of the structure–property relationship and applications in light emitting devices and radiation detectors*. J. Mater. Chem. A, 9:11931–11943, 2021. `http://dx.doi.org/10.1039/D1TA01737C`. Citado na página 17.

[23] Ghosh, Sukanya, Hari Shankar e Prasenjit Kar: *Recent developments of lead-free halide double perovskites: a new superstar in the optoelectronic field*. Mater. Adv., 3:3742–3765, 2022. Citado na página 17.

[24] Kumar, Venkatramanan, Arunkumar Kathiravan e Mariadoss Asha Jhonsi: *Beyond lead halide perovskites: Crystal structure, bandgaps, photovoltaic properties and future stance of lead-free halide double perovskites*. Nano Energy, 125:109523, 2024, ISSN 2211-2855. Citado na página 17.

[25] De Souza, G., V. Nascimento, R. De Paiva e A. Rappe: *Thermoelectric properties of M2AgAlBr6 (M = K, Rb, Cs) double perovskites: A first principles study*. Solid State Communications, 378, 2024. Citado na página 18.

[26] Igbari, F., R. Wang, Z. Wang, X. Ma, Q. Wang, K. Wang, Y. Zhang, L. Liao e Y. Yang: *Composition Stoichiometry of $Cs_2AgBiBr_6$ Films for Highly Efficient Lead-Free Perovskite Solar Cells*. Nano Lett, 19:2066–2073, 2019. Citado na página 17.

[27] Filip, M., S. Hillman, A. Haghighirad, H. Snaith e F. Giustino: *Band Gaps of the Lead-Free Halide Double Perovskites $Cs_2BiAgCl_6$ and $Cs_2BiAgBr_6$ from Theory and Experiment*. J. Phys. Chem Lett, 7:2579–2585, 2016. Citado na página 17.

[28] Ji, F., J. Klarbring, F. Wang, W. Ning, L. Wang, C. Yin, J. Figueroa, C. Christensen, M. Etter, T. Ederth, L. Sun, S. Simak, I. Abrikosov e F. Gao: *Lead-Free Halide Double Perovskite $Cs_2AgBiBr_6$ with Decreased Band Gap*. Angew. Chem. Int. Ed, 59:15191–15194, 2020. Citado na página 17.

[29] Chen, H., C. Zhang, Z. Liu, J. Gong, W. Wang, Y. Wu e H. Chen: *Vacancy defects on optoelectronic properties of double perovskite $Cs_2AgBiBr_6$*. Mater. Sci. Semicond. Process, 123, 2021. Citado na página 17.

[30] Gao, W., C. Ran, J. Xi, B. Jiao, W. Zhang, M. Wu, X. Hou e Z. Wu: *High-Quality $Cs_2AgBiBr_6$ Double Perovskite Film for Lead-Free Inverted Planar Heterojunction Solar Cells with 2.2 % Efficiency*. ChemPhysChem, 19:1696–1700, 2018. Citado na página 17.

[31] Dong, L., S. Sun, Z. Deng, W. Li, F. Wei, Y. Qi, Y. Li, X. Li, P. Lu e U. Ramamurty: *Elastic properties and thermal expansion of lead-free halide double perovskite $Cs_2AgBiBr_6$*. Comput. Mater. Sci, 141:49–58, 2018. Citado na página 17.

[32] Xiao, Z., W. Meng, J. Wang e Y. Yan: *Thermodynamic Stability and Defect Chemistry of Bismuth-Based Lead-Free Double Perovskites*. ChemSusChem, 9:2628–2633, 2016. Citado na página 17.

[33] Zhou, J., X. Rong, M. Molokeev, X. Zhang e Z. Xia: *Exploring the transposition effects on the electronic and optical properties of $Cs_2AgSbCl_6$ via a combined computational-experimental approach*. J. Mater. Chem. A, 6:2346–2352, 2018. Citado na página 17.

[34] Tran, T., J. Panella, J. Chamorro, J. Morey e T. McQueen: *Designing indirect–direct bandgap transitions in double perovskites*. Mater. Horiz, 4:688–693, 2017. Citado na página 17.

[35] Wei, F., Z. Deng, S. Sun, N. Hartono, H. Seng, T. Buonassisi, P. Bristowe e A. Cheetham: *Enhanced visible light absorption for lead-free double perovskite $Cs_2AgSbBr_6$*. Chem. Commun, 55:3721–3724, 2019. Citado na página 17.

[36] Yu, G., S. Xue, R. Yin, Q. Wu, T. Gao, Y. Song, R. Wang, W. Cong, C. Guan e Y. Lu: *How the Copper Dopant Alters the Geometric and Photoelectronic Properties of the Lead-Free $Cs_2AgSbCl_6$ Double Perovskite*. Adv. Theory Simul, 4, 2021. Citado na página 17.

[37] Zhao, X., J. Yang, Y. Fu, D. Yang, Q. Xu, L. Yu, S. Wei e L. Zhang: *Design of Lead-Free Inorganic Halide Perovskites for Solar Cells via Cation-Transmutation*. J. Am. Chem. Soc, 139:2630–2638, 2017. Citado na página 17.

[38] Volonakis, George, Amir Abbas Haghighirad, Rebecca L. Milot, Weng H. Sio, Marina R. Filip, Bernard Wenger, Michael B. Johnston, Laura M. Herz, Henry J. Snaith e Feliciano Giustino: *Cs2InAgCl6: A New Lead-Free Halide Double Perovskite with Direct Band Gap*. The Journal of Physical Chemistry Letters, 8(4):772–778, 2017. Citado na página 17.

[39] Rodrigues, J., C. Escanhoela, B. Fragoso, G. Sombrio e M. Ferrer: *Álvarez-Galván, C., Fernández-Díaz, M., Souza, J., Ferreira, F., Pecharromán, C. & Alonso, J.* Experimental and Theoretical Investigations on the Structural, Electronic, and Vibrational Properties of $Cs_2AgSbCl_6$ Double Perovskite, 60:18918–18928, 2021. Citado na página 17.

[40] Tress, W. e M. Sirtl: *$Cs_2AgBiBr_6$ Double Perovskites as Lead-Free Alternatives for Perovskite Solar Cells?* Sol. RRL, 6, 2022. Citado na página 17.

[41] Liu, M., G. Zhong, Y. Yin, J. Miao, K. Li, C. Wang, X. Xu, C. Shen e H. Meng: *Aluminum-Doped Cesium Lead Bromide Perovskite Nanocrystals with Stable Blue*

Photoluminescence Used for Display Backlight. Adv. Sci, 4:1700335, 2017. Citado na página 18.

[42] Groszewicz, P., L. Koch, S. Steiner, A. Ayrikyan, K. Webber, T. Fr"omling, K. Albe e G. Buntkowsky: *The fate of aluminium in (Na,Bi)TiO_3-based ionic conductors*. J. Mater. Chem. A, 8:18188–18197, 2020. Citado na página 18.

[43] Li, L., H. Shao, X. Wu, W. Chen, J. Zhu, B. Dong, L. Xu, W. Xu, J. Hu, M. Zhou, Y. Ji, H. Song e X. Bai: *Aluminum-doped lead-free double perovskite $Cs_2AgBiCl_6$ nanocrystals with ultrahigh stability towards white light emitting diodes*. Mater. Res. Bull, 147:111645, 2022. Citado na página 18.

[44] Ghosh, S. e A. Sil: *Enhancement of photoresponse property of perovskite solar cell by aluminium chloride ($AlCl_3$)*. Semicond. Sci. Technol, 33:055002, 2018. Citado na página 18.

[45] Tang, T., X. Zhao, D. Hu, Q. Liang, X. Wei e Y. Tang: *Theoretical exploration of mechanical, electronic structure and optical properties of aluminium based double halide perovskite*. RSC Adv, 12:10209–10218, 2022. Citado 2 vezes nas páginas 18 e 96.

[46] Haq, A., T. Ahmad, M. Amin, A. Bakar, A. Afaq, N. Ehsan, S. Ramay e A. A Siddig: *first principle investigation of electronic, mechanical, optical and transport properties of A_2AgAlI_6(A = Rb, K, Na) for energy harvesting*. Phys. Scr, 98:115972, 2023. Citado na página 18.

[47] Wolf, Nathan R., Bridget A. Connor, Adam H. Slavney e Hemamala I. Karunadasa: *Doubling the Stakes: The Promise of Halide Double Perovskites*. Angewandte Chemie International Edition, 60(30):16264–16278, 2021. Citado na página 19.

[48] Ghorbani-Asl, Mahdi: *Electronic transport through two-dimensional transition-metal chalcogenides*. Tese de Doutoramento, Jacobs University, setembro 2014. Citado 2 vezes nas páginas 20 e 21.

[49] Margulis, L, G Salitra e Reshef Tenne: *Nested fullerene-like structures*. Nature, 365(6442):113–114, 1993. Citado na página 20.

[50] Tenne, Reshef, L Margulis, M ea Genut e Gary Hodes: *Polyhedral and cylindrical structures of tungsten disulphide*. Nature, 360(6403):444–446, 1992. Citado na página 20.

[51] Van Baren, Jeremiah, Gaihua Ye, Jia An Yan, Zhipeng Ye, Pouyan Rezaie, Peng Yu, Zheng Liu, Rui He e Chun Hung Lui: *Stacking-dependent interlayer phonons in 3R and 2H MoS2*. 2D Materials, 6(2):025022, 2019. Citado na página 20.

[52] Mak, Kin Fai, Changgu Lee, James Hone, Jie Shan e Tony F. Heinz: *Atomically Thin* MoS_2*: A New Direct-Gap Semiconductor*. Phys. Rev. Lett., 105:136805, Sep 2010. Citado na página 22.

[53] Ugeda, Miguel M, Aaron J Bradley, Su Fei Shi, Felipe H Da Jornada, Yi Zhang, Diana Y Qiu, Wei Ruan, Sung Kwan Mo, Zahid Hussain, Zhi Xun Shen *et al.*: *Giant bandgap renormalization and excitonic effects in a monolayer transition metal dichalcogenide semiconductor*. Nature materials, 13(12):1091–1095, 2014. Citado na página 22.

[54] Chhowalla, Manish, Hyeon Suk Shin, Goki Eda, Lain Jong Li, Kian Ping Loh e Hua Zhang: *The chemistry of two-dimensional layered transition metal dichalcogenide nanosheets*. Nature chemistry, 5(4):263–275, 2013. Citado na página 22.

[55] Miró, Pere, Martha Audiffred e Thomas Heine: *An atlas of two-dimensional materials*. Chemical Society Reviews, 43(18):6537–6554, 2014. Citado na página 22.

[56] Xu, Mingsheng, Tao Liang, Minmin Shi e Hongzheng Chen: *Graphene-like two-dimensional materials*. Chemical reviews, 113(5):3766–3798, 2013. Citado na página 22.

[57] Li, Hai, Jumiati Wu, Zongyou Yin e Hua Zhang: *Preparation and Applications of Mechanically Exfoliated Single-Layer and Multilayer MoS2 and WSe2 Nanosheets*. Accounts of Chemical Research, 47(4):1067–1075, 2014. PMID: 24697842. Citado na página 22.

[58] Frindt, RF: *Single crystals of MoS2 several molecular layers thick*. Journal of Applied Physics, 37(4):1928–1929, 1966. Citado na página 22.

[59] Coleman, Jonathan N, Mustafa Lotya, Arlene O'Neill, Shane D Bergin, Paul J King, Umar Khan, Karen Young, Alexandre Gaucher, Sukanta De, Ronan J Smith *et al.*: *Two-dimensional nanosheets produced by liquid exfoliation of layered materials*. Science, 331(6017):568–571, 2011. Citado na página 22.

[60] Huo, Chengxue, Zhong Yan, Xiufeng Song e Haibo Zeng: *2D materials via liquid exfoliation: a review on fabrication and applications*. Science Bulletin, 60(23):1994–2008, 2015, ISSN 2095-9273. Citado na página 22.

[61] Zhan, Yongjie, Zheng Liu, Sina Najmaei, Pulickel M Ajayan e Jun Lou: *Large area vapor phase growth and characterization of MoS2 atomic layers on SiO2 substrate*. arXiv preprint arXiv:1111.5072, 2011. Citado na página 22.

[62] Giessibl, Franz J.: *Advances in atomic force microscopy*. Rev. Mod. Phys., 75:949–983, Jul 2003. `https://link.aps.org/doi/10.1103/RevModPhys.75.949`. Citado na página 22.

[63] Ferrari, AC e DM Basko: *Nat. Nanotechnol.* Nat. Nanotechnol., 8:235–246, 2013. Citado na página 22.

[64] Chhowalla, Manish, Zhongfan Liu e Hua Zhang: *Two-dimensional transition metal dichalcogenide (TMD) nanosheets.* Chem. Soc. Rev., 44:2584–2586, 2015. Citado na página 22.

[65] Chen, Jun, Nobuhiro Kuriyama, Huatang Yuan, Hiroyuki T Takeshita e Tetsuo Sakai: *Electrochemical hydrogen storage in MoS2 nanotubes.* Journal of the American Chemical Society, 123(47):11813–11814, 2001. Citado na página 22.

[66] Molina-Sánchez, Alejandro, Kerstin Hummer e Ludger Wirtz: *Vibrational and optical properties of MoS2: From monolayer to bulk.* Surface Science Reports, 70(4):554–586, 2015, ISSN 0167-5729. Citado na página 22.

[67] Jariwala, Deep, Vinod K Sangwan, Lincoln J Lauhon, Tobin J Marks e Mark C Hersam: *Emerging device applications for semiconducting two-dimensional transition metal dichalcogenides.* ACS nano, 8(2):1102–1120, 2014. Citado na página 22.

[68] Sangwan, Vinod K, Hong Sub Lee, Hadallia Bergeron, Itamar Balla, Megan E Beck, Kan Sheng Chen e Mark C Hersam: *Multi-terminal memtransistors from polycrystalline monolayer molybdenum disulfide.* Nature, 554(7693):500–504, 2018. Citado na página 22.

[69] Ramasubramaniam, Ashwin: *Large excitonic effects in monolayers of molybdenum and tungsten dichalcogenides.* Phys. Rev. B, 86:115409, Sep 2012. Citado na página 22.

[70] Li, Yilei, Alexey Chernikov, Xian Zhang, Albert Rigosi, Heather M. Hill, Arend M. van der Zande, Daniel A. Chenet, En Min Shih, James Hone e Tony F. Heinz: *Measurement of the optical dielectric function of monolayer transition-metal dichalcogenides:* MoS_2*,* $MoSe_2$*,* WS_2*, and* WSe_2. Phys. Rev. B, 90:205422, Nov 2014. Citado na página 22.

[71] Wang, Xiaonan e Alireza Tabarraei: *Phonon thermal conductivity of monolayer MoS2.* Applied Physics Letters, 108(19):191905, maio 2016, ISSN 0003-6951. Citado na página 22.

[72] Mermin, N. D.: *Crystalline Order in Two Dimensions.* Phys. Rev., 176:250–254, Dec 1968. `https://link.aps.org/doi/10.1103/PhysRev.176.250`. Citado na página 23.

[73] Nelson, D., T. Piran e S. Weinberg: *Statistical Mechanics Of Membranes And Surfaces: 2nd Edition.* World Scientific Publishing Company, 2004, ISBN 9789814483223. `https://books.google.com/books?id=nQrJCgAAQBAJ`. Citado na página 23.

[74] Fasolino, Annalisa, JH Los e Mikhail I Katsnelson: *Intrinsic ripples in graphene*. Nature materials, 6(11):858–861, 2007. Citado na página 23.

[75] Meyer, Jannik C, Andre K Geim, Mikhail I Katsnelson, Konstantin S Novoselov, Tim J Booth e Siegmar Roth: *The structure of suspended graphene sheets*. Nature, 446(7131):60–63, 2007. Citado na página 23.

[76] Brivio, Jacopo, Duncan T. L. Alexander e Andras Kis: *Ripples and Layers in Ultrathin MoS2 Membranes*. Nano Letters, 11(12):5148–5153, 2011. PMID: 22010987. Citado 2 vezes nas páginas 23 e 120.

[77] Anees, P., M. C. Valsakumar e B. K. Panigrahi: *Delineating the role of ripples on the thermal expansion of 2D honeycomb materials: graphene, 2D h-BN and monolayer (ML)-MoS2*. Phys. Chem. Chem. Phys., 19:10518–10526, 2017. Citado na página 24.

[78] Li, Songge, Yun Peng Wang, Shoucong Ning, Kai Xu, Sokrates T. Pantelides, Wu Zhou e Junhao Lin: *Revealing 3D Ripple Structure and Its Dynamics in Freestanding Monolayer MoSe2 by Single-Frame 2D Atomic Image Reconstruction*. Nano Letters, 23(4):1298–1305, 2023. PMID: 36779843. Citado na página 24.

[79] Sholl, D. S. e J. A. Steckel: *Density Functional Theory: A Practical Introduction*. John Wiley & Sons, Ltd, 2009, ISBN 9780470447710. Citado na página 26.

[80] Born, Max e Robert Oppenheimer: *On the quantum theory of molecules*. Em *Quantum Chemistry: Classic Scientific Papers*, páginas 1–24. World Scientific, 2000. Citado na página 27.

[81] Nakashima, Hiroyuki e Hiroshi Nakatsuji: *Solving the Schrödinger equation for helium atom and its isoelectronic ions with the free iterative complement interaction (ICI) method*. The Journal of Chemical Physics, 127(22):224104, dezembro 2007. Citado na página 27.

[82] Pachucki, Krzysztof: *Born-Oppenheimer potential for* H_2. Phys. Rev. A, 82:032509, Sep 2010. Citado na página 27.

[83] Giustino, F.: *Materials Modelling Using Density Functional Theory: Properties and Predictions*, capítulo 2. Oxford University Press, 2014, ISBN 9780199662449. Citado na página 29.

[84] Hohenberg, P. e W. Kohn: *Inhomogeneous Electron Gas*. Phys. Rev., 136:B864–B871, Nov 1964. `https://link.aps.org/doi/10.1103/PhysRev.136.B864`. Citado na página 32.

[85] Kohn, W. e L. J. Sham: *Self-Consistent Equations Including Exchange and Correlation Effects*. Phys. Rev., 140:A1133–A1138, Nov 1965. `https://link.aps.org/doi/10.1103/PhysRev.140.A1133`. Citado na página 33.

[86] Perdew, J. P. e Alex Zunger: *Self-interaction correction to density-functional approximations for many-electron systems*. Phys. Rev. B, 23:5048–5079, May 1981. Citado na página 35.

[87] Perdew, J., K. Burke e M. Ernzerhof: *Generalized gradient approximation made simple*. Phys. Rev. Lett, 77:3865, 1996. Citado na página 35.

[88] Giustino, F.: *Materials Modelling Using Density Functional Theory: Properties and Predictions*, capítulo 3. Oxford University Press, 2014, ISBN 9780199662449. Citado na página 36.

[89] Ceperley, D. M. e B. J. Alder: *Ground State of the Electron Gas by a Stochastic Method*. Phys. Rev. Lett., 45:566–569, Aug 1980. `https://link.aps.org/doi/10.1103/PhysRevLett.45.566`. Citado 2 vezes nas páginas 36 e 37.

[90] Wigner, E.: *On the Interaction of Electrons in Metals*. Phys. Rev., 46:1002–1011, Dec 1934. `https://link.aps.org/doi/10.1103/PhysRev.46.1002`. Citado na página 36.

[91] Hung, Nguyen, Ahmad Nugraha e Riichiro Saito: *Quantum ESPRESSO Course for Solid-State Physics*. Jenny Stanford Publishing, novembro 2022, ISBN 9781003290964. Citado na página 38.

[92] Perdew, John P., J. A. Chevary, S. H. Vosko, Koblar A. Jackson, Mark R. Pederson, D. J. Singh e Carlos Fiolhais: *Atoms, molecules, solids, and surfaces: Applications of the generalized gradient approximation for exchange and correlation*. Phys. Rev. B, 46:6671–6687, Sep 1992. `https://link.aps.org/doi/10.1103/PhysRevB.46.6671`. Citado na página 38.

[93] Heyd, J., G. Scuseria e M. Ernzerhof: *Hybrid functionals based on a screened Coulomb potential*. J. Chem. Phys, 118:8207–8215, 2003. Citado na página 39.

[94] Monkhorst, Hendrik J e James D Pack: *Special points for Brillouin-zone integrations*. Physical review B, 13(12):5188, 1976. Citado na página 41.

[95] Hamann, D. R.: *Optimized norm-conserving Vanderbilt pseudopotentials*. Phys. Rev. B, 88:085117, Aug 2013. Citado na página 43.

[96] Schlipf, Martin e François Gygi: *Optimization algorithm for the generation of ONCV pseudopotentials*. Computer Physics Communications, 196:36–44, 2015, ISSN 0010-4655. Citado na página 43.

[97] Rappe, Andrew M., Karin M. Rabe, Efthimios Kaxiras e J. D. Joannopoulos: *Optimized pseudopotentials*. Phys. Rev. B, 41:1227–1230, Jan 1990. `https://link.aps.org/doi/10.1103/PhysRevB.41.1227`. Citado na página 43.

[98] Ramer, Nicholas J. e Andrew M. Rappe: *Designed nonlocal pseudopotentials for enhanced transferability*. Phys. Rev. B, 59:12471–12478, May 1999. `https://link.aps.org/doi/10.1103/PhysRevB.59.12471`. Citado na página 43.

[99] Vanderbilt, David: *Soft self-consistent pseudopotentials in a generalized eigenvalue formalism*. Phys. Rev. B, 41:7892–7895, Apr 1990. `https://link.aps.org/doi/10.1103/PhysRevB.41.7892`. Citado na página 43.

[100] Garrity, Kevin F., Joseph W. Bennett, Karin M. Rabe e David Vanderbilt: *Pseudopotentials for high-throughput DFT calculations*. Computational Materials Science, 81:446–452, 2014, ISSN 0927-0256. `https://www.sciencedirect.com/science/article/pii/S0927025613005077`. Citado na página 43.

[101] Giannozzi, Paolo, Stefano Baroni, Nicola Bonini, Matteo Calandra, Roberto Car, Carlo Cavazzoni, Davide Ceresoli, Guido L Chiarotti, Matteo Cococcioni, Ismaila Dabo, Andrea Dal Corso, Stefano de Gironcoli, Stefano Fabris, Guido Fratesi, Ralph Gebauer, Uwe Gerstmann, Christos Gougoussis, Anton Kokalj, Michele Lazzeri, Layla Martin-Samos, Nicola Marzari, Francesco Mauri, Riccardo Mazzarello, Stefano Paolini, Alfredo Pasquarello, Lorenzo Paulatto, Carlo Sbraccia, Sandro Scandolo, Gabriele Sclauzero, Ari P Seitsonen, Alexander Smogunov, Paolo Umari e Renata M Wentzcovitch: *QUANTUM ESPRESSO: a modular and open-source software project for quantum simulations of materials*. Journal of Physics: Condensed Matter, 21(39):395502, sep 2009. Citado na página 43.

[102] Ziman, J.: *Electrons and Phonons: The Theory of Transport Phenomena in Solids*. Oxford University Press, 2001. Citado na página 44.

[103] Ziman, J.: *Principles of the Theory of Solids. (Cambridge University Press*. Cambridge University Press, 1972. Citado na página 49.

[104] Brennan, K. F.: *Nonequilibrium statistical Mechanics*. Em *The Physics of Semiconductors: With Applications to Optoelectronic Devices*, páginas 323–357. Cambridge University Press, chapter, Cambridge, 1999. Citado na página 49.

[105] Wang, Q., L. Han, L. Wu, T. Zhang, S. Li e P. Lu: *Strain effect on thermoelectric performance of InSe monolayer*. Nanoscale Res. Lett, 14:287, 2019. Citado na página 52.

[106] Yang, K., S. Cahangirov, A. Cantarero, A. Rubio e R. D'Agosta: *Thermoelectric properties of atomically thin silicene and germanene nanostructures*. Phys. Rev. B, 89:125403, Mar 2014. Citado na página 52.

[107] Huang, W., H. Da e G. Liang: *Thermoelectric performance of MX2 (M=Mo, W; X= S, Se) monolayers*. Journal of Applied Physics, 113:10, 2013. Citado na página 52.

[108] al., Duck Young Chung: *Complex bismuth chalcogenides as thermoelectrics*. Em 97., Xvi Ict (editor): *97. Proceedings ICT*, páginas 459–462, Dresden, Germany, 1997. 16th International Conference on Thermoelectrics (Cat. No.97TH8291). Citado na página 52.

[109] Venkatasubramanian, R., E. Siivola, T. Colpitts *et al.*: *Thin-film thermoelectric devices with high room-temperature figures of merit*. Nature, 413:597–602, 2001. Citado na página 52.

[110] Zhao, LD., SH. Lo, Y. Zhang *et al.*: *Ultralow thermal conductivity and high thermoelectric figure of merit in SnSe crystals*. Nature, 508:373–377, 2014. Citado na página 52.

[111] Hinterleitner, B., I. Knapp, M. Poneder *et al.*: *Thermoelectric performance of a metastable thin-film Heusler alloy*. Nature, 576:85–90, 2019. Citado na página 52.

[112] Lee, J., J. Wu e J. Grossman: *Enhancing the thermoelectric power factor with highly mismatched isoelectronic dopagem*. Phys. Rev. Lett, 104:016602, 2010. Citado na página 52.

[113] Ioffe, .F.: *Semiconductor Thermoelements, and Thermoelectric Cooling*. Infosearch, Limited, 1957. Citado na página 52.

[114] Liebl, Johannes, Stephan Neugebauer, Andreas Eder, Matthias Linde, Boris Mazar e Wolfgang Stütz: *The thermoelectric generator from BMW is making use of waste heat*. MTZ worldwide, 70(4):4–11, 2009. Citado na página 52.

[115] Madsen, G. e D. BoltzTraP. A Singh: *code for calculating band-structure dependent quantities*. Comput. Phys. Commun, 175:67–71, 2006. Citado na página 52.

[116] Taflove, Allen: *Application of the Finite-Difference Time-Domain Method to Sinusoidal Steady-State Electromagnetic-Penetration Problems*. IEEE Transactions on Electromagnetic Compatibility, EMC-22(3):191–202, 1980. Citado na página 53.

[117] Landau, David P. e Kurt Binder: *A Guide to Monte Carlo Simulations in Statistical Physics*. Cambridge University Press, 4ª edição, 2014. Citado na página 53.

[118] Allen, Michael P. e Dominic J. Tildesley: *Computer Simulation of Liquids*. Oxford University Press, junho 2017, ISBN 9780198803195. Citado na página 53.

[119] Rapaport, D. C.: *The Art of Molecular Dynamics Simulation*. Cambridge University Press, 2ª edição, 2004. Citado na página 53.

[120] Goldstein, H.: *Classical Mechanics*. Pearson Education, 2002, ISBN 9788177582833. Citado 2 vezes nas páginas 53 e 73.

[121] Snook, I.: *The Langevin and Generalised Langevin Approach to the Dynamics of Atomic, Polymeric and Colloidal Systems*. Elsevier Science, 2006, ISBN 9780080467924. `https://books.google.com.br/books?id=_XWJGs75oIwC`. Citado na página 54.

[122] Caillol, J. M., D. Levesque e J. J. Weis: *Theoretical calculation of ionic solution properties*. The Journal of Chemical Physics, 85(11):6645–6657, dezembro 1986, ISSN 0021-9606. Citado na página 55.

[123] Kittel, C.: *Introduction to Solid State Physics*. Wiley, 2004, ISBN 9780471415268. Citado na página 57.

[124] Rahman, A.: *Correlations in the Motion of Atoms in Liquid Argon*. Phys. Rev., 136:A405–A411, Oct 1964. Citado na página 57.

[125] Hancock, Steven Bennett: *Langevin Dynamics/Monte Carlo Simulations of Dielectric Properties of Materials*. Tese de Doutoramento, University of Georgia, 2023. Citado na página 58.

[126] Stillinger, Frank H. e Thomas A. Weber: *Computer simulation of local order in condensed phases of silicon*. Phys. Rev. B, 31:5262–5271, Apr 1985. Citado 2 vezes nas páginas 58 e 59.

[127] Tersoff, J.: *New empirical approach for the structure and energy of covalent systems*. Phys. Rev. B, 37:6991–7000, Apr 1988. Citado na página 60.

[128] Jorgensen, William L., Jayaraman Chandrasekhar, Jeffry D. Madura, Roger W. Impey e Michael L. Klein: *Comparison of simple potential functions for simulating liquid water*. The Journal of Chemical Physics, 79(2):926–935, julho 1983, ISSN 0021-9606. Citado na página 60.

[129] Braun, Daniel, Stefan Boresch e Othmar Steinhauser: *Transport and dielectric properties of water and the influence of coarse-graining: Comparing BMW, SPC/E, and TIP3P models*. The Journal of Chemical Physics, 140(6):064107, fevereiro 2014, ISSN 0021-9606. Citado na página 60.

[130] Höchtl, Peter, Stefan Boresch, Wolfgang Bitomsky e Othmar Steinhauser: *Rationalization of the dielectric properties of common three-site water models in terms of their force field parameters*. The Journal of Chemical Physics, 109(12):4927–4937, setembro 1998, ISSN 0021-9606. Citado na página 60.

[131] Daw, Murray S. e M. I. Baskes: *Embedded-atom method: Derivation and application to impurities, surfaces, and other defects in metals.* Phys. Rev. B, 29:6443–6453, Jun 1984. Citado na página 60.

[132] Vashishta, P., Rajiv K. Kalia, José P. Rino e Ingvar Ebbsjö: *Interaction potential for* SiO_2*: A molecular-dynamics study of structural correlations.* Phys. Rev. B, 41:12197–12209, Jun 1990. Citado na página 60.

[133] Hess, Berk, Carsten Kutzner, David Van Der Spoel e Erik Lindahl: *GROMACS 4: algorithms for highly efficient, load-balanced, and scalable molecular simulation.* Journal of chemical theory and computation, 4(3):435–447, 2008. Citado na página 63.

[134] Thompson, A. P., H. M. Aktulga, R. Berger, D. S. Bolintineanu, W. M. Brown, P. S. Crozier, P. J. in 't Veld, A. Kohlmeyer, S. G. Moore, T. D. Nguyen, R. Shan, M. J. Stevens, J. Tranchida, C. Trott e S. J. Plimpton: *LAMMPS - a flexible simulation tool for particle-based materials modeling at the atomic, meso, and continuum scales.* Comp. Phys. Comm., 271:108171, 2022. Citado 2 vezes nas páginas 64 e 67.

[135] Tuckerman, M., B. J. Berne e G. J. Martyna: *Reversible multiple time scale molecular dynamics.* The Journal of Chemical Physics, 97(3):1990–2001, agosto 1992, ISSN 0021-9606. `https://doi.org/10.1063/1.463137`. Citado na página 64.

[136] Nosé, Shūichi: *A molecular dynamics method for simulations in the canonical ensemble.* Molecular Physics, 52(2):255–268, 1984. Citado na página 65.

[137] Unke, Oliver T., Stefan Chmiela, Huziel E. Sauceda, Michael Gastegger, Igor Poltavsky, Kristof T. Schütt, Alexandre Tkatchenko e Klaus Robert Müller: *Machine Learning Force Fields.* Chemical Reviews, 121(16):10142–10186, 2021. PMID: 33705118. Citado na página 70.

[138] Artrith, Nongnuch e Alexander Urban: *An implementation of artificial neural-network potentials for atomistic materials simulations: Performance for TiO2.* Computational Materials Science, 114:135–150, 2016, ISSN 0927-0256. Citado na página 70.

[139] Cooper, April M, Johannes Kästner, Alexander Urban e Nongnuch Artrith: *Efficient training of ANN potentials by including atomic forces via Taylor expansion and application to water and a transition-metal oxide.* npj Computational Materials, 6(1):54, 2020. Citado na página 70.

[140] Chen, Michael S, Tobias Morawietz, Hideki Mori, Thomas E Markland e Nongnuch Artrith: *AENET–LAMMPS and AENET–TINKER: Interfaces for accurate and efficient molecular dynamics simulations with machine learning potentials.* The Journal of Chemical Physics, 155(7), 2021. Citado na página 70.

[141] Hornik, Kurt, Maxwell Stinchcombe e Halbert White: *Multilayer feedforward networks are universal approximators*. Neural Networks, 2(5):359–366, 1989, ISSN 0893-6080. Citado na página 72.

[142] Rowe, Patrick, Volker L. Deringer, Piero Gasparotto, Gábor Csányi e Angelos Michaelides: *An accurate and transferable machine learning potential for carbon*. The Journal of Chemical Physics, 153(3):034702, julho 2020, ISSN 0021-9606. Citado na página 72.

[143] Ko, Tsz Wai e Shyue Ping Ong: *Recent advances and outstanding challenges for machine learning interatomic potentials*. Nature Computational Science, 3(12):998–1000, 2023. Citado na página 73.

[144] Behler, Jörg e Michele Parrinello: *Generalized Neural-Network Representation of High-Dimensional Potential-Energy Surfaces*. Phys. Rev. Lett., 98:146401, Apr 2007. Citado na página 73.

[145] Batatia, Ilyes, David P Kovacs, Gregor Simm, Christoph Ortner e Gábor Csányi: *MACE: Higher order equivariant message passing neural networks for fast and accurate force fields*. Advances in neural information processing systems, 35:11423–11436, 2022. Citado na página 74.

[146] Batatia, Ilyes, Philipp Benner, Yuan Chiang, Alin M. Elena, Dávid P. Kovács, Janosh Riebesell, Xavier R. Advincula, Mark Asta, Matthew Avaylon, William J. Baldwin, Fabian Berger, Noam Bernstein, Arghya Bhowmik, Samuel M. Blau, Vlad Cărare, James P. Darby, Sandip De, Flaviano Della Pia, Volker L. Deringer, Rokas Elijošius, Zakariya El-Machachi, Fabio Falcioni, Edvin Fako, Andrea C. Ferrari, Annalena Genreith-Schriever, Janine George, Rhys E. A. Goodall, Clare P. Grey, Petr Grigorev, Shuang Han, Will Handley, Hendrik H. Heenen, Kersti Hermansson, Christian Holm, Jad Jaafar, Stephan Hofmann, Konstantin S. Jakob, Hyunwook Jung, Venkat Kapil, Aaron D. Kaplan, Nima Karimitari, James R. Kermode, Namu Kroupa, Jolla Kullgren, Matthew C. Kuner, Domantas Kuryla, Guoda Liepuoniute, Johannes T. Margraf, Ioan Bogdan Magdău, Angelos Michaelides, J. Harry Moore, Aakash A. Naik, Samuel P. Niblett, Sam Walton Norwood, Niamh O'Neill, Christoph Ortner, Kristin A. Persson, Karsten Reuter, Andrew S. Rosen, Lars L. Schaaf, Christoph Schran, Benjamin X. Shi, Eric Sivonxay, Tamás K. Stenczel, Viktor Svahn, Christopher Sutton, Thomas D. Swinburne, Jules Tilly, Cas van der Oord, Eszter Varga-Umbrich, Tejs Vegge, Martin Vondrák, Yangshuai Wang, William C. Witt, Fabian Zills e Gábor Csányi: *A foundation model for atomistic materials chemistry*, 2024. `https://arxiv.org/abs/2401.00096`. Citado na página 74.

[147] Artrith, Nongnuch, Alexander Urban e Gerbrand Ceder: *Efficient and accurate machine-learning interpolation of atomic energies in compositions with many spe-*

cies. Phys. Rev. B, 96:014112, Jul 2017. https://link.aps.org/doi/10.1103/PhysRevB.96.014112. Citado na página 74.

[148] BROYDEN, C. G.: *The Convergence of a Class of Double-rank Minimization Algorithms 1. General Considerations*. IMA Journal of Applied Mathematics, 6(1):76–90, março 1970, ISSN 0272-4960. Citado na página 76.

[149] Car, R. e M. Parrinello: *Unified Approach for Molecular Dynamics and Density-Functional Theory*. Phys. Rev. Lett., 55:2471–2474, Nov 1985. https://link.aps.org/doi/10.1103/PhysRevLett.55.2471. Citado na página 78.

[150] Aagren, Hans, M. Aida, Jean Marie André, Paul Bagus, Deleep Bhattacharya, Jean Louis Brèdas, Nathan Brener, J. Callaway, Seisyou Chin, Zacharias Christidis, Enrico Clementi, Giorgina Corongiu, Ernest Davidson, T. Delbecque, Michel Dupuis, L. Evans, Abbas Farazdel, P. Ferron, Brian Feuston e E. Zhong: *MOTECC-90: Modern Techniques in Computational Chemistry. Input/Output Documentation*. IBM Corporation, janeiro 1990. Citado na página 78.

[151] Srivastava, G.P.: *The Physics of Phonons*. Routledge, 1990, ISBN 9780203736241. Citado na página 82.

[152] Feynman, R. P.: *Forces in Molecules*. Phys. Rev., 56:340–343, Aug 1939. https://link.aps.org/doi/10.1103/PhysRev.56.340. Citado na página 92.

[153] Tadano, T, Y Gohda e S Tsuneyuki: *Anharmonic force constants extracted from first-principles molecular dynamics: applications to heat transfer simulations*. Journal of Physics: Condensed Matter, 26(22):225402, may 2014. Citado na página 92.

[154] Baroni, Stefano, Stefano de Gironcoli, Andrea Dal Corso e Paolo Giannozzi: *Phonons and related crystal properties from density-functional perturbation theory*. Rev. Mod. Phys., 73:515–562, Jul 2001. https://link.aps.org/doi/10.1103/RevModPhys.73.515. Citado na página 92.

[155] Fox, M.: *Optical Properties of Solids*. Oxford Master Series in Physics. OUP Oxford, 2010, ISBN 9780199573363. Citado na página 93.

[156] Bührer, W. e P. Brüesch: *Phonons: Theory and Experiments II: Experiments and Interpretation of Experimental Results*. Springer Series in Solid-State Sciences. Springer Berlin Heidelberg, 2012, ISBN 9783642522635. https://books.google.com/books?id=nlTsCAAAQBAJ. Citado na página 94.

[157] Giannozzi, Paolo e Stefano Baroni: *Vibrational and dielectric properties of C60 from density-functional perturbation theory*. The Journal of chemical physics, 100(11):8537–8539, 1994. Citado na página 94.

[158] Gonze, Xavier e Changyol Lee: *Dynamical matrices, Born effective charges, dielectric permittivity tensors, and interatomic force constants from density-functional perturbation theory.* Physical Review B, 55(16):10355, 1997. Citado na página 94.

[159] Fuchs, Martin e Matthias Scheffler: *Ab initio pseudopotentials for electronic structure calculations of poly-atomic systems using density-functional theory.* Computer Physics Communications, 119(1):67–98, 1999. Citado na página 95.

[160] Li, T., X. Zhao, D. Yang, M. Du e L. Zhang: *Intrinsic defect properties in halide double perovskites for optoelectronic applications.* Phys. Rev. Applied, 10:041001, 2018. Citado na página 96.

[161] Murnaghan, F.: *The compressibility of media under extreme pressures.* Proc. Natl. Acad. Sci. USA, 30:244–247, 1944. Citado na página 96.

[162] Menedjhi, A., N. Bouarissa, S. Saib e K. Bouamama: *Halide double perovskite $Cs_2AgInBr_6$ for photovoltaic's applications: Optical properties and stability.* Optik, 243:167198, 2021. Citado na página 98.

[163] Chibani, S., O. Arbouche, M. Zemouli, K. Amara, Y. Benallou, Y. Azzaz, B. Belgoumène, A. Bentayeb e M. Ameri: *Ab initio prediction of the structural, electronic, elastic, and thermoelectric properties of half-Heusler ternary compounds TiIrX (X= As and Sb).* J. Electron. Mater, 47:196–204, 2018. Citado na página 100.

[164] Muhammad, S., Q. Mahmood, N. Singh e J. A. Larsson: *Ultralow Lattice Thermal Conductivity in Double Perovskite Cs_2PtI_6: A Promising Thermoelectric Material.* ACS Appl. Energy Mater, 3:11293–11299, 2020. Citado na página 100.

[165] Klarbring, Johan, Olle Hellman, Igor A. Abrikosov e Sergei I. Simak: *Anharmonicity and Ultralow Thermal Conductivity in Lead-Free Halide Double Perovskites.* Phys. Rev. Lett., 125:045701, Jul 2020. Citado na página 100.

[166] Lee, W., H. Li, A. B. Wong, D. Zhang, M. Lai, Y. Yu, Q. Kong, E. Lin, J. J. Urban, J. C. Grossman e P. Yang: *Ultralow thermal conductivity in all-inorganichalide perovskites.* Proc. Natl. Acad. Sci. USA, 114:8693–8597, 2017. Citado na página 100.

[167] Rabina, O., Y. Lin e M. Dresselhaus: *Anomalously high thermoelectric figure of merit in $Bi_{1-x}Sb_x$ nanowires by carrier pocket alignment.* Appl. Phys. Lett, 79:81–83, 2001. Citado na página 101.

[168] Takeuchi, T.: *Conditions of Electronic Structure to Obtain Large Dimensionless Figure of Merit for Developing Practical Thermoelectric Materials.* Mater. Trans, 50:2359–2365, 2009. Citado na página 101.

[169] Iqbal, S., G. Mustafa, M. Asghar, N. Noor, M. Iqbal, A. Mahmood e Y. Shin: *Tuning the optoelectronic and thermoelectric characteristics of narrow bandgap Rb_2AlInX_6(X= Cl, Br, I) double perovskites: A DFT study.* Mater. Sci. Semicond. Process, 143:106551, 2022. Citado na página 101.

[170] Haid, S., W. Benstaali, A. Abbad, B. Bouadjemi, S. Bentata e Z. Thermoelectric Aziz: *Structural, Optoelectronic and Magnetic properties of double perovskite Sr_2CrTaO_6: First principle Study.* Mater. Sci. Eng.: B, 245:68–74, 2019. Citado na página 101.

[171] Jiang, Jin Wu, Harold S Park e Timon Rabczuk: *Molecular dynamics simulations of single-layer molybdenum disulphide (MoS2): Stillinger-Weber parametrization, mechanical properties, and thermal conductivity.* Journal of Applied Physics, 114(6), 2013. Citado na página 104.

[172] Jiang, Jin Wu: *Parametrization of Stillinger–Weber potential based on valence force field model: application to single-layer MoS2 and black phosphorus.* Nanotechnology, 26(31):315706, jul 2015. Citado 2 vezes nas páginas 104 e 108.

[173] Ostadhossein, Alireza, Ali Rahnamoun, Yuanxi Wang, Peng Zhao, Sulin Zhang, Vincent H. Crespi e Adri C. T. van Duin: *ReaxFF Reactive Force-Field Study of Molybdenum Disulfide (MoS2).* The Journal of Physical Chemistry Letters, 8(3):631–640, 2017. PMID: 28103669. Citado na página 104.

[174] Dickinson, Roscoe G. e Linus Pauling: *THE CRYSTAL STRUCTURE OF MOLYBDENITE.* Journal of the American Chemical Society, 45(6):1466–1471, 1923. Citado na página 105.

[175] James, Philip B e MT Lavik: *The crystal structure of MoSe2.* Acta Crystallographica, 16(11):1183–1183, 1963. Citado na página 105.

[176] Grieder, Andrew C, Kwangnam Kim, Liwen F Wan, James Chapman, Brandon C Wood e Nicole Adelstein: *Effects of Nonequilibrium Atomic Structure on Ionic Diffusivity in LLZO: A Classical and Machine Learning Molecular Dynamics Study.* J. Phys. Chem. C, 128(21):8560–8570, 2024. Citado na página 108.

[177] Song, Zichen, Jian Han, Graeme Henkelman e Lei Li: *Charge-Optimized Electrostatic Interaction Atom-Centered Neural Network Algorithm.* J. Chem. Theory Comput., 20(5):2088–2097, 2024. Citado na página 108.

[178] Lim, Jinyoung, Youngseon Shim, Jaehong Park, Hongkee Yoon, Munbo Shim, Young Gu Kim e Dae Sin Kim: *Molecular Dynamics Study of Silicon Carbide Using an Ab Initio-Based Neural Network Potential: Effect of Composition and Temperature on Crystallization Behavior.* J. Phys. Chem. C, 127(46):22692–22703, 2023. Citado na página 108.

[179] Tornatzky, Hans, Roland Gillen, Hiroshi Uchiyama e Janina Maultzsch: *Phonon dispersion in* MoS_2. Phys. Rev. B, 99:144309, Apr 2019. Citado 3 vezes nas páginas 108, 109 e 110.

[180] Lee, Changgu, Hugen Yan, Louis E. Brus, Tony F. Heinz, James Hone e Sunmin Ryu: *Anomalous Lattice Vibrations of Single- and Few-Layer MoS2*. ACS Nano, 4(5):2695–2700, 2010. PMID: 20392077. Citado na página 109.

[181] Wieting, T. J. e J. L. Verble: *Infrared and Raman Studies of Long-Wavelength Optical Phonons in Hexagonal* MoS_2. Phys. Rev. B, 3:4286–4292, Jun 1971. Citado na página 109.

[182] Garg, A.K., H.K. Sehgal e O.P. Agnihotri: *Infrared optical properties of MoSe2*. Solid State Communications, 12(12):1261–1263, 1973, ISSN 0038-1098. Citado na página 109.

[183] Sun, Q. C., X. S. Xu, L. I. Vergara, R. Rosentsveig e J. L. Musfeldt: *Dynamical charge and structural strain in inorganic fullerenelike* MoS_2 *nanoparticles*. Phys. Rev. B, 79:205405, May 2009. Citado na página 109.

[184] Kandemir, Ali, Haluk Yapicioglu, Alper Kinaci, Tahir Çağın e Cem Sevik: *Thermal transport properties of MoS2 and MoSe2 monolayers*. Nanotechnology, 27(5):055703, jan 2016. Citado na página 110.

[185] Sekine, Tomoyuki, Mitsuru Izumi, Tsuneo Nakashizu, Kunimitsu Uchinokura e Etsuyuki Matsuura: *Raman Scattering and Infrared Reflectance in 2H-MoSe2*. Journal of the Physical Society of Japan, 49(3):1069–1077, 1980. Citado 2 vezes nas páginas 111 e 116.

[186] Jin, Mingge, Wei Zheng, Ying Ding, Yanming Zhu, Weiliang Wang e Feng Huang: *Raman Tensor of van der Waals MoSe2*. The Journal of Physical Chemistry Letters, 11(11):4311–4316, 2020. PMID: 32393031. Citado na página 111.

[187] Tongay, Sefaattin, Jian Zhou, Can Ataca, Kelvin Lo, Tyler S. Matthews, Jingbo Li, Jeffrey C. Grossman e Junqiao Wu: *Thermally Driven Crossover from Indirect toward Direct Bandgap in 2D Semiconductors: MoSe2 versus MoS2*. Nano Letters, 12(11):5576–5580, 2012. PMID: 23098085. Citado na página 111.

[188] Uchida, Shin ichi e Shoji Tanaka: *Optical phonon modes and localized effective charges of transition-metal dichalcogenides*. Journal of the Physical Society of Japan, 45(1):153–161, 1978. Citado na página 111.

[189] Lucovsky, G., R. M. White, J. A. Benda e J. F. Revelli: *Infrared-Reflectance Spectra of Layered Group-IV and Group-VI Transition-Metal Dichalcogenides*. Phys. Rev. B, 7:3859–3870, Apr 1973. Citado na página 111.

[190] Wieting, T. J. e J. L. Verble: *Infrared and Raman Investigations of Long-Wavelength Phonons in Layered Materials*, página 385. Springer Netherlands, Dordrecht, 1979, ISBN 978-94-009-9370-9. Citado na página 111.

[191] Garg, A.K., H.K. Sehgal e O.P. Agnihotri: *Infrared optical properties of MoSe2*. Solid State Communications, 12(12):1261–1263, 1973, ISSN 0038-1098. Citado na página 111.

[192] Hancock, Steven B., David P. Landau, Neda Alsadat Aghamiri e Yohannes Abate: *Langevin dynamics/Monte Carlo simulations method for calculating nanoscale dielectric functions of materials*. Phys. Rev. Mater., 6:076001, Jul 2022. Citado na página 111.

[193] Ponomareva, I., L. Bellaiche, T. Ostapchuk, J. Hlinka e J. Petzelt: *Terahertz dielectric response of cubic* $BaTiO_3$. Phys. Rev. B, 77:012102, Jan 2008. Citado na página 111.

[194] Wieting, T. J. e J. L. Verble: *Infrared and Raman Studies of Long-Wavelength Optical Phonons in Hexagonal* $Mo S_2$. Phys. Rev. B, 3:4286–4292, Jun 1971. Citado na página 113.

[195] Sahoo, Satyaprakash, Anand P. S. Gaur, Majid Ahmadi, Maxime J. F. Guinel e Ram S. Katiyar: *Temperature-Dependent Raman Studies and Thermal Conductivity of Few-Layer MoS2*. The Journal of Physical Chemistry C, 117(17):9042–9047, 2013. Citado 2 vezes nas páginas 113 e 115.

[196] Wilson, J.A. e A.D. Yoffe: *The transition metal dichalcogenides discussion and interpretation of the observed optical, electrical and structural properties*. Advances in Physics, 18(73):193–335, 1969. Citado na página 115.

[197] Bhatt, Sandip V., M. P. Deshpande, Vasant Sathe, Rekha Rao e S. H. Chaki: *Raman spectroscopic investigations on transition-metal dichalcogenides MX2 (M = Mo, W; X = S, Se) at high pressures and low temperature*. Journal of Raman Spectroscopy, 45(10):971–979, 2014. Citado 2 vezes nas páginas 115 e 117.

[198] Najmaei, Sina, Pulickel M. Ajayan e J. Lou: *Quantitative analysis of the temperature dependency in Raman active vibrational modes of molybdenum disulfide atomic layers*. Nanoscale, 5:9758–9763, 2013. Citado na página 115.

[199] Paul, Suvodeep, Saheb Karak, Annie Mathew, Ankita Ram e Surajit Saha: *Electron-phonon and phonon-phonon anharmonic interactions in* $2H-\mathrm{Mo}X_2$ *($X = \mathrm{S}, \mathrm{Te}$): A comprehensive resonant Raman study*. Phys. Rev. B, 104:075418, Aug 2021. Citado na página 115.

[200] Pawbake, Amit S., Mahendra S. Pawar, Sandesh R. Jadkar e Dattatray J. Late: *Large area chemical vapor deposition of monolayer transition metal dichalcogenides and their temperature dependent Raman spectroscopy studies.* Nanoscale, 8:3008–3018, 2016. Citado na página 115.

[201] Yang, Mei, Xuerui Cheng, Yuanyuan Li, Yufen Ren, Miao Liu e Zeming Qi: *Anharmonicity of monolayer MoS2, MoSe2, and WSe2: A Raman study under high pressure and elevated temperature.* Applied Physics Letters, 110(9):093108, março 2017, ISSN 0003-6951. Citado na página 115.

[202] Lanzillo, Nicholas A., A. Glen Birdwell, Matin Amani, Frank J. Crowne, Pankaj B. Shah, Sina Najmaei, Zheng Liu, Pulickel M. Ajayan, Jun Lou, Madan Dubey, Saroj K. Nayak e Terrance P. O'Regan: *Temperature-dependent phonon shifts in monolayer MoS2.* Applied Physics Letters, 103(9):093102, agosto 2013, ISSN 0003-6951. Citado na página 115.

[203] Li, Zhiwei, Yawei Lv, Liwang Ren, Jia Li, Lingan Kong, Yujia Zeng, Quanyang Tao, Ruixia Wu, Huifang Ma, Bei Zhao *et al.*: *Efficient strain modulation of 2D materials via polymer encapsulation.* Nature communications, 11(1):1151, 2020. Citado na página 115.

[204] Conley, Hiram J., Bin Wang, Jed I. Ziegler, Richard F. Jr. Haglund, Sokrates T. Pantelides e Kirill I. Bolotin: *Bandgap Engineering of Strained Monolayer and Bilayer MoS2.* Nano Letters, 13(8):3626–3630, 2013. PMID: 23819588. Citado na página 115.

[205] Rice, C., R. J. Young, R. Zan, U. Bangert, D. Wolverson, T. Georgiou, R. Jalil e K. S. Novoselov: *Raman-scattering measurements and first-principles calculations of strain-induced phonon shifts in monolayer MoS_2.* Phys. Rev. B, 87:081307, Feb 2013. Citado na página 115.

[206] Basu, Nilanjan, Ravindra Kumar, D. Manikandan, Madhura Ghosh Dastidar, Praveen Hedge, Pramoda K. Nayak e Vidya Praveen Bhallamudi: *Strain relaxation in monolayer MoS2 over flexible substrate.* RSC Adv., 13:16241–16247, 2023. Citado na página 115.

[207] Cai, Yongqing, Jinghua Lan, Gang Zhang e Yong Wei Zhang: *Lattice vibrational modes and phonon thermal conductivity of monolayer MoS_2.* Phys. Rev. B, 89:035438, Jan 2014. Citado na página 115.

[208] Öper, Merve, Yahaya Shehu e Nihan Kosku Perkgöz: *Temperature-dependent Raman modes of MoS2/MoSe2 van der Waals heterostructures.* Semiconductor Science and Technology, 35(11):115020, 2020. Citado na página 117.

[209] Kumar, Deepu, Vivek Kumar, Rahul Kumar, Mahesh Kumar e Pradeep Kumar: *Electron-phonon coupling, thermal expansion coefficient, resonance effect, and phonon dynamics in high-quality CVD-grown monolayer and bilayer* $MoSe_2$. Phys. Rev. B, 105:085419, Feb 2022. Citado na página 117.

[210] Late, Dattatray J., Sharmila N. Shirodkar, Umesh V. Waghmare, Vinayak P. Dravid e C. N. R. Rao: *Thermal Expansion, Anharmonicity and Temperature-Dependent Raman Spectra of Single- and Few-Layer MoSe2 and WSe2.* ChemPhysChem, 15(8):1592–1598, 2014. Citado na página 117.

[211] Horzum, S., H. Sahin, S. Cahangirov, P. Cudazzo, A. Rubio, T. Serin e F. M. Peeters: *Phonon softening and direct to indirect band gap crossover in strained single-layer* $MoSe_2$. Phys. Rev. B, 87:125415, Mar 2013. Citado na página 117.

[212] Cheng, Xuerui, Liying Jiang, Yuanyuan Li, Huanjun Zhang, Chuansheng Hu, Shiyu Xie, Miao Liu e Zeming Qi: *Using strain to alter the energy bands of the monolayer MoSe2: A systematic study covering both tensile and compressive states.* Applied Surface Science, 521:146398, 2020, ISSN 0169-4332. Citado na página 117.

[213] Bertrand, PA: *Surface-phonon dispersion of* MoS_2. Physical Review B, 44(11):5745, 1991. Citado 2 vezes nas páginas 125 e 126.

[214] Patterson, C. H.: *Validity of the HREELS surface dipole selection rule at semiconductor surfaces: Si(001)-(2×1)H/D.* Europhysics Letters, 98(6):66001, jun 2012. `https://dx.doi.org/10.1209/0295-5075/98/66001`. Citado na página 125.

Appendix

APPENDIX A – List of Published Papers

The following publications resulted from this thesis:

1. "Thermoelectric properties of $M_2AgAlBr_6$ (M = K, Rb, Cs) double perovskites: A first principles study", G.B.G. de Souza, V.B. Nascimento, R. de Paiva, A.M. Rappe, Solid State Communications, **378**, 115399 (2024).

2. "Revealing the role of ripples in phonon modes for MoS_2 and $MoSe_2$: Insights from molecular dynamics and machine learning", G.B.G. de Souza, S.B. Hancock, D.P. Landau, Y. Abate, R. de Paiva, V.B. Nascimento, Physical Chemistry Chemical Physics, **27**, 16768 (2025) – Selected as Back Cover of Issue.

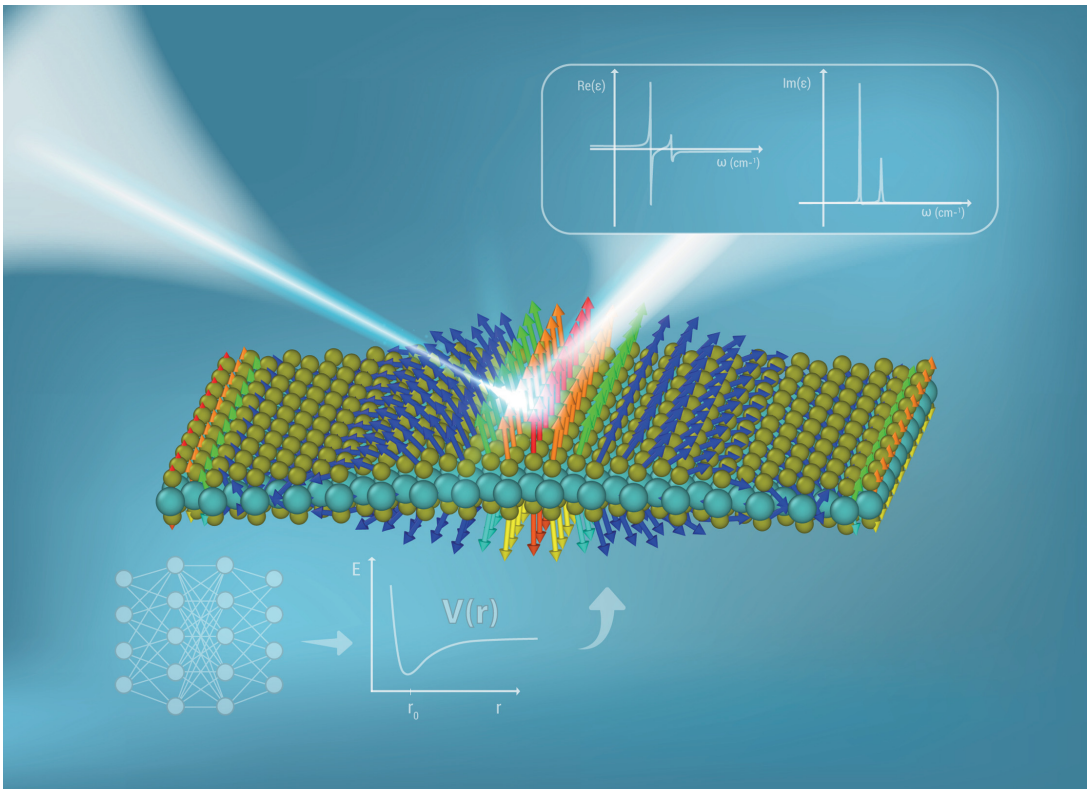

Showcasing research by Souza *et al.* from Universidade Federal de Minas Gerais and Universidade Federal de São João del Rei in Brazil, and University of Georgia and Johns Hopkins Applied Physics Laboratory in the USA.

Revealing the role of ripples in phonon modes for MoS_2 and $MoSe_2$: insights from molecular dynamics and machine learning

Machine learning potentials trained with *ab initio* data were developed for single-layers MoS_2 and $MoSe_2$ with the goal of reproducing their respective phonon dispersions. Molecular dynamics simulations using these newly developed potentials show that rippling caused by thermal fluctuations in the height of the layer can activate several vibrational modes in the infrared dielectric spectra for transition metal dichalcogenides.

Image reproduced by permission of Gabriel Bruno G. de Souza from *Phys. Chem. Chem. Phys.*, 2025, **27**, 16768.

Cover image created by Leonardo Bulhões.

As featured in:

See Gabriel Bruno G. de Souza *et al.*, *Phys. Chem. Chem. Phys.*, 2025, **27**, 16768.

ROYAL SOCIETY OF CHEMISTRY

rsc.li/pccp

Registered charity number: 207890

PCCP Owner Societies

Back Cover of *Phys. Chem. Chem. Phys., 2025,* **27**, *16768.*

APPENDIX B – List of Presentations

The results of this thesis have been presented at the following conferences and workshops:

1. De Souza, G. B., Hancock, S. B., Abate, Y., De Paiva, R., Landau, D. P., Nascimento, V. B. Revealing the role of ripples in phonon modes for MoS_2 and $MoSe_2$: Insights from molecular dynamics and machine learning. *Fronteiras Computacionais e Experimentais em Materiais Funcionais, UNESP - Bauru*, 2025. Invited Talk.

2. De Souza, G. B., Hancock, S. B., Abate, Y., De Paiva, R., Landau, D. P., Nascimento, V. B. Revealing the role of ripples in phonon modes for MoS_2 and $MoSe_2$: Insights from molecular dynamics and machine learning. *38th CSP Annual Workshop*, 2025. Contributed Talk.

3. De Souza, G. B., Hancock, S. B., Landau, D. P., Abate, Y., De Paiva, R., Nascimento, V. B. Combining *ab initio* accuracy and large-scale Molecular Dynamics with Machine Learning: an application on transition-metal dichalcogenides. *APS March Meeting*, 2024. Contributed Talk.

4. De Souza, G. B., Hancock, S. B., Landau, D. P., Abate, Y., De Paiva, R., Nascimento, V. B. Combining *ab initio* accuracy and large-scale Molecular Dynamics with Machine Learning: an application on transition-metal dichalcogenides. *37th CSP Annual Workshop*, 2024. Contributed Talk.

5. De Souza, G. B., Nascimento, V. B., Landau, D. P., Abate, Y., De Paiva, R., Hancock, S. B. A Machine Learning/Molecular Dynamics approach for dielectric properties calculations of nanomaterials. *CSP Lunch Seminar*, 2023. Seminar.

6. De Souza, G. B., Nascimento, V. B., De Paiva, R., Landau, D. P., Hancock, S. B., Abate, Y. Simulation of the dielectric properties through machine learning. *Encontro de Outono da Sociedade Brasileira de Física*, 2023. Contributed Talk.

7. De Souza, G. B., Hancock, S. B., Nascimento, V. B., Landau, D. P., De Paiva, R. Far-infrared dielectric properties on monolayer MoS_2: A Molecular Dynamics / Machine Learning approach. *XI Brazilian Meeting on Simulational Physics*, 2023. Poster.

APPENDIX C – Calculation of Eigenmodes on Rippled Supercell

The supercell used on the calculation of eigenmodes is included in Figure C.1 and was used for both MoS_2 and $MoSe_2$. This cell was constructed by the replication of the rectangular unit cell of $MoS(Se)_2$ (see green rectangle at Figure 4.1 at main manuscript). The unit cell was replicated 17 times in the direction of $\mathbf{a}_1$ and 10 times in the direction of $\mathbf{a}_2$, resulting on a approximately square cell with a total of 1020 atoms. In order to model the ripple, an overall sine function with wave vector parallel to the zig-zag direction (referred as $\mathbf{x}$ in the main text) and peak-to-peak amplitude of 1Å were added to the z component of each atom of the supercell:

$$\Delta z_i = (0.5\ \text{Å}) \times \sin\left(\frac{2\pi}{17a_0} x_i\right).$$

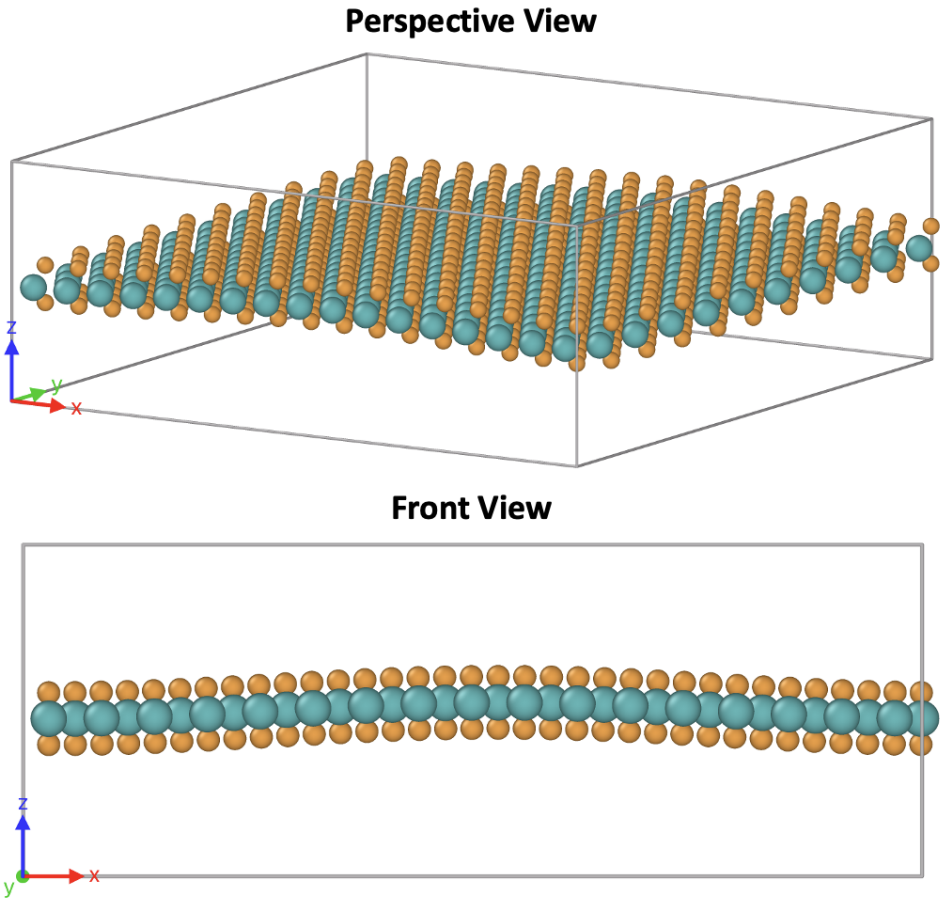

Figure C.1 – Supercell of 1020 atoms containing a sinusoidal wave in the x direction used in the calculation made by finite displacements.

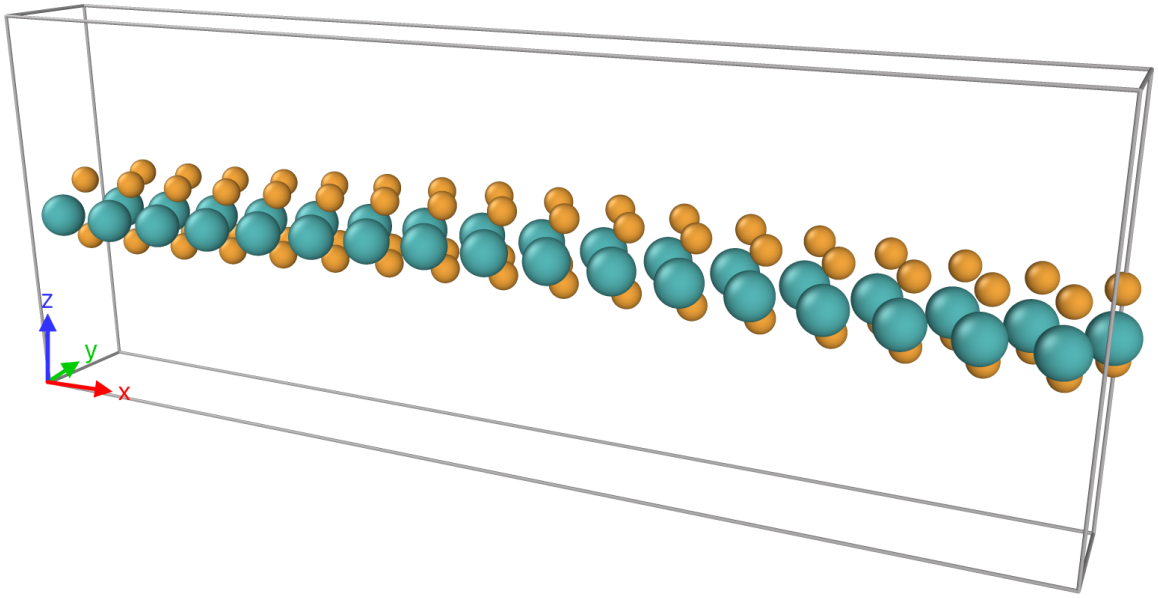

Figure C.2 – Primitive rippled cell of 102 atoms. The supercell at Figure C.1 is made by 10 units of this primitive cell repeated on the y (armchair) direction

The amplitude was chosen so that the deformed system is very similar to the original, but the perturbation allows a qualitative investigation of any new peaks in the spectra without losing correspondence of peaks between the perturbed and original systems. After adding the deformation, the energy of the model cell must be minimized to ensure that the dynamical matrix is being calculated at a local minimum of the energy. Minimization usually does not significantly affect the model structure and can eliminate strain in the **x** direction. After minimization, the dimensions for each cell were 54.26 Å$\times$ 55.28 Å for MoS_2 and 56.46 Å$\times$ 57.53 Å for $MoSe_2$. Alamode detected that this supercell can be assigned to a primitive cell with 102 atoms shown in Figure C.2. Therefore, the calculation resulted in a total of 306 eigenmodes, some of which were mentioned in the main manuscript.

APPENDIX D – Parallelization in LAMMPS

As suggested by its name — Large-scale Atomic/Molecular Massively *Parallel* Simulator — one of the defining features of LAMMPS is its capacity for massive *parallelization*. This capability is a key reason for its widespread adoption in the MD and material science community. Here, we briefly discuss the strategies and methods underlying LAMMPS parallel implementation, which enable efficient simulations of large-scale atomic and molecular systems.

At the core of the parallelization scheme is the *spatial decomposition* method. The simulation box is partitioned into smaller subdomains, each assigned to a different processor. Each processor is responsible for updating the positions, velocities, and forces of atoms within its respective subdomain. This decomposition ensures that the computational workload is evenly distributed, enabling *linear scaling* with the number of processors, provided that the system size is sufficiently large. Figure D.1 shows examples for distribution scheme for three types of simulation boxes. To compute interatomic interactions that cross subdomain boundaries, processors must exchange information about atoms located near these boundaries, commonly referred to as *ghost atoms*.

Communication between processors is essential to maintain data consistency and ensure accurate force calculations, being implemented through *explicit parallel communication routines*, which are highly optimized for distributed-memory jobs. The primary communication tasks include:

- **Atom Migration:** When an atom moves across a subdomain boundary, it must be *transferred* to the new owning processor.

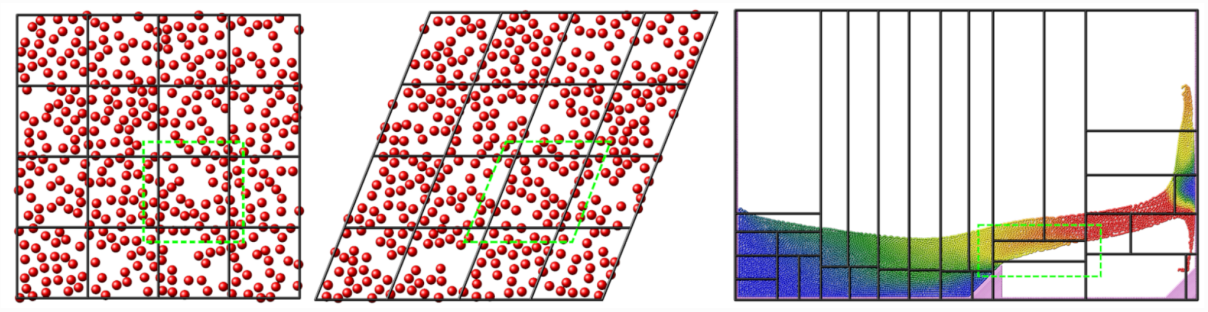

Figure D.1 – Spatial decomposition. The domain is divided into subdomains (black lines) for parallel processing: (Left) cubic system, (Center) triclinic system, and (Right) non-uniform distribution with load balancing. Green lines indicate communication regions. Reproduced from LAMMPS documentation, available at `https://docs.lammps.org/Developer_par_part.html`

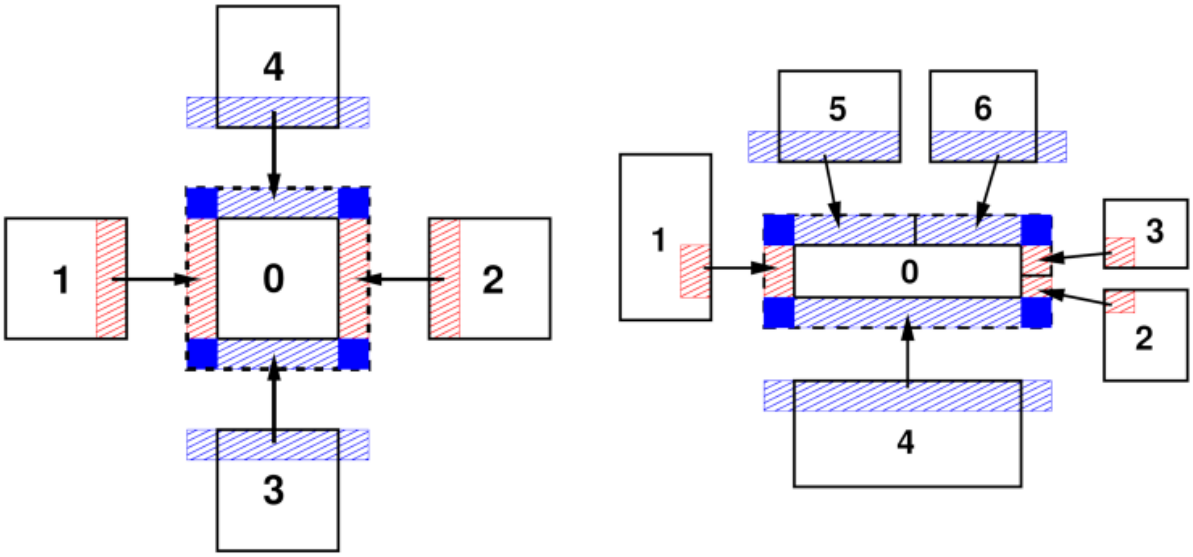

Figure D.2 – Ghost atom communication in LAMMPS: Processor 0 exchanges boundary atom data (red and blue regions) with neighboring processors - (Left) 1-4 in uniform, (Right) 1–6 in non-uniform grids - for force computations near subdomain interfaces. Reproduced from LAMMPS documentation `https://docs.lammps.org/Developer_par_comm.html`.

- **Ghost Atom Exchange:** Processors exchange information about atoms near their boundaries to compute *neighbor interactions* correctly.
- **Force Communication:** For force calculations involving shared atoms, processors may need to include interactions from multiple subdomains.

Figure D.2 illustrates the communication strategy employed by LAMMPS in domain-decomposed simulations. Subdomain of the simulation box (e.g., processor 0), and neighboring subdomains (e.g., processors 1–4 in uniform grids or 1–6 in non-uniform grids) must exchange information about atoms located near their shared boundaries. These "ghost atoms" (represented by the shaded red and blue regions), are required to accurately compute interatomic forces that extend beyond the local subdomain. This communication ensures that each processor has access to all necessary data within the cutoff radius.

LAMMPS utilizes the *Message Passing Interface (MPI)* standard to implement parallel communication. MPI is a widely adopted protocol for programming parallel computers, particularly effective for *distributed-memory systems*. Within LAMMPS, MPI functions are invoked to:

- *Send and receive* atom data between neighboring processors.
- *Synchronize* global operations, such as computing collective properties (e.g., energy, pressure).

- Perform *reduction operations* and *barrier synchronizations* as required by the simulation workflow.

The use of MPI enables LAMMPS to achieve *high-performance parallel efficiency*, minimizing communication overhead and ensuring scalability to hundreds of even thousands of processors. In summary, LAMMPS parallelization is based on an efficient *spatial decomposition* strategy coupled with *optimized communication routines* implemented via *MPI*. This design allows LAMMPS to simulate *large-scale atomic and molecular systems* with high computational efficiency.

Annex

ANNEX A – Python code for damped harmonic oscillator

```
import numpy as np
import matplotlib.pyplot as plt

# Parameters
m = 1.0
k = 1.0
gamma = 0.25
omega_0 = np.sqrt(k / m)
zeta = gamma / (2 * np.sqrt(k * m))
omega_d = omega_0 * np.sqrt(1 - zeta**2)

# Initial conditions
x0 = 1.0
v0 = 0.0

# Time setup
dt = 0.2
t = np.arange(0, 20, dt)

# Analytical solution
A = x0
B = (v0 + zeta * omega_0 * x0) / omega_d
x_analytical = np.exp(-zeta * omega_0 * t) * (A * np.cos(omega_d * t) + &
    B * np.sin(omega_d * t))

# Arrays for numerical solutions
x_euler, v_euler = [x0], [v0]
x_rk4, v_rk4 = [x0], [v0]
x_pc, v_pc = [x0], [v0]
x_leap, v_leap = [x0], [v0]
x_verlet = [x0]
x_verlet_prev = x0 - v0 * dt  # backward step for Verlet

# Force function
def accel(x, v):
    return -(k/m) * x - (gamma/m) * v

# Numerical Integration
for i in range(1, len(t)):
    # Euler
    a = accel(x_euler[-1], v_euler[-1])
    x_euler.append(x_euler[-1] + v_euler[-1] * dt)
    v_euler.append(v_euler[-1] + a * dt)

    # Runge-Kutta 4
    x, v = x_rk4[-1], v_rk4[-1]
    k1_v = accel(x, v)
    k1_x = v
```

```
49
50      k2_v = accel(x + 0.5 * k1_x * dt, v + 0.5 * k1_v * dt)
51      k2_x = v + 0.5 * k1_v * dt
52
53      k3_v = accel(x + 0.5 * k2_x * dt, v + 0.5 * k2_v * dt)
54      k3_x = v + 0.5 * k2_v * dt
55
56      k4_v = accel(x + k3_x * dt, v + k3_v * dt)
57      k4_x = v + k3_v * dt
58
59      x_rk4.append(x + (dt / 6) * (k1_x + 2 * k2_x + 2 * k3_x + k4_x))
60      v_rk4.append(v + (dt / 6) * (k1_v + 2 * k2_v + 2 * k3_v + k4_v))
61
62      # Predictor-Corrector
63      a = accel(x_pc[-1], v_pc[-1])
64      x_pred = x_pc[-1] + v_pc[-1] * dt
65      v_pred = v_pc[-1] + a * dt
66      a_pred = accel(x_pred, v_pred)
67      x_pc.append(x_pc[-1] + 0.5 * (v_pc[-1] + v_pred) * dt)
68      v_pc.append(v_pc[-1] + 0.5 * (a + a_pred) * dt)
69
70      # Leapfrog
71      v_half = v_leap[-1] + 0.5 * accel(x_leap[-1], v_leap[-1]) * dt
72      x_new = x_leap[-1] + v_half * dt
73      v_new = v_half + 0.5 * accel(x_new, v_half) * dt
74      x_leap.append(x_new)
75      v_leap.append(v_new)
76
77      # Verlet
78      a = accel(x_verlet[-1], (x_verlet[-1] - x_verlet_prev)/dt)
79      x_new = 2 * x_verlet[-1] - x_verlet_prev + a * dt**2
80      x_verlet_prev = x_verlet[-1]
81      x_verlet.append(x_new)
82
83
84
85  siz= 4
86  # Plotting
87  plt.figure(figsize=(10, 6))
88  plt.plot(t, x_euler, 'o--', markevery=1 , ms = siz,lw = 0.9, label='Euler')
89  plt.plot(t, x_rk4, 's--', markevery=1   , ms = siz,lw = 0.9, label='Runge-Kutta 4')
90  plt.plot(t, x_pc, 'd--', markevery=1    , ms = siz,lw = 0.9,
91          label='Predictor-Corrector')
92  plt.plot(t, x_leap, 'v--', markevery=1  , ms = siz,lw = 0.9, label='Leapfrog')
93  plt.plot(t, x_verlet, '^--', markevery=1, ms = siz,lw = 0.9, label='Verlet')
94  plt.plot(t, x_analytical, 'k-', label='Analytical',lw = 2)
95
96  plt.title(f'Integration Methods Comparison')
97  plt.xlabel('Time')
98  plt.ylabel('x(t)')
99  plt.ylim(-1.1,1.1)
100 plt.legend()
101 plt.grid()
102 plt.show()
```

ANNEX B – LAMMPS Tutorial for Beginners

Introduction to LAMMPS Simulations

Author: Gabriel Bruno Garcia de Souza
Advisors: Von Braun Nascimento & David Paul Landau

Introduction

LAMMPS (Large-scale Atomic/Molecular Massively Parallel Simulator) is a powerful, open-source code used for simulating the behavior of atoms, molecules, and particles. It's widely used in fields like materials science, chemistry, and physics to model systems from simple molecules to complex materials.

This tutorial is designed for beginners who are new to molecular dynamics simulations, although some previous knowledge of those methods are desired. We will walk you through the basics of how to set up and run a simple simulation using LAMMPS, step by step, with easy-to-follow explanations. By the end of this tutorial, you will:

- Understand the basic structure of a LAMMPS simulation.
- Know how to create an input file and run your first LAMMPS simulation.
- Learn how to view and interpret your simulation results.

This guide will provide you with the essential knowledge to start using LAMMPS in your molecular dynamics projects, helping you focus on learning the underlying principles while taking advantage of an established tool to handle the simulation process.

1 Basic Structure of LAMMPS

Writing an input to run a simulation with LAMMPS is very similar to writing code. Although we are not writing the proper algorithm that we intend to use from scratch, learning how LAMMPS works requires understanding what each command executes or defines and not understanding how a LAMMPS input is structured can lead to several errors while running the simulation. In that way, you can "debug" a LAMMPS input just like you debug a code and debugging skills can also be useful while writing a LAMMPS input before running a simulation.

To run a simulation using LAMMPS, one needs to write a series of **commands** in an input script (text file). Each command has a specific function and LAMMPS executes calculations by reading commands from this input script, one line at a time, and when the input script ends, LAMMPS exits and the simulation is finished. This means that each command causes LAMMPS to take some immediate action without regard for any commands that may be processed later. Commands may set an internal variable, read/write in a external file, or run a simulation. For the sake of clarity, commands will be grouped in five categories which we are going to explain one by one:

1. Initialization
2. System definition
3. Simulation settings
4. Visualization
5. Execution.

For a detailed explanation of each command discussed here, the reader is invited to access `https://docs.lammps.org/Manual.html`.

1.1 Initialization

Commands that belong to this section will compose the "head" of your input script and are supposed to make more basic definitions as units and boundary conditions. Let us look for a generic header for a LAMMPS input:

LAMMPS Header

```
# My First LAMMPS Input
units lj
atom_style atomic
dimension 3
processors * * *
boundary p p p
```

Each one of these commands will give a basic definition. The command `units` will define units for mass, distance, time, velocity, energy, forces, temperature, charge, etc. For example, writing "`units lj`" will set the system to work with reduced units, i.e., in terms of ε and σ used to parametrize a Lennard Jones potential[1]. Therefore, energies would be given in units of ε, distances in σ,forces in ϵ/σ, temperature in ε/k_B ($k_B = 1$), etc. On the other hand, writing "`units metal`" will set the energy to be in eV, distances in angstroms ($1\text{Å} = 10^{-10}$ m), forces in eV/Å, time in picoseconds ($1\text{ps} = 10^{-12}$ s), temperature in Kelvin, etc. Writing "`units si`" will set the simulation to be in the International System of units and so on.

The command `atom_style` will tell LAMMPS which attributes each atom will be assigned. The minimum subset of those attributes can be set with "`atom_style atomic`", which will assign an ID, a type, a position, a velocity and a force to each atom for simulation with point particles. Every other style is an extension of `atomic`, for example, "`atom_style charge`" will also assign a charge to each atom in addition to the original attributes and "`atom_style body`" will also assign a particle radius, angular momentum and torque to each particle for simulation with coarse grained models.

The command `dimension` will set the dimensionality of the simulation. Writing "`dimension 3`" will set a 3D simulation while "`dimension 2`" will set a 2D simulation.

The command "`processors`" will tell LAMMPS how the global simulation box will be partitioned among processors. Writing "`processors Px Py Pz`" such that `Px`×`Py`×`Pz` = Nº of processors will factorize the box so that there are Px processors in the x dimension and similarly for the y and z dimensions. If any of the three parameters is specified with an asterisk "*", LAMMPS will choose the number of processors in that direction of the grid automatically. For example, is very common to use "`processors * * 1`" for simulations with 2D systems.

The command "`boundary`" will set boundary conditions for each direction. The style `p` means the direction is periodic while styles `f`, `s`, `m` means the direction is non-periodic, each with their own peculiarity. For example, writing "`boundary p p p`" will tell LAMMPS to set periodic boundary conditions on all three directions while writing "`boundary p p f`" will tell LAMMPS to set periodic boundary conditions on the x and y directions and non-periodic on the z direction.

1.2 System Definition

Commands that belong to this section will be right after the header section and are supposed to define the region that the simulation will happen (also known as simulation box), create atoms inside this simulation box and assign attributes and interactions between the atoms. Let us look for the following example:

LAMMPS Simulation Cell

```
# Simulation Cell and Atoms
lattice fcc 6.0
region boxID block -10 10 -10 10 -10 10
create_box 1 boxID
create_atoms 1 box
```

The command "`lattice`" provides a quick way to specify some standard lattice patterns. On the example above, the command creates a face-centered cubic lattice to get started with a lattice constant of 6 units (if you used the command "`units metal`" before, the lattice constant will be 6 Å, hence the importance of the order of the commands while writing a LAMMPS input). Other possible lattices that can be set with

[1] As a reminder, the Lennard Jones potential is $E(r) = 4\varepsilon\left[\left(\frac{\sigma}{r}\right)^{12} - \left(\frac{\sigma}{r}\right)^{6}\right]$

this command are `sc`, `bcc`, `diamond` and `hcp` for simple cubic, body-centered cubic, diamond and hexagonal close packed lattices and 2D lattices also can be defined by using `sq` for square lattice and `hex` for hexagonal lattice for example.

The command "region" allows you to specify geometrical regions of the simulation box. On the example above, writing "region `boxID block` ..." after defining a lattice, you tell LAMMPS to make a region that it some multiple of the specified lattice constant (from -60 Å to 60 Å in the above case for each direction) and assigns this region to an identifier called "`boxID`".

The command "create_box" is used to construct the simulation box, differently from the previous command that only defines it. The number between the command and the identifier specifies the number of atom types that will be on the simulation. It is worth mentioning that both commands "region" and "create_box" does not create atoms inside the simulation box.

The command "create_atoms" is used to fill the simulation box with atoms. Writing "`create_atoms 1 box`" tells LAMMPS to fill the previously defined lattice with atoms of the type "1", putting one atom on every vertex of the lattice. There are other ways to fill the box with atoms, for example "`create_atoms 1 random`..." tells LAMMPS to fill the simulation box with atoms of the type "1" in random positions inside the box.

With the four lines on the example above, you are able to create a fcc lattice with atoms of one type using LAMMPS. There are other ways of creating a simulation box with atoms, for example, using the command "`read_data external_file`" tells LAMMPS to define and create the simulation box based on a external file which will have the definition of the lattice cell, the types of atoms and its positions. This cell can be replicated in any direction using the command "`replicate Nx Ny Nz`".

Having created the simulation box with atoms, now we need to tell LAMMPS how the atoms interact with each other, i.e., what is the potential energy between a pair of atoms of a given type. In order to define interatomic interactions, let us look for the following example:

Lennard Jones Interaction

```
# Define Atomic Masses and Interactions
mass 1 10.0

pair_style lj/cut 2.5
pair_coeff 1 1 2.0 3.5

neighbor 2.0 bin
neigh_modify every 3 delay 0 check yes
```

These commands will be responsible of defining atomic masses, interactions and listing neighbors respectively. The command "`mass 1 10.0`" assigns a mass of 10 units (for example, "units" is `metal`, masses are in atomic units, i.e., grams/mole) to the atom of type 1.

The command "pair_style" specifies the form of the interaction potential using during the simulation. Writing "`pair_style lj/cut 2.5`" tells LAMMPS that the atoms will interact with themselves according to the Lennard Jones potential and that a cutoff radius of 2.5 units (e.g. 2.5 σ if "`units lj`" or 2.5 Å if "`units metal`") will be used to defining neighbors per atom. Other forms of interaction potentials in LAMMPS can also be used, for example, `coul` for Coulomb potential, `buck` for Buckingham potential and `sw` for Stillinger-Weber potential. Once defined the type of potential, we need to define its parameters. This is accomplished by the command "pair_coeff", that will assign values for each parameter on the potential. Writing "`pair_coeff 1 1 2.0 3.5`" will tell LAMMPS that the Lennard Jones potential between atoms of type 1 will have the parameters $\varepsilon = 2.0$ (units of energy) and $\sigma = 3.5$ (units of distance). For each atomic type on the simulation, you will need to define at least one "pair_coeff". Parameters between different atomic types can also be defined by "pair_coeff" but, if not, LAMMPS will use their geometrical average as default. With those definitions, LAMMPS will have defined the interaction between atoms.

The last two commands on the above example will be related to the Verlet lists used to define neighbors of an atom. In this list, all atom pairs within a neighbor cutoff distance equal to the their force cutoff plus a value called "skin" distance are stored. The command "neighbor" is used to define this "skin" distance and writing "`neighbor 2.0 bin`" will tell LAMMPS that this skin distance is 2.0 units and the "binning" algorithm is used to create a list. In general, the larger the skin distance, the less often neighbor lists need to be built, but more pairs must be checked for possible force interactions every timestep. The command "neigh_modify" is used to define how often these neighbor lists are calculated. Writing "neigh_modify

`every 3 check yes`" tells LAMMPS to recalculate the neighbor lists every 3 timesteps, checking if any changes needs to be made on the lists. For the reader who is interested in these neighbor lists (also known as Verlet lists), we recommend the read of Chapter 5 of the book "Computer Simulation of Liquids" by Allen & Tildesley

1.3 Simulation Settings

Commands that belong to this section will be responsible to set the main conditions of the simulation, e.g., timesteps and fixed quantities. Let us look for the following example:

Simulation Settings

```
# Define Timestep, Initial Velocities and Ensemble
timestep 0.001
velocity all create 300 123456 dist gaussian
fix 1 all nvt temp 300 300 0.1
```

The command "`timestep`" specifies the timestep used on the molecular dynamics simulation, i.e., the size of the δt used between every iteration. Writing "`timestep 0.001`" tells LAMMPS that the timestep will be of 0.001 units. If "`units metal`" was defined earlier, the chosen timestep would be of 0.001ps = 1fs. If "`units lj`" was defined, the chosen timestep would be of 0.001 in reduced units.

The command "`velocity`" specifies the initial velocity of each atom before the simulation starts. Writing "`velocity all create 300 123456 dist gaussian`" will tell LAMMPS to create a set of velocities for all particles such that their average will correspond to 300 units of temperature (in "`units metal`" it would be 300 Kelvin). The option `all` is used to assign these velocities to all particles, the option `create` is used to create this set of velocities (other possible options are related to rescaling velocities on a simulation), the value `300` tells the desired temperature of the distribution of velocities, the number `123456` is a seed for the pseudo-random number generators and the option `dist gaussian` tells that the velocities will follow a gaussian distribution. Using this command, you prevent starting the simulation without any initial velocity for the atoms

In LAMMPS, the command "`fix`" is used on a set of very broad situations and for a lot of purposes such that getting used to them might be confusing. In a nutshell, a "`fix`" is any operation that is applied to the system during timestepping, with examples that include updating of atom positions and velocities due to time integration, controlling temperature, applying constraint forces to atoms, enforcing boundary conditions, computing quantities, etc. Here, the discussion will treat only "fixes" that can be used as thermostats of the system. The command "`fix ... nvt ...` " is responsible to assign a temperature to the simulation and "thermostatting" the system around this chosen temperature. This command is an implementation of the Nosé-Hoover thermostat in LAMMPS and can be described as follows: during the evolution of the equations of motion for a system with N particles, there are three quantities that are conserved during the simulation: Number of Particles (N), Volume (V), and Energy = Kinetic Energy + Potential Energy (E). Since there is no way to limit the conversion between potential energy and kinetic energy, there is no apparent way to define a temperature we want to use as a constraint during the simulation. What the Nosé-Hoover thermostat does is attach the N particle system to a external "heat bath" with a external degree of freedom. With that, the equations of motion of the system with this additional degree of freedom are solved and their related quantities are conserved. In those fixes, the the quantities being made constant are always in the name of the command, e.g., "`fix ... nvt ...`" or "`fix ... npt ...`" in which you also attach the system to a barostat to make the pressure (P) constant.

Writing "`fix 1 all nvt temp 300 300 0.1`" tells LAMMPS to thermostat the system around 300K throughout all the simulation using the Nosé Hoover thermostat. The value "`1`" assigns an identifier for this fix, the keyword "`temp T_i T_f`" assigns an initial and final temperature for the simulation and the value "`0.1`" is a parameter that is controls the coupling between the thermostat and the real system (usually set to be around 100δt). Another way to define a thermostat for the system is using the Langevin thermostat by writing, instead of "`fix ... nvt ...`"

Langevin Thermostat

```
fix 1 all nve
fix 2 all langevin 300 300 0.1 123465 # last number is seed for random numbers
```

in which in the lines above, the simulation is being maintaining the energy constant, but a random force is added to the atoms to emulate the effects of temperature, also known as the Langevin thermostat.

1.4 Visualization

While running a simulation, it is very useful to be able to have your code to print some thermodynamic information (e.g., temperature, energy) in the screen of the terminal or in a external output file. These "logs" are useful to "debug" a LAMMPS script or verify if everything is working as expected. Also, suppose you want to make a movie of your simulation to include on a presentation. Those are tasks related to **visualization** and there are commands that are able to control these tasks. Let us look for the following example:

Visulization Settings

```
# Commands that prints information on screen
thermo_style custom step temp etotal press
thermo 50

# Commands that print atoms for movie
dump myDump all xyz 100 my_movie_file.xyz
dump_modify myDump element Ar
```

The command "thermo_style" specifies which thermodynamic quantities are printed on screen (or output file). The option `custom` tells LAMMPS that you would like to customize your style of printing instead of using the default one. On the way written above, LAMMPS will respectively print the number of timesteps taken so far, the temperature, the total energy and the pressure of the system. Other quantities are also possible to be printed, e.g., `vol` prints the volume of the simulation box (useful on a simulation using "`fix npt`"), `density` prints the density of the system and so on. The command "thermo" will simply tells how frequently you want those quantities to be printed. Writing "`thermo 50`" will tell LAMMPS to print those quantities once in every 50 timesteps.

The command "dump" is responsible to define an external file that will receive the position of the atoms once in every given amount of steps. Since for simulations of big systems these files take up a lot of space on disk, these files are commonly known as "dump files" in which LAMMPS "dumps" the positions of all atoms in it. Writing the command the way above will assign an identifier called "`myDump`" to this task, will tell LAMMPS to dump all the atoms with "`all`", will choose the format `.xyz` for the dump files (other possible formats are `.cfg`, `.trj`, etc.), will tell LAMMPS to dump the positions once every 100 timesteps and will call the dump file "`my_movie_file.xyz`". The last line "dump_modify `myDump element Ar`" will assign an label for the type ID of the atom, in case, the label for the element Argon. This last line is optional and ignoring it will just assign the label "1" instead of "Ar" for the type of the atoms in the dump file. A common option for visualizing simulation movie is the open-source software OVITO (`https://www.ovito.org/`)

1.5 Execution

The command regarding the proper execution of the molecular dynamics simulation, i.e., iterating of the timesteps and solving the equations of motion is perhaps the simplest one:

Running the Simulation

```
run 100000
```

That's it! You simply write "run" and the number of iterations you want to evolve the equations of motion (e.g., 100000 timesteps). This means that all the intricacy on the usage of LAMMPS is related to defining the thermodynamic quantities of interest in the correct way rather than the simulation itself. As LAMMPS processes the input script line by line, interpreting and executing the commands as they are read until reaching the "run" command at which LAMMPS interrupts the previous definitions and starts the simulation, if there is any incorrect or ill defined configuration in the script, LAMMPS will only give an error when it reaches the "run" command, potentially generating an error message at that point, even if it was not previously detected. When LAMMPS reaches "run" command while reading the input, the simulation starts and the information you told it to print on screen starts appearing, for example:

Typical LAMMPS Output

```
Step          Temp          TotEng         Press
      0   300           -1515723.6      975.99191
     50   185.75804     -1515721.7     -1577.9974
    100   203.22047     -1515717.9     -125.8266
    150   160.72101     -1515713.2      1174.9589
    (...)
```

Usually, the "run" command is the last one of your input script, located on its very bottom. However your script does not have to end on it. Suppose that you want to fix the temperature only for some part of the simulation (e.g., until the system is thermodynamically equilibrated) and then you want "turn off" the thermostat. You can write something like:

NVT to NVE example

```
(...)

fix 1 all nvt temp 300 300 0.1

(...)

run 10000

unfix 1
fix 2 all nve

run 50000
```

The "unfix" command will unset the constraint imposed by the "fix" with identifier "1" and, at the second time LAMMPS reaches the command "run", it will perform a simulation on the NVE ensemble, i.e., with Number of Particles, Volume and Energy fixed during the simulation. Also, you can tell lammps to print the final state of your simulation in a format you are able to use as an initial configuration for a next one:

Simulation Settings

```
(...)
run 100000

write_data final_state.lmp
```

The "write_data" command creates a file called `final_state.lmp` with the same format used by the "read_data" command. With that, you can use it as a "checkpoint" for the simulation, saving your progress and not have to perform the previous part again. After all this explanation, we are able to go for our first example.

2 Simulation of Argon atoms using LAMMPS

2.1 Input Script

This section contains an input script for a simulation of point particles which interact via a Lennard-Jones potential suitable for Argon atoms. You will be able to perform the same simulation of the system but now using LAMMPS and be able to compare the efficiency between it and a simulation made with the code you've written earlier this semester. You will also be able to check on how the simulation time decreases with the number of processors used on the simulation. with all the discussion made before start writing the script for a simulation with constant temperature:

LAMMPS Input for Argon Atom Simulation

```
# Specifying Characteristic of Simulation
units metal    # Time in Picoseconds, Energy in eV, ...
atom_style atomic   # Most Basic atom_style LAMMPS can Use
dimension 3
processors * * *    # Let LAMMPS automatically assign the processors
boundary p p p   # Periodic Boudary Conditions in all three directions

# Simulation Cell and Atoms
lattice fcc 8.0    # Face-centered cubic with a lattice constant of 8 Angstroms
region boxID block 0 8 0 8 0 8     # A box from 0 to 64 Angstroms in all directions
create_box 1 boxID    # Create the Simulation Box with one atomic type
create_atoms 1 box    # Create the atoms of type "1" with the FCC arrangement defined above


# Define Atomic Masses and Interactions
mass 1 39.948     # Mass in atomic units

pair_style lj/cut 9.0    # Cutoff radius is 9 Å
pair_coeff 1 1 1.0324e-2 3.405     # LJ parameters between type 1 in eV and Angstrom recpectively

neighbor 2.0 bin
neigh_modify every 5 delay 0 check yes
```

```
23 # Define Timestep, Initial Velocities and Temperature
24 timestep 0.001     # in picosseconds
25 velocity all create 300 123456 dist gaussian      # Maxwell-Boltzmann distribution for velocities
26
27 # Fixing Ensemble
28 fix 1 all nvt temp 300 300 0.1                 # Nose-Hoover Thermostat
29
30 # Commands that prints information on screen
31 thermo_style custom step temp etotal ke pe econverve
32 thermo 50
33
34 # Commands that print atoms for movie
35 dump myDump all xyz 100 simulation_argon.xyz
36 dump_modify myDump element Ar
37
38 # Start the Simulation With Fixed Temperautre
39 run 50000
40
41 # Turn off the Thermostat and fix NVE simulation
42 unfix 1
43 fix 1 all nve
44
45 # Change printed info on screen
46 thermo_style custom step temp etotal ke pe
47
48 # Start the Simulation With Fixed Energy
49 run 50000
```

Create a file called `in.argon` with the lines above. It will perform a simulation with 2048 Argon atoms with constant room temperature. The number of atoms in the simulation can be changed by changing the numbers in the `region` command. You can change the temperature of the simulation in the commands `velocity` and `fix nvt` and check how the motion of the atom changes. There are some things above that are worth explanation:

- This simulation contains two parts (each belonging to a `run` command): A simulation with constant temperature (Nosé-Hoover Thermostat) and with constant energy (without Thermostatting). This is a common practice in MD simulations in which we call the "NVT" part of the simulation as "Thermalization", i.e., perform a number of timesteps with the thermostat "on" to ensure the temperature is equilibrated around a desired value and then "turn off" the thermostat. It is not guaranteed that, after turning the thermostat off, the temperature is equilibrated, so you should always check the temperature on the NVE part of the simulation.
- We have the following printing style in line 9:

  ```
  thermo_style custom step temp etotal ke pe econverve
  ```

  Since, with the thermostat turned on, the total energy (`etotal = ke + pe`) is not conserved due to the coupling with the external heat bath. However, there is a conserved quantity (a sort of generalized energy) which accounts for the degree of freedom of the thermostat, and it can be printed with `econserve`. You can tell LAMMPS to print this quantity if you want to check your simulation is running without issues regarding the integration of the equations of motion, and to see how precise is your simulation and how changing parameters as timestep and cutoff radius change this precision.

2.2 Running LAMMPS

With the input script written, we are ready to run our simulation. We will be using one of UFMG Simulation Laboratory's computers run our simulations. Since LAMMPS is coded in such a way that allows very efficient executions in parallel (and this is the main reason why it became so popular), we will learn how to execute it in two ways: **serial** and **parallel**. By running LAMMPS in serial we will learn how to interpret the data in our outputs since it's the simplest case. Running LAMMPS in parallel should give the same results as running it in serial, but we will learn how to check the optimal number of processors to run a job. There comes a stage in which adding processors to a job does not improve the simulation time due to communications between processors.

2.2.1 Serial Execution

Let's first login in one of the computers. After you open your terminal, you will run the command

```
ssh -p${PORT} ${YOUR_USERNAME}@${COMPUTER_NAME}.fisica.ufmg.br
```

and type your password. As in the Shell programming language, you will substitute each `${...}` for what the space is asking for, i.e., `${YOUR_USERNAME}` for the username you chose for your account, `${COMPUTER_NAME}` for the name of the computer and `${PORT}` by the port chosen for that computer. A version of LAMMPS will be already compiled in a folder that is in your directory. Inside the LAMMPS folder there will be another folder called "`src/`" and inside that one you will find two executable files: "`lmp_serial`" and "`lmp_mpi`". If you type

```
${PATH_TO_LAMMPS}/lmp_serial
```

and substitute `${PATH_TO_LAMMPS}` with all the path from your directory until the LAMMPS executable (e.g., `~/lammps-stable_2Aug2023/src`). You can check if it loaded correctly by executing "`lmp_serial`"[2]. If everything loaded properly, in your screen should appear

```
LAMMPS (23 Jun 2022 - Update 4)
OMP_NUM_THREADS environment is not set. Defaulting to 1 thread. (src/comm.cpp:98)
  using 1 OpenMP thread(s) per MPI task
```

and then LAMMPS waits for the next command to be given. You can exit LAMMPS by typing "`quit`". There are two ways to run LAMMPS with the input file. The first is

```
${PATH_TO_LAMMPS}/lmp_serial -in in.argon
```

which will write the output of the run in the screen of your terminal (except any dump files you told it do create during the simulation). The other way is

```
${PATH_TO_LAMMPS}/lmp_serial -in in.argon > out.argon
```

which, instead of writing things on the terminal screen, will write the same output in a file called "`out.argon`" and the terminal will "hang" while the simulation is running. You will run the second command so that we can go through the output file line by line. After your simulation is completed (when you be able to execute bash commands again), open the output file "`out.argon`" (you can use `nano`, `vim` or whatever you are most used to). The first lines of your output file should be

LAMMPS Output

```
1  LAMMPS (23 Jun 2022 - Update 4)
2  OMP_NUM_THREADS environment is not set. Defaulting to 1 thread. (src/comm.cpp:98)
3    using 1 OpenMP thread(s) per MPI task
4  Lattice spacing in x,y,z = 8 8 8
5  Created orthogonal box = (0 0 0) to (64 64 64)
6    1 by 1 by 1 MPI processor grid
7  Created 2048 atoms
8    using lattice units in orthogonal box = (0 0 0) to (64 64 64)
9    create_atoms CPU = 0.000 seconds
10 Generated 0 of 0 mixed pair_coeff terms from geometric mixing rule
11 Neighbor list info ...
12   update every 5 steps, delay 20 steps, check yes
13   max neighbors/atom: 2000, page size: 100000
14   master list distance cutoff = 11
15   ghost atom cutoff = 11
16   binsize = 5.5, bins = 12 12 12
17   1 neighbor lists, perpetual/occasional/extra = 1 0 0
18   (1) pair lj/cut, perpetual
19       attributes: half, newton on
20       pair build: half/bin/atomonly/newton
21       stencil: half/bin/3d
22       bin: standard
23 Setting up Verlet run ...
24   Unit style    : metal
25   Current step  : 0
26   Time step     : 0.001
```

[2] You can use "`mpirun -np 1 ${PATH_TO_LAMMPS}/lmp_mpi` instead of "`${PATH_TO_LAMMPS}/lmp_serial`" if you want.

which are the lines printed before the simulation starts. It's worth say that not every command in the input file produces a line in the output file so that we focus in the ones that produce. Lines 1-3 are always printed by default and only means that LAMMPS is being initialized. Line 4 is created by command `lattice`. Lines 5-6 are created by command `create_box` and lines 7-9 created by command `create_atoms`. All lines after 10 are created by command `run`, which means that when LAMMPS reaches the line `run`, it does the final definitions regarding neighboring lists and prints some parameters of the simulation (e.g., the chosen timestep, the units being used, etc.) and starts to run the simulation. The following lines are printed while the simulation in being ran.

```
   Step          Temp          TotEng         KinEng         PotEng       Econserve
         0   300           55.095638      79.378655     -24.283017      55.095638
        50   301.0391      55.083472      79.653595     -24.570123      55.095639
       100   303.62377     54.853251      80.337489     -25.484238      55.065822
       150   305.38097     53.674717      80.802437     -27.127719      54.941534
       200   302.37915     51.016878      80.008167     -28.99129       54.825784
       250   296.90426     49.208534      78.559536     -29.351001      54.734441
       300   289.6149      48.800487      76.630804     -27.830317      54.66529
       350   292.41518     49.618672      77.371746     -27.753074      54.618527
       400   300.4081      51.141821      79.486637     -28.344815      54.577608
       450   308.25551     52.151399      81.563027     -29.411628      54.55123
       500   310.27738     51.955681      82.098005     -30.142323      54.529822
       550   306.76122     50.505408      81.167645     -30.662237      54.512104
       600   303.31978     48.774784      80.257055     -31.482271      54.499745
       650   303.08262     47.677362      80.194302     -32.516939      54.49961
       700   302.78778     46.834703      80.116288     -33.281586      54.499255
       750   302.00804     45.951383      79.909972     -33.958589      54.496003
       800   300.21649     45.009454      79.435938     -34.426484      54.490994
      (...)
     49800   295.26677     42.491927      78.126263     -35.634336      54.418017
     49850   297.07219     43.046639      78.603969     -35.55733       54.409671
     49900   303.18942     43.83165       80.222562     -36.390912      54.407473
     49950   305.16291     44.257511      80.744738     -36.487227      54.407627
     50000   303.18849     44.039257      80.222315     -36.183058      54.409079
```

Notice that the simulation start at 300K (because of the command `velocity`) and does not keep fixed exactly at this value but rather oscillates around it. This is the effect of the thermostatting which takes the instantaneous temperature given by the kinetic energy ($KE = 3k_BT/2$) and rescales it to be always around the desired temperature (300K in our case). Also, notice that `Econserve` variates less than `TotEng` since, with the thermostat on, the first quantity is supposed not to change. You can verify the precision of your simulation by plotting the `Econserve` column by the `Step` column (by using `gnuplot` or `matplotlib`) and do the same plot for different choices of timestep (do 0.01, 0.005, 0.002, 0.001 for example). You'll notice that as the chosen timestep decreases, the amplitude of the oscillation will be smaller and smaller. You might want to divide the `Econserve` column by the number of atoms since it's a extensive quantity. After these 50000 steps you'll have completed the first part of your simulation in which the temperature is fixed. After that LAMMPS will print the following:

```
Performance: 128.626 ns/day, 0.187 hours/ns, 1488.725 timesteps/s
99.2% CPU use with 1 MPI tasks x 1 OpenMP threads

MPI task timing breakdown:
Section |  min time  |  avg time  |  max time  |%varavg| %total
---------------------------------------------------------------
Pair    | 29.269     | 29.269     | 29.269     |   0.0 | 87.15
Neigh   | 1.0531     | 1.0531     | 1.0531     |   0.0 |  3.14
Comm    | 0.58002    | 0.58002    | 0.58002    |   0.0 |  1.73
Output  | 1.1434     | 1.1434     | 1.1434     |   0.0 |  3.40
Modify  | 1.4282     | 1.4282     | 1.4282     |   0.0 |  4.25
Other   |            | 0.1122     |            |       |  0.33

Nlocal:           2048 ave        2048 max        2048 min
Histogram: 1 0 0 0 0 0 0 0 0 0
Nghost:           2928 ave        2928 max        2928 min
Histogram: 1 0 0 0 0 0 0 0 0 0
Neighs:          44342 ave       44342 max       44342 min
Histogram: 1 0 0 0 0 0 0 0 0 0

Total # of neighbors = 44342
Ave neighs/atom = 21.651367
Neighbor list builds = 525
Dangerous builds = 0
```

Those lines are related to the usage of CPU by specific tasks on LAMMPS and are not important for our purposes. It says how much time in total will have been used on tasks like constructing neighbor lists, calculating interactions, writing in output file, communicating between processors, etc.

After that, LAMMPS will turn off the thermostat by reading the lines "`unfix 1`" and "`fix 1 all nve`", change the `thermo_style` and start a simulation with fixed energy. The last lines above will be followed by:

```
Generated 0 of 0 mixed pair_coeff terms from geometric mixing rule
Setting up Verlet run ...
  Unit style    : metal
  Current step  : 50000
  Time step     : 0.001
Per MPI rank memory allocation (min/avg/max) = 4.369 | 4.369 | 4.369 Mbytes
   Step          Temp          TotEng         KinEng         PotEng
     50000   303.18849      44.039257      80.222315     -36.183058
     50050   302.22262      44.038299      79.966749     -35.92845
     50100   301.54314      44.043959      79.786963     -35.743004
     50150   303.55348      44.050869      80.31889      -36.268022
     50200   303.48451      44.055531      80.300641     -36.245111

     (...)

     99800   303.53399      44.06055       80.313733     -36.253183
     99850   303.78079      44.061536      80.379036     -36.3175
     99900   305.19171      44.063306      80.752358     -36.689053
     99950   305.14737      44.056495      80.740627     -36.684132
    100000   304.3752       44.0571        80.536314     -36.479214
Loop time of 32.7407 on 1 procs for 50000 steps with 2048 atoms

Performance: 131.946 ns/day, 0.182 hours/ns, 1527.151 timesteps/s
99.7% CPU use with 1 MPI tasks x 1 OpenMP threads

MPI task timing breakdown:
Section |  min time  |  avg time  |  max time  |%varavg| %total
---------------------------------------------------------------
Pair    | 29.347     | 29.347     | 29.347     |   0.0 | 89.63
Neigh   | 1.0538     | 1.0538     | 1.0538     |   0.0 |  3.22
Comm    | 0.58044    | 0.58044    | 0.58044    |   0.0 |  1.77
Output  | 0.98349    | 0.98349    | 0.98349    |   0.0 |  3.00
Modify  | 0.66409    | 0.66409    | 0.66409    |   0.0 |  2.03
Other   |            | 0.1118     |            |       |  0.34

Nlocal:           2048 ave        2048 max        2048 min
Histogram: 1 0 0 0 0 0 0 0 0 0
Nghost:           2894 ave        2894 max        2894 min
Histogram: 1 0 0 0 0 0 0 0 0 0
Neighs:          44286 ave       44286 max       44286 min
Histogram: 1 0 0 0 0 0 0 0 0 0

Total # of neighbors = 44286
Ave neighs/atom = 21.624023
Neighbor list builds = 525
Dangerous builds = 0
Total wall time: 0:01:06
```

This means that it set up another run, performed it and finished it by printed the CPU information just as before. The very last line printed in this LAMMPS output is "`Total wall time:  0:01:06`" which tells the time spent on the simulation in the format `HH:MM:SS`. Let's focus on the lines printed while the simulation is being ran (the column lines).

Firstly, you will notice that, despite the thermostat was turned off, the system was properly equilibrated and the temperature keeps oscillating around 300K. This means the thermalization was successful. Secondly, you will notice that the `Econserve` column is not being plotted anymore. In fact, since we have turned off the thermostat, we decoupled the system from the additional degree of freedom such that `TotEng` becomes a conserved quantity again. If you plot the `TotEng` column in terms of the `Step` column for the NVE part of the simulation, you will notice that the oscillations have the same order of magnitude as plotting `Econserve` in terms of `Step` for the NVT part of the simulation. An example of this output can be found at Fig. 1. You will notice that in the NVT part of the simulation, the total energy has a bigger oscillation than `Econserve` which suddenly drops when the simulation enters NVE regime. In fact, `Econserve` in NVT and total energy in NVT are conserved quantities and their variation is only due to numerical imprecisions. Fig. 1 also shows the evolution of temperature during both regimes. You will notice that oscillations in the temperature are also bigger in the NVT regime and that they also drop when the thermostat is turned off. You can also

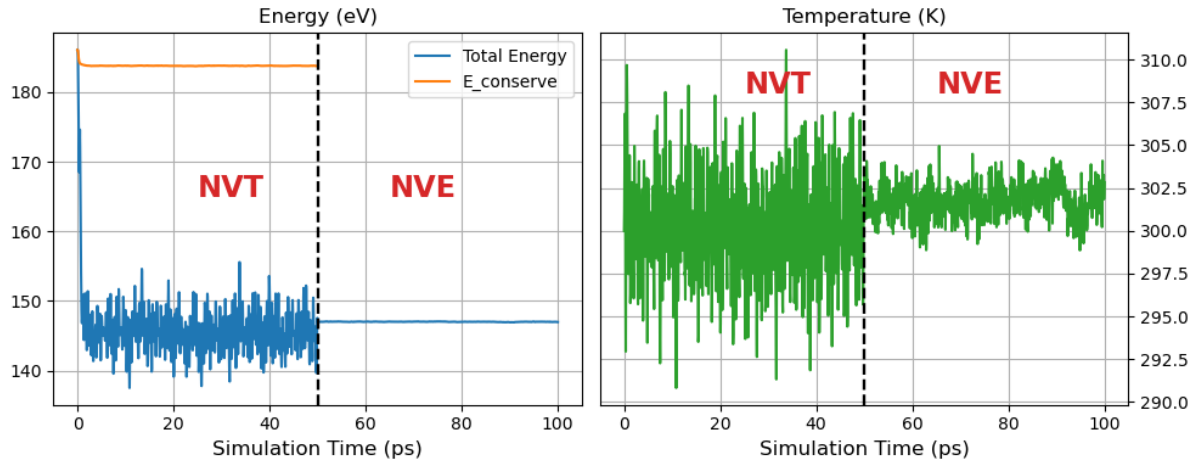

Figure 1: (Left) Total Energy and `Econserve` evolution during simulation. (Right) Temperature evolution during simulation. Both plots contains the NVT and NVE part of the simulation.

notice that, even without the thermostat, the temperatures keeps oscillating around 300K, showing that the system was properly thermalized.

You will notice on your directory that a file called `simulation_argon.xyz` was created. This is the file with the movie of your simulation and we encourage you to watch it with a visualization software like OVITO. Depending of the number of atoms of your simulation and how often you told LAMMPS to dump the coordinates, these files can become very big and opening them will take a lot of time. If you don't want LAMMPS to generate this file, you can comment the "dump" related commands in the input file since they take some time of your simulation to write the coordinates in the external file in every fixed amount of steps:

```
# dump myDump all xyz 100 simulation_argon.xyz
# dump_modify myDump element Ar
```

2.2.2 Parallel Execution

After we run LAMMPS serially and dissected its output, we are ready to run it in parallel. There will be no major differences between the output of both runs. Before the execution, we recommend the following changes in `in.argon`:

- Increase the number of atoms of you simulation to 6912 by changing line 10 of your the script to

  ```
  region boxID block 0 12 0 12 0 12
  ```

  The effects of parallelization are more noticeable when the more atoms it has. This simulation should take around 4 minutes to finish in one processor.

- Comment the "dump" related lines as above since those files can become very big and will not be important for our analysis.

With those changes, you will start using the other executable to run your jobs.

```
mpirun -np ${NUM_PROC} ${PATH_TO_LAMMPS}/lmp_mpi
```

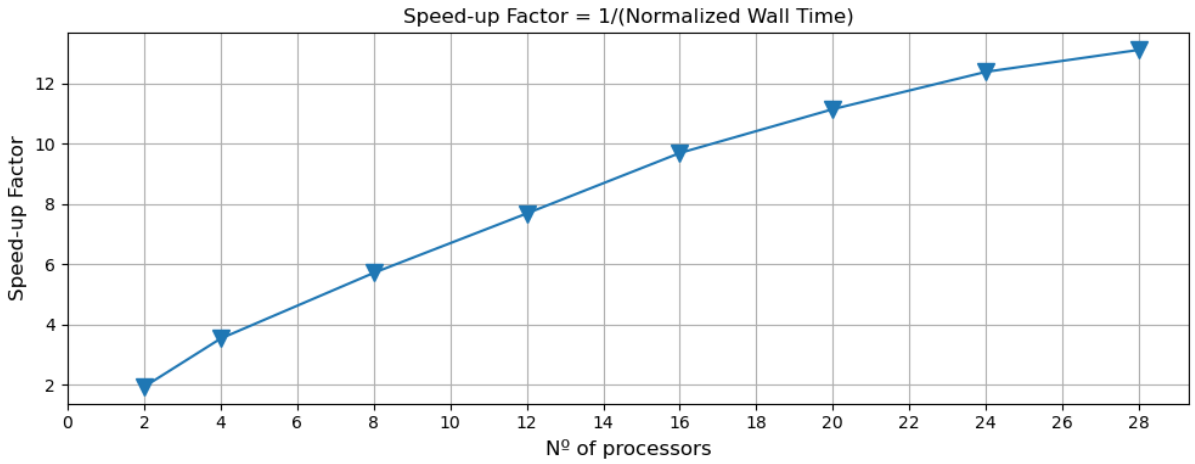

Figure 2: Speed-up Factor in terms of the number of processors. The speed-up factor is defined as the inverse of the wall time normalized by the serial wall time.

This time, you will use the Message Passing Interface (MPI) application to run LAMMPS. For example, if you want to run with 28 processors, you write

```
mpirun -np 28 ${PATH_TO_LAMMPS}/lmp_mpi -in in.argon > out.argon_28core
```

which means you use the flag "`-np`" and the number of processors to execute LAMMPS and after "`mpirun -np $NUMPROC`" the command is the same as before. In your output, you will notice, after LAMMPS creating the simulation box, it will say in lines 5-6

```
Created orthogonal box = (0 0 0) to (96 96 96)
2 by 4 by 4 MPI processor grid
```

which is different from the serial run which says "`1 by 1 by 1 MPI processor grid`". The way parallelism works in LAMMPS is by dividing the whole simulation box in a "grid" with different chunks, each one assigned to a processor. This grid can be specified in the input script by change the numbers beside the command "`processors`" but letting LAMMPS assign it automatically is the default. The rest of the output file is the same as the serial run.

Although LAMMPS allows efficient parallelization of the simulation, the scaling of simulation speed with number of processors is not linear but tends to saturate when a lot of processors are used. This is due to communication between processors: during a simulation, each processor has to communicate with others, for example, whether atoms leave these chunks to others, share information of the total energy of the system, etc. This communication can take time and affect the speed scaling. This can be tested in a simple way: doing a lot of simulations with different number of processors and track the time taken for it to finish. You can check the time by looking the last line of your output file or by executing the same command with the word `time` in the beginning

```
time mpirun -np 28 ${PATH_TO_LAMMPS}/lmp_mpi -in in.argon > out.argon_28core
```

which will print in screen the time after the execution. You will check always the "`real`" time.

Exercise: Run LAMMPS with the input script "`in.argon`" with 1, 2, 4, 8, 12, 16, 20, 24, 28 processors and track the wall time for each simulation to finish and then plot the simulation time vs. the number of processors. Also, divide all times obtained by the serial execution time and plot its inverse just as in Fig. 2. You will see that this factor will not correspond to the number of processors, and the greater the number of processors, the more different this factor will be from it and reaches a plateau.

3 More Examples

There are other two examples we would like to propose you to show show different ways to use the commands discussed above. It recommended to run the simulation in parallel due to the number of atoms in both systems.

3.1 Lennard Jones binary fluid

With this input we will explore a simulation of a Lennard Jones fluid made of two types of atoms with a single rule: strong interactions between atoms of same type and weak interactions between atoms of different types. It is a good example to exemplify the use of reduced units (`units lj`) and explore some new commands.

LAMMPS Input for LJ binary fluid

```
# Specifying Characteristic of Simulation
units    lj                                     # All units in terms of LJ parameters
atom_style    atomic                            # Most Basic atom_style LAMMPS can Use
dimension    3
processors    * * *                             # Let LAMMPS automatically assign the processors
boundary    p p p                               # Periodic Boudary Conditions in all three directions

# Simulation Cell and Atoms
region    boxID block 0 40 0 40 0 40            # A box from 0 to 40 units of sigma in all directions
create_box      2 boxID                         # Create the Simulation Box with two atomic types
create_atoms    1 random 2000 984512 boxID      # Create 2000 atoms of type "1" in random positions
create_atoms    2 random 2000 735173 boxID      # Create 2000 atoms of type "2" in random positions

# Define Atomic Masses and Interactions
mass 1 1                                        # Mass of 1 in arbitrary units
mass 2 1                                        # Mass of 2 in arbitrary units

pair_style    lj/cut 2.5                        # Cutoff radius is 2.5 times sigma
pair_coeff    1 1 5.0  1.5                       # LJ parameters for atom 1
pair_coeff    2 2 5.0  1.5                       # LJ parameters for atom 2
pair_coeff    1 2 0.05 1.5                       # LJ parameters for mixed Interactions

# Energy Minimization using conjugated gradient
thermo_style      custom step etotal            #
thermo      10                                  # Only for Minimization
minimize 1.0e-4 1.0e-6 1000 10000

# Verlet Lists definitions
neighbor    2.0 bin
neigh_modify    every 5 delay 20 check yes

# Timestep, Initial Velocities and Temperature
reset_timestep 0
timestep       0.005                            # in reduced LJ units
velocity       all create 1.0 123456 dist gaussian  # Temperature in reduced LJ units

fix    1 all npt temp 1.0 1.0 0.5 iso 0.1 0.1 5.0   # Nose Hoover Thermostat + Barostat

# Commands that prints information on screen
thermo_style      custom step temp etotal ke pe press vol
thermo      50

# Commands that print atoms for movie
dump             myDump all atom 100 sim_lj_fluid.atom

# Start the Simulation
run      20000
```

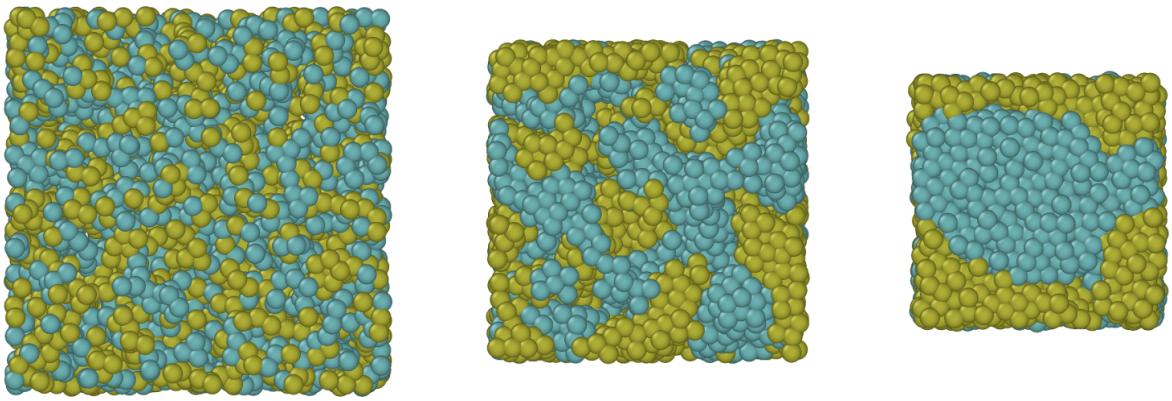

Figure 3: Snapshots taken at different times showing the particles of type 1 and type 2 of the Lennard Jones fluid progressively demixing and forming large demixed areas.

There are some commands worth discussing about the script above:

- This time, instead of using "`create_atoms`" to generate atoms in a lattice, we are creating a box as before but creating the atoms at random positions. Notice that now, the command "`create_box`" has a 2 instead of a 1, indicating that in that box will have two types of particles.
- Since atoms were created in random positions, it can happen of one atom to be so close to another such that their energy is too big. If we start the simulation with that configuration, the integrators will deal with huge numbers such that it will lead to overflow and numerical errors. Therefore, it was included the command "`minimize`" to move the initial configuration to a local minima of energy. Since the minimization steps are counted as timesteps in LAMMPS, we used the command "`reset_timestep`" to reset it to 0.
- In this simulation, if the volume is fixed, atoms can stay close to each other but leaving empty space (vacuum) between them. Since this is not desired, we instead to do a simulation with fixed volume, we do a simulation with fixed pressure which allows the simulation box to change to eliminate this empty space. In the command "`fix npt`", the system is coupled to a thermostat and a barostat. The option "`iso`" tells that all sides of the box will change proportionally to each other.

Our model is defined by the command "`pair_coeff`", in which we assign an interaction of 5ε for atoms of the same type and 0.05ε for mixed interactions. After running the simulation, you will notice that the system will start very mixed and then the particles of the same type will agglutinate forming clusters, resulting in the demixing of the system as shown in Fig. 3. **Question:** Do you know the minimum temperature to carry out a simulation at which the particles will remain mixed?

3.2 Heating and Cooling of Argon System

With this input we go back to simulating Argon atoms but will explore different kind of boundary conditions. The next input will start from a FCC lattice, will heat the system and cool it again.

LAMMPS Input for Heating and Cooling of Argon System

```
# Specifying Characteristic of Simulation
units     metal                                   # Time in Picoseconds, Energy in eV, ...
atom_style     atomic                             # Most Basic atom_style LAMMPS can Use
dimension     3
processors     * * *                              # Let LAMMPS automatically assign the processors
boundary     f f f                               # Fixed Boundary Conditions in all three directions

# Simulation Cell and Atoms
region         outer_box block 0 70 0 70 0 70 units box          # Full Simulation Box
region         inner_box block 20 50 20 50 20 50 units box         # Box used for create atoms

```

```
create_box    1 outer_box
lattice       fcc 4.58
create_atoms  1 region inner_box

# Assign reflective boundary conditions to walls
fix           r  all wall/reflect xlo 0.0 xhi 70 ylo 0.0 yhi 70 zlo 0.0 zhi 70 units box

# Define Atomic Masses and Interactions
mass          1 39.948
pair_style    lj/cut 9.0
pair_coeff    1 1 1.02383e-2 3.405

# Verlet Lists definitions
neighbor       2.0 bin
neigh_modify    every 5 delay 20 check yes

# Energy Minimization using conjugated gradient
thermo_style      custom step etotal                #
thermo      10                                      # Only for Minimization
minimize 1.0e-4 1.0e-6 1000 10000

# Timestep, Initial Velocities and Temperature
reset_timestep 0
timestep      0.01        # 0.01 ps = 10 fs
velocity      all create 1 102939 dist gaussian mom yes rot yes

# Commands that prints information on screen
thermo_style  custom step temp etotal press
thermo        100

# Commands that print atoms for movie
dump          dump_1 all  custom 200 sim_heat_cool.atom id type x y z vx vy vz

# Start motion of atoms
fix           1 all nve
run           1000
unfix         1

# Heat system up to room temperature
print         "################# HEATING ###################################"
variable      t1 equal temp
fix           2 all nvt temp $t1 300 1
run           30000
unfix         2

# Cool system down to next 0K
print         "################ COOLING ####################################"
variable      t2 equal temp
fix           3 all nvt temp $t2 0.0001 1
run           160000
unfix         3

fix           4 all nve
run           10000
```

There are some commands worth discussing about the script above:

- The command "`boundary f f f`" defines fixed boundary conditions in the three directions. This only means that atoms will not interact across the boundary and do not move from one side of the box to the other. However, to make the walls reflective, we need to use the command "`fix wall/reflect`", otherwise atoms will end up going outside the simulation box.
- You can notice that we have the definition of two regions: `outer_box` and `inner_box`, with the latter inside the first. In that case, we are telling LAMMPS to define a region where the whole simulation will happen (`outer_box`) that is bigger than the region where the atoms will be created (`inner_box`). LAMMPS will create atoms in a FCC arrangement such that they do not the entire box and have space to diffuse.
- You can notice that the input script tells LAMMPS to perform 1000 steps in NVE before start heating the system up to room temperature. This means that the heating is done in such a continuous and smooth way, instead of instantly assign a temperature and heating the system. The same is done in the end of the cooling process to guarantee this smoothness of the process.

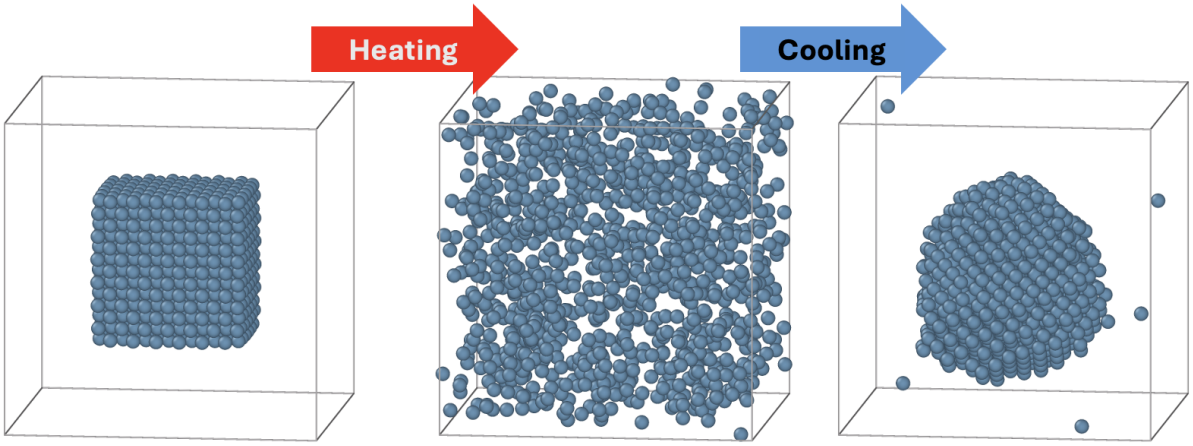

Figure 4: Snapshots of the Argon system taken before the simulation, after heating and after cooling respectively.

- You can notice the presence of the command "`variable`" above. In LAMMPS, you are able to define internal variables with this command. Variables are defined before the simulation starts such that its value is updated after every timestep. Those variables can be also passed to other commands, e.g., the command "thermo_style" in a way you are able to print the evolution of this variable during the simulation. In the case above, "`variable`" is being used to assign the instantaneous temperature to `t1` and `t2`, in order to pass those values to the "fixes" commands related to the heating and cooling of the system.
- the options `mom yes rot yes` in the command "`velocity`" were used in order to sort a set velocities to the particles in a way that the linear momentum and the angular momentum of their center of mass is zero, i.e., the initial system does not translates as a group neihter rotates around their center of mass. If you are curious, try to run the simulation wthout those options.
- The "`print`" has the purpose of printing a string on the screen (or output file).

After running the simulation, you can see in the movie that the system starts as FCC lattice, starts behaves like a gas after heating and condenses into some kind of lattice again after cooling similar to what is shown in Fig. 4. **Question:** By looking at the movie, can you guess the type of lattice that results after condensation? Is it face centered cubic (fcc)? Is it body centered cubic (bcc)? Is it hexagonal close packed (hcp)? **Hint:** Pick the last frame of the simulation and try to look at the system as layers of atoms stacked on each other. What is the type of lattice os that single layer and in how many different ways can you stack several layers upon each other?

4 Further Reading

- "Computer Simulation of Liquids" by Allen & Tildesley
- "The Art of Molecular Dynamics Simulation" by D. C. Rapaport
- `https://docs.lammps.org/Manual.html`